université
PARIS-SACLAY

Inclusive J/ψ production in pp and Pb-Pb collisions at forward rapidity at $\sqrt{s_{\mathrm{NN}}}$ = 5.02 TeV in ALICE at the LHC

Thèse de doctorat de l'Université Paris-Saclay

École doctorale n° 576, Particules, Hadrons, Énergie, Noyau, Instrumentation, Imagerie, Cosmos et Simulation (PHENIICS)

Spécialité de doctorat: physique hadronique

Unité de recherche: Université Paris-Saclay, CNRS, IJCLab, 91405, Orsay, France

Référent: Faculté des sciences d'Orsay

Thèse présentée et soutenue à Orsay, le 19/10/2020, par

Chun-Lu HUANG

Composition du jury:

Dr. Philippe Rosnet Professeur, Université Clermont Auvergne	Président
Dr. Cvetan Cheshkov Directeur de recherche, Université Claude Bernard Lyon 1	Rapporteur
Dr. Burkhard Schmidt Chercheur, CERN	Rapporteur
Dr. Alberto Baldisseri Directeur de recherche, Université Paris-Saclay	Examinateur
Dr. Elena Ferreiro Professeur, University of Santiago de Compostela	Examinatrice
Dr. Laure Massacrier Chercheur, Université Paris-Saclay	Examinatrice
Dr. Cynthia Hadjidakis Chercheur, Université Paris-Saclay	Directrice

Thèse de doctorat

NNT: 2020UPASP036

Acknowledgements

首先要感謝我的家人在這三年的博士學業中不時鼓勵我與支持我，沒有你們的陪伴我很難完成在法國的博士學位。由衷感謝章文箴老師當初讓我知道巴黎南區大學的博士生招生訊息，另外，我仍然記得您在2017年時到巴黎的到來，著實是一個很大的鼓勵。也很感謝彭仁傑老師與陳家益學長在申請這個博士班之前給予的意見以及彭老師的推薦信。也特別感謝教育部世界百大提供我機會來修讀博士班以及駐法教育組的幫助。前前後後的三年也認識許多巴黎南大的同學與學長姐：陳智民，周巧玲，韓承佑，李旻怡，羅映筑，林欣平；也謝謝你們在我需要的時候給予幫助。在法國偶然認識到林伯儒學長實在倍感親切，特別感謝你常常跟我哈拉。也特此感謝修賢，博翔，愉眉，煒喆，成翰。 I must also thank Stephen Ohlander, my great English teacher.

I would like to express my deepest appreciation to my supervisor, Cynthia Hadjidakis, for giving me the opportunity to study in France. She was always patient with me when I asked questions and always provided me valuable advises when I faced with problems in my study or even in my daily life in France. She, with her immense knowledge of research, has taught me how to carry out study independently, how to present works clearly and how to write thesis and papers. It was a great privilege to receive her training. I am also very grateful to my co-supervisor, Laure Massacrier, who continuously supported me in my study. Her helpful guidance led me to perform detailed study and to present works properly and clearly. Also her help to my analysis to track bugs in my macros really saved me much time. Special thanks also go to the members of the ALICE group in IJCLab. They are Bruno Espagnon who always gave me administrative supports and whom I practiced French with, Christophe Suire who also always supported me administratively, Zaida who helped me a lot in my French life, and Charlotte. In addition, many thanks to my great jury composed by Cvetan Cheshkov, Burkhard Schmidt, Philippe Rosnet, Alberto Baldisseri and Elena Ferreiro who all spend a lot of time on the reading of my thesis.

I also wish to thank my office-mate, Jana who helped me a lot in my first year of the PhD programme and gave me insights which I probably could not gain from the French, Sizar who told me many jokes (in which I learned a lot of useless English words), brought his nice homemade biscuits to me, invited me including our friends to his place for dinner or BBQ and had fun together in Paris all the time. Thanks also to the PhD students in the JLab group at IJCLab. Pierre, Ho San, Mylène and Mathieu who organised many activities and brought me to many places in France especially in Paris, which indeed broaden my horizons. I cannot leave without mentioning other PhD students, Melih, Shengying, Robin, Florian, Charles, Guillaume.

Finalement, je remercie tous ceux qui m'ont aidé en France.

Synthèse en français

Chapitre 1 : motivations physiques

Les quarks et les gluons, qui forment les hadrons, sont les constituants fondamentaux de la matière et sont décrits par le Modèle Standard. La chromodynamique quantique (QCD) est la théorie développée pour décrire les interactions entre les quarks et les gluons et entre les hadrons. Les quarks et les gluons sont confinés dans la matière nucléaire ordinaire. À très haute température et/ou densité, les quarks et les gluons sont déconfinés, ils peuvent se déplacer librement (liberté asymptotique) et forment un plasma de quarks et de gluons (QGP). On pense que cet état de matière existait au tout début de l'Univers après le Big Bang. Les expériences utilisent les collisions d'ions lourds ultra-relativistes afin d'atteindre les conditions extrêmes qui permettent de créer le QGP. Dans ces expériences, les caractéristiques du QGP ne peuvent pas être mesurées directement à cause de son temps de vie très court. Ce chapitre décrit brièvement 5 sondes expérimentales qui permettent d'accéder au QGP de façon indirecte :

- la production d'étrangeté : les constituants de la matière déconfinée, tels que les gluons, sont capables de se mouvoir librement et ils peuvent produire des paires de quarks étranges rapidement, dans l'échelle de temps requise. L'abondance des quarks s et $\bar{s}$ est donc plus importante dans le QGP que celle des quarks légers ou celle des quarks étranges dans les collisions hadron-hadron lorsqu'il n'y a pas de formation de QGP. L'augmentation de la production de particules étranges est considérée comme une signature du QGP.

- le flot hydrodynamique : une collisions d'ions lourds crée un milieu qui thermalise de par les collisions secondaires de ses constituants, et qui s'étend librement. Cette expansion conduit à un flot hydrodynamique dans le cas des collisions semi-centrales. Afin d'étudier les propriétés hydrodynamiques (température, viscosité) du milieu en pleine expansion, les distributions azimutales des particules produites par rapport au plan de réaction peuvent être exprimées en série de Fourier où le coefficient de second ordre donne le flot elliptique.

- les bosons de l'interaction faible : ils n'interagissent pas avec le QGP car ils ne portent pas de charge de couleur. Comme leurs productions ne sont pas affectées par la présence du QGP, les bosons de l'interaction faible permettent de sonder les effets nucléaires autres que ceux dûs au QGP.

- le "jet quenching" : dans une collisions d'ions lourds, un jet qui traverse le milieu chaud et dense va intéragir avec celui-ci et perdre une partie de son énergie. Ce phénomène est appelé "jet quenching". En particulier,

les événements constitués de deux jets (dijet) permettent d'étudier cet effet. Dans le vide, les deux jets ont la même impulsion transverse par rapport à l'axe du faisceau et sont émis dos à dos. En présence de QGP, l'énergie des jets peut être perdue lors de leurs passages dans le mileu par émission de gluons, et cet effet peut modifier significativement la balance en énergie des deux jets.

- la production de saveurs lourdes : les hadrons de saveurs lourdes sont composés au moins d'un quark lourd (charme ou beauté). Les quarks lourds sont produits au tout début de la collision et traversent ses différentes étapes. Lorsque les quarks lourds se propagent dans le milieu, ils interagissent avec ses constituants et perdent une partie de leur énergie lors d'intéractions élastiques ou inélastiques (émission de gluons). Les saveurs lourdes peuvent hadroniser en se combinant avec des quarks légers et former des hadrons qui seront sensibles aux effets de perte d'énergie dans le milieu. D'autres types de hadrons de saveurs lourdes sont composés d'une paire de quarks de charme (charmonium) ou de quarks de beauté (bottomonium). Ces particules, qui permettent de sonder le QGP, sont décrites au Chapitre 2.

Chapitre 2 : production de charmonia

Ce chapitre présente un aperçu des propriétés des charmonia et de leurs mécanismes de production. De plus, une sélection de résultats de mesures de charmonia dans des collisions hadron-hadron et d'ions lourds est présentée. Le charmonium est un méson composé d'un quark charmé et de son anti-quark. Dans la famille du charmonium, le J/ψ a d'abord été découvert en 1974. Sa masse est approximativement de 3.1 GeV/c^2. Ensuite d'autres états ont été découverts, tel que le ψ(2S).

En collisions hadroniques, trois sources contribuent à la production inclusive de J/ψ : la production directe de J/ψ , la production par décroissance des états excités du charmonium et la production par décroisance des mésons B. Les deux premières productions sont appelés "promptes" tandis que la dernière est appelée "non-prompte". La production de J/ψ est étudiée dans le cadre de la théorie de la QCD. La plupart des modèles théoriques considère une factorisation entre la production de la paire $c\bar{c}$ et son évolution en état lié de J/ψ . Dans ce chapitre, trois modèles sont décrits : le modèle d'évaporation de couleur (CEM), le modèle singlet de couleur (CSM) et le modèle de QCD non relativiste (NRQCD) qui inclue les mécanismes singlet et octet de couleurs. Les trois modèles considèrent différentes approches pour la partie non-perturbative de transition entre la paire $c\bar{c}$ et le J/ψ . Les J/ψ peuvent aussi être produits via la décroissance de méson B, qui n'est pas négligeable aux énergies du LHC. Un des modèles de QCD pour cette contribution est le modèle Fixed-Order-Next-to-Leading-Log (FONLL) qui décrit la production de paires $b\bar{b}$.

En collisions d'ions lourds ultra-relativistes, les particules produites peuvent être affectées par le QGP. On s'attend à ce que la paire $c\bar{c}$ soit produite à un temps d'environ 0.25 fm/c après le début de l'interaction dure initiale et que le QGP soit en équilibre thermique après un temps d'environ 2 fm/c. La production de la paire $c\bar{c}$ est donc antérieure à la thermalisation du QGP et celle-ci va être sensible aux effets de milieu qui ont lieu pendant l'évolution

de la collision. Les effets de milieu sont classifiés en deux catégories. La première catégorie est responsable de la modification de la production de J/ψ à cause de la formation du QGP et comprend les effets nucléaires chauds tels que l'écrantage de couleur, la (re)génération de charmonia, la perte d'énergie et les partons co-voyageurs. La seconde catégorie est également responsable de la modification de la production de J/ψ en collisions AA mais n'est pas reliée au QGP. Elle peut être étudiée en collisions pA lorsque le QGP n'est pas formé. Les effets de cette seconde catégorie sont appelés effets nucléaire froids et regroupent la modification des fonctions de distributions de partons, l'absorption nucléaire, la diffusion de partons multiples et la perte d'énergie, ainsi que la saturation de gluon.

Chapitre 3: équipement expérimental

Les données utilisées dans cette thèse ont été collectées par l'expérience ALICE (A Large Ion Collider Experiment) qui se situe au LHC (Large Hadron Collider). Les faisceaux de protons et plombs peuvent être accélérés jusque 6.5 TeV pour les protons et 2.51 A.TeV pour les plombs. ALICE est constituée de détecteurs centraux et à l'avant. Dans cette thèse, les détecteurs utilisés sont le V0, deux compteurs à scintillation utilisés comme déclencheur de Biais Minimum (MB), le SPD, un détecteur à pixel de Silicium, pour les mesures de vertex, le T0, un compteur Cherenkov, utilisé comme déclencheur MB en collisions pp, le ZDC, un calorimètre à zéro degré, permettant de rejeter le bruit de fond en collisions Pb–Pb, ainsi que le spectromètre à muons. Ce dernier est composé :

- d'un absorbeur frontal permettant de stopper les hadrons et les muons de basses impulsions;
- d'un aimant dipolaire pour dévier la trajectoire des muons afin d'obtenir leurs impulsions et charges;
- de chambres de trajectographie qui enregistrent la position 3D de la trajectoire des muons;
- de chambres de déclenchement qui entraînent l'enregistrement d'un événement contenant un muon et identifient les muons.

La qualité des données collectées est vérifiée pour chaque détecteur avec des critères donnés (data quality assurance ou QA). J'ai contribué au sein de la collaboration ALICE à définir la qualité des données enregistrées par les chambres de trajectographie et les chambres de déclenchement pour les collisions pp et Pb–Pb de 2017 et 2018. Les données collectées à $\sqrt{s_{\rm NN}}$ = 5.02 TeV, en collisions pp en 2017 et en collisions Pb–Pb en 2015 et 2018, ont été analysées pour cette thèse. La luminosité intégrée des données pp 2017 est environ 10 fois supérieure à celle des données pp de 2015 qui ont été utilisées pour une analyse précédente. La luminosité intégrée des donnnées Pb–Pb de 2018 est 2.4 fois supérieure à celle des données Pb–Pb de 2015. L'ensemble des données de 2015 et 2018 ont été analysées pour obtenir les résultats Pb–Pb de cette thèse.

Chapitre 4: production inclusive de J/ψ en collisions pp

L'analyse de la production inclusive de J/ψ en collisions pp à $\sqrt{s_{\rm NN}}$ = 5.02 TeV pour $2.5 < y < 4.0$ avec les

données de 2017 est présentée dans ce chapitre. Les événements analysés sont des événements CMUL7. Les critères de sélection de physique (PS) sont appliqués aux événements afin de rejeter les événements liés au bruit de fond induit par le faisceau. Ensuite les traces reconstruites sont sélectionnées en fonction de quatre critères de sélection détaillés dans la thèse. Les traces muons de charges opposées sont combinées pour former une paire de muons. La masse invariante de la paire est utilisée pour extraire le nombre de J/ψ avec un ajustement des données par une fonction (fit). Dans cette thèse, la section efficace de la production inclusive de J/ψ est mesurée en fonction de p_{T}, y, p_{T}/y (mesure double-différentielle) et intégrée sur les variables cinématiques. Ces mesures permettent de tester le mécanisme de production du J/ψ et servent de référence à la production de J/ψ en collisions Pb–Pb. Les ingrédients de la section efficace sont le rapport de branchement, le nombre de J/ψ extraits, la correction en acceptance et efficacité et la luminosité intégrée. Afin d'extraire le nombre de J/ψ et déterminer les incertitudes systématiques, plusieurs méthodes de fit sont utilisées sur la masse invariante des paires de muons. L'acceptance et l'efficacité est définie comme le rapport entre le nombre de J/ψ reconstruits sur le nombre de J/ψ générés à partir de simulations Monte-Carlo. Les incertitudes systématiques de l'acceptance efficacité sont estimées en étudiant la corrélation en p_{T}/y à partir des mesures double-différentielles. La luminosité intégrée est calculée comme le nombre d'événements MB équivalents divisé par la section efficace MB. Le nombre équivalent d'événements MB est le produit du nombre d'événements CMUL7 et d'un facteur de normalisation. La section efficace MB considérée est celle du T0 mesurée avec un scan de Van der Meer. L'incertitude de la section efficace du T0 est dominée par les incertitudes de la mesure du scan de Van der Meer et se retrouve dans les incertitudes sur la luminosité intégrée. Les autres sources d'incertitudes systématiques, reliées à l'efficacité de trajectographie, de déclenchement, et d'association des traces entre les chambres de trajectographie et de déclenchement, sont également estimées dans cette thèse.

La section efficace intégrée pour $0 < p_{\mathrm{T}} < 20$ GeV/c et pour $2.5 < y < 4$ est 5.88 ± 0.03 (stat.) ± 0.33 (syst.) μb. La dépendence en p_{T} de la section efficace est plus précise que les mesures précédentes et permet d'atteindre des valeurs de p_{T} jusque 20 GeV/c. Les résultats sont comparés aux calculs théoriques de la production de J/ψ prompts basés sur le modèle d'évaporation de couleur (CEM) et sur le modèle de QCD non relativiste (NRQCD). La section efficace différentielle en fonction de p_{T} pour la production inclusive de J/ψ est présentée sur la Figure 1 et est comparée aux calculs théoriques. La contribution théorique de la production de J/ψ non-prompts à partir du modèle FONLL est ajoutée aux calculs théoriques de la production de J/ψ prompts et est également indiquée séparément sur la figure. Cette contribution augmente avec p_{T} et est de 1% à $p_{\mathrm{T}} \sim 1$ GeV/c et de 42% pour le plus grand interval en p_{T}. Le calcul théorique de Butenschoen *et al.* combiné avec les estimations de FONLL reproduit correctement les données pour $p_{\mathrm{T}} > 3$ GeV/c. Le modèle NRQCD de Ma *et al.* + FONLL est en accord avec les données pour $p_{\mathrm{T}} > 5$ GeV/c. Le modèle NRQCD couplé au modèle de CGC par Ma *et al.* + FONLL est compatible avec les données pour $p_{\mathrm{T}} < 8$ GeV/c. Une bonne description des sections efficaces mesurées est obtenue par le modèle ICEM + FONLL pour l'ensemble de l'intervalle en p_{T}. Finalement le modèle NLO CEM + FONLL décrit les données pour $p_{\mathrm{T}} > 10$ GeV/c mais sous-estime les données dans l'intervalle $4 < p_{\mathrm{T}} < 10$ GeV/c. Plus de résultats sont discutés dans ce chapitre.

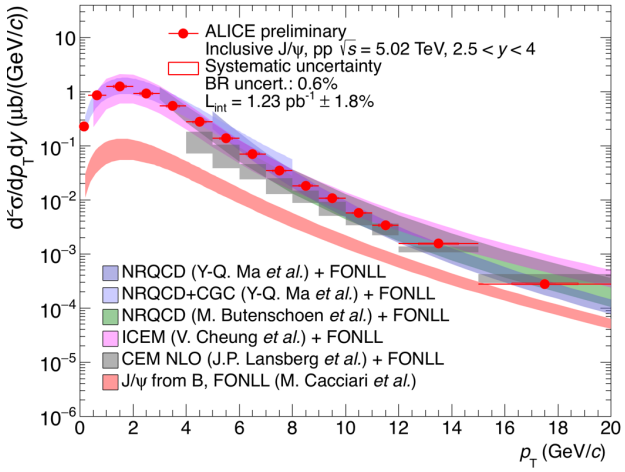

Figure 1: Section efficace différentielle de la production inclusive de J/ψ en fonction de p_{T} à rapidité vers l'avant à $\sqrt{s} = 5.02$ TeV. Les données sont comparées aux calculs théoriques basés sur les modèles de CEM [1], ICEM [2], NRQCD [3, 4] et NRQCD couplé au modèle du CGC [5] pour la production prompt et FONLL [6] pour la production non-prompt.

Chapitre 5: production inclusive de J/ψ en collisions Pb–Pb

L'analyse de données des collisions Pb–Pb à $\sqrt{s_{\mathrm{NN}}} = 5.02$ TeV pour la production inclusive de J/ψ à $2.5 < y < 4$ avec les données collectées en 2015 et 2018 est présentée dans ce chapitre. Les événements analysés sont les événements CMUL7. La PS est appliquée à ces événements. Dans cette thèse, le facteur de modification nucléaire, R_{AA}, pour la production inclusive de J/ψ est mesuré. Ce facteur est le taux invariant de J/ψ divisé par la moyenne de la fonction de recouvrement nucléaire et par la section efficace pp. La section efficace pp, dont la mesure est détaillée au Chapitre 4, est utilisée. Le taux invariant est défini comme le rapport entre le nombre de J/ψ extraits et le produit du rapport de branchement, de la correction acceptance efficacité du J/ψ et du nombre d'événements MB. Comme pour l'analyse en collision pp, plusieurs méthodes de fit sont effectuées afin d'extraire le nombre de J/ψ à partir des spectres de masse invariante des paires de muons. L'acceptance efficacité du détecteur est estimée en utilisant des simulation Monte Carlo où le signal est intégré dans de vraies collisions Pb–Pb au niveau des signaux reçus par les détecteurs. L'incertitude systématique sur l'acceptance et l'efficacité est estimée en variant la dépendance en p_{T} et en y de la distribution de J/ψ . Le nombre d'événements MB équivalent est obtenu en multipliant le nombre d'événements CMUL7 par le facteur de normalisation. Plusieurs méthodes sont utilisées pour obtenir ce facteur de normalisation, qui permettent également d'estimer l'incertitude systématique sur ce facteur. Les autres sources d'incertitude systématique, telles que la fonction de recouvrement nucléaire, les limites des intervalles en centralité, l'efficacité de trajectographie, de déclenchement ou d'association des traces entre les chambres de trajectographie et de déclenchement, sont également estimées dans cette thèse ou lors d'études précédentes.

Le R_{AA} pour la production inclusive de J/ψ est mesuré en fonction de p_{T} et pour différents intervalles de centralité pour $2.5 < y < 4$. La Figure 2 montre à gauche la nouvelle mesure d'ALICE pour les événements les plus

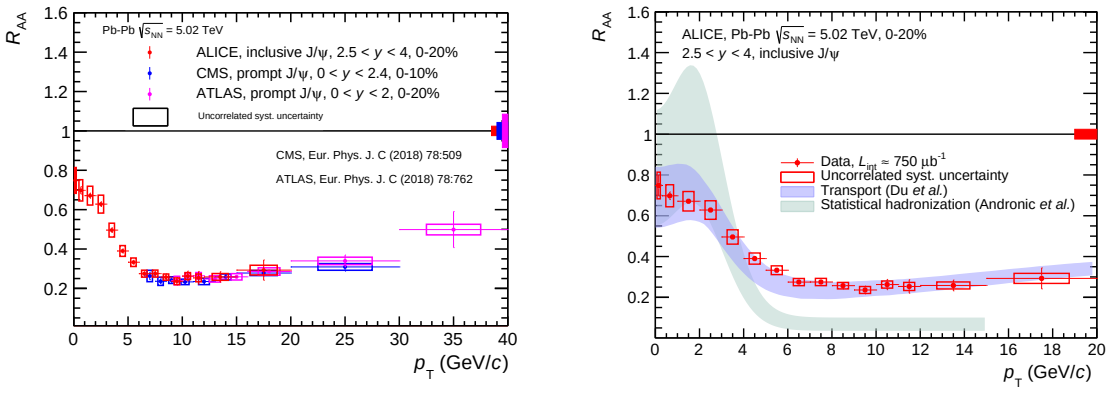

Figure 2: Gauche: $R_{\rm AA}$ pour la production inclusive de J/ψ en fonction de $p_{\rm T}$ pour $2.5 < y < 4$ et la classe en centralité 0–20%, comparé aux résultats de CMS [7] et ATLAS [8]. L'incertitude statistique est représentée par une barre d'erreur verticale et l'incertitude systématique est représentée par un rectangle autour des points. [This thesis]. Droite: $R_{\rm AA}$ du J/ψ en fonction de $p_{\rm T}$ pour $2.5 < y < 4$ et la classe en centralité 0–20% avec les données Pb–Pb du Run 2, comparé aux calculs théoriques basés sur le modèle de transport [9] et sur le modèle de l'hadronisation statistique [10] [This thesis].

centraux (classe de centralité 0-20%). Ces résultats sont comparées aux résultats de CMS pour les J/ψ prompts dans la classe de centralité 0-10% et pour $0 < y < 2.4$, ainsi qu'aux résultats d'ATLAS pour les J/ψ prompts dans la classe de centralité 0-20% et pour $0 < y < 2$. La mesure d'ALICE est consistante avec celles de CMS et d'ATLAS pour $6 < p_{\rm T} < 20$ GeV/c malgré les différents intervalles en rapidité et la mesure de J/ψ inclusifs ou prompts. La Figure 2 présente à droite le $R_{\rm AA}$ comparée à des calculs théoriques basés sur le modèle de transport [9] et sur le modèle d'hadronisation statistique (SHM) [10]. Le modèle de transport considère une compétition entre la suppression de J/ψ par le QGP et son augmentation par le mécanisme de (re)génération à bas $p_{\rm T}$. Les J/ψ primordiaux qui survivent au QGP contribuent à la production de J/ψ à grand $p_{\rm T}$. Dans le modèle SHM, les J/ψ primordiaux produits dans le coeur de la collision sont tous considérés comme supprimés par le QGP. Les J/ψ sont (re)générés à la limite de la phase d'hadronisation avec une petite valeur de $p_{\rm T}$. Quelques J/ψ primordiaux produits dans la couronne de la zone de recouvrement des noyaux n'intéragissent pas avec le QGP et contribuent à la production de J/ψ de grand $p_{\rm T}$. Les calculs du modèle de transport sont compatibles avec les données pour $0 < p_{\rm T} < 20$ GeV/c. Les calculs basés sur le modèle SHM décrivent les données pour $p_{\rm T} < 5$ GeV/c mais sous-estiment les données pour $p_{\rm T} \geq 5$ GeV/c. Plus de résultats tels que le $R_{\rm AA}$ pour les classes de centralité 20–40% et 40–90% sont présentés dans ce chapitre.

Chapitre 6: conclusions et perspectives

Il est important de mesurer la production de J/ψ en collisions pp pour étudier ses méchanismes de production. En collisions Pb–Pb, la production de J/ψ permet de sonder le QGP. Dans ce document, les analyses de la production inclusive de J/ψ pour $2.5 < y < 4$, en collisions pp et Pb–Pb à $\sqrt{s_{\rm NN}} = 5.02$ TeV, sont présentées. Le J/ψ est détecté

via son canal de désintégration muonique et les analyses utilisent la majeur partie de la statistiques des données du Run2 du LHC. En collisions pp, la section efficace de J/ψ inclusifs est mesurée en fonction de p_{T} , y et en fonction de y pour quatre intervalles de p_{T}. Les résultats sont en accord avec les résultats précédemment publiés. La plus grande statistique permet d'obtenir des résultats plus précis et d'atteindre des valeurs de p_{T} de 20 GeV/c. Les données sont bien reproduites par des calculs théoriques basés sur les modèles CEM et NRQCD. En collisions Pb–Pb, le R_{AA} des J/ψ inclusifs est mesuré en fonction de p_{T} pour trois classes de centralité. Ces résultats sont en accord avec les résultats précédemment publiés et montrent une suppression de la production de J/ψ en collisions Pb–Pb pour les classes de centralité mesurées. Pour les collisions les plus centrales, l'augmentation du R_{AA} à bas p_{T} est attribué à la (re)génération de J/ψ car la production de quarks charmés est importante au énergie du LHC. Pour $6 < p_{\mathrm{T}} < 20$ GeV/c et les collisions les plus centrales, le R_{AA} est compatible avec celui mesuré pour les J/ψ prompts par les expériences ATLAS et CMS à rapidité centrale. Les mesures de l'expérience ATLAS montrent également qu'à haut p_{T}, le R_{AA} des J/ψ prompts est similaire à celui des particules chargées, ce qui est interprété comme une signature de la perte d'énergie de paires de quarks lourds et/ou de gluons dans le milieu. La production de J/ψ à grand p_{T} est probablement affectée à la fois par les effets d'écrantage de couleur et de perte d'énergie.

Le LHC est maintenant entré dans une deuxième phase d'arrêt long (LS2) entre 2019 et 2021 pour des améliorations du LHC et des expériences. Dans l'expérience ALICE, deux améliorations profiteront à l'étude de la production de charmonia à rapidité vers l'avant : l'installation d'un trajectographe vers l'avant, le Muon Forward Tracker (MFT), et la nouvelle électronique de lecture du spectromètre à muon. Après le LS2, le LHC commencera les périodes de Run 3 et 4 et ALICE a pour objectif d'enregistrer une luminosité dix fois supérieure à celle enregistrée pendant le Run 2. Cette augmentation en luminosité permettra d'étudier la production de quarkonia, J/ψ, ψ(2S) et Υ(nS), de façon plus précise. De plus, des sondes rares telles que la production double de J/ψ ou la corrélation de particules produites à l'avant et à rapidité centrale pourront être étudiées.

Contents

Introduction

The Standard Model describes the fundamental particles and forces which allow us to understand the universe. The quantum chromodynamics (QCD) is a theoretical framework that was developed to describe the interaction between quarks and gluons, and between hadrons. Nowadays, nearly all theoretical models study hadron productions by applying the factorization theorem under the QCD frameworks. Hence, measuring hadron production in hadronic collision experiments provides an opportunity to test theoretical models. On the other hand, one of the QCD prediction is that a phase of the nuclear matter, in which quarks and gluons are deconfined, is formed under extreme conditions at high temperatures and/or at high matter density. This phase, which is different from the ordinary nuclear matter where the quarks and gluons are confined, is known as quark-gluon plasma (QGP). In order to recreate the QGP, a heavy-ion collision at high energy that creates such extreme conditions in laboratory is used. In heavy-ion experiments, the QGP is probed and characterised by measuring the production of various particles that are affected by the QGP. The productions of some particles are, however, affected as well by cold nuclear matter (CNM), i.e. nuclear matter without the presence of QGP.

In hadron-hadron collisions, measuring charmonium production is motivated not only by the interests to understand the charmonium production mechanism, but also by providing a reference for charmonium production in heavy-ion collisions. Measuring charmonium production in heavy-ion collisions can characterise the QGP properties. Pre-resonant $c\bar{c}$ pairs are produced at the very early stage of heavy-ion collisions and, as a consequence, they can experience the whole evolution of the collisions in the presence of QGP. At the Large Hadron Collider (LHC), one of the four major experiments, A Large Ion Collider Experiment (ALICE), was designed to study the QGP in heavy-ion collisions. In addition, ALICE also studies pp and p-Pb collisions in order to understand particle production mechanism and the CNM effects, respectively. In particular, the J/ψ production can be measured through its di-electron or dimuon decay channels at mid- or forward-rapidity, respectively. In this thesis, two analyses are reported on J/ψ production at forward-rapidity in pp and Pb-Pb collisions at the collision energy per nucleon pair of $\sqrt{s_{\rm NN}}$ = 5.02 TeV.

The structure of this thesis is arranged as follows: chapter one describes the physics motivations. The Standard

Model and the QCD framework are introduced with its particularities, such as confinement and asymptotic freedom. In addition, the QGP that is formed at high temperatures and/or high matter density in laboratory is described. In chapter one, some probes of the QGP are discussed shortly as well. In chapter two, several theoretical models are discussed in order to understand the current descriptions of charmonium production mechanism in hadron-hadron and in heavy-ion collisions; notable experimental results from RHIC and LHC are also discussed and are compared to theoretical models. Chapter three describes the experimental apparatus at the LHC. The four major experiments are mentioned, and ALICE and its detectors are especially described in more details. The analyses of J/ψ production in pp and Pb-Pb collisions at $\sqrt{s_{\mathrm{NN}}}$ = 5.02 TeV are presented in chapter four and five, respectively. In particular, the J/ψ production cross section by using the 2017 pp collisions is measured and compared to several theoretical models. Besides, the pp J/ψ cross-section measurement provides a reference for the J/ψ analysis in Pb-Pb collisions. In chapter five, the J/ψ nuclear modification factor is obtained by using the full Run 2 Pb-Pb statistics and compared to some theoretical calculations.

Chapter 1

Physics motivations: QCD and QGP

This chapter aims at giving an overview of the quark-gluon plasma (QGP). The quantum chromodynamics (QCD) is also introduced since the theory of the QGP is based on the QCD. Heavy-ion collision is an experimental tool that allows one to create the QGP in the laboratory and it is also discussed in this chapter. Finally, some experimental probes for characterizing the QGP are briefly presented.

1.1 The standard model

The standard model describes three fundamental forces of the universe which are related to the electromagnetic, weak and strong interactions. It also classifies the elementary particles which are shown in Figure 1.1. The elementary particles are the observed particles at the smallest size scale nowadays. The elementary particles are classified according to their spin value. The particles with a half-integer spin are called fermions while the particles with an integer spin are the bosons.

Fermions are categorized as leptons (l) and quarks (q) depending on their colour charge properties. Quarks interact via the colour force through the strong interaction. There are six flavours of quarks and each flavour possesses a mass and a fractional electric charge. The up (u), charm (c) and top (t) quarks have a positive charge of $+2/3$ while the down (d), strange (s) and bottom (b) quarks have a negative charge of -1/3. The most massive quark is the t quark and the lightest one is the u quark. Besides, for each quark, it exists an antiquark ($\bar{q}$) with an opposite electric charge but the same mass. They are the antiup ($\bar{\text{u}}$), anticharm ($\bar{\text{c}}$), antitop ($\bar{\text{t}}$), antidown ($\bar{\text{d}}$), antistrange ($\bar{\text{s}}$) and antibottom ($\bar{\text{b}}$). On the other hand, the leptons do not interact with other particles through the strong interaction since they do not carry any colour charge. Instead they interact via electroweak interaction. There are six flavours of leptons, three of them have an integer electric charge but the other three do not. The best-known lepton is the electron (e). The other two are the muon (μ) and tau (τ). The leptons without electrical charges are the three

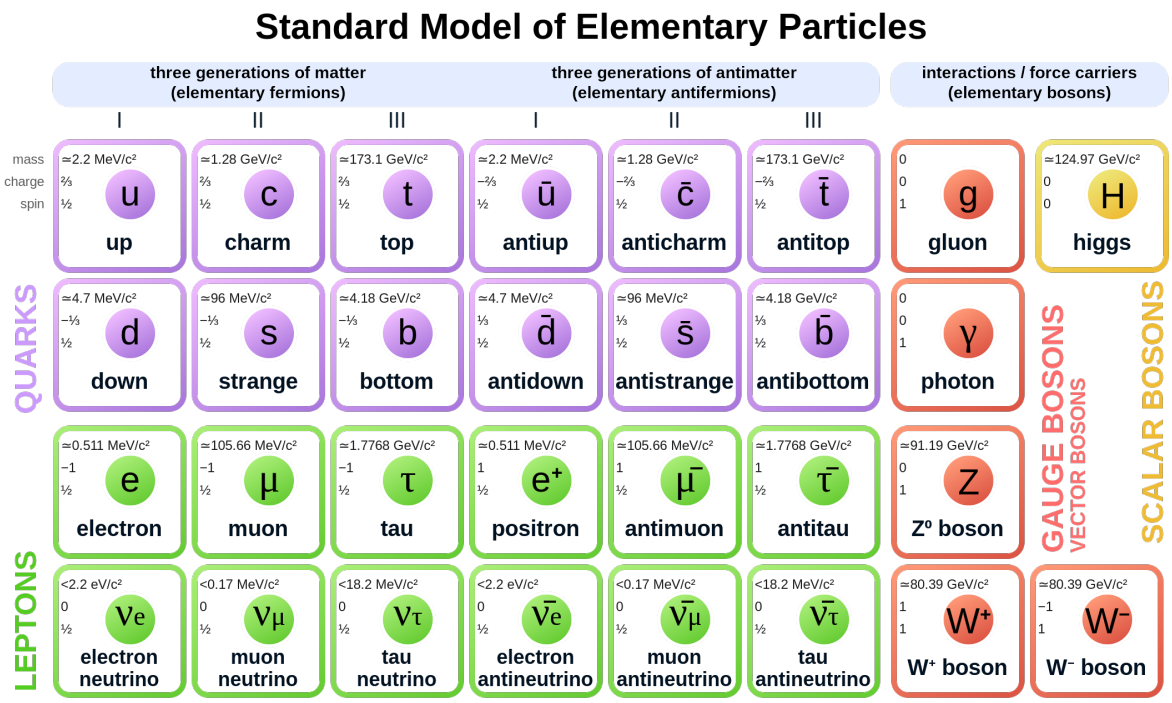

Figure 1.1: Elementary particles and their antiparticles in the standard model.

types of neutrinos (ν_e, ν_μ, and ν_τ) and they have a small mass [11], according to the observation of neutrino flavour oscillations. Likewise, for each lepton, there is a corresponding antilepton with an opposite electrical charge but the same mass. They are the positron (e^+), the antimuon (μ^-), the antitau (τ^-), the electron antineutrino (ν_e^-), the muon antineutrino (ν_μ^-), and the tau antineutrino (ν_τ^-).

Bosons include the gauge bosons (photons, gluons, W and Z bosons) and the scalar boson (Higgs bosons). They are the force-carrier particles. Photons are the force carriers of the electromagnetic interaction. Particles with electrical charges interact with other charged particles by exchanging photons. The quantum electrodynamics (QED) [12] is the fundamental theory describing the electromagnetic forces based on the relativistic quantum field framework. W and Z bosons are the force carriers of the weak interaction, which is responsible for the decay of massive quarks and leptons into light quarks and leptons. W and Z bosons have large masses but their interaction strengths are very weak compared to the electromagnetic and strong interactions. For this reason, this interaction is named the weak interaction. The electromagnetic and weak interactions are unified into the electroweak interaction. Gluons are the force carriers of the strong interaction. Particles carrying colour charges can interact via the strong interaction [13]. The strong interaction strength is around 100 times stronger than the electromagnetic interaction strength at short distance. The quantum chromodynamics (QCD) theory describes the strong interaction between quarks and gluons and how they bind into hadrons, such as the proton. Higgs bosons give the mass to particles including W and Z bosons, via the Higgs field.

All particles with mass interact via the gravitational force. The strength of the gravitational force is the weakest among the four fundamental forces, at short distances. Gravitons are believed to be the force carrier but they have not been observed yet. Figure 1.1 does not show the gravitational force carrier because the Standard Model does not include the gravitational force. The difficulty in describing gravity by the Standard Model comes from the fact that it should be consistent with the description from the general theory of relativity. For instance, the Standard Model particle fields are defined on a flat space-time while the general theory of relativity postulates a curved space-time which evolves with the motion of mass-energy [14]. Therefore, nowadays, the Standard Model is used to describe the microscopic world, and the general theory of relativity governs physics in the macroscopic and cosmic scales.

1.1.1 Quantum Chromodynamics: quarks and gluons

The quantum chromodynamics (QCD) is the theory that describes the strong interaction between quarks and gluons. The QCD was developed in analogy to the QED, which describes the electromagnetic interaction between charged particles and photons. The electric charges have positive and negative values. The force carrier, the photon is electrically neutral. In QCD, quarks have not only electric charges but also colour charges. Gluons also have colour charges and there are eight gluons in total. These extra charges are conventionally called red, green and blue colours for quarks, and anti-red, anti-green and anti-blue colours for antiquarks. Quarks carry one of the three possible colour charges. The composite particles, such as the protons and the neutrons, made of three quarks have no colour charge. They are colour neutral (also called white). Besides, colour charge is always conserved in a system. Quarks interact by exchanging gluons. When a quark emits or absorbs gluons, the quark must change its colour to conserve the colour charge since the gluons carry a colour charge and an anticolour charge. Furthermore, for short interquark distance, single gluon exchange dominates and the perturbative QCD can be applied in that condition. However, for long interquark distance, the contribution from self-gluon interaction is also important and the perturbative QCD framework is not valid anymore. The QCD factorization theorem is therefore developed, and it separately handles the short-distance and long-distance interactions (see section 1.1.2 for details).
Colour-neutral particles exist as baryon or as meson [15]. A baryon is a particle that consists of three constituent quarks whose colour charges are different but the mixture of the three quarks produces a colour-neutral particle. The common baryons are protons and neutrons. A meson, such as a pion, is built from a quark and an antiquark. Particles that are either baryons or mesons are called hadrons.

1.1.2 Confinement and asymptotic freedom

In QED, the vacuum is subject to quantum fluctuation where many virtual electro-positron pairs, e^+e^-, can appear in space. This is known as the vacuum polarisation. In vacuum, a charged particle is screened by those e^+e^- pairs.

When two charged particles electromagnetically interact over a long distance, the screening effect increases and the interaction strength is weaker. The strength of the electromagnetic interaction is quantified by a coupling constant α depending on the momentum transfer in the interaction, Q, between particles. When the distance between two electromagnetic charges is large, Q is small. Thus the electromagnetic interaction strength between two charged particles decreases with increasing distance (or decreasing Q). An analogy to the vacuum polarization exists in QCD as well. The QCD vacuum is indeed full of many virtual quark-antiquark pairs $q\bar{q}$. By analogy, one could expect the QCD coupling constant α_s to act similarly as the QED coupling constant. However, virtual gluon pairs also exist in the vacuum since gluons have colour charges. This is different from electromagnetically-neutral photons. The existence of virtual gluon pairs causes antiscreening which exceeds the screening from virtual quark pairs. It results in an increase of the strong interaction strength with an increasing distance (or a decreasing momentum transfer). In Figure 1.2, α_s is shown as a function of the momentum transfer. The QCD coupling constant increases at low momentum transfer (or at long distance). When Q is smaller than the QCD scale ($\Lambda_{QCD} \approx 200$ MeV), perturbative QCD can not be applied anymore, the calculations do not converge because α_s is too large. The quarks in this regime strongly bind to each other and are formed hadrons. This phenomenon is called confinement and it explains that the observation of an isolated quark or gluon does not happen. On the other hand, the value of α_s is small at large Q. The quarks interact weakly with each other and can be treated as quasi free at the limit of very high Q. This regime is known as asymptotic freedom [16, 17].

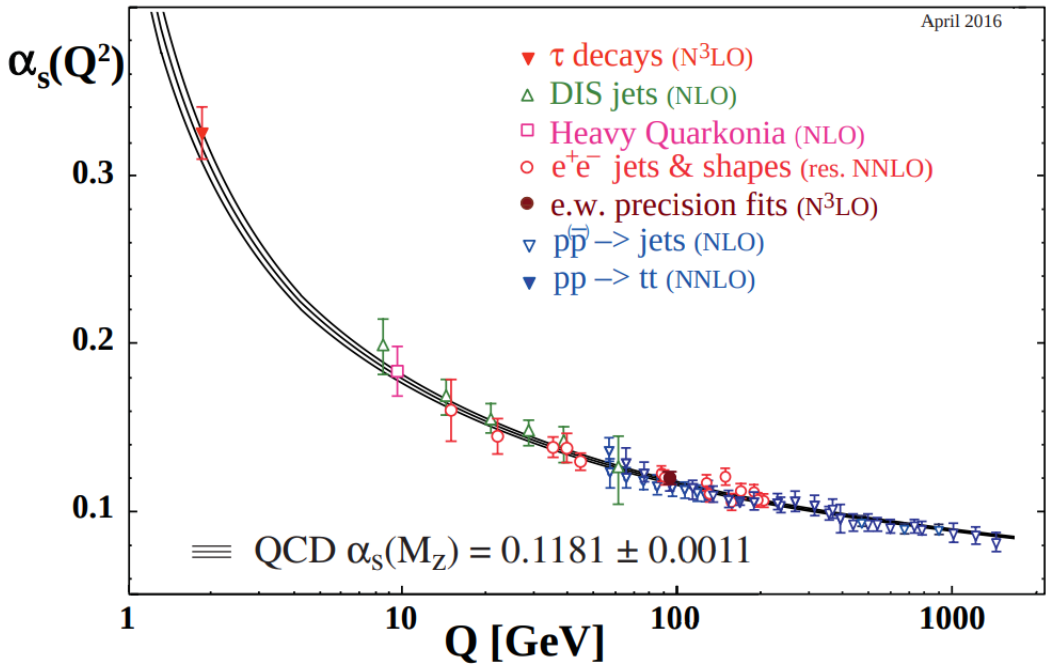

Figure 1.2: Values of the strong coupling constant (α_s) as a function of the transferred momentum (Q). Figure from [18].

1.2 QCD phase diagram

It is believed that the universe, for a few millionths of a second after the Big Bang, was filled with a high energy density and high temperature soup in which elementary particles, such as quarks and gluons, were de-confined. This soup is known as the Quark-Gluon Plasma (QGP). A few microseconds later, the soup started to cool down and the de-confined particles formed into hadrons and consequently into matters. The phases of the de-confined and other QCD states of matter are characterized in the (T, μ_B) phase-space, where T is the temperature of the system and μ_B is the baryo-chemical potential. μ_B measures the baryon density of the system. The phase diagram of the strongly interacting matter is presented in Figure 1.3. The nature of the transition between the QGP and the hadronic matter is not confirmed yet. At large values of μ_B and T, a phase transition occurs at first order. However at low values of μ_B and large values of T, the transition is expected to be rapid and continuous, but it is not clear yet if the transition is of first order or is a cross-over [19]. A critical point of second order separates those two regions. Theoretical calculation based on lattice QCD (lQCD) predicts the critical temperature to be about 160 MeV [20] at zero μ_B when the phase transition takes place between the QGP and the hadronic matter. The arrows represent the hypothetical places in the QCD phase diagram reached by heavy-ion collisions in various colliders or experiments: the QGP is created at large T and various μ_B values (see below). When the medium expands, it cools down and a hadron gas is formed (see section 1.3).

Several experiments have searched for the transitions from the QGP to hadronic matter using heavy-ion collisions at different energies. The NA49 experiment [22] at the Super Proton Synchrotron (SPS[1]) released results about the phase transition phenomena [23]. The Beam Energy Scan phase one (BES I) programme at RHIC [24] studied Au-Au collisions at the center of mass energy per nucleon pair, $\sqrt{s_{\mathrm{NN}}}$, from 7.7 GeV to 200 GeV. At the Large Hadron Collider (LHC[2]) and the Relativistic Heavy Ion Collider (RHIC) [25], the collision energy is higher than that at SPS and allows one to reach higher temperature and lower μ_B. These conditions correspond to the ones of the early universe.

At large values of μ_B but low values of T, the QCD phase of matter becomes a colour superconductor [26]. In this phase of matter, the quarks near the Fermi surface correlates with a condensate of Cooper pairs. In the universe, neutron stars are expected to be the only known place in this QCD phase region where μ_B is likely high enough to produce quark matter and T is low enough for color superconductivity to occur. However, it is unknown whether neutron star cores are dense enough.

[1]The SPS is the seond-largest accelerator at CERN and it is described in more detail in section 3.1.2.
[2]The LHC is presented in section 3.1

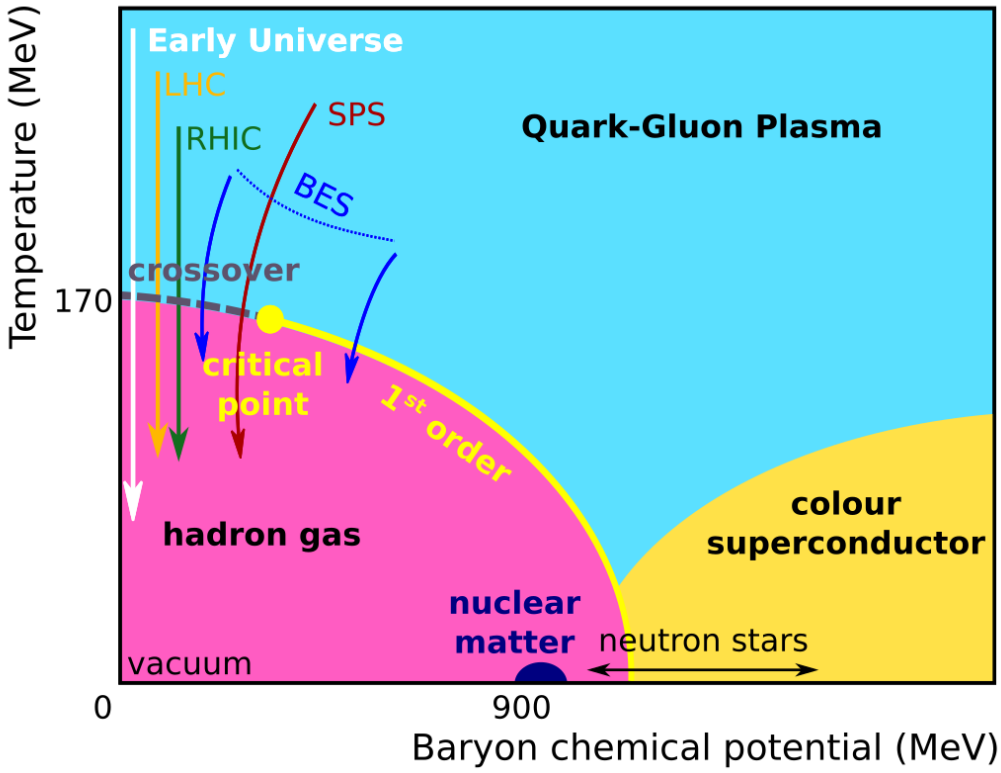

Figure 1.3: QCD phase diagram. Figure from [21].

1.3 Study of the QGP in heavy-ion collisions

1.3.1 Space-time evolution

Heavy-ion collisions are employed to create the quark-gluon plasma at high temperature and/or high baryon density in laboratory. The evolution of a heavy-ion collision at the LHC energies is illustrated in the Minkowski space coordinate [27], shown in Figure 1.4, where τ the longitudinal proper time and the beam direction are indicated with arrows [28]. In the Minkowski space coordinate, τ is defined by:

$$\tau = \sqrt{t^2 - z^2}, \tag{1.1}$$

where t and z are the time and the longitudinal coordinate (i.e. in the beam direction) in the laboratory frame, respectively. The region where $t^2 - z^2 > 0$ is the time-like region and its space-time rapidity η_s is defined as:

$$\eta_s = \frac{1}{2}\, ln\left(\frac{t+z}{t-z}\right). \tag{1.2}$$

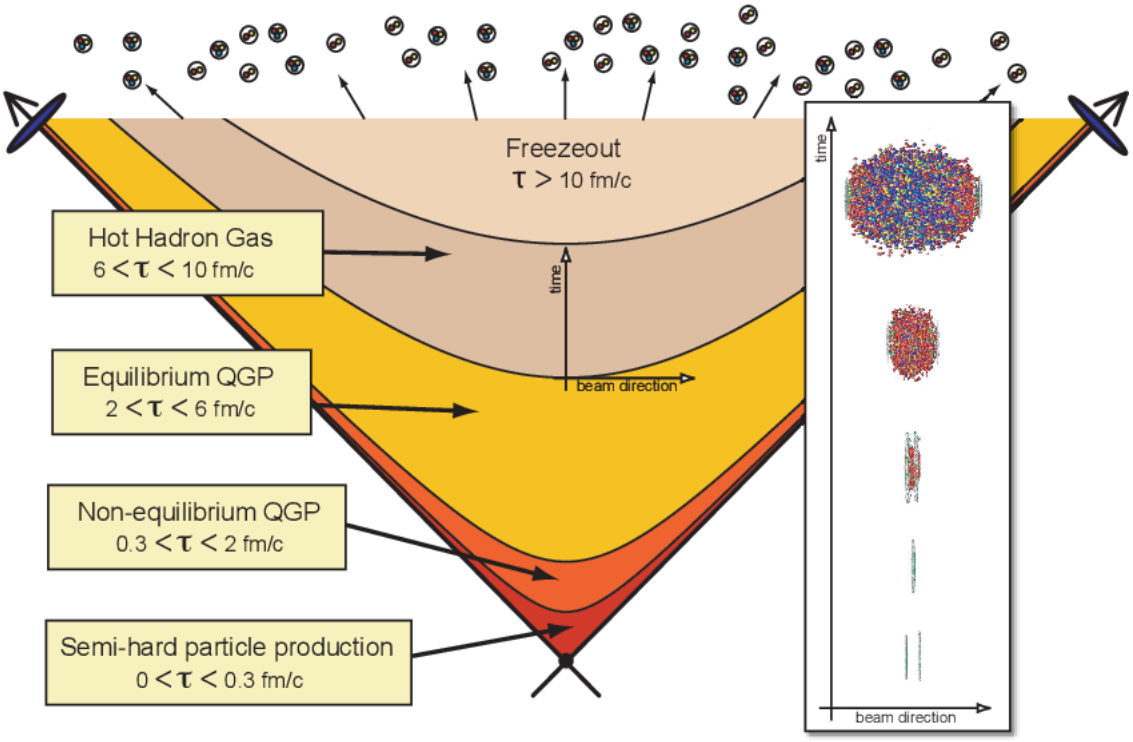

Figure 1.4: The space-time evolution of a heavy-ion collision (Pb-Pb) at the LHC energies. The insert shows the corresponding stages in the laboratory frame. Figure from [27].

The rapidity y can also be defined for a produced particle and it is expressed as:

$$y = \frac{1}{2}\, ln\left(\frac{E + p_z}{E - p_z}\right), \tag{1.3}$$

where E and p_z are the energy and the longitudinal momentum of the particle, respectively. Besides, the moving particle obeys the energy conservation law $E^2 = p^2 + m^2$, where p is the total momentum and m is the mass. Eq. 1.3 can then be reformulated as:

$$y = \frac{1}{2}\, ln\left(\frac{\sqrt{m^2 + p^2} + p\ cos\theta}{\sqrt{m^2 + p^2} - p\ cos\theta}\right), \tag{1.4}$$

where θ is the angle of the particle with respect to the longitudinal direction. At very high energy, the particle mass can be neglected such that $p >> m$, Eq. 1.4 can be approximated as:

$$y \approx \frac{1}{2}\, ln\left(\frac{p + p\ cos\theta}{p - p\ cos\theta}\right) = -ln\ tan\ \theta/2 \equiv \eta. \tag{1.5}$$

The pseudorapidity η can therefore be defined only by measuring the angle θ for any particle. Hence, η as well as E and the azimuthal angle, ϕ, are usually used in high energy collisions.

The particles produced in a heavy-ion collision experience different stages starting from the beginning of the

collision, and those stages are listed below:

- as soon as two heavy ions collide, the partons of the nuclei experience multiple scatterings because of the high density of nuclear matter, and in consequence many particles are produced;
- the next stage is the one of the non-equilibrium QGP. The produced particles and multiple scatterings cause a rapid increase of the entropy of the system. The system thermalizes and its temperature becomes high. Meanwhile the system starts to expand;
- in the third stage, the system reaches a deconfined phase where the quarks and gluons are deconfined. The system is expanding and its temperature cools down;
- the system becomes a hot hadron gas when its temperature is less than the critical temperature T_c, at which the phase transition happens. In this stage, quarks and gluons are not de-confined anymore: they hadronize into hadrons;
- the hadron gas continues to expand and its temperature cools down. When the number of formed hadrons does not change because no more inelastic scatterings happen, the system is at the stage of the chemical freeze-out. Then the system cools down further. When the density of the system is too low to produce elastic scatterings among hadrons, the hadron momenta are fixed and the system reaches the kinetic freeze-out stage.

1.3.2 Collision geometry

Heavy ion collisions give the opportunity to create the QGP in the laboratory. In this section, the geometry of the collision is defined. Figure 1.5 shows two nuclei approaching each other along the z axis with two different views. The distance between the center of the two nuclei in a plane transverse to the beam axis is called the impact parameter $\vec{b}$. The collisions are classified depending on their impact parameter value.

- $\vec{b} \approx 0$, it refers to head-on collision where the centers of the two nuclei approach along the same trajectory. This type of collisions is called central.
- $\vec{b}$ is approximately the sum of the two ion radius. The two nuclei are far from each other at the interaction. This type of collisions is called peripheral.

Nuclei are normally spherical at rest. When nuclei travel nearly at the speed of light, they are Lorentz-contracted along their direction of motion and their shapes become as pancakes. This characteristic is also illustrated in Figure 1.5. In heavy-ion collisions, the Glauber model [29] is commonly used to characterise the collisions. This model considers that nucleus-nucleus collision is a superposition of independent nucleon-nucleon collisions. It provides several quantities such as the number of participating nucleons N_{part}, the number of binary nucleon-nucleon collisions N_{coll}, and the number of spectators N_{spec}. The spectators are the nucleons which do not participate in the collision.

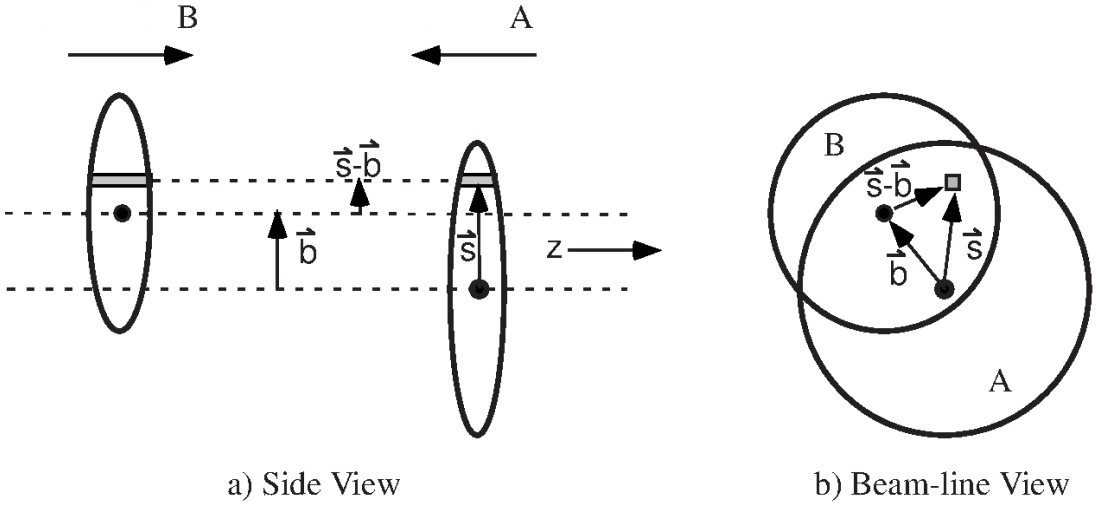

Figure 1.5: Schematic illustrations of the initial geometry of two ions which are going to collide along the longitudinal axis z with side (a) and beam-line (b) views. Figure from [29].

Those variables can be calculated with the Glauber model and their values characterize the type of collision. Looking at Figure 1.5, the two heavy ions A and B separated by an impact parameter $\vec{b}$ are going to collide along the z axis, and $\vec{s}$ specifies the distance from the nucleus center to the grey tube of ion A. The probability per unit transverse area of finding a given nucleon in the grey tube of the ion A is expressed as:

$$T_{\mathrm{A}}(\vec{s}) = \int \mathrm{d}z \rho(\vec{s}, z), \tag{1.6}$$

where $\rho(\vec{s}, z)$ is the probability, per unit volume, of finding the nucleon at a given position. Similarly, the probability, per unit transverse area, of finding a given nucleon in the grey tube of ion B is written as $T_{\mathrm{B}}(\vec{s}-\vec{b}) = \int \mathrm{d}z \rho(\vec{s}-\vec{b}, z)$. With the above ion probabilities, the nuclear overlap function $T_{\mathrm{AB}}(\vec{b})$ is defined for a given $\vec{b}$ and it specifies the effective overlap area in which a given nucleon in ion A can interact with a given nucleon in ion B. It is expressed mathematically as:

$$T_{\mathrm{AB}}(\vec{b}) = \int T_{\mathrm{A}}(\vec{s})\ T_{\mathrm{B}}(\vec{s}-\vec{b})\mathrm{d}^2\vec{s}. \tag{1.7}$$

The probability of one nucleon-nucleon interaction taking place in the collision is written as $T_{\mathrm{AB}}(\vec{b})\sigma_{\mathrm{inel}}^{\mathrm{NN}}$, where $\sigma_{\mathrm{inel}}^{\mathrm{NN}}$ is the nucleon-nucleon inelastic cross section. The probability can be expanded to have n interactions in the collision, and is given as a binomial distribution:

$$P(n, \vec{b}) = \binom{AB}{n} \left[T_{\mathrm{AB}}(\vec{b})\sigma_{\mathrm{inel}}^{\mathrm{NN}}\right]^n \left[1 - T_{\mathrm{AB}}(\vec{b})\sigma_{\mathrm{inel}}^{\mathrm{NN}}\right]^{AB-n}, \tag{1.8}$$

where A and B are the number of nucleons in the nucleus A and B, respectively. The first term is the number of combination for finding n interactions out of all possible nucleon-nucleon interactions. The second term is the

probability of having n interactions and the last term is the probability of missing (AB - n) interactions. The total number of binary nucleon-nucleon collisions, considering all possible interactions is therefore defined as:

$$N_{\rm coll}(\vec{b}) = A \times B \times T_{\rm AB}(\vec{b})\ \sigma_{\rm inel}^{\rm NN}. \tag{1.9}$$

The number of participants at an impact parameter $\vec{b}$ is also defined by

$$N_{\rm part}(\vec{b}) = A \int {\rm d}^2 s\ T_{\rm A}\Big\{1 - \Big[1 - \sigma_{\rm inel}^{\rm NN} T_{\rm B}(\vec{b} - \vec{s})\Big]^B\Big\} + B \int {\rm d}^2 s T_{\rm B}\Big\{1 - \big[1 - \sigma_{\rm inel}^{\rm NN} T_{\rm A}(\vec{s})\big]^A\Big\}. \tag{1.10}$$

The centrality classes and the related quantities, such as $N_{\rm part}$, $N_{\rm coll}$ and $T_{\rm AA}$ are obtained by MC simulations based on the Glauber model and on the measured charged particle multiplicity in data. The relation between the centrality determined according to experimental data and that obtained by Glauber MC simulations is presented in Appendix A.

1.4 Probing the QGP

The QGP characteristics cannot be directly measured in heavy-ion experiments because of its very short lifetime. Hence, many signatures have been proposed to indirectly probe the QGP. This section aims at giving a brief description for some of the major signatures.

1.4.1 Strangeness production

Constituents of the de-confined matter, such as gluons, are able to move freely and they can produce strange quark pairs rapidly, on the required time scale. The abundance of s and $\bar{s}$ quarks is therefore highly enhanced in the QGP compared to that of lighter quarks and with respect to the strangeness production in hadron-hadron collisions where there is no QGP. Hence, the strangeness enhancement [30] is considered as a signature of the QGP. Several experiments launched beam-energy scan programmes to probe the nature of the phase transition between hadrons and the QGP. The left panel of Figure 1.6 shows the full phase space ratio of the $< K^+ >$ production to the $< \pi^+ >$ production as a function of the collision energy. This ratio is proportional to the strangeness production divided by the entropy in the Statistical Model of the Early Stage (SMES) [51]. The results from heavy-ion collision experiments (NA49 [22] at SPS, FOPI, E802, E866, E877, E895 and E917 at AGS [52] and, BRAHMS, PHOBOS, PHENIX and STAR at RHIC [25]) do not behave like pp data [53, 54] with open symbols which show a monotonic increase with increasing energy. The right panel in Figure 1.6 presents the full phase space E_s ratio with $E_s = (< \Lambda > + < K + \bar{K} >)/ < \pi >$, which measures roughly the ratio of total strangeness to entropy [23], as a function of the collision energy. The two observables, $< K^+ > / < \pi^+ >$ and E_s, rise up with increasing energy, then decrease (turnover in [23]) and finally saturates. Both observables show peaks at the NA49 energy and this behaviour is described by the SMES model

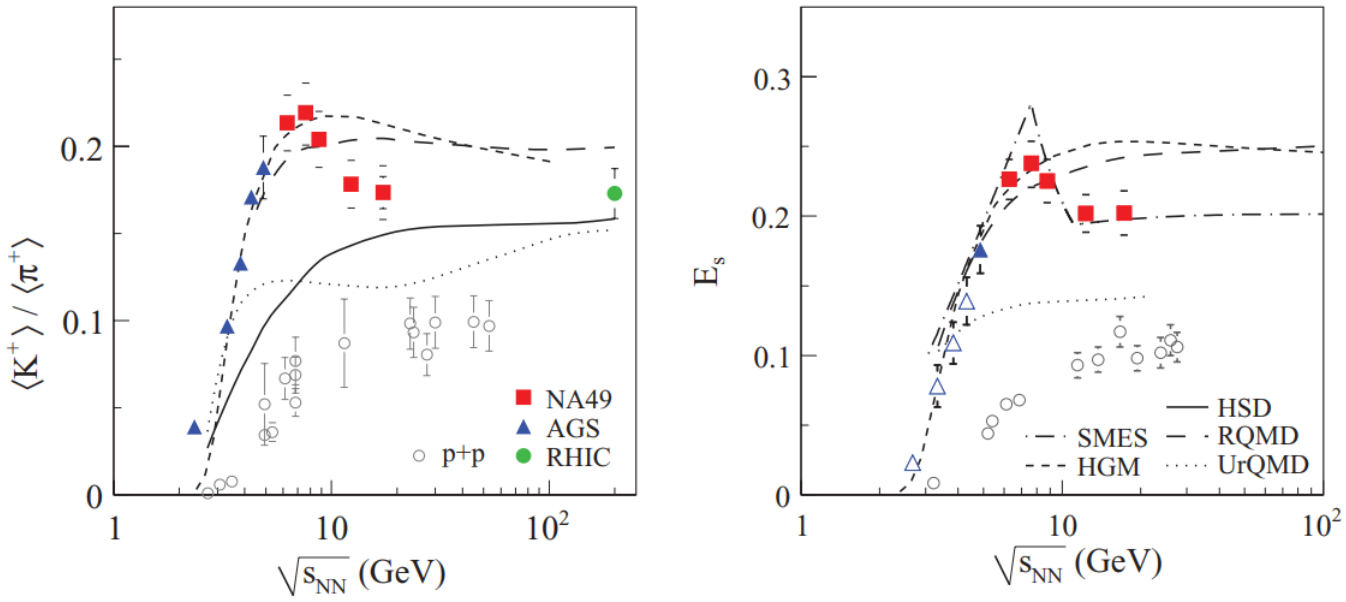

Figure 1.6: Left: Energy dependence of the $< K^+ > / < \pi^+ >$ ratio measured in central Pb+Pb and Au+Au collisions at NA49 [23], AGS [31, 32, 33, 34, 35, 36, 37, 38, 39, 40, 41] and RHIC [42, 43, 44, 45, 46, 47, 48, 49, 50], compared with the corresponding results from pp collisions. Right: Energy dependence of the relative strangeness production as measured by the E_s ratio ($E_s = (< \Lambda > + < K + \bar{K} >) / < \pi >$ as in [23]) in central Pb+Pb and Au+Au collisions at NA49 [23], AGS [31, 32, 33, 34, 35, 36, 37, 38, 39, 40, 41] and RHIC [42, 43, 44, 45, 46, 47, 48, 49, 50], compared with results from pp collisions. Figure from [23].

which assumes a phase transition. The peaks are known as "horn", and indicate and a decrease of the strangeness yield as a consequence of the phase transition from de-confined to confined matter.

1.4.2 Hydrodynamic flow

A heavy-ion collision creates a medium which thermalizes through secondary collisions of its constituents, and expands freely. This expansion leads to a hydrodynamic flow as illustrated in Figure 1.7 in case of semi-peripheral and peripheral heavy-ion collisions. Such collisions, in which the nuclear overlap area has an almond shape, cause different pressure in different spatial directions in the medium. Therefore, the medium created in the collision expands anisotropically. The pressure gradient in the medium is stronger in the direction with fewer produced particles and hence with less resistance for traveling. The initial spatial anisotropy is transferred into a momentum space asymmetry of the produced particles, via multiple scatterings, if the matter is strongly interacting.

The momentum space anisotropies of the produced particles are studied with the Fourier expansion of their azimuthal distributions with respect to a reaction plane [56]. The elliptic flow (v_2) is the second order coefficient in the Fourier series. Measuring the elliptic flow of particles offers the opportunities to study the hydrodynamical properties of the expanding medium, like for example its temperature and viscosity. The ratio, η/s, of the shear viscosity to

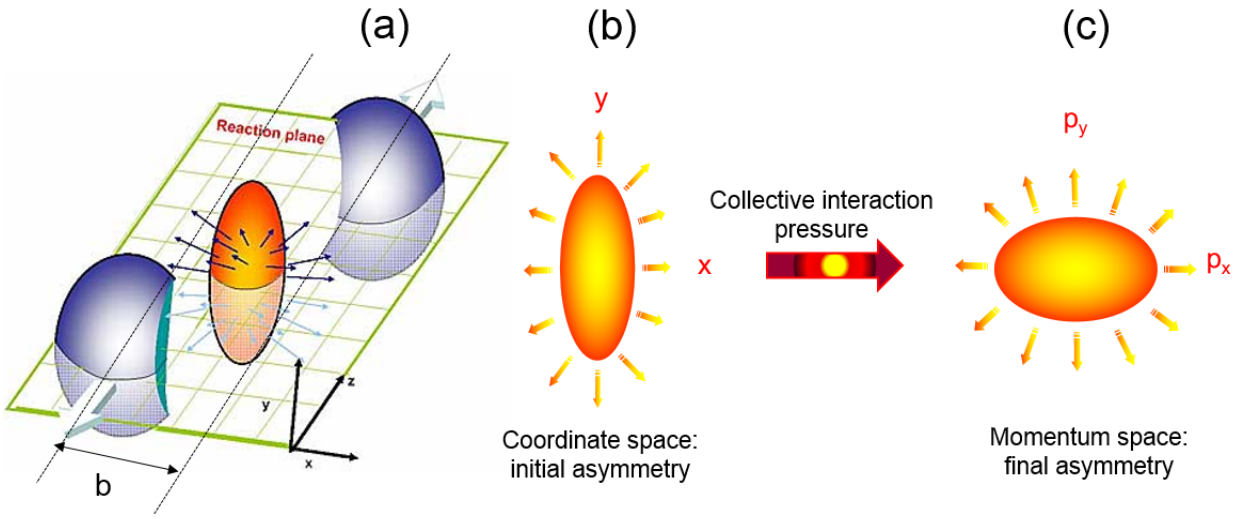

Figure 1.7: (a) A peripheral collision of two nuclei with an impact parameter b creates an almond-shaped medium; (b) The asymmetry of the medium with respect to the reaction plane translates via pressure gradients into (c) an anisotropic distribution of particles in momentum space. Figure from [55].

entropy density indicates if the particles of the medium strongly interact such as in a perfect liquid ($\eta/s \to 0$). The η/s ratio is dependent on the temperature of the medium [57] and it has a minimum around the phase transition/crossover region between hadronic matter and the QGP [58]. Furthermore, v_2 and higher-order coefficients (v_3, v_4, v_5) of charged particles have been measured in the ALICE experiment [59, 60, 61, 62]. The even-order coefficients are expected to originate from the anisotropy of the medium while the odd-order coefficients are given rise by initial state fluctuations in the positions of participating nucleons in the nuclei. Figure 1.8 shows the measurement of the multiple particle flow as a function of multiplicity, $N_{\rm ch}$, in pp, p-Pb, Xe-Xe and Pb-Pb collisions from ALICE [62]. The anisotropic flow coefficients obtained from 2-particle correlations are denoted $v_n\{2\}$. Figures 1.8(a)–1.8(c) show the $v_2\{2\}, v_3\{2\}$ and $v_4\{2\}$ measurements with a pseudorapidity separation ($|\Delta\eta| > 1.4,\ 1$ and 1, respectively). The v_2 in Xe-Xe and Pb-Pb collisions is larger than that in p-Pb and pp collisions for $N_{\rm ch} > 60$. The Pb-Pb v_2 is larger than the Xe-Xe one for $N_{\rm ch} > 300$. $v_2 > v_3 > v_4$, is observed for the large systems except at high multiplicities where $v_2 \approx v_3$. The data for large systems are also compared to theoretical calculations which use impact-parameter Glasma (IP-Glasma) initial conditions, MUSIC hydrodynamic model and the ultrarelativistic quantum molecular dynamics (UrQMD) model for hadronic rescatterings [63, 64]. These calculations reproduces the v_2 measurements in Xe-Xe and Pb-Pb collisions at high multiplicity but overestimates the ones at low multiplicity. Besides, it also overestimates the v_3 measurements in Xe-Xe and Pb-Pb collisions at high multiplicity and is compatible with that at very low multiplicity. Furthermore, it qualitatively describes the v_4 measurements in Xe-Xe and Pb-Pb collisions. In pp collisions, the flow measurements, especially for v_2, cannot be explained by model calculations without collective effects, as demonstrated by model calculations without collective effects, as demonstrated by the comparison with PYTHIA 8 [65], but the IP-Glasma+MUSIC+UrQMD model also fails at describing the pp data. In p-Pb collisions,

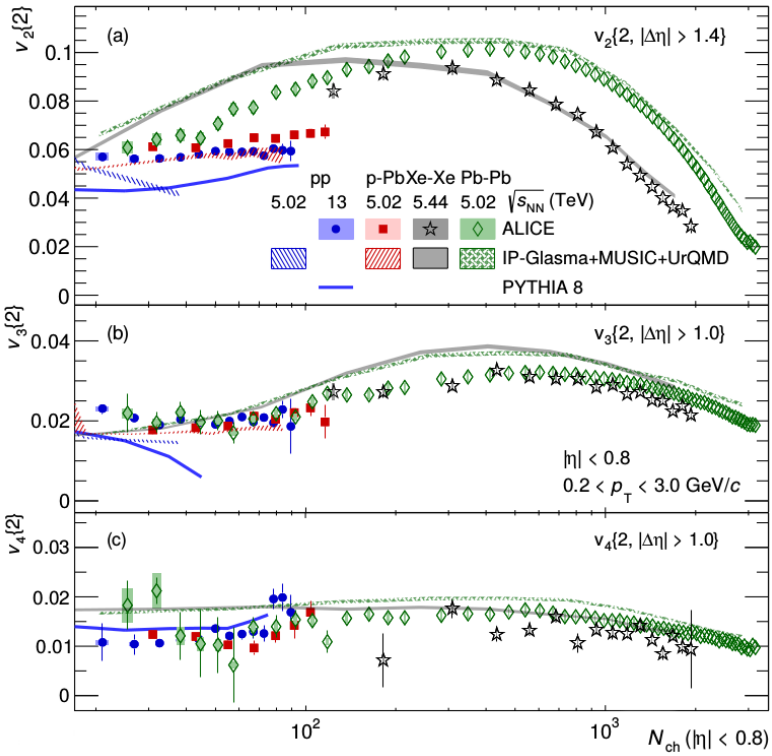

Figure 1.8: The harmonics $v_n\{2\}$ of multiple particles as a function of multiplicity in pp, p-Pb, Xe-Xe and Pb-Pb collisions. Figure from [62].

the v_2 and v_3 measurements are well reproduced by this hydrodynamical model.

1.4.3 Weak bosons

The carriers of the weak interaction, W and Z bosons are produced in the initial stage of heavy-ion collisions [66]. The decay time for the Z is 0.08 fm/c and for the W, it is 0.09 fm/c [18]. Their decay products are di-leptons (Z), single lepton + neutrino (W) or mostly into hadrons (W and Z). The weak bosons do not interact with the QGP because the weak bosons do not carry any colour charge. In other words, the weak boson production is not affected by the presence of the QGP. The weak bosons are therefore a clean probe of the nuclear effects in heavy-ion collisions, which do not originate from the QGP. This probe provides a reference for the QGP study. Weak boson productions were measured in Pb-Pb collisions at the LHC by ALICE [67], ATLAS [68] and CMS [69, 70].

1.4.4 Jet quenching

In particle physics, a jet is a collimated cone of high-momentum particles which are produced by the hadronization of a quark or a gluon. At the initial stage of heavy-ion collisions, partons including quarks and gluons are produced prior to the formation of the QGP, for example a quark and an antiquark propagating in an opposite direction. Those partons carrying colour charges try to form another colour-neutral particle by exchanging gluons. Those

original parton produces partons of lower momenta and finally fragment into hadrons. The produced partons and hadrons tend to move in the same direction. In a heavy-ion collision, the jet travels through and interact with the hot and high-density medium. It leads to a reduction of the jet energy. This phenomenon is called jet quenching [71]. In order to study the jet quenching in experiments, the yields of produced jets are measured in heavy-ion and in hadron-hadron collisions. In particular, dijet, consisting of the most energetic and second most energetic jets in an event, are studied because it provides a large cross section. The two jets, which have equal p_{T} with respect to the beam axis, are emitted almost back to back. However, medium-induced gluon emission can significantly affect the energy balance between the back-to-back jets [72] and then a relative energy loss is extracted. Recently, the measurements of jets and Z bosons (Z+jet probe) simultaneously were performed in Pb-Pb collisions by CMS [73]. The Z+jet events can be used to study an absolute energy loss. Besides, there is no background process which contaminates the boson selection. Therefore, the Z+jet probe is expected to characterize the QGP properties more precisely than measuring only jets. Figure 1.9 shows the average number of jet partners per Z boson, R_{JZ}. For all the Z boson p_{T} bins, R_{JZ} is systematically smaller in central Pb-Pb collisions (0–30%) than that in pp collisions and this suggests that in Pb-Pb collisions a larger fraction of partons associated with a Z boson loses energy in medium and falls below the jet threshold.

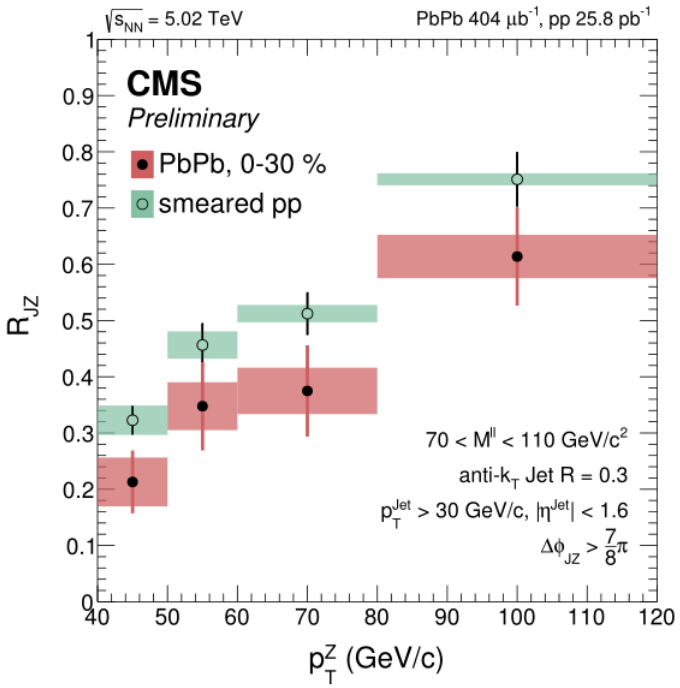

Figure 1.9: The R_{JZ} average number of jet partners per Z boson, measured in Pb-Pb and pp collisions at $\sqrt{s_{\mathrm{NN}}}$ = 5.02 TeV by the CMS experiment. Figure from [73].

1.4.5 Heavy flavours

Heavy flavour hadrons, such as D, J/ψ, Υ mesons, contain at least one charm or beauty quark with large mass. Heavy quarks are produced in the early stage of heavy-ion collisions and they are expected to experience the whole stages of a heavy-ion collision. For the charmonium excited states, for example the χ_c and ψ(2S), they are expected to dissociate earlier than the J/ψ in the QGP because they are less bound [74]. Several mechanisms and effects, such as the colour screening [75], the charmonium regeneration [76, 77] and the energy loss [78, 79], are affecting the production of these probes in heavy-ion collisions. This will be discussed in the next chapter. In addition, when heavy quarks propagate through the medium, they interact with the medium constituents and lose part of their energy via elastic or inelastic scatterings (gluon radiation). Open heavy flavours hadronizing with other lighter quark of the medium are sensitive to such kind of effects.

Chapter 2

Charmonium production

Charmonium is considered as a hard probe of the QGP in heavy-ion collisions. Measuring modification of the J/ψ production in medium gives an opportunity to characterise the QGP properties in heavy-ion collisions. This chapter presents an overview of the charmonium properties and production mechanisms. Furthermore, a selection of charmonium results in hadron-hadron collisions and heavy-ion collisions, from the major experiments, are shown.

2.1 Charmonium family

The charmonium family includes the ground and excited charmonium states which are mesons composed of a charm and an anticharm quarks. The J/ψ was the first state of the charmonium family which was discovered simultaneously at the Alternating Gradient Synchrotron (AGS) in Brookhaven National Laboratory (BNL) [80] and at the Stanford Positron-Electron Asymmetric Rings (SPEAR) in Stanford Linear Accelerator Center (SLAC) [81] in 1974. Soon many other states of the charmonium family, such as ψ(2S) [82] were also discovered[1]. Their properties, such as their quantum numbers, mass, width, decay mode and branching ratio are summarized in Table 2.1. Charmonium states are conventionally labeled according to their quantum numbers using the notation, $n^{2S+1}L_J$, with n the radial quantum number, S the total intrinsic spin, L the orbital angular momentum given in spectroscopic notation (S for L=0, P for L=1, D for L=2, etc.), and J the total angular momentum. Besides, each charmonium state has many decay modes but only few decay modes discussed in this thesis are tabulated.

Each charmonium state has its own lifetime τ, such as 7.2×10^{-21} s for J/ψ. For a given resonance state, the width Γ is related to the lifetime of the state $\Gamma = \hbar/\tau$ where $\hbar$ is the Planck constant. Charmonium states have a probability to decay through different decay channels. Figure 2.1 shows the hadronic and the radiative decays from different charmonium states in the mass versus J^{PC} plane, where J is the total angular momentum, P is the

[1]The history about the discovery of J/ψ and ψ(2S) is described in [83]

Charmonium	$n^{2S+1}L_J$	mass (MeV/c^2)	width Γ (MeV/c^2)	notable decay mode	branching ratio (%)
η_c	1^1S_0	2983.9 ± 0.5	32.0 ± 0.8	$\gamma\gamma$	(1.57± 0.12)×10^{-2}
J/ψ	1^3S_1	3096.9 ± 0.006	0.093 ± 0.0028	e^+e^-	5.97 ± 0.03
				$\mu^+\mu^-$	5.961 ± 0.033
χ_{c0}	1^3P_0	3414.71 ± 0.30	10.8 ± 0.6	J/ψ +γ	1.40 ± 0.05
χ_{c1}	1^3P_1	3510.67 ± 0.05	0.84 ± 0.04	J/ψ +γ	34.3 ± 1.0
χ_{c2}	1^3P_2	3556.17 ± 0.07	1.97 ± 0.09	J/ψ +γ	19.0 ± 0.5
ψ(2S)	2^3S_1	3686.097 ± 0.025	0.294 ± 0.008	e^+e^-	0.79 ± 0.017
				$\mu^+\mu^-$	0.8 ± 0.06

Table 2.1: Properties of charmonium bound states [18]. In quantum mechanics, n, S, L, J represent the radial quantum number, total intrinsic spin, orbital angular momentum, and total angular momentum, respectively.

parity, and C is called the charge parity. The probability values for each decay channel are indicated in percent. The horizontal dashed line at 3.73 GeV/c^2 corresponds to the production threshold for open charm pair $D^0\bar{D}^0$.

In QCD, the strength of the strong interaction depends on the distance as discussed in section 1.1.2. At short distance, the QCD coupling constant is rather small. The short distance behaviour of QCD dominates by one-gluon exchange, similarly to the quantum electrodynamics (QED) case where one-photon exchange is dominated [12]. Therefore, a Coulomb-like potential, at short distance, can be used by analogy with QED. On the other hand, at large distance, the QCD coupling constant increases and the quark confinement should be accounted for. For a charmonium bound state, considering a Coulomb-like and a quark confinement terms, one can use a non-relativistic potential $V(r)$ which describes the interquark potential. $V(r)$ is mathematically expressed as:

$$V(r) = -\frac{\alpha}{r} + \sigma r, \tag{2.1}$$

where r is the distance between the charm and anticharm quarks in vacuum, α is a gauge coupling which is related to the QCD coupling constant α_s, and σ is the string tension for the heavy quark-antiquark system which can be obtained experimentally [84]. The colour factor depends on the colour state of interacting quarks. For a system made of a charm and an anticharm quarks, they can make a colour singlet, or a colour octet. Indeed, quark colour changes at a quark-gluon vertex when a gluon is emitted, since a gluon carries one colour and one anticolour. Namely there should be nine colour-anticolour combinations for gluons. There are eight gluons which form a SU(3) octet: $R\bar{G}, R\bar{B}, G\bar{R}, G\bar{B}, B\bar{R}, B\bar{G}, \frac{1}{\sqrt{2}}(R\bar{R} - G\bar{G}), \frac{1}{\sqrt{6}}(R\bar{R} + G\bar{G} - 2B\bar{B})$. The singlet state $\frac{1}{\sqrt{3}}(R\bar{R} + G\bar{G} + B\bar{B})$ does not exist because it does not mediate colour. Back to Eq. 2.1, the string tension σ is about 0.2 GeV^2 [74] whose sign indicates that the force is attractive and keeps the $c\bar{c}$ pair attached to each other. The gauge constant α is about $\pi/12$ [74] for a charmonium bound state. By solving the corresponding Schrödinger equation [74], some properties of a given charmonium state can be obtained such as its mass and binding radius, which are given in Table 2.2 for few charmonium states.

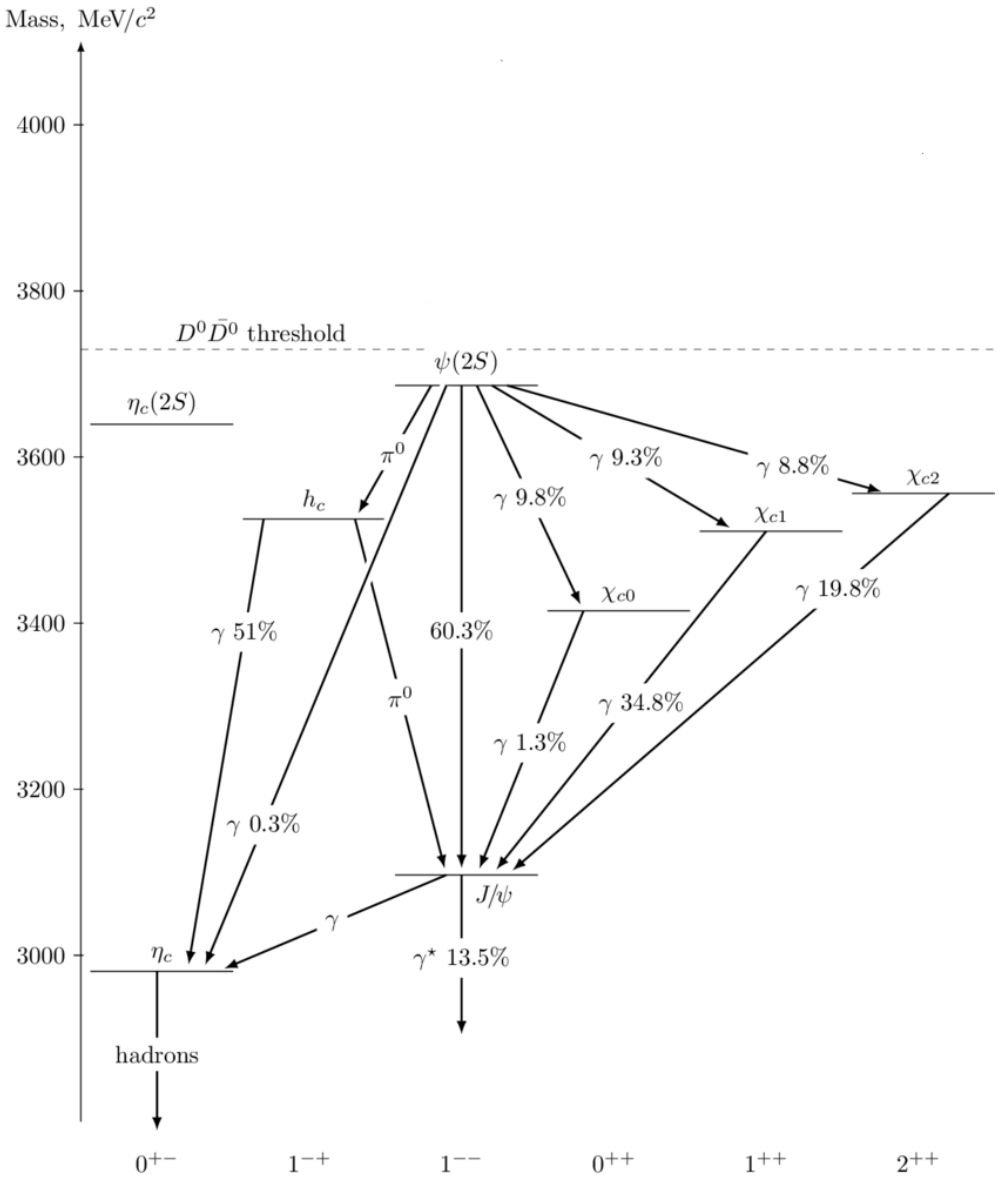

Figure 2.1: Scheme of the experimentally observed charmonium states and few decay modes. Figure from [18].

	J/ψ	χ_{c0}	ψ(2S)
m (GeV/c^2)	3.10	3.53	3.68
r (fm)	0.50	0.726	0.90

Table 2.2: Masses and binding radii of some charmonium states [74].

2.2 J/ψ production in pp collisions

In this thesis, the inclusive J/ψ production cross section is studied in pp collisions at forward-rapidity in ALICE[2] at the LHC. There are several sources that can contribute to the inclusive J/ψ production. They are classified into three categories:

- the direct J/ψ production, which only involves the J/ψ produced from the hadronisation of the initial $c\bar{c}$ pair in the collision;
- the J/ψ production by feed-down of excited charmonium states, such as ψ(2S) and χ_c, which are produced themselves from the hadronisation of the initial $c\bar{c}$ pair in the collision. In other words, this source is associated to the decay channels $\psi(2S) \rightarrow J/\psi + X$ or $\chi_c \rightarrow J/\psi + X$, where X means any particle;
- the J/ψ production by feed-down of B mesons which have a probability to decay into J/ψ with a branching fraction, for example, of 1.09 $\pm$ 0.03% for $B^{\pm}/B^0$ admixture $\rightarrow J/\psi + X$ [18]. The B meson decay length $c\tau_B$ is around 500 μm. The J/ψ are therefore produced at a secondary vertex where the B meson decays. This source of J/ψ is non-negligible at the LHC energies;

The first and the second contributions together are conventionally called the prompt J/ψ production while the last contribution is known as the non-prompt J/ψ production. The inclusive J/ψ is the sum of the prompt and non-prompt contributions. The feed-down contribution is described in more details, especially along with the experimental results in section 2.2.2.

Nowadays, the theoretical study of the J/ψ production processes is performed under the QCD framework (for a theoretical review see [85]). Nearly all the theoretical models handle separately the $c\bar{c}$ pair production and later its binding by applying a factorization approach. The initial production of the $c\bar{c}$ pair, (which will form a pre-resonant state and then will evolve into a charmonium), is expected to be perturbative because it involves momentum transfers as large as the mass of a charm quark. However, the hadronization from a $c\bar{c}$ pair into a charmonium state is considered to be non-perturbative over long distances. Indeed, the momentum scales are of the order of $m_Q v$, where v is the typical heavy quark velocity in the quarkonium rest frame ($v^2 \approx 0.3$ for a charmonium), and m_Q is the mass of the heavy quark. In this thesis, three major models are introduced: the Colour-Evaporation Model (CEM) [86, 87],

[2]ALICE is an experiment at the LHC. It is described in more detail in chapter 3 of this thesis.

the Colour-Singlet Model (CSM) [88, 89], and the non-relativistic QCD (NRQCD) model that incorporates the CSM and the Colour-Octet Mechanism (COM) [90]. Those three models have different approaches on the non-perturbative transition from the $c\bar{c}$ pair into a chamonium state.

2.2.1 J/ψ production mechanisms

Colour-evaporation model [86, 87]: this model considers that the production cross section for the charmonium is directly related to the one of the $c\bar{c}$ pair with the idea that the invariant mass range of the $c\bar{c}$ pair is restricted to the region where its hadronisation is possible. The mass range of the $c\bar{c}$ pair is constrained between the charm quark pair mass $2m_c$ and the mass of a pair of the lightest open charm hadrons $2M_D$. In this model, the $c\bar{c}$ pairs can be produced with different colours and quantum properties than the final charmonium state. The charm quark pair neutralises its colour (colour evaporated) by the multiple soft-gluon interactions with the collision-induced colour field, as shown in Figure 2.2. The charm and anticharm quarks either combine with light quarks to produce heavy-flavour hadrons or bind with each other to form a charmonium.

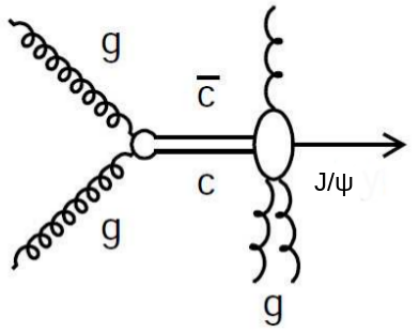

Figure 2.2: Example of the lowest-order diagram for direct J/ψ production from gluon fusion with the colour evaporation model. Multiple soft-gluons are emitted. Figure modified from [91].

The J/ψ total production cross section is mathematically written as:

$$\sigma_{\psi}^{CEM} = F_{\psi} \int_{2m_c}^{2M_D} \frac{d\sigma_{c\bar{c}}}{dm_{c\bar{c}}} dm_{c\bar{c}}. \tag{2.2}$$

As can be seen in Eq. 2.2, the cross section to produce a given charmonium state ψ is obtained using a phenomenological constant factor F_{ψ}, which is a probability that the $c\bar{c}$ pair hadronises into this charmonium state. F_{ψ} is determined by fitting the data. The CEM model was phenomenologically successful but does not predict polarisation observables and has difficulties to reproduce some transverse momentum spectra of charmonium, for example, for 9 $< p_{\mathrm{T}} <$ 14 GeV/c in Figure 9 in [85].

Recently, an improved color evaporation model (ICEM) for charmonium production was proposed [92]. During the charmonium hadronisation in a high energy collision, the ICEM distinguishes soft gluons exchanged between the $c\bar{c}$ pair and other sources from soft gluons emitted by the $c\bar{c}$ pair. This distinction is made because the latter will evolve to particles, which is not the case of the former. Another difference between CEM and ICEM is the momentum shift between the $c\bar{c}$ pair and the charmonium. This model also imposes that the invariant mass of the $c\bar{c}$ pair is larger than the mass of the produced charmonium. The theoretical calculations by the ICEM are in general agreement with the p_{T} dependence of the J/ψ and the ψ(2S) data [92].

Colour-singlet model: it was first proposed in 1980 [88, 89]. It handles the charmonium production cross section with a perturbative and a non-perturbative parts by applying the factorisation approach. The model requires that the quantum numbers of the created $c\bar{c}$ pair are the same as the one of the produced J/ψ particle. Therefore, the hard scattering can only produce colour-singlet $c\bar{c}$ pairs. Figure 2.3 illustrates the lowest-order diagram for J/ψ production from gluon fusion in the colour-singlet model. Specifically, the quantum numbers, $^{2S+1}\mathrm{L}_J$, of the $c\bar{c}$ pair should be $^3\mathrm{S}_1$, and the $c\bar{c}$ pair should be in the colour-singlet state such as the formed J/ψ. The charmonium cross section $d\sigma^{CSM}_{\psi+X}$ is expressed as:

$$\mathrm{d}\sigma^{CSM}_{\psi+X} = \sum_{i,j} \int \mathrm{d}x_i \mathrm{d}x_j f_i(x_i, \mu_F) f_j(x_j, \mu_F) \mathrm{d}\hat{\sigma}_{i+j\to(c\bar{c})+X}(\mu_R, \mu_F) |\psi(0)|^2, \tag{2.3}$$

where $f_i(x_i, \mu_F)$ and $f_j(x_j, \mu_F)$, are the parton densities (i.e. the parton distribution function (PDF)) in the two colliding hadrons. The PDF describes the probability of finding a parton carrying a fraction, Bjorken x, of the nucleon's longitudinal momentum at a given energy scale, μ_F. The two scales, μ_F and μ_R are the factorisation and renormalisation scales, respectively. The partonic cross section $d\hat{\sigma}_{i+j\to(c\bar{c})+X}(\mu_R, \mu_F)$ specifies the production cross section of the charm quark pair with zero relative velocity, v, and with the same angular momentum and spin state as the subsequently formed charmonium. $|\psi(0)|^2$ is the square of the Schrödinger wave function at the origin in the position space. $\psi(0)$ is fixed thanks to decay-width measurements and this model has no free parameters at Leading Order. This model describes well the main hadroproduction energy and rapidity dependences of data from RHIC to LHC energies [93, 94], and gives an acceptable description of the J/ψ photoproduction[3] data at HERA [89, 95]. However, the model underestimates the J/ψ production cross section for $5 < p_{\mathrm{T}} < 20$ GeV/c in $p\bar{p}$ collisions at $\sqrt{s} =$ 1.8 TeV in the Tevatron [96]. Nowadays, it has been shown that NLO and next-to-next-to-leading order (NNLO) give large corrections of α_S to the CSM and the higher-order calculations enhance the cross section in the high-p_{T} region [97].

Non-relativistic QCD model includes not only the colour-singlet but also the colour-octet contributions and this model has been developed since 1995 [90]. This model also treats separately the perturbative and the non-perturbative parts by applying the factorization approach in order to obtain the charmonium production cross

[3]The J/ψ photoproduction is introduced in section 2.3.3

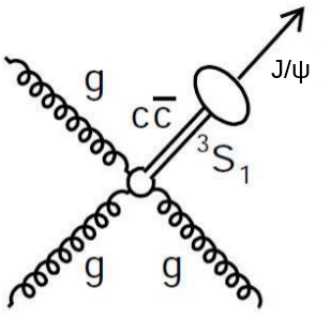

Figure 2.3: Example of the lowest-order diagram for direct J/ψ production from gluon fusion with the colour singlet model. The $c\bar{c}$ pair is in the colour singlet state. Figure modified from [91].

section. The charmonium is formed from a colour octet or singlet $c\bar{c}$ pair emitting one or more soft gluons, as shown in Figure 2.4 in case of a colour octet $c\bar{c}$ state. The hadronic cross section in this model is defined as:

$$\mathrm{d}\sigma_{\psi}^{NRQCD} = \sum_{i,j,n} \int \mathrm{d}x_i \mathrm{d}x_j f_i(x_i, \mu_F) f_j(x_j, \mu_F) \mathrm{d}\hat{\sigma}_{i+j\to(c\bar{c})_{n+X}}(\mu_R, \mu_F, \mu_\Lambda) < O_{\psi}^{n} >, \tag{2.4}$$

where μ_Λ is a non-physical scale and $< O_{\psi}^{n} >$ is the Long Distance Matrix Elements (LDME), which describes the hadronisation probability for a given charmonium state with n the quantum number of the $c\bar{c}$ state, such as the angular momentum, spin and colour. Unlike the probability $|\psi(0)|^2$ in Eq. 2.3, $< O_{\psi}^{n} >$ cannot be fixed by decay-width measurements. In order to determine the LDMEs, three groups [98, 99, 100] have analysed the p_{T} dependence of the charmonium cross-section at different energies.

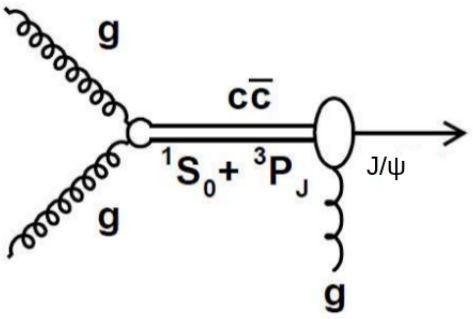

Figure 2.4: Example of the lowest-order diagram for direct J/ψ production from gluon fusion with the colour octet mechanism. The $c\bar{c}$ pair is in the colour octet state. Figure modified from [91].

This model describes the charmonium data at the RHIC and the LHC energies in ALICE, as it will be shown in section 2.2.3. However, this model fails at describing the charmonium polarisation results at high p_{T} in $p\bar{p}$ collisions at the Tevatron [101, 102] and in pp collisions at the LHC [103].

Recently, a NRQCD model coupled to the **Color Glass Condensate** (CGC) [104] framework was developed [5] to investigate the heavy quarkonium production in the low p_{T} ($p_{\mathrm{T}} \leq m$, the quarkonium mass) region. In particular, the framework of the Color Glass Condensate describes the behaviour of the small Bjorken-x partons of the hadron at high energy, where the density of low-momentum gluons is high. "Color" corresponds to the quantum number that gluons carry. "Glass" implies that the partons in hadrons are disordered at low momenta and evolve slowly on the long time scale. This behaviour is analogous to the principles of glass formation so it is named after glass. The calculation in the CGC framework employed within NRQCD describes charmonium production as a function of y and at low p_{T} in pp collisions at RHIC and LHC [5].

2.2.2 Feed-down contribution

Charmonia are also produced from B meson decays. One of the QCD model for this contribution is based on the Fixed-Order-Next-to-Leading-Log (FONLL) approach for the $b\bar{b}$ production cross-section [6]. At small p_{T} at the LHC energies, the production of heavy quark probes small-x values, a region in which large higher-order (NLO) corrections need to be resummed. Furthermore, for very large transverse momenta of heavy quarks ($p_{\mathrm{T}} >> m_Q$), the resummation of next-to-leading log (NLL) terms becomes crucial.

The J/ψ from B contribution is non-negligible at the LHC energies.

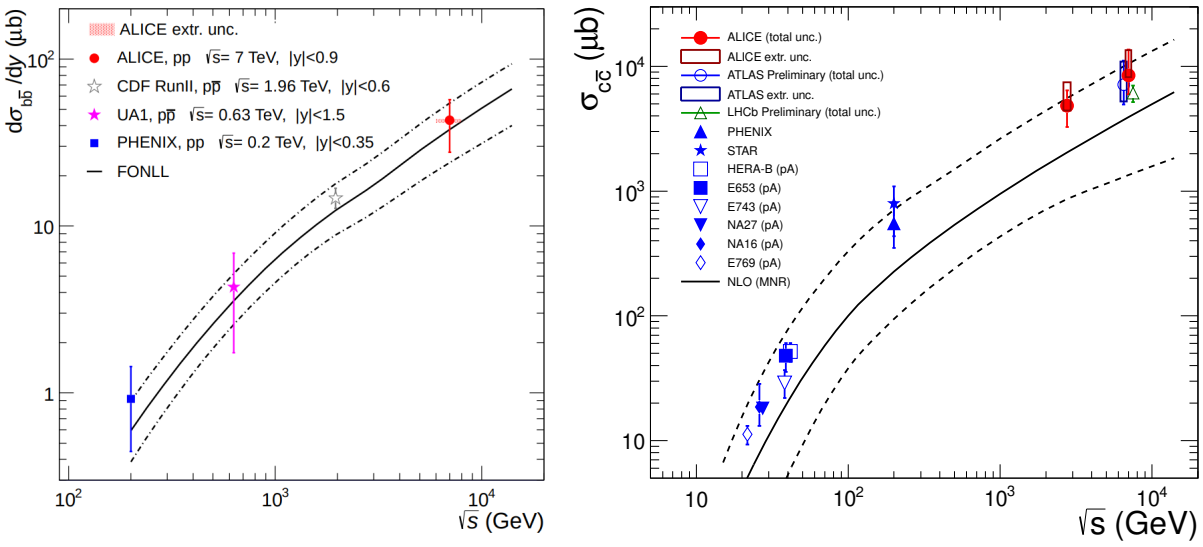

Figure 2.5: Left: $\mathrm{d}\sigma_{b\bar{b}}/\mathrm{d}y$ as a function of $\sqrt{s}$ in pp and p$\bar{\mathrm{p}}$ collisions, at mid-rapidity. See the text for details. Figure from [105]. Right: total charm cross section as a function of energy [106, 107, 108, 109, 110]. The NLO MNR calculation [111] and its uncertainties are represented by solid and dashed lines, respectively. Figure from [112].

The left panel of Figure 2.5 shows the mid-rapidity differential $b\bar{b}$ production cross section as a function of the collision energy in pp and p$\bar{\mathrm{p}}$ collisions from $\sqrt{s}$ = 200 GeV to 7 TeV. The PHENIX [113] and ALICE results in

pp collisions are shown in blue and red, respectively. The UA1 [114] and CDF [115] results from $p\bar{p}$ collisions are shown in pink and green, respectively. The ALICE measures larger $b\bar{b}$ cross section with respect to the lower-energy CDF, UA1, and PHENIX results (about a factor of 5 bigger than CDF data). Furthermore, the FONLL central value of the model calculation is shown as solid line and its uncertainties as dashed lines. This model describes well the energy dependence of the data. The right panel of Figure 2.5 shows the total charm-anticharm production cross section as a function of energy measured by several experiments [106, 107, 108, 109, 110]. In the case of pA or dA collisions, their measured cross sections are scaled by the number of binary nucleon–nucleon collisions obtained from a Glauber model of the proton–nucleus or deuteron–nucleus collision geometry. The cross section at the LHC energies [112, 106, 107] is larger than that at the RHIC and SPS energies [108, 109, 110].

In the forward-rapidity region, the fraction of J/ψ from B meson decays, known as fraction of non-prompt J/ψ, is measured as a function of p_{T} in pp collisions at $\sqrt{s}$ = 13 TeV with the LHCb experiment[4]. The result is shown in Figure 2.6 and the values of the non-prompt fraction ranges from about 10% for $p_{\mathrm{T}} = 0$ to about 40% for $p_{\mathrm{T}} =$ 13 GeV/c. The ratio of non-prompt J/ψ to prompt J/ψ production cross sections integrated over p_{T} and rapidity is around 15% at this energy [116].

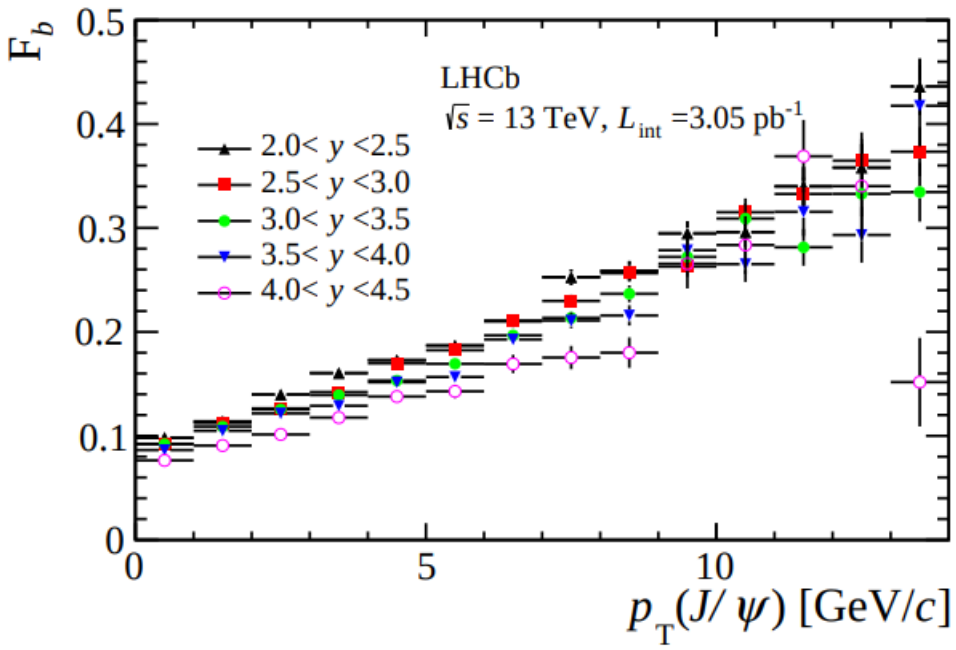

Figure 2.6: Fractions of J/ψ from B mesons as a function of the J/ψ p_{T} in y ranges, measured by LHCb in pp collisions at $\sqrt{s}$ = 13 TeV. Figure from [116].

The prompt J/ψ component includes the J/ψ that are produced from the decay of excited charmonium states, such as ψ(2S) and χ_c. The feed-down fraction from ψ(2S) and χ_c are denoted as $R_{\psi(2S)}$ and R_{χ_c}, respectively. They can

[4]The LHCb experiment is described in chapter 3 of this thesis.

be expressed as:

$$R_{\psi(2S)} = \mathrm{Br}(\psi(2\mathrm{S}) \to \mathrm{J}/\psi + \mathrm{X}) \frac{\sigma(\psi(2\mathrm{S}))}{\sigma(\mathrm{J}/\psi)}, \tag{2.5}$$

and

$$R_{\chi_c} = \mathrm{Br}(\chi_\mathrm{c} \to \mathrm{J}/\psi + \mathrm{X}) \frac{\sigma(\chi_\mathrm{c})}{\sigma(\mathrm{J}/\psi)}, \tag{2.6}$$

where $\mathrm{Br}(\psi(2\mathrm{S}) \to J/\psi + X)$ and $\mathrm{Br}(\chi_c \to J/\psi + X)$ are the branching ratio of the χ_c and $\psi(2\mathrm{S})$ in the J/ψ decay channel, respectively. $\sigma(\psi(2S))$, $\sigma(\chi_c)$, and $\sigma(J/\psi)$ are the prompt production cross section of $\psi(2\mathrm{S})$, χ_c and J/ψ particles, respectively.

Those contributions were studied at forward-rapidity in pp collisions at $\sqrt{s} = 7$ TeV [117, 118, 119] by the LHCb and CMS experiments, The fraction of prompt $\psi(2\mathrm{S})$ to J/ψ as a function of p_T measured by LHCb is shown in the left panel of Figure 2.7. The values of the fraction increase from about 1% to about 4% with increasing p_T. In the CMS[5] experiment, the ratios of prompt $\psi(2\mathrm{S})$ to J/ψ cross section have been measured as well. The result is shown in the right panel of Figure 2.7. The contribution of prompt $\psi(2\mathrm{S})$ is small ($\approx$4%) with respect to the prompt J/ψ contribution, and does not vary significantly with p_T in this p_T region.

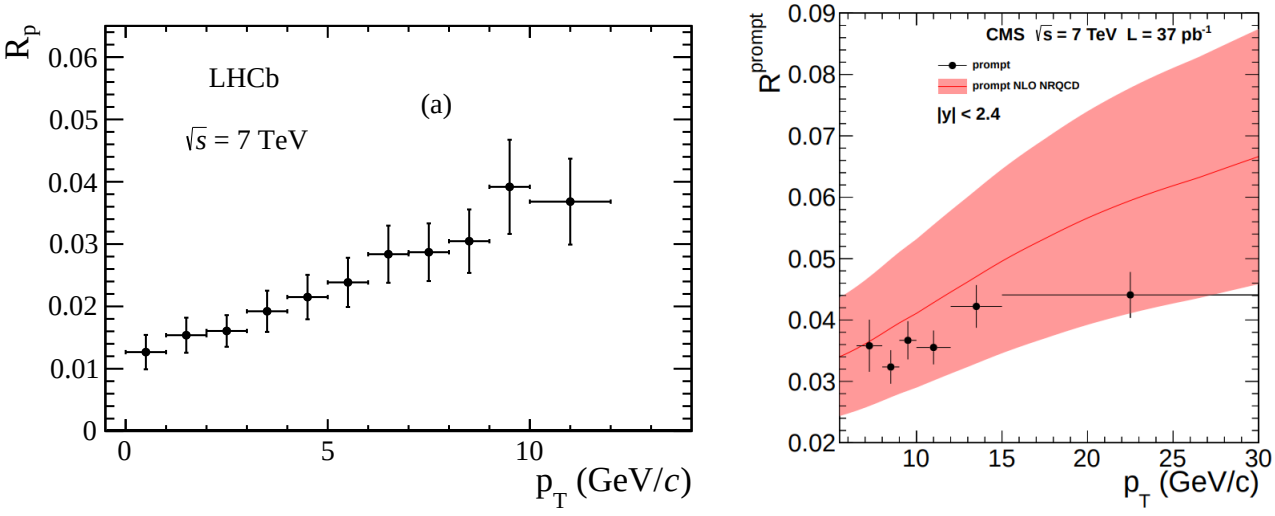

Figure 2.7: Left: fraction of prompt $\psi(2\mathrm{S})$ to J/ψ measured as a function of p_T for $2.5 < y < 4$ in pp collisions at $\sqrt{s} = 7$ TeV with LHCb (left) [117] and with CMS (right) [119].

The prompt χ_c contribution was also studied in the LHCb experiment [118]. The measured ratio of prompt χ_c to J/ψ differential cross sections as a function of p_T raises up from 14% for $p_\mathrm{T} = 2.5$ GeV/c to 27% for $p_\mathrm{T} = 14.5$ GeV/c. This contribution is larger than the prompt $\psi(2\mathrm{S})$ one.

[5]CMS is one of the LHC experiments. It is described in more details in chapter 3

2.2.3 J/ψ measurements at the RHIC and the LHC

The inclusive J/ψ production cross section at mid-rapidity is measured as a function of p_{T} in pp collisions at $\sqrt{s}$ = 200 GeV by STAR [120, 121] and by PHENIX [122] at the Relativistic Heavy Ion Collider (RHIC). The results along with the model comparisons are shown in Figure 2.8.

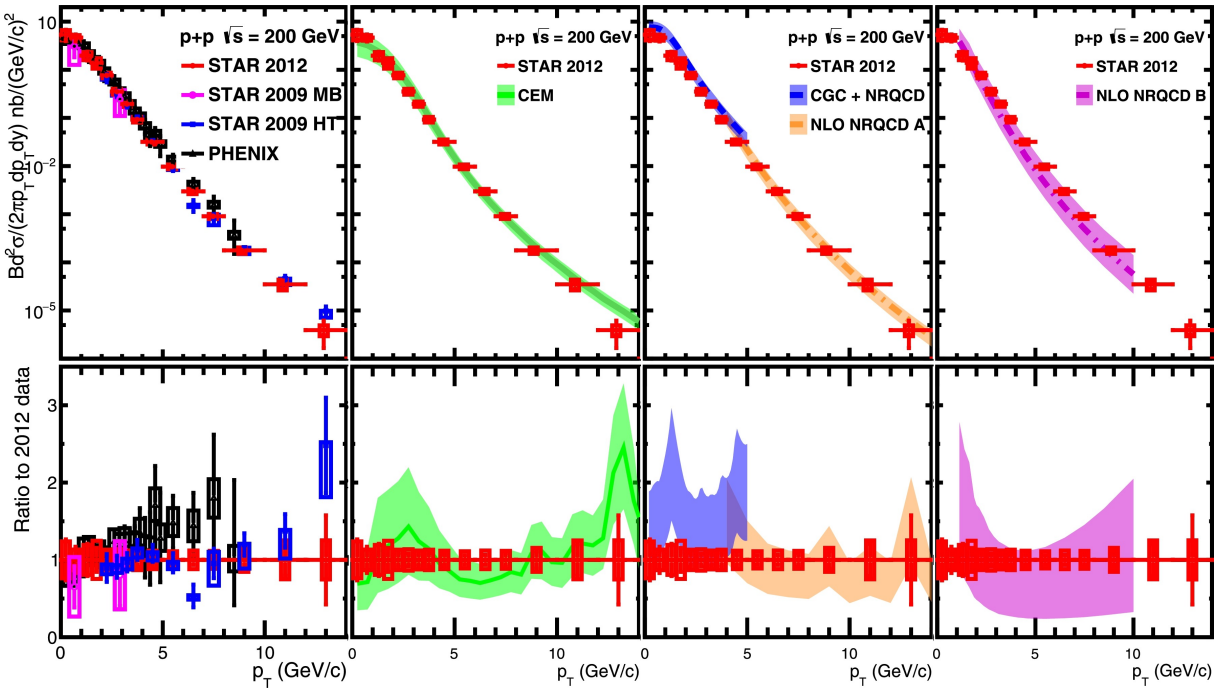

Figure 2.8: Top: inclusive J/ψ differential cross section times the dielectron branching ratio $\mathrm{B}_{J/\psi\to e^+e^-}$ as a function of p_{T} in pp collisions at $\sqrt{s}$ = 200 GeV. Pink circles, red circles and blue squares are the published results for $|y| < 1$ from STAR; black triangles are the published results for $|y| < 0.35$ from PHENIX [122]. The curves are the theoretical calculations of CEM (green) [123], NLO NRQCD from Ma *et al.* (orange) [124], CGC+NRQCD (blue) [5], and NLO NRQCD from Buttenschoen *et al.* (magenta) [103]. Bottom: ratios of these results with respect to the central value from STAR 2012. Figure from [120].

The STAR 2012 result is consistent with their published results from 2009 and shows better statistical precision for $p_{\mathrm{T}} < 10$ GeV/c. It is also consistent with the published PHENIX result at the same energy. The green band represents the calculation result from CEM model [123] for $0 < p_{\mathrm{T}} < 14$ GeV/c and $|y| < 0.35$. The orange band shows the one from NLO NRQCD calculation from Ma *et al.* [124] for $4 < p_{\mathrm{T}} < 14$ GeV/c and $|y| < 1$, while the blue band depicts the result from NRQCD calculation [5] for $0 < p_{\mathrm{T}} < 5$ GeV/c and $|y| < 1$ which incorporates a CGC effective theory framework for small-x resummation. The magenta band shows the calculation from NLO NRQCD from Buttenschoen *et al.* [103] for $1.1 < p_{\mathrm{T}} < 10$ GeV/c and $|y| < 0.35$. The CEM and NLO NRQCD calculations reproduce well the data in most of the measured p_{T} bins. The CGC+NRQCD calculations are consistent with the data within uncertainties, however, the data are close to the lower uncertainty boundary of the theoretical calculation. As can be seen, except for the two bins at the highest p_{T}, the uncertainties on the experimental results are smaller than those on the theoretical calculations. These experimental results are therefore helpful for constraining the theoretical model calculations.

J/ψ production in pp collisions is also studied in the four major experiments at the LHC. ATLAS and CMS measure the prompt and non-prompt J/ψ at large p_{T} and at mid-rapidity. Likewise, LHCb performs the prompt and non-prompt J/ψ production measurements at forward-rapidity. ALICE measures the prompt and the non-prompt J/ψ productions at low p_{T} and at mid-rapidity and measures the inclusive J/ψ production at forward rapidity. The most recent published results on the inclusive J/ψ production at forward-rapidity in pp collisions at $\sqrt{s}$ = 5.02 and 13 TeV are reported in [125]. Figure 2.9 shows the inclusive J/ψ differential cross section as a function of p_{T} up to 30 GeV/c (left panel) and as a function of y (right panel) at $\sqrt{s}$ = 13 TeV in the ALICE and LHCb experiments. Their statistical uncertainties are represented with vertical lines and their systematic uncertainties are marked with boxes. In this figure, the LHCb results are the sum of the prompt and the non-prompt J/ψ contributions. The two measurements are consistent within 1σ of their total uncertainties, although the LHCb points seem to be systematically lower than the ALICE points, as a function of rapidity (especially while going towards the mid-rapidity region). Figure 2.10 shows the inclusive J/ψ production cross section measurements performed by ALICE in pp

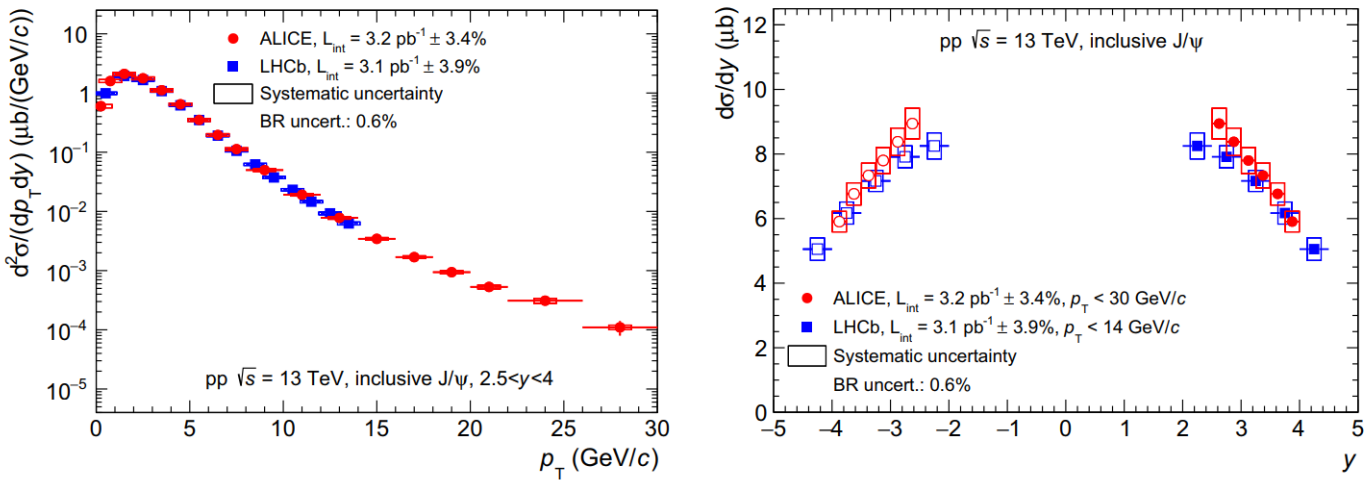

Figure 2.9: Inclusive J/ψ differential cross section as a function of p_{T} (left panel) and y (right panel) in pp collisions at $\sqrt{s}$ = 13 TeV measured by ALICE and LHCb experiments. Figure from [125].

collisions at $\sqrt{s}$ = 5.02 TeV as a function of p_{T} in the left panel and of y in the right panel. A new measurement in pp collisions at $\sqrt{s}$ = 5.02 TeV with a higher luminosity is performed in this thesis. The results and discussion can be found in chapter 4.

The ALICE results on the inclusive J/ψ production at $\sqrt{s}$ = 13 TeV are compared to two calculations, the prompt J/ψ by the NLO NRQCD calculation [4] and the prompt J/ψ by the LO NRQCD calculation coupled with a CGC calculation [5]. The non-prompt J/ψ contribution is modeled by the FONLL calculation and is summed to the prompt J/ψ calculations in order to describe the inclusive J/ψ yield. The model comparisons are shown in Figure 2.11. In the left panel of the figure, below p_{T} of 8 GeV/c, the NRQCD coupled with the CGC calculation for prompt J/ψ can

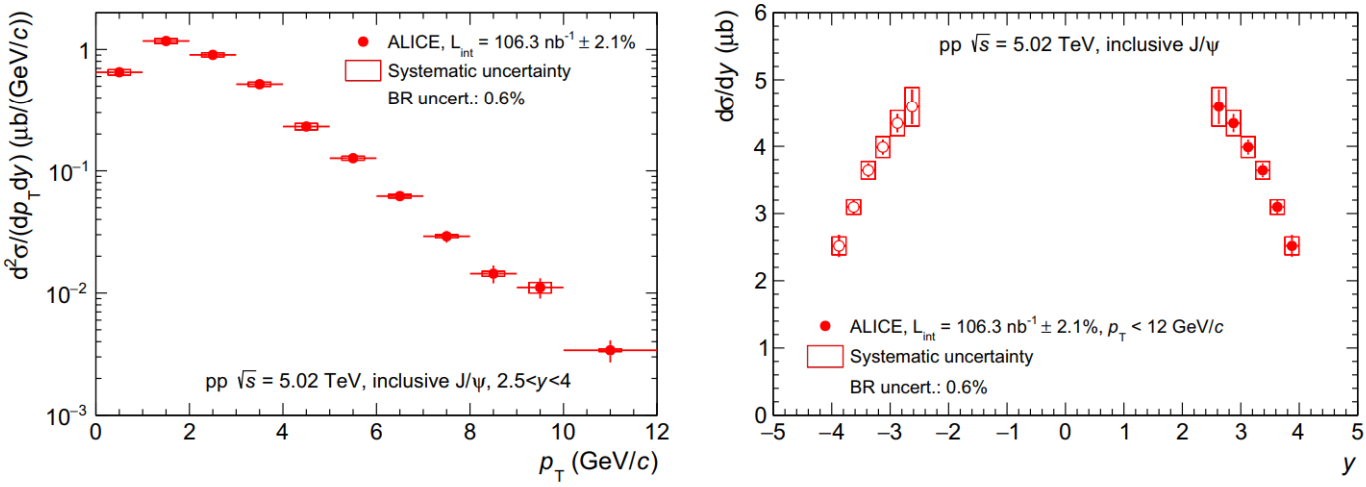

Figure 2.10: ALICE measurement on inclusive J/ψ differential cross section as a function of p_{T} (left panel) and as a function of y (right panel) in pp collisions at $\sqrt{s} = 5.02$ TeV. Figure from [125].

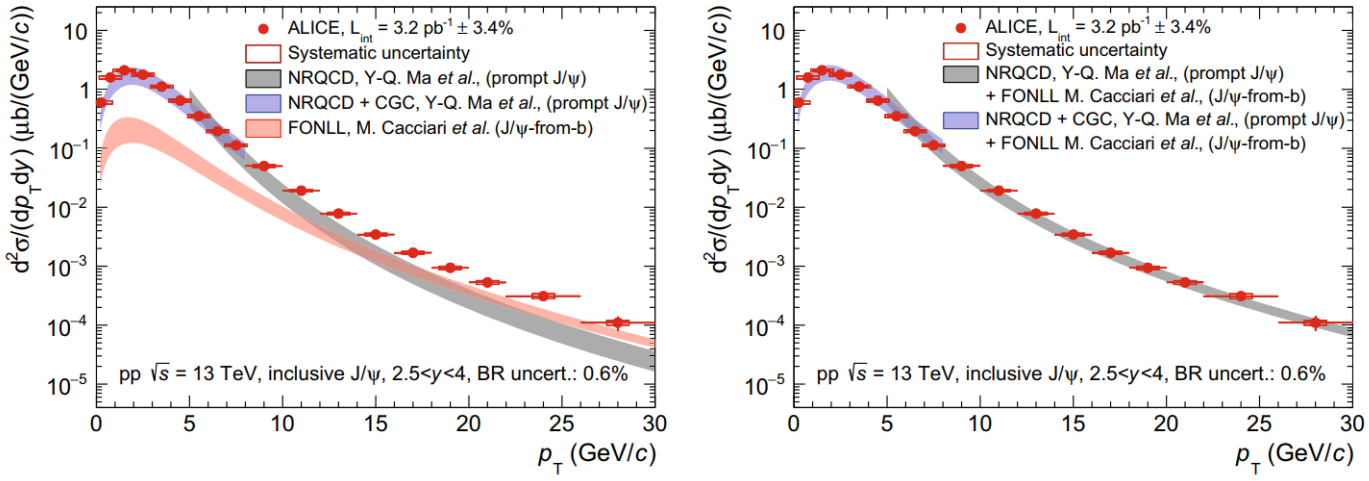

Figure 2.11: Left: inclusive J/ψ p_{T}-differential cross section in pp collisions at $\sqrt{s} = 13$ TeV compared with the NLO NRQCD [4] (grey), the LO NRQCD coupled with CGC [5] (blue) and the FONLL [126] (red) theoretical calculations. Right: the non-prompt J/ψ contribution estimated by FONLL theoretical calculation is included in the NLO NRQCD (grey), and the LO NRQCD coupled with CGC models (blue). Figure from [125].

already reproduce the data well. The non-prompt J/ψ by FONLL calculation is shown separately. In the high-p_{T} region, the prompt J/ψ by NLO NRQCD calculation alone cannot describe well the data with increasing p_{T}. This is because the non-prompt J/ψ contribution, can become as large as the prompt contribution at high p_{T} (as shown by the FONLL calculation). In the right panel of Figure 2.11, the non-prompt J/ψ production estimation by FONLL calculation is summed to the prompt J/ψ production from the NLO NRQCD calculation and the NRQCD+CGC calculation. Both modelisations reproduce the data well in the whole measured p_{T} region.

The prompt J/ψ production cross section is also measured in pp collisions at mid-rapidity by several LHC experiments. The p_{T} differential results obtained in pp collisions at $\sqrt{s}$ = 7 TeV at ALICE, CMS and ATLAS are shown in the left panel of Figure 2.12.

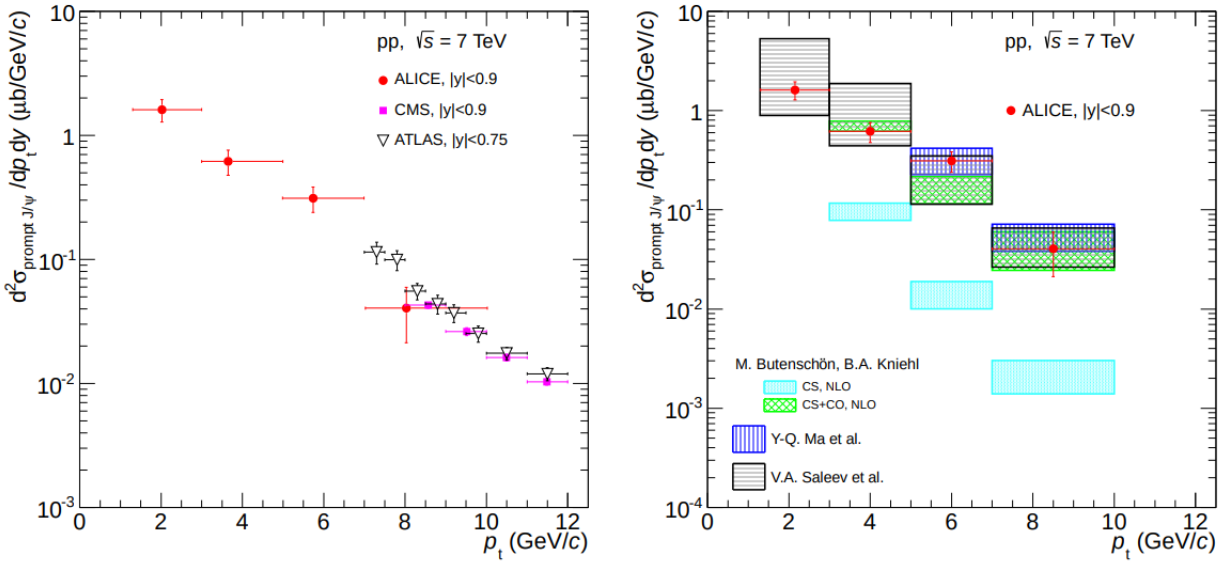

Figure 2.12: Prompt J/ψ p_{T} differential cross section measurement at mid-rapidity in pp collisions at $\sqrt{s}$ = 7 TeV from the ALICE experiment compared to the results from ATLAS and CMS experiments (left panel) and to theoretical calculations (right panel). Figure from [127].

The ALICE measurement at low p_{T} complements the data from CMS for $|y| < 0.9$ and $p_{\mathrm{T}} > 8$ GeV/c, and from ATLAS for $|y| < 0.75$ and $p_{\mathrm{T}} > 7$ GeV/c. In the right panel of Figure 2.12, the ALICE measurement is compared to NLO NRQCD theoretical calculations by M. Butenschon *et al.* [3] and by Y.-Q. Ma *et al.* [4]. Both calculations include colour-singlet, colour-octet, and heavier charmonium feed-down contributions. For one of the two models (M. Butenschon *et al.*) the partial results with only the colour-singlet contribution are also shown. The comparison indicates that the colour-octet processes are needed to describe the data for $p_{\mathrm{T}} < 10$ GeV/c. The model of V.A. Saleev result [128] is also compared to the ALICE measurement. This model is also based on the NRQCD framework and includes the contribution of partonic sub-processes involving t-channel parton exchanges. It provides predictions down to $p_{\mathrm{T}} = 0$ [6]and reproduces well the ALICE data.

[6]The model of V.A. Saleev fits the CDF data [129, 130, 101, 131] on charmonium production to obtain the non-perturbative long-

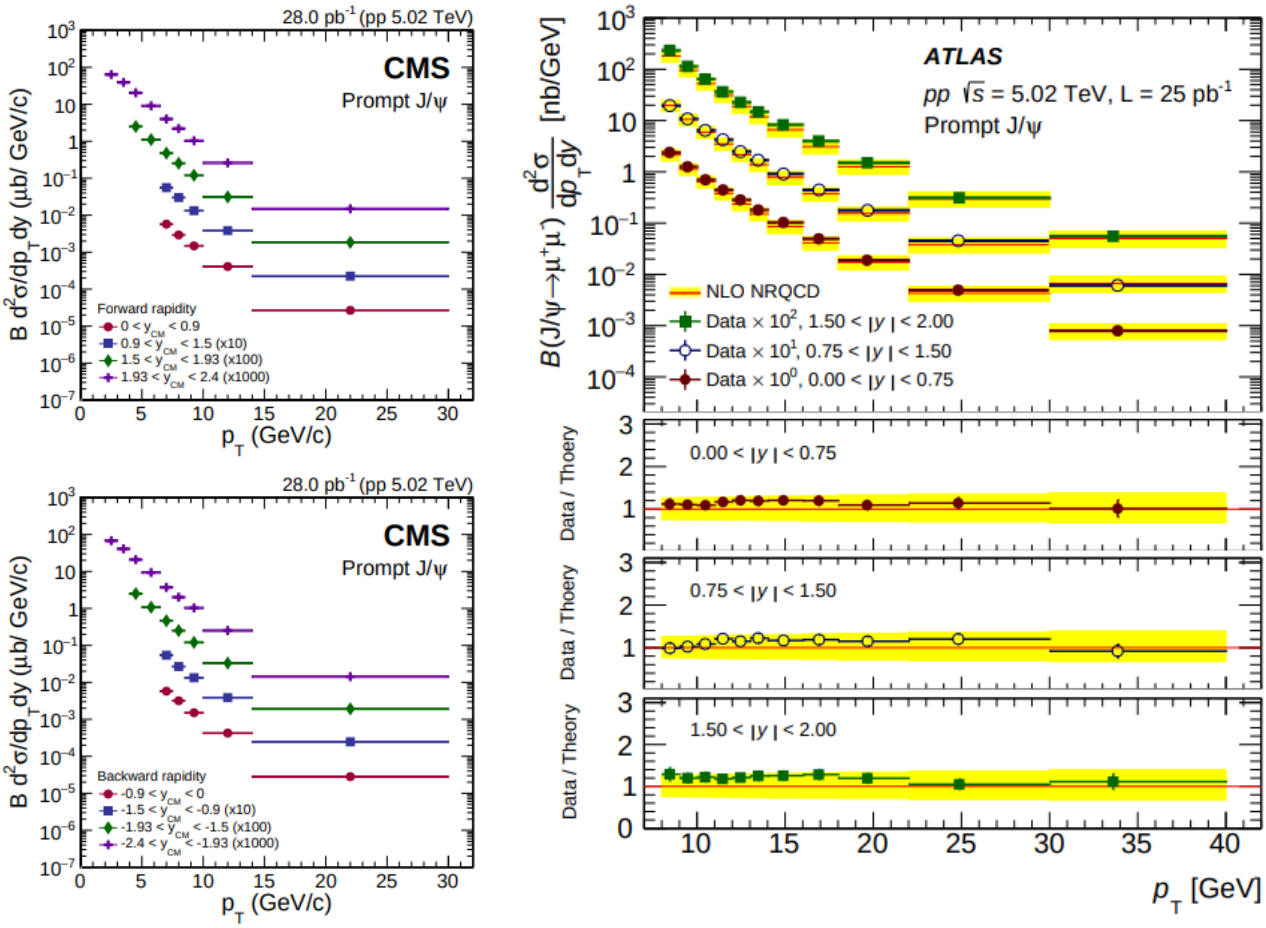

Figure 2.13: Left: prompt J/ψ p_{T}-differential cross section measured in four forward (top) and four backward (bottom) rapidity intervals in pp collisions at $\sqrt{s} = 5.02$ TeV by the CMS experiment. The fully correlated global uncertainty from the integrated luminosity determination is 2.3%. Right: prompt J/ψ p_{T}-differential cross section for three intervals of rapidity in pp collisions at $\sqrt{s} = 5.02$ TeV measured by the ATLAS experiment and compared to NRQCD calculations [4, 132]. The left panel is from [133] and the right panel is from [134].

The prompt J/ψ production cross section at mid-rapidity is also measured in pp collisions at $\sqrt{s} = 5.02$ TeV by ATLAS and CMS. The left panel of Figure 2.13 shows the p_{T} and y double-differential prompt J/ψ cross sections multiplied by the dimuon branching ratio, measured with the CMS experiment [133]. The right panel of Figure 2.13 shows the p_{T} and y double-differential prompt J/ψ cross sections multiplied by the dimuon branching ratio, measured by the ATLAS experiment [134] and compared with NRQCD theoretical calculations [4, 132]. A good description of the data is provided by the NLO NRQCD calculations in the full p_{T} and rapidity ranges of the ATLAS measurement.

2.3 J/ψ production in heavy-ion collisions

As discussed in section 1.2, the quark-gluon plasma (QGP) is expected to be created in heavy-ion collisions. The QGP can affect the particles produced in the collisions because they can interact with the formed medium. Especially, charmonia, and in particular the J/ψ particle (studied in this thesis), are interesting tools to probe the QGP. The pre-resonant $c\bar{c}$ state is estimated to be created at the colour neutralization time of about 0.25 fm/c [74], which is a short time scale regarding the time evolution of a heavy-ion collision. As seen in section 1.3, the equilibrium QGP is expected to be formed in a heavy-ion collision at the LHC energy after a time of about 2 fm/c starting from the initial collision. Therefore, the creation of the $c\bar{c}$ pair is expected to occur before the thermalisation of the QGP. Hence, the $c\bar{c}$ pair can experience medium effects during the evolution of the heavy-ion collision. The medium effects are, in principle, classified into two categories. The first class of effects is responsible for the modification of the J/ψ yield because of the QGP formation and is called hot nuclear matter effects. The other class of effects on is responsible for the modification of the J/ψ yield in AA collisions but is not related to the presence of a QGP. This second class of effects can be studied separately in pA collisions, where the formation of a QGP is not expected and is called cold nuclear matter effects.

The hot nuclear matter effects can be classified into four main mechanisms or effects for charmonium production:

- colour screening and sequential dissociation;
- charmonium (re)generation;
- energy loss;
- comovers.

The cold nuclear matter effects comprise the following mechanisms or effects:

- modification of nuclear parton distribution function;
- nuclear absorption;

distance matrix elements which are then taken into account for prediction of the charmonium production at the LHC energy. In particular, the p_{T} distribution of the J/ψ data can be down to $p_{\mathrm{T}} = 0$.

- parton multiple scattering and energy loss;
- gluon saturation.

The following sections describe the above mechanisms or effects in more details. Besides, J/ψ photoproduction occurring at very low p_{T} is not negligible in peripheral collisions and is introduced in section 2.3.3. The recent experimental results on inclusive J/ψ production in heavy-collisions at RHIC and at the LHC are presented in section 2.3.4.

2.3.1 Hot nuclear matter effects on J/ψ production

Colour screening and sequential dissociation: as discussed in section 2.1, the potential of a $c\bar{c}$ system in vacuum can be described with Eq. 2.1 with a repulsive Coulomb-like and a confinement linear terms. At finite temperature T and at high density of colour charges in the medium, Eq. 2.1 is modified to account for the colour screening of the interquark potential whose effect is described by an additional term containing the Debye screening radius $r_D(T)$, a variable depending on the temperature. This screening radius affects the interaction range of quarks. If the medium temperature raises up, $r_D(T)$ decreases and the quarks only interact with other quarks within $r_D(T)$. Therefore, any $c\bar{c}$ pair whose binding radius into a charmonium state is larger than $r_D(T)$ cannot be bound anymore because the charm and anticharm quarks cannot interact, consequently, the charmonium state is expected to be dissociated in the QGP (or not formed at all). A charmonium state dissociates at a given dissociation temperature T_d. The binding radii of the J/ψ, ψ(2S) and *chi*$_c$ are given in Table 2.2 where one can see that the radii depend on the charmonium state. For instance the J/ψ is more bound than its excited states. Therefore, some states are unbound earlier than the other states with increasing medium temperature. Following this physics idea, some approaches are introduced to determine the dissociation temperature of the corresponding charmonium state.

As mentioned before, the potential of a $c\bar{c}$ pair system is modified in the QGP at high temperature and at high density. T. Matsui and H. Satz [75] proposed that the Coulomb-like potential is modified into a short-range Yukawa potential (Coulomb potential screened). Besides, the confinement term is also modified to include a colour screening term [74]. Finally Eq. 2.1 becomes:

$$V(r,T) = -\frac{\alpha_c}{r} e^{-\frac{r}{r_D}} + \sigma \cdot r_D (1 - e^{-\frac{r}{r_D}}), \tag{2.7}$$

With the interquark potential in Eq. 2.7, one can solve the Schrödinger equation [135] by considering the temperature dependence to determine the dissociation temperature of a charmonium state. As a results, both ψ(2S) and χ_c become dissociated essentially at $T_D \approx T_c$, while the J/ψ persists up to about 1.2 T_c [74], where T_c, the critical temperature, is defined in section 1.2.

Another approach is also based on the potential described in Eq. 2.7, which is additionally assumed to be equal to the free energy $F(r,T)$. In order to fulfill the assumption, the entropy term $T(\frac{\partial F(r,T)}{\partial T})$ is neglected in the following equation:

$$V(r,T) = F(r,T) - T(\frac{\partial F(r,T)}{\partial T}) \tag{2.8}$$

Then the dissociation temperatures are obtained by solving the Schrödinger equation using lattice QCD results for the free energy [136, 137]. The obtained results show that the J/ψ dissociation temperature is approximatly 2 T_c and that the ψ(2S) and χ_c ones are around 1.1 T_c.
Therefore, the calculation demonstrates that charmonia dissociate sequentially with increasing temperature due to the colour screening effect from the QGP created in heavy-ion collisions.

Charmonium (re)generation: in the medium which is created in heavy-ion collisions, a deconfined c quark produced in an initial hard scatterings can be bound with a deconfined $\bar{c}$ from another initial hard scattering, because of the high charm pair density in the medium produced at the LHC collision energies [76, 77]. This production mechanism is known as (re)generation and it enhances the number of observed charmonia in heavy-ion collisions with respect to nucleon-nucleon collisions.
There are several theoretical models that try to explain the data by taking into account the J/ψ (re)generation from uncorrelated c and $\bar{c}$. A brief introduction to those models is given below:

- **transport model** [9]: it considers the dynamical evolution of the J/ψ in the QGP. Indeed, there is a dynamical competition between the J/ψ suppression by the QGP and the (re)generation mechanism. Besides, the J/ψ are unlikely fully thermalized with the medium. Thus their phase space distribution should obey a transport equation. The Boltzmann transport equation is used to describe the space-time evolution of a charmonium in the medium. In the model [138, 9], by integrating over the spatial and momentum dependence of the Boltzmann equation, one obtains a simple rate equation including a charmonium dissociation and a charmonium formation terms. The rate equation is given by:

$$\frac{dN_\psi}{d\tau} = -\Gamma_\psi(N_\psi - N_\psi^{\text{eq.}}), \tag{2.9}$$

  where Γ_ψ is the reaction rate for dissociation and formation, $N_\psi^{\text{eq.}}$ is the number of charmonium in thermal equilibrium. The first term refers to the charmonium dissociation and the second term is dominated by the recombination of a c and a $\bar{c}$ in the medium into secondary charmonium states. The theoretical calculations from this model reproduce the J/ψ yield modification data measured in SPS and in RHIC [139]. On the other hand, the models [140, 141] consider not only the terms for the J/ψ suppression and regeneration in hot medium, but also a term for the leakage effect. This effect considers that the charmonium suppression due to the colour screening takes a certain time to occur. During this time, the J/ψ at high p_{T} may leak out of the

colour deconfined region;

- **statistical hadronisation model** [142]: it assumes the deconfinement and a thermal equilibrium of the bulk. The model considers all the J/ψ are suppressed or are not formed in the bulk and the J/ψ are then only produced at the phase boundary by statistical hadronisation. Besides, few primordial J/ψ that are produced in the nucleus corona contribute to the production at large p_{T}. The model uses the grand canonical approach to describe the statistical production of hadrons in the hadronisation phase. This approach has three parameters, which are the chemical freeze-out temperature T_{fr}, the baryo-chemical potential μ_b, and the fireball volume V. The values of the three parameters are fixed thanks to the measured light hadron yields for each beam energy. Another additional input parameter needed is the initial total charm production cross section in Pb-Pb collisions which still suffers from large experimental uncertainties. This model describes well the rapidity and centrality dependence of the J/ψ production from RHIC and the ψ(2S) to J/ψ ratio from NA50 at the SPS [143, 144]. Besides, the theoretical calculations obtained from this model are compatible with the J/ψ production at low p_{T} but underestimate that at high p_{T} in central collisions from ALICE [145].

Energy loss [146]: the energy loss of quarks and gluons produced in a collision can experience multiple scattering in the QGP and they can lose energy. This is related to the observed jet quenching as detailed in section 1.4.4. Indeed, the suppression, with respect to pp collisions, of particle produced at high p_{T} was observed in AuAu and CuCu collisions at $\sqrt{s_{\mathrm{NN}}}$ = 130 and 200 GeV at RHIC and in Pb-Pb collisions at $\sqrt{s_{\mathrm{NN}}}$ =2.76 and 5.02 TeV at the LHC. The usual way to model energy loss effects on the production of particles in heavy-ion collisions is via a rescaling of the particle production cross section in pp collisions. The rescaling is performed involving the so-called quenching weight which represents the probability density for a particle losing a certain amount of energy while traversing the hot medium. However, the detected hadron is not the quark or the gluon that experienced the energy loss. Hence, the fragmentation function D_k^h of a parton k into a hadron h is used to describe the hadronisation of the parton. The hadron p_{T}-differential cross section in heavy-ion collisions can then be written as:

$$\frac{d\sigma_{AA}^{h}(p_{\mathrm{T}})}{dydp_{\mathrm{T}}} = A^2 \sum_k \int_0^1 dz D_k^h(z) \int_0^\infty dx \frac{d\hat{\sigma}_{pp}^{k}(p_{\mathrm{T}}/z + \omega_c x/z)}{dydp_{\mathrm{T}}} \frac{1}{z} \bar{P}_k(x/z), \tag{2.10}$$

where z is the momentum fraction of the parton carried by the hadron, ω_c is a scale and $x \equiv z\epsilon/\omega_c$ with ϵ the energy lost by the parton. $\bar{P}_k$ is the quenching weight of the parton as a function of x/z (in the approximation that the hadron's energy E is greater than ω_c). One can integrate Eq. 2.10 over z by assuming $\frac{1}{z}\bar{P}_k(x/z)$ to be a smooth function of z compared to the rest of the integrals, and assuming that only one partonic channel dominates the production of the measured hadron. Then according to [146], one can finally express the nuclear modification factor with a simple scaling function of $p_{\mathrm{T}}/n\bar{\omega}_c$ where $\bar{\omega}_c \equiv \langle z \rangle\ \omega_c$. The parameter n and the energy loss scale $\bar{\omega}_c$ are obtained from fits to the pp and Pb-Pb data at the corresponding center-of-mass energy, respectively. This energy

loss model reproduces the nuclear modification factor of charmed mesons, measured at different $\sqrt{s_{\rm NN}}$ and in various centrality classes. However, the estimation of energy loss for $p_{\rm T} < 10$ GeV/c by the model is still not under control yet.

Comover interactions [147]: comovers are partons produced in the interaction at the same rapidity as the $c\bar{c}$ pairs and they can scatter with the $c\bar{c}$ pair. The scattering from comovers causes the dissociation of charmonium. The comover interaction model (CIM) was developed in order to explain the anomalous charmonium suppression observed in Pb-Pb collisions at SPS [148]. This model uses the same approach as in transport models to describe the evolution of the number of charmonium by using the relativistic Boltzmann equation. In the CIM, the probability of charmonium that survives after comoving interactions is given by:

$$S(b) \approx exp\left[- \int {\rm d}\tau < \sigma_{co\nu} > N^{co}(\tau, b) \right], \tag{2.11}$$

where $N^{co}(\tau, b)$ is the comover density at the time, τ, and at the impact parameter, b; ν is the velocity of charmonium relative to the comovers; and the σ_{co} is the effective charmonium-comover cross section, which was fixed from fits to low-energy experimental data ($\sigma_{co} = 0.65$ mb [147]).

At the LHC, the effect of charmonium regeneration is non-negligible. Therefore, a gain term for the regeneration is included in the rate equation in the CIM [149]. The charmonium density is then generalized:

$$\frac{{\rm d}N_{\psi}}{d\tau} = -\frac{\sigma_{co}}{\tau}\left[N^{co}N_{\psi} - N_c N_{\bar{c}}\right]. \tag{2.12}$$

In Eq. 2.12, the first term refers to the charmonium dissociation and the second term takes into account the regeneration of the $c\bar{c}$ pair into secondary charmonium states. Note that the effects of nuclear absorption (which is negligible at the LHC [150]) and shadowing [151] are also included in [149].

2.3.2 Cold nuclear matter effects on J/ψ production

In this section, the modification of the parton distribution functions in the nuclei, the gluon saturation, the energy loss and parton multiple scattering, and the nuclear absorption are introduced. They can modify the J/ψ production yield in heavy-ion collisions even without the presence of the QGP and they are referred to as cold nuclear matter effects. Note that the energy loss from parton multiple scattering was already discussed in section 2.3.1 in the context of hot nuclear matter.

Nuclear parton distribution functions and gluon (anti)shadowing: as discussed in section 2.2.1, the parton distribution function describes the probability of finding a parton carrying a fraction, x, of the nucleon's longitudinal momentum at a given energy scale, Q. The PDFs are assumed to be universal and independent of any process. The PDFs are obtained among others by fitting the data from deep inelastic scattering (DIS) experiments [152]. In

1983, the European Muon Collaboration (EMC) discovered that the parton distribution in nucleus is modified and different from the one in a free nucleon [152]. Consequently, this phenomenon was studied with different targets. For example, the ratio of the nuclear structure function in Calcium to the one in Deuterium as a function of x is shown in the left panel of Figure 2.14. As can be seen, the ratio of the structure function is not equal to one in almost the whole x range. The underline effects are related to the different dynamics of partons within free nucleons with respect to those bounded in a nucleus, mainly as a consequence of the larger resulting density of partons in a nucleus. Those effects are dependent on x and on the energy scale of the momentum transfer in the interaction Q^2. Four main regions of the nuclear PDFs (nPDF) to PDFs ratio of parton flavour i, $R_i(x, Q^2)$, as a function of x can be identified, as shown schematically in the right panel of Figure 2.14.

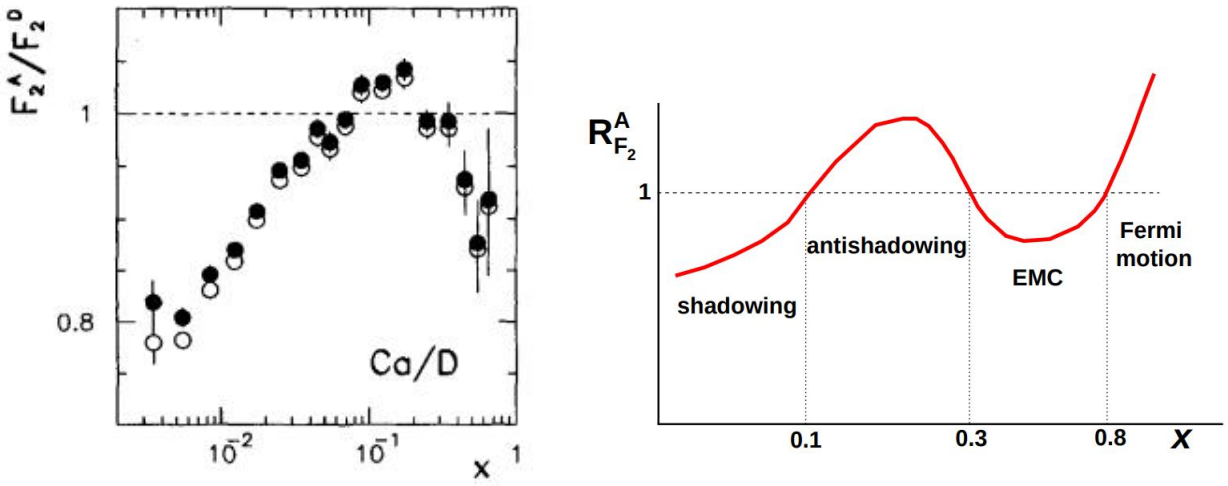

Figure 2.14: Left: ratio of the nuclear structure function F_2 measured on Calcium (Ca) to the deuterium (D) one as a function of x. The full circle represents a re-evaluation of the ratio. Figure from [153]. Right: schematic x-dependence of the structure function ratio of a nucleon bound in a nuclei A to a free nucleon. Figure from [154].

Those effects on the different x regions are briefly introduced below:

- **shadowing** for $x \lesssim 0.1$, R^A shows a depletion below unity. At the LHC energies, the gluon shadowing can be explained by recombination of gluons due to the high parton density. The recombined gluon will then carry higher momentum, causing a depletion at small x;
- **anti-shadowing** for $0.1 \lesssim x \lesssim 0.3$, unlike shadowing, R^A shows an enhancement above unity;
- **EMC effect** for $0.3 \lesssim x \lesssim 0.8$, R^A shows a depletion below unity. This effect was discovered by the EMC Collaboration (see [152]) but its origin is not fully understood. Short-range nucleon-nucleon correlations may play an important role for the observed nuclear modifications [155];
- **Fermi-motion** for $x \gtrsim 0.8$, R^A shows an enhancement. The nucleons are not stationary in the nucleus, their dynamics are known as Fermi-motion.

Figure 2.15 shows the nuclear modification factor of a gluon in a lead nucleus at the charm quark mass energy scale with the parametrisation of EPPS16. The LHC energy range probes the shadowing at very low x[7] and the anti-shadowing regions. Therefore, the J/ψ yield is expected to be modified in particular due to the strong gluon shadowing effect in pA (and AA) collisions.

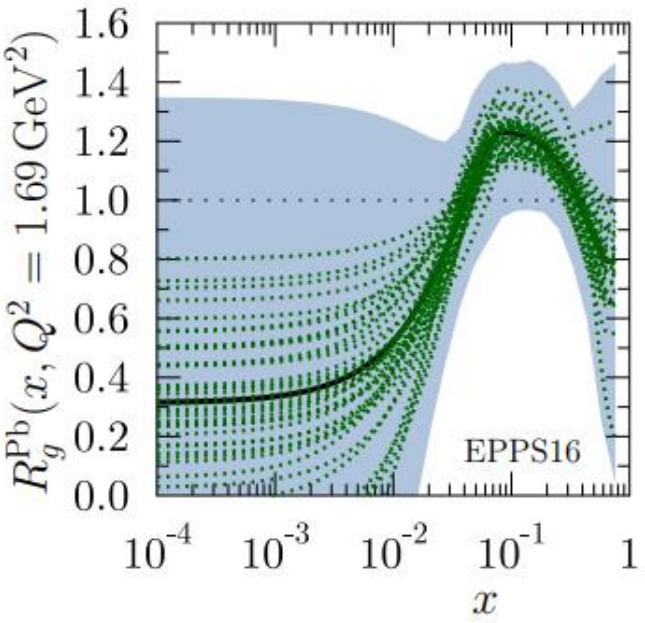

Figure 2.15: Nuclear modification factor R_g^{Pb} for lead ion at a parametrisation scale $Q^2 = 1.69$ GeV with the EPPS16 nPDFs. The solid black line corresponds to the central fit and the dotted curve to the individual error sets. The total uncertainties are shown as blue band. Figure from [157].

Nuclear absorption [158, 159, 150]: when a pre-resonant $c\bar{c}$ pair produced from initial hard scatterings traverse the nucleus, it may dissociate from the interaction with the nucleus constituents. This dissociation is known as nuclear absorption and is described by an effective absorption cross section σ_{abs}. For the J/ψ, the energy dependence of the effective absorption cross section $\sigma_{abs}^{J/\psi}$ in pA collisions, was extracted in [159] and is shown in Figure 2.16.

One can see a decrease of the absorption cross section with increasing collision energies. Indeed, the crossing time, which is the time for $c\bar{c}$ pair to cross over the nuclear matter, affects the pair survival probability and at high energy, the crossing time is smaller than the formation time of the various charmonium states because of the Lorentz boost. Therefore, the effect from the nuclear absorption on charmonium production is expected to be negligible at the LHC.

Parton multiple scattering and energy loss: similarly to energy loss in hot nuclear matter, multiple scattering of partons and of the $c\bar{c}$ pair in the nucleus can lead to parton energy loss in cold nuclear matter (also see

[7]The momentum fraction x can be computed assuming a 2-to-1 production kinematics for the J/ψ ($gg \rightarrow J/\psi$) such as $x = (m_{J/\psi}/\sqrt{s})exp(\pm y)$ with $m_{J/\psi}$ the J/ψ mass and y its rapidity. For collisions at the LHC, the x values probed with J/ψ production at low p_{T} and at $2.5 < y < 4$ in pp or heavy-ion collisions at $\sqrt{s_{\mathrm{NN}}} = 5.02$ TeV are $2 \times 10^{-5} < x < 9 \times 10^{-5}$ for the nucleus moving away from the J/ψ rapidity range and $10^{-2} < x < 6 \times 10^{-2}$ for the nucleus moving toward the J/ψ rapidity range [156].

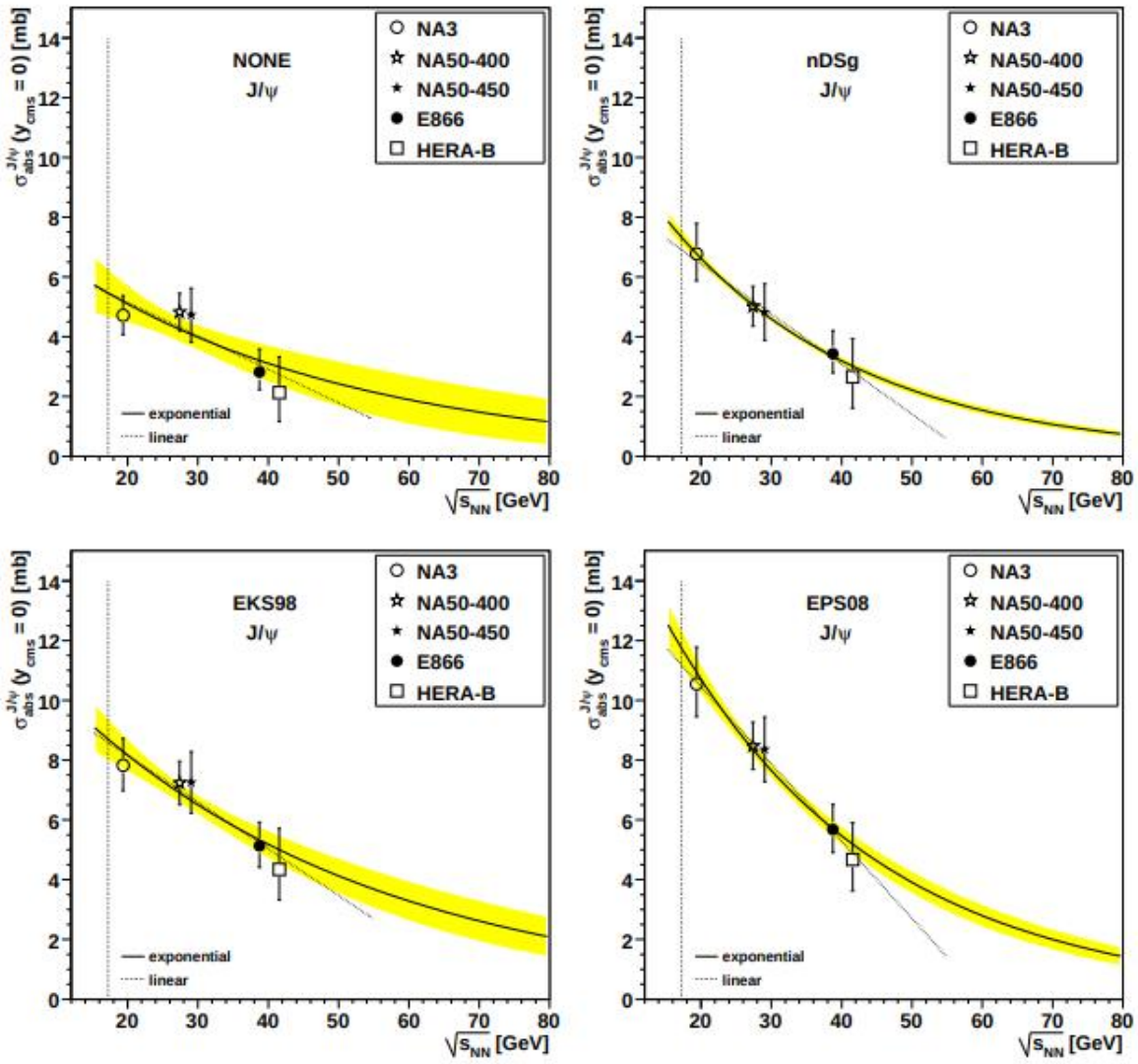

Figure 2.16: The J/ψ absorption cross section $\sigma_{abs}^{J/\psi}$ as a function of the collision energy $\sqrt{s_{\rm NN}}$ for a free proton PDFs (top left panel) and for three different sets of nPDFs. Figure from [159].

chapter 3 in [85]). The initial and final state energy loss as well as the Cronin effect are briefly introduced below. The energy loss approaches consider that the cold nuclear matter effect can be evaluated and related to the transportation of partons in a large nuclei [160].

- **initial and final state energy loss**: before or after the hard interaction, the partons or the $c\bar{c}$ pair can be affected by multiple scattering in the nucleus. Medium-induced radiation can occur via soft gluon emission. This is the phenomenon of energy loss.

- **Cronin effect**: while crossing the nucleus, partons incoherently collides with many nucleons of the nucleus, exchanging transverse momentum, which leads to a smearing of the J/ψ p_{T} distribution in the intermediate p_{T} region with respect to that in pp collisions. This is known as the Cronin effect.

Gluon saturation[161]: as mentioned earlier, the PDF describes the probability of finding a parton carrying a longitudinal momentum fraction, x, at a given energy scale, Q. In a very high energy nuclear collision (correspond to small x), the gluon PDF rises up with decreasing x and more gluons are produced and populate the hadron with a high density. By the time when the (produced) gluons overlap with each other in the hadron, as shown in Figure 2.17, this high-density system saturates and the gluonic interaction is no more linear. The saturation scale, Q_s which depends on x, characterises the region of gluon saturation. As noted earlier, the CGC framework can be applied to hadronic collisions at the RHIC and LHC energies.

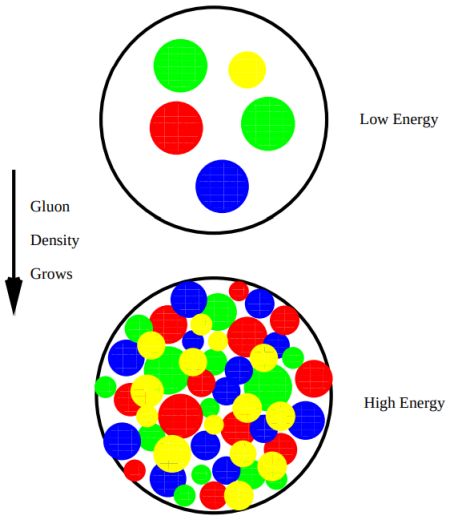

Figure 2.17: The small-x gluon density saturates in a hadron when the collision energy increases. Figure from [104].

2.3.3 J/ψ photoproduction

J/ψ can also be produced by photoproduction in nucleus-nucleus collisions, especially in ultra-peripheral collisions (UPC). The UPC are collisions with a large impact parameter greater than the sum of their radii. In that condition,

the ions mainly interact through virtual photon exchanges, leading to a photon-ion or a photon-photon interaction.

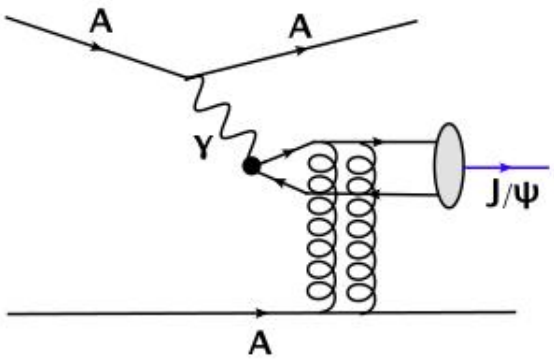

Figure 2.18: An example diagram of the J/ψ photoproduction mechanism in ultra-peripheral nucleus-nucleus collision. Figure from [162].

In the case of the J/ψ photoproduction, one example diagram of mechanism is shown in Figure 2.18. An incoming nuclei emits a photon which splits into a virtual quark-antiquark pair. This quark pair interacts with the other nuclei by exchanging gluons, and then evolves into a J/ψ meson. J/ψ are photoproduced either coherently or incoherently. If the photon interacts with the full nucleus without breaking it, the J/ψ are photoproduced coherently and their p_{T} are very low ($p_{\mathrm{T}} < 60$ MeV/c). However, if the photon interacts with one nucleon inside the nucleus, the J/ψ are photoproduced incoherently and have a higher average transverse momentum of about $p_{\mathrm{T}} \approx 500$ MeV/c [163]. The J/ψ photoproduction measurements give insight into the gluon distributions in the incoming nuclei in a broad range of momentum fraction x (as in Eq. 2.3), providing complementary information on the J/ψ hadronic production in heavy-ion collisions.

Photoproduced J/ψ have also been observed at the LHC for collisions with an impact parameter smaller than twice of the nucleus radii [164]. Figure 2.19 shows the p_{T} spectrum of opposite-sign dimuon measured in the invariant mass range $2.8 < \mathrm{m}_{\mu\mu} < 3.4$ GeV/c^2 in Pb-Pb collisions at $\sqrt{s_{\mathrm{NN}}} = 2.76$ TeV for the centrality range 70–90% in ALICE. There is an excess at very low p_{T} and in a mass window in which the J/ψ yield is dominant over the background. This excess is attributed to coherent photoproduction of J/ψ. The contribution from coherent J/ψ photoproduction in UPC from the STARLIGHT MC generator [164] is compared to the data in the figure. The p_{T} distribution of the coherently photoproduced J/ψ is compatible with the one from the peripheral Pb-Pb data for $p_{\mathrm{T}} < 0.2$ GeV/c. In addition, this excess at very low pt is also now observed in Pb–Pb collisions at $\sqrt{s_{\mathrm{NN}}} = 5.02$ TeV in ALICE, with a good significance in the centrality range 30–90% (preliminary results [165]).

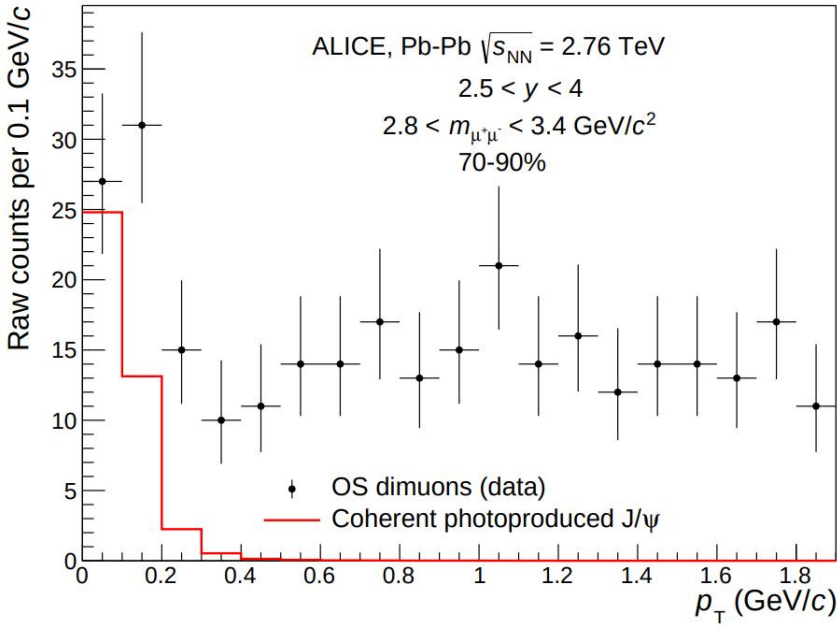

Figure 2.19: Transverse momentum distribution of opposite-sign muon pairs in the J/ψ mass range (2.8 < $m_{\mu\mu}$ < 3.4 GeV/c^2) in Pb-Pb collisions at $\sqrt{s_{NN}}$ = 2.76 TeV, and in the centrality range 70–90%. Figure from [164].

2.3.4 J/ψ measurements in heavy-ion collisions

The nuclear modification factor R_{AA} is an observable that quantifies the J/ψ yield modification due to medium effects with respect to the yield measured in pp collisions. It is defined as:

$$R_{AA} = \frac{Y^{AA}_{J/\psi}}{< T_{AA} > \cdot \sigma^{pp}_{J/\psi}}, \tag{2.13}$$

where $Y^{AA}_{J/\psi}$ is the J/ψ invariant yield in nucleus-nucleus collisions, $\sigma^{pp}_{J/\psi}$ is the J/ψ cross section in pp collisions at the same energy, and $< T_{AA} >$ is the average nuclear overlap function which is defined in Eq. 1.7.

At the RHIC, recent results on the inclusive J/ψ R_{AA} as a function of p_T were obtained for different centrality classes of Au+Au collisions at $\sqrt{s_{NN}}$ = 200 GeV with the STAR experiment, and are shown in Figure 2.20. The J/ψ production is suppressed in the full measured p_T intervals. There are several effects, such as cold nuclear matter effect and colour screening that could explain the p_T dependence of the suppression [166].

The STAR results are compared to their previously published results and one can see a good agreement in the overlapping region. The inclusive J/ψ STAR results in the centrality range 0–80% are compared to ALICE and CMS measurements at mid-rapidity in Pb-Pb collisions at $\sqrt{s_{NN}}$ = 2.76 TeV. The inclusive J/ψ measurement from ALICE is reported for p_T below 6 GeV/c in the 0–40% centrality interval while the prompt J/ψ measurement from CMS is reported for p_T between 6.5 and 15 GeV/c in the 0–100 % centrality interval. The STAR results at low p_T are substantially below those of the LHC, but systematically larger at high p_T (although it is not very significant given the large uncertainties). Shaded areas represent a transport model calculation for $\sqrt{s_{NN}}$ = 200 GeV Au+Au

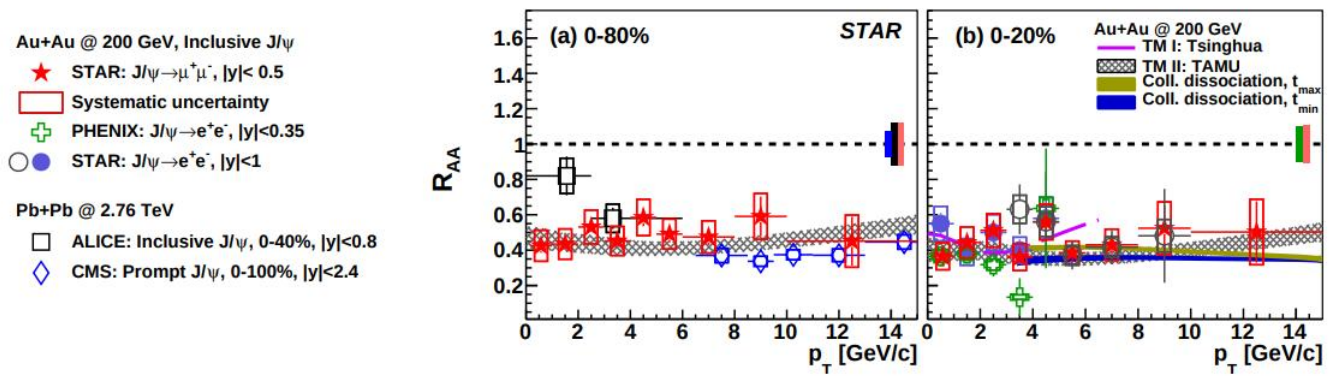

Figure 2.20: Inclusive J/ψ nuclear modification factor $R_{\rm AA}$ as a function of $p_{\rm T}$ in different centrality intervals of Au+Au collisions at $\sqrt{s_{\rm NN}}$ = 200 GeV in STAR [167, 166, 168]. The STAR results are compared to PHENIX [169], ALICE[170], CMS [171] data and to several model calculations. Figure from [166].

collisions, from TAMU groups [139], which takes into account dissociation and a small J/ψ regeneration contribution. The TAMU model gives, in general, a good description of the data in the full $p_{\rm T}$ range. The right panel of Figure 2.20 shows the $p_{\rm T}$ dependence of the J/ψ $R_{\rm AA}$ in the 0–20% centrality interval. Long dashed lines and shaded areas are two transport model calculations, from Tsinghua[8] [172] and TAMU groups, respectively. The Tsinghua model reproduces the data well at low $p_{\rm T}$, but overestimate the data for $p_{\rm T}$ above 5 GeV/c. The theoretical calculation by TAMU is in a good agreement with the data in the full $p_{\rm T}$ range. The extra two solid bands covering $p_{\rm T}$ from 3.5 to 15 GeV/c are collisional dissociation models [173] of J/ψ production which use two different values for the J/ψ formation time in Au+Au collisions. These calculations use the vacuum J/ψ wave function without any screening effect and include both collisional dissociation of J/ψ and energy loss of the colour-octet $c\bar{c}$ pairs. The regeneration contribution is ignored because it is expected to be negligible at high $p_{\rm T}$. Both theoretical calculations are consistent with the data. All the model calculations include feed-down contributions from excited charmonia, b-hadron decays, and cold nuclear matter effects.

At the LHC, the J/ψ production has been measured in Pb-Pb collisions at $\sqrt{s_{\rm NN}}$ = 2.76 TeV and 5.02 TeV.

Figure 2.21 shows the $p_{\rm T}$ and rapidity dependence, integrated over centrality, of the inclusive J/ψ $R_{\rm AA}$ measured by ALICE at forward rapidity in Pb-Pb collisions at both energies. The results are compared to the theoretical calculation from a transport model [174]. The $R_{\rm AA}$ decrease with increasing $p_{\rm T}$ up to about 6 GeV/c and stay constant over this value, showing a suppression of the J/ψ production by about a factor of 4. The $R_{\rm AA}$ is flat in the whole measured rapidity ranges. Besides, transport model calculation is in qualitative agreement with the data. In conclusion, the J/ψ production is suppressed at forward-rapidity and especially at high $p_{\rm T}$ with respect to pp collisions and the J/ψ production is enhanced at low $p_{\rm T}$ with respect to higher $p_{\rm T}$ which is interpreted as a hint of J/ψ (re)generation.

Prompt and non-prompt J/ψ $R_{\rm AA}$ in central Pb-Pb collisions at $\sqrt{s_{\rm NN}}$ = 5.02 TeV have been measured by ATLAS

[8]The transport model calculation from the Tsinghua groups also considers dissociation and a small J/ψ regeneration contribution.

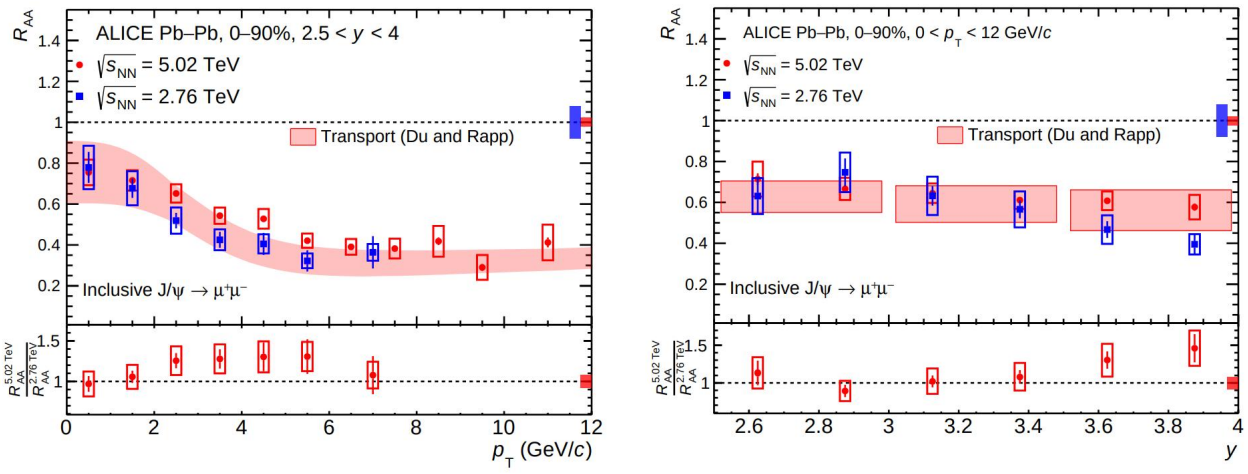

Figure 2.21: Inclusive J/ψ nuclear modification factor R_{AA} as a function of p_{T} (left), and rapidity (right) in Pb-Pb collisions at $\sqrt{s_{\mathrm{NN}}} = 2.76$ TeV and 5.02 TeV, measured at forward rapidity with ALICE. The data are compared to a transport model calculation [174]. Figure from [145].

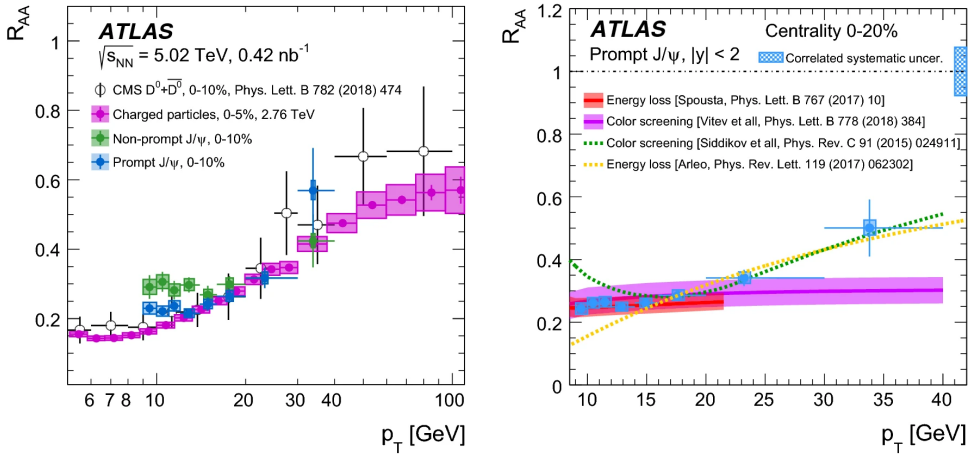

Figure 2.22: Prompt and non-prompt J/ψ nuclear modification factor R_{AA} as a function of p_{T} in central Pb-Pb collisions at $\sqrt{s_{\mathrm{NN}}} = 5.02$ TeV in ATLAS. The data are compared to theoretical calculations, to charged particle measurement from ATLAS, and to D meson measurement from CMS. Figure from [8].

at mid-rapidity and for $p_{\rm T} > 9$ Gev/c. The ATLAS results along with the comparison to the $R_{\rm AA}$ of charged particles [175], D-mesons in CMS [176] and different theoretical models[177, 178, 179, 146] are shown in Figure 2.22. The J/ψ $R_{\rm AA}$ for both prompt and non-prompt contributions are strongly suppressed. For $p_{\rm T} > 12$ GeV, an increase of the $R_{\rm AA}$ with increasing $p_{\rm T}$ is observed. For $p_{\rm T} > 14$ GeV/c, the prompt and non-prompt $R_{\rm AA}$ values are similar in shape and size to that observed for charged particles and D-mesons. This is, typically attributed to parton energy-loss processes, which can be seen in the right panel of Figure 2.22. The prompt J/ψ $R_{\rm AA}$ evaluated for the 0–20% centrality class is compared to several models, and shows that the data for 15 $<p_{\rm T} <$ 40 GeV/c (9 $<p_{\rm T} <$ 30 GeV/c) are consistent with the colour screening model from [177] ([178]), as well as the parton energy-loss model from [179] for 9 $<p_{\rm T} <$ 30 GeV/c and from [146] for 15 $<p_{\rm T} <$ 40 GeV/c. The theoretical calculation based on the energy loss model by F. Arleo does not reproduce the data for $p_{\rm T} < 15$ GeV/c. We indeed expect in the intermediate $p_{\rm T}$ region to have an interplay between colour screening and parton energy-loss effects.

In addition, it is important to measure the J/ψ polarisation. It can give insights to the production mechanisms in pp and Pb-Pb collisions. In order to study the J/ψ polarisation [180], the polarisation parameters, $\lambda_\theta, \lambda_\phi$ and $\lambda_{\theta\phi}$ are measured in the helicity and Collins-Soper reference frames [181]. The polar (θ) and azimuthal (ϕ) are the production angles, relative to a given axis, of the two-body decay products in the quarkonium rest frame. The quarkonium is unpolarised only if the polarisation parameters are $\lambda_\theta = 0,\ \lambda_\phi = 0$ and $\lambda_{\theta\phi} = 0$, while the two cases $\lambda_\theta = 1,\ \lambda_\phi = 0$ and $\lambda_{\theta\phi} = 0$, and $\lambda_\theta = -1,\ \lambda_\phi = 0$ and $\lambda_{\theta\phi} = 0$ correspond to the transverse and longitudinal polarisations of the quarkonium, respectively. Figure 2.23 shows the inclusive J/ψ polarisation parameters as a function of $p_{\rm T}$ for $2.5 < y < 4$ in Pb–Pb collisions at $\sqrt{s_{\rm NN}} = 5.02$ TeV [181]. The polarisation parameters are obtained in the helicity and Collins-Soper reference frames. All the parameters are close to zero within about 2.1σ and indicate a transverse (longitudinal) polarisation for $p_{\rm T} < 6$ GeV/c in the helicity (Collins-Soper) frame. The data are compared to the polarisation measurement for $2.5 < y < 4$ in pp collisions at $\sqrt{s} = 8$ TeV in ALICE [182] and to the prompt J/ψ polarisation measurement for $3 < y < 3.5$ in pp collisions at $\sqrt{s} = 7$ TeV in LHCb [183]. The measurement in Pb-Pb collisions is compatible with that in pp collisions in ALICE within a large uncertainty. On the other hand, the comparison of the polarisation between the Pb-Pb ALICE and the pp LHCb measurements shows a different trending for λ_θ and for $p_{\rm T} < 6$ GeV/c in the helicity frame.

In this thesis, in order to see the behaviour of the inclusive J/ψ $R_{\rm AA}$ especially at high $p_{\rm T}$ and at forward rapidity in ALICE, the $p_{\rm T}$ reach from previous measurements is extended up to 20 GeV/c, thanks to the high-luminosity Pb-Pb collisions collected in 2018. Those new results on the inclusive J/ψ production at forward-rapidity with the full Run 2 Pb-Pb collisions at $\sqrt{s_{\rm NN}} = 5.02$ TeV in the ALICE experiment also permit to improve the statistical precision of previous measurements and are presented in chapter 5.

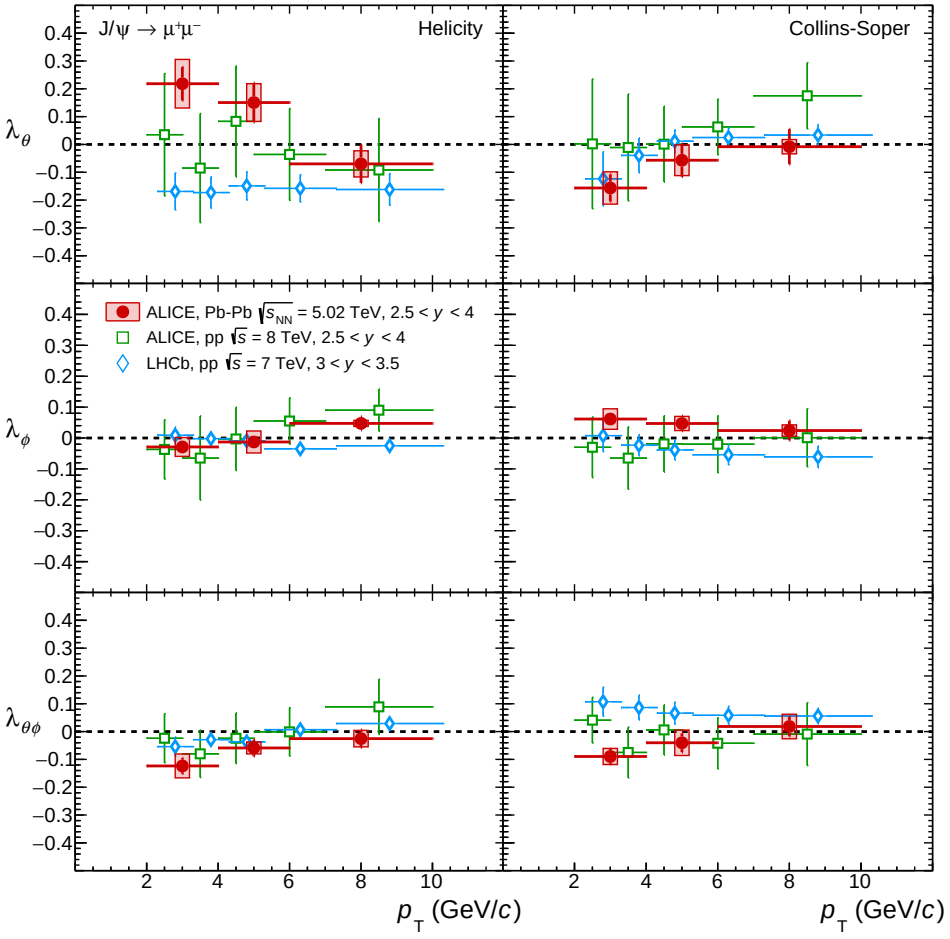

Figure 2.23: Inclusive J/ψ polarisation parameters as a function of p_{T} for $2.5 < y < 4$ in Pb–Pb collisions at $\sqrt{s_{\mathrm{NN}}} = 5.02$ TeV [181] and in pp collisions at $\sqrt{s} = 8$ TeV by ALICE [182], compared to the p_{T} dependence of the prompt J/ψ polarisation measurement for $3 < y < 3.5$ in pp collisions at $\sqrt{s} = 7$ TeV by LHCb [183] (its data points are shifted horizontally by +0.3 GeV/c for better visibility). Figure from [181].

Chapter 3

LHC and ALICE experiment

In this chapter, the Large Hadron Collider (LHC) along with its main experiments: A Large Ion Collider Experiment (ALICE), Compact Muon Solenoid (CMS), A Toroidal LHC ApparatuS, (ATLAS) and LHC-beauty (LHCb) will be described. Since this study involves the ALICE detectors, more details on those detectors are given. The service task that I performed for the ALICE community, which was the quality assurance of the muon-data in the muon spectrometer, will be presented as well in the last section.

3.1 The LHC

3.1.1 Overview of LHC

The LHC [184] is the largest and most powerful particle collider in the world. It was built beneath the France-Switzerland border near Geneva from 1998 and accomplished in 2008. Its geographic view is illustrated in Figure 3.1. The collider is a circle of 27 km long. The main beams can be of two types: protons and ions. The first run took place in 2010 at an energy of 3.5 TeV per proton beam. The LHC had a long shut-down in 2013 for an upgrade lasting two years. The LHC started to run again in 2015 up to 2018. This second period defines the Run 2 period. The second upgrade is currently ongoing. In 2015, the energy per proton beam was increased to 6.5 TeV, which is the highest proton beam energy nowadays.

3.1.2 Accelerator Complex

Each accelerator, shown in Figure 3.2, boosts the energy of a beam to reach the required energy and then injects the beam into the next machine. The LHC is integrated in the CERN accelerator complex, and is the last station in this series. Two main types of beam are delivered to the LHC: the proton and the lead-ion (Pb) beams. Xenon ion beams were also used for a short LHC run in 2017 [185].

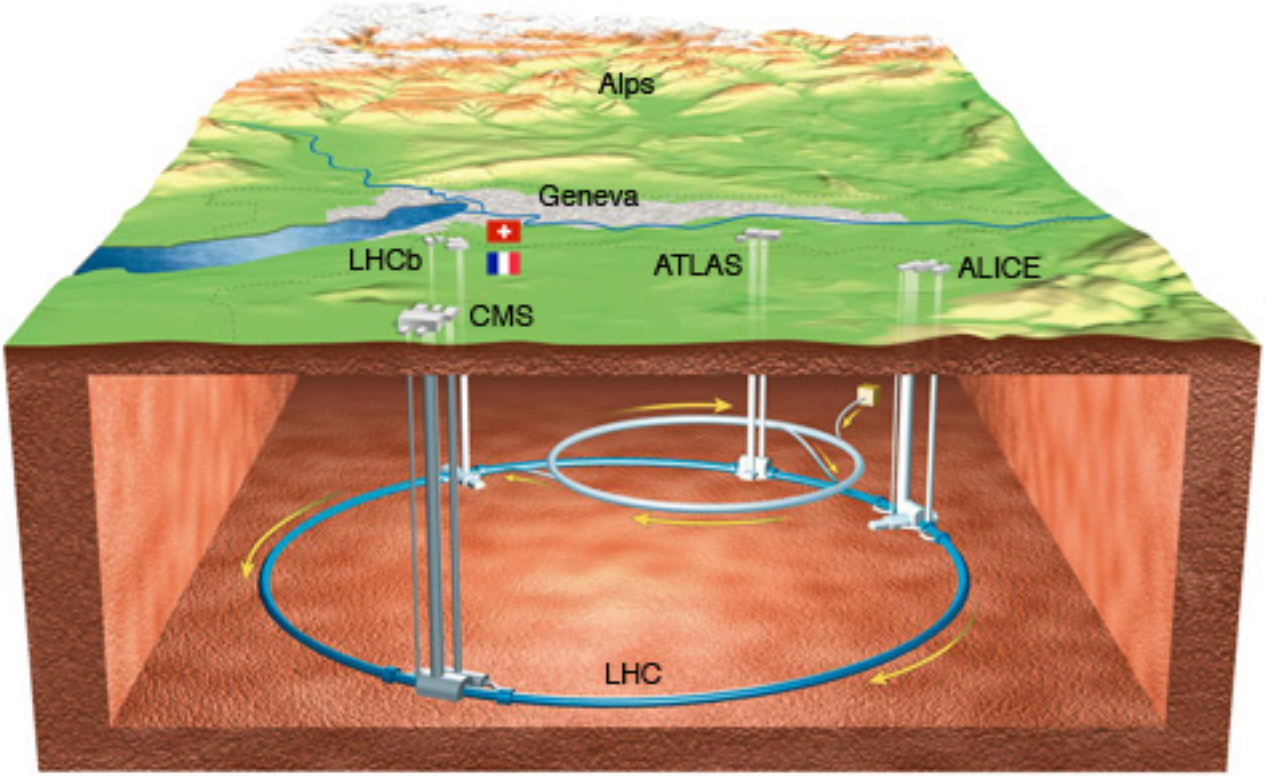

Figure 3.1: The LHC and the main four experiments underground.

To produce proton beam [186], the hydrogen gas is injected into a machine called a duoplasmatron. That machine strips the hydrogen gas of electrons and then produces a plasma of protons, electrons and ions. The plasma expands towards the extraction electrodes and a proton beam is formed. The produced proton beam is then injected into the Linear accelerator 2 (Linac 2) [187] and is accelerates to the energy of 50 MeV. It is transferred to the Proton Synchrotron Booster (PSB) [188], which accelerates the proton beam to the energy of 1.4 GeV. Then the Proton Synchrotron (PS) [189] and the Super Proton Synchrotron (SPS) [190] consequently accelerate the beam to 450 GeV. Afterwards, the proton beam is delivered from the SPS to the two beam pipes of the LHC where they are accelerated to the energy of 6.5 TeV. One beam travels clockwise in one pipe while the other beam travels anticlockwise. The two beams are brought to collide inside four interaction points where lie the four experiments: ALICE, ATLAS, CMS and LHCb.

The Pb beam is produced by ionising vaporised lead and is delivered into Linear accelerator 3 (Linac 3) [191]. The Pb beam is stripped off its electrons through Linac 3. When all the electrons are removed and the Pb beams turn into bare nuclei, Linac 3 injects the Pb beams to the Low Energy Ion Ring (LEIR) [192] to accelerate it up to an energy of the Pb beam per nucleon of 72 MeV. Then the Pb beam travels the same route of accelerators as the proton beam until the two beam pipes of the LHC. Finally, the energy of the Pb beam per nucleon is 2.76 TeV at the LHC.

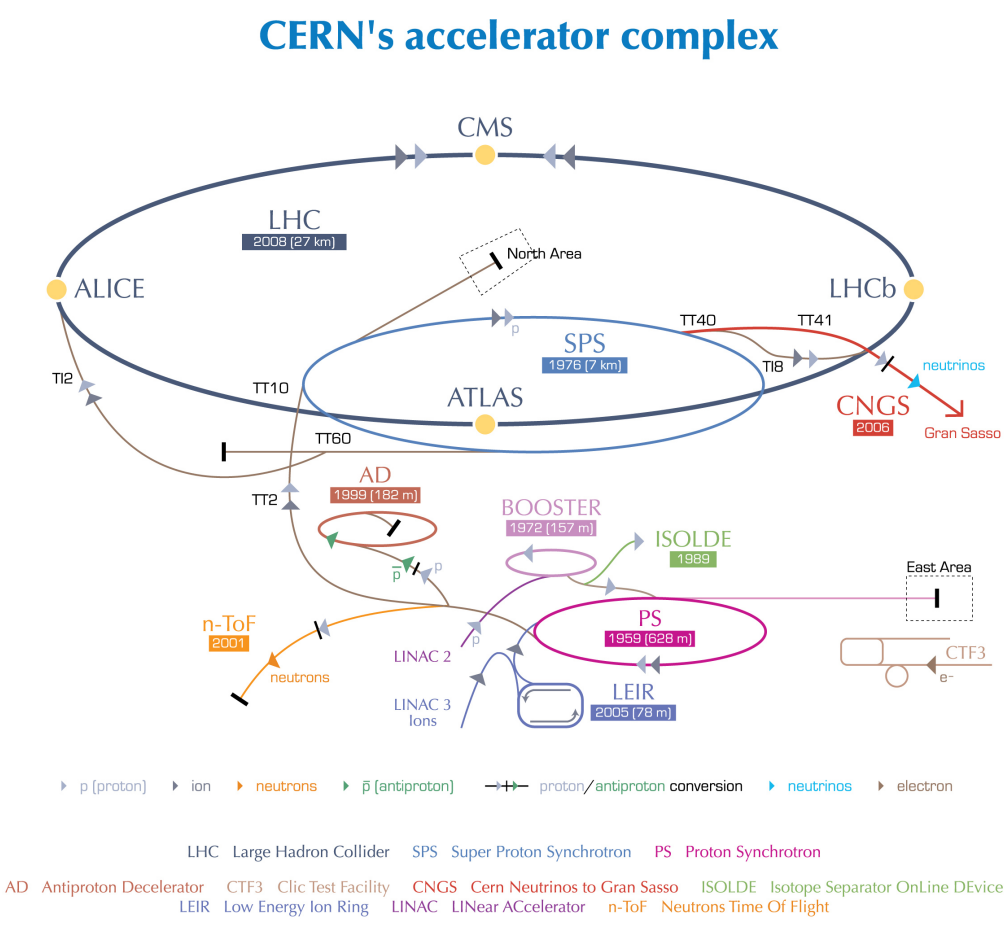

Figure 3.2: The CERN accelerator complex.

3.2 The main experiments at the LHC

3.2.1 ATLAS

The ATLAS [193] experiment was designed for general-purpose to study many physics topics from the search for the supersymmetry (SUSY) particles to the search of particles that would be compounds of dark matter. ATLAS accomplished an achievement when it discovers the Higgs boson in 2012 together with CMS. The ATLAS collaboration nowadays involves around 3000 scientists from 183 institutions worldwide.

The ATLAS experiment has a cylinder shape of 25 m in diameter and a length of 46 m as shown in Figure 3.3. It weighs 7000 tonnes and sits in a cavern 100 m underground. The LHC beams collide at the center of the ATLAS detector. Three major components, the Inner Detector, the Calorimeters, and the Muon Chambers detect the produced particles from the collision of the two beams. The Trigger and Data Acquisition System select physics events. The Computing System then store the data of the selected events in the Worldwide LHC Computing Grid (WLCG) as for the other LHC experiments.

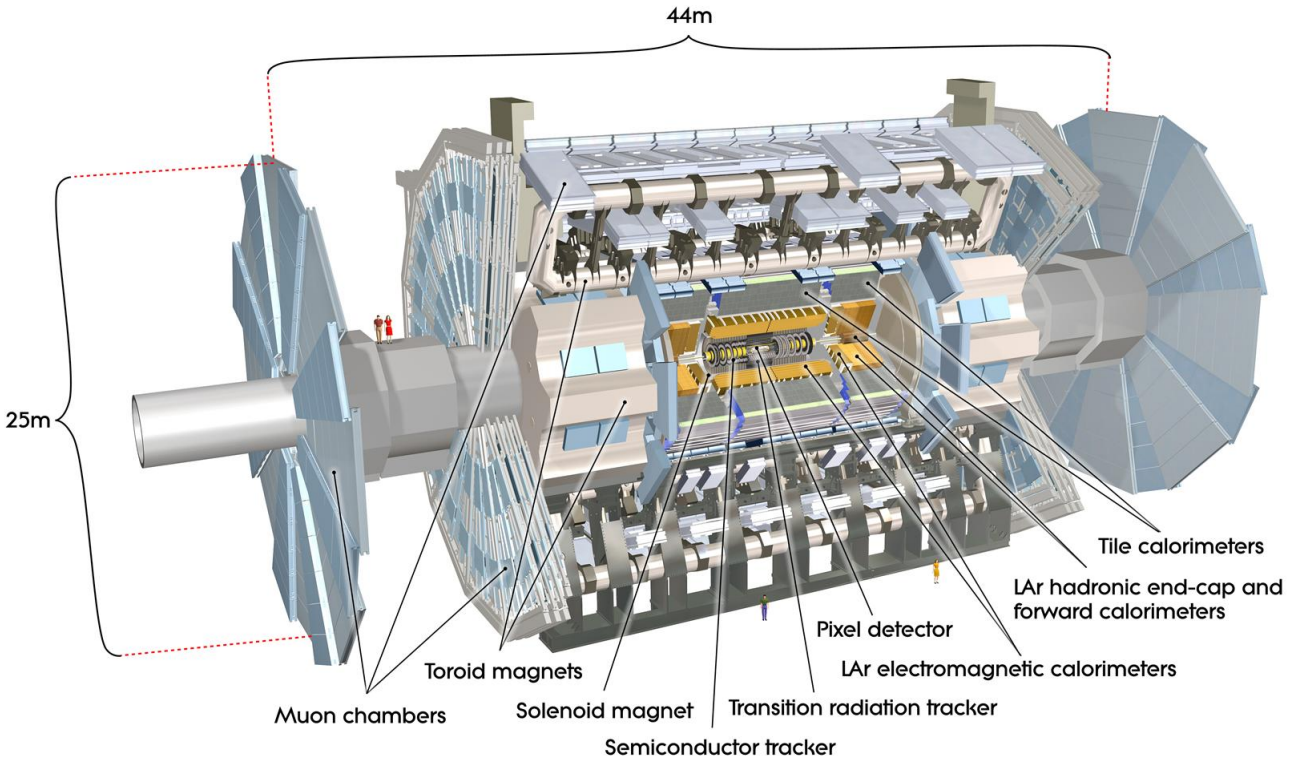

Figure 3.3: The ATLAS detectors

3.2.2 CMS

CMS [194] is a general-purpose experiment at the LHC. It is complementary to ATLAS and search for similar physics topics. CMS contributed to the discovery of the Higgs bosons with ATLAS. The CMS collaboration consists of about 3800 scientists from 199 institutes in 43 countries.

The size of the CMS detector is 21 m long, 15 m wide and 15 m high. The detector with a weight of about 14000 tonnes is placed in a cavern at a diameter of 15 m and a depth of 100 m from the ground. The interaction point of the LHC beams is in the center of the CMS detector. The produced particles from the collisions traveling outwards experience the different layers of the detectors as shown in Figure 3.4. The first layer consists of the tracker, then the electromagnetic calorimeter, the hadron calorimeter, and the muon detectors. The purpose is to detect every types of particle produced in the collision with a very high acceptance. The trigger system is employed to select the physics events. The triggered data are then handled by the WLCG.

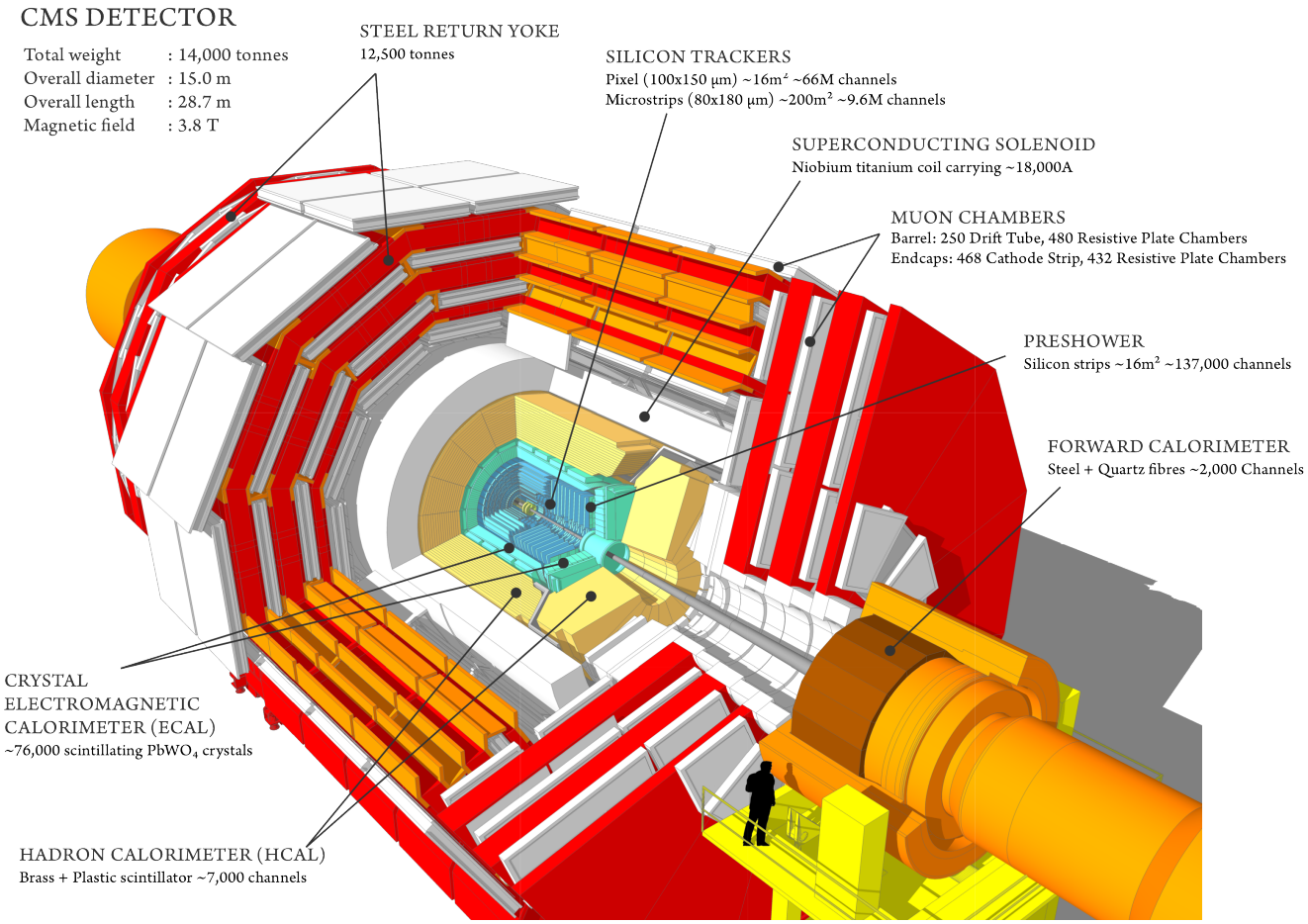

Figure 3.4: Sectional view of the CMS detectors.

3.2.3 LHCb

LHCb [195] experiment focuses on the beauty quark physics in order to understand the asymmetry between matter and antimatter. The LHCb detector was designed considering the fact that the two b-hadrons are mainly produced in the same cone at forward rapidity. The detector stretches along the beam pipe for 20 m and the main sub-detectors are a vertex detector (VELO), a tracking system, the RICH detectors, an electromagnetic and a hadronic calorimeters and a muon system as shown in Figure 3.5. The LHCb collaboration involves around 850 scientists from 79 institutes in 18 countries around the world.

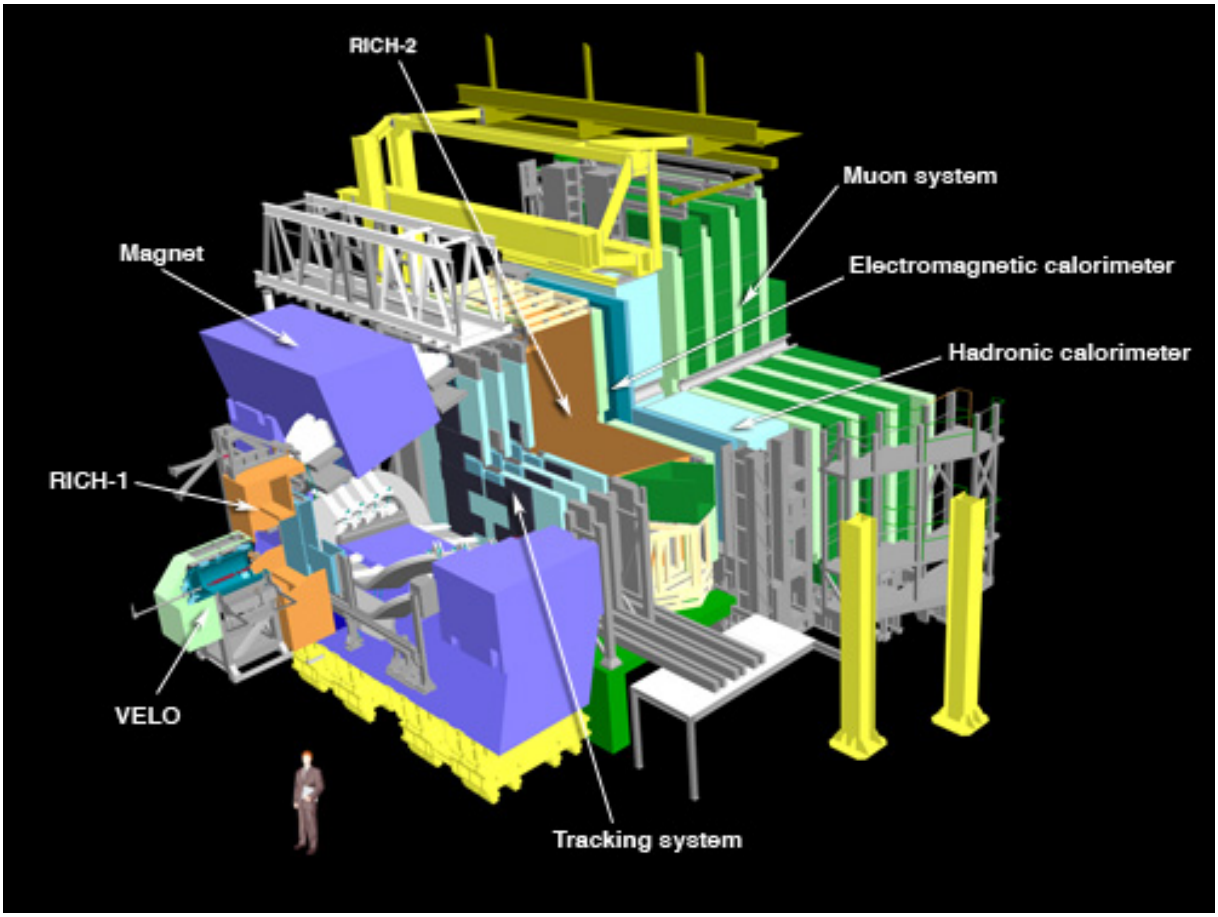

Figure 3.5: Overview of the LHCb detectors.

3.2.4 ALICE

The ALICE [196] experiment was first proposed in 1993 with the central detector and then the supplementary forward muon spectrometer was designed in 1997. ALICE was designed to study the QGP in heavy-ion collisions. Through over ten years of effort on detectors R&D and construction, ALICE recorded the first Pb-Pb collisions in 2010. Nowadays, not only the physics of heavy-ion collisions but also the extensive physics subjects of pp and p-Pb collisions are studied in ALICE with a collaboration consisting of 2000 scientists from over 174 physics institutes in 39 countries.

The ALICE detector, occupying a space of 26 m long, 16 m high, and 16 m wide with a weight of around 10 000 tonnes, sits in a cavern underground nearby the village of St Genis-Pouilly in France. The whole layout of the ALICE detector is shown in Figure 3.6 in which the beam pipes, the central detectors, the forward detectors and the muon spectrometer are displayed. Each component of the ALICE detector is labeled with a number to indicate the names of the sub-detectors. Since the ALICE experiment focuses on probing the QGP in heavy-ion collisions, the ALICE detectors were mainly design to identify the particles produced in these types of collisions. The central-barrel detectors are surrounded by the L3 magnet that delivers a magnetic field of 0.5 T to deflect charged particles. They measure particle properties, such as velocities and momenta in the mid-rapidity region. The forward detectors are used for event multiplicity studies, event centrality estimation and triggering. The muon spectrometer is placed in the forward region to measure muon particles. Note that the acceptance of each sub-detectors is given by η (the pseudorapidity) and by the angular coverage, ϕ.

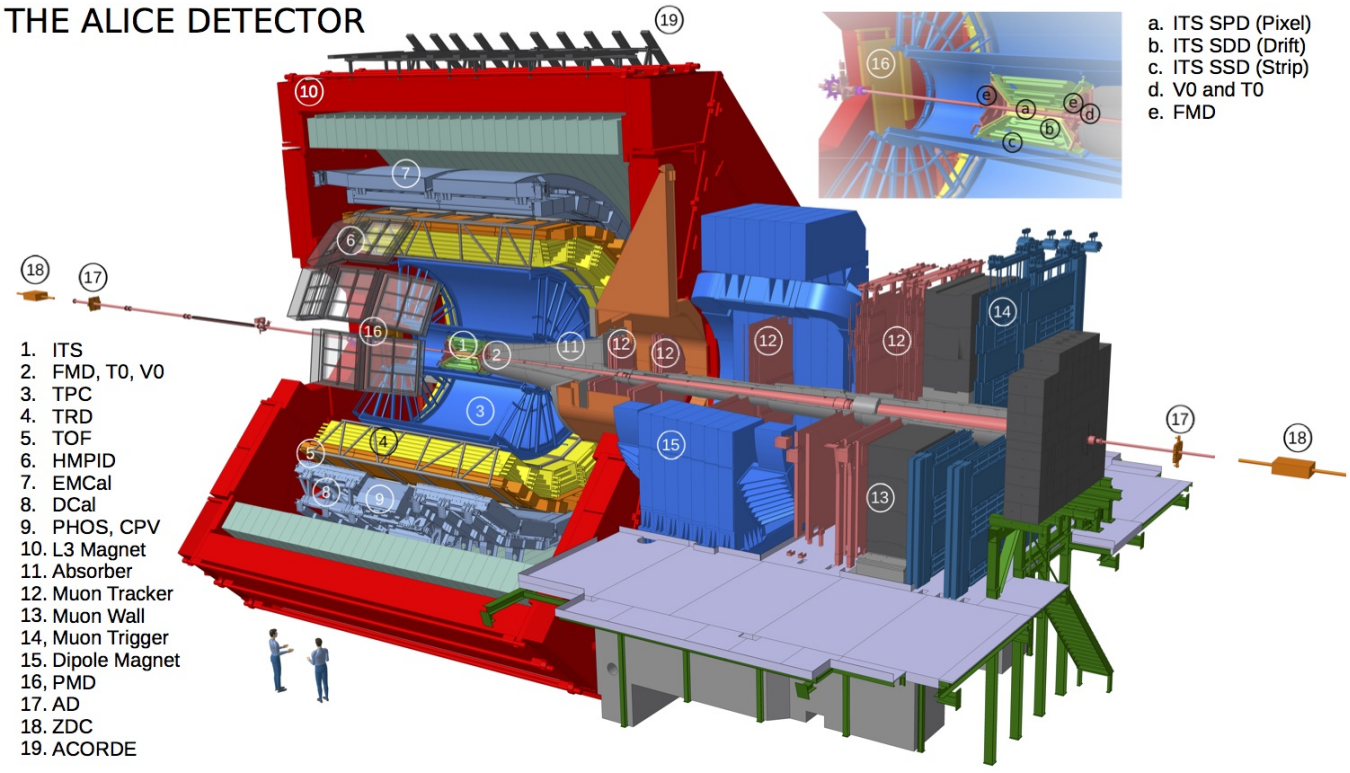

Figure 3.6: The ALICE detector with the names of the sub-detectors. The insert shows the inner structure with the ITS, the PMD, the FMD, the V0 and the T0. The ALICE coordinate system is defined as following. The C-side indicates the region from the interaction point (IP) to the end of the muon spectrometer while the A-side means the opposite region of the ALICE detectors to the C-side.

3.3 The detectors in ALICE

3.3.1 The central detectors

The Inner Tracking System (ITS) is located in the center of ALICE close to the IP, as shown in Figure 3.7. The ITS [197] is a tracking detector made of six layers of silicon detectors surrounding the beam pipe. Different technologies are used for the ITS. The most inner two layers form the Silicon Pixel Detector (SPD), the two middle layers form the Silicon Drift Detectors (SDD) and the outer two layers form the Silicon Strip Detectors (SSD). The pseudorapidity of the SPD is for $|\eta| < 2$. The other task of the SPD is to reconstruct the primary vertex of a collision and the vertices of heavy flavour and strange particle decays. The SDD and the SSD measure the energy loss along the trajectories to identify the low-momentum particles. The pseudorapidity of the SDD and the SSD are for $|\eta| < 0.9$ and $|\eta| < 0.97$, respectively.

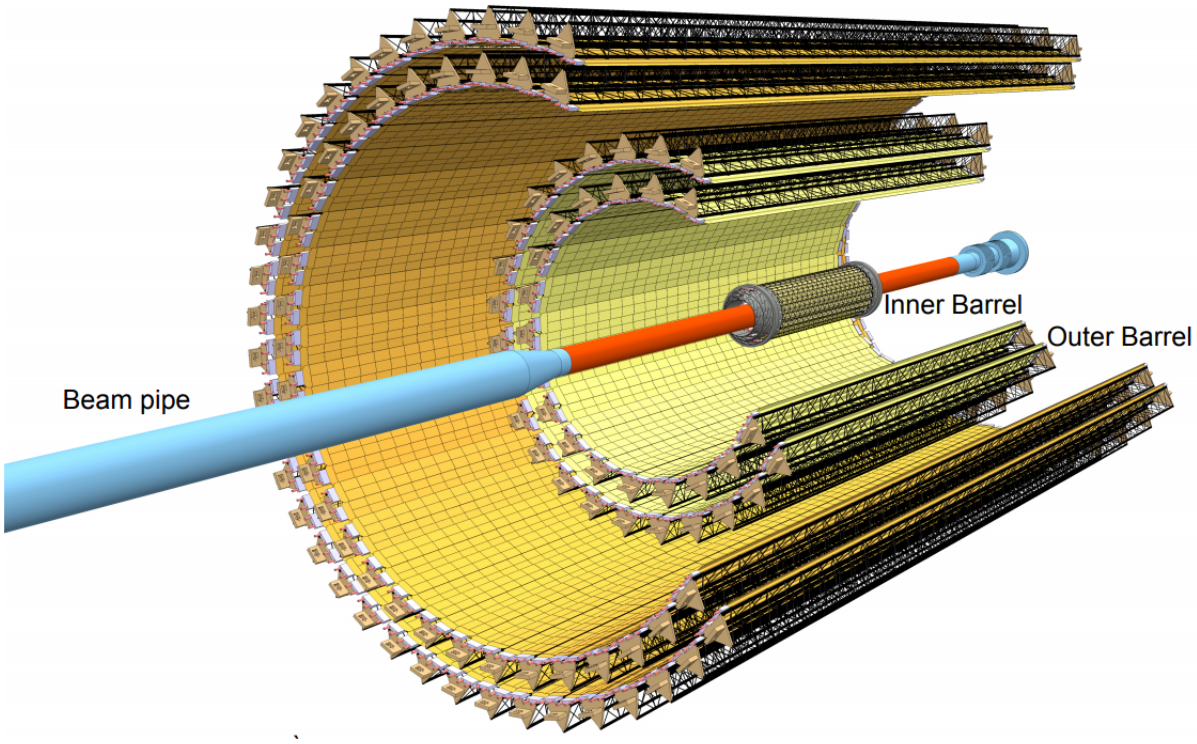

Figure 3.7: Layout of the ITS detector. Figure from [197].

The Time Projection Chamber (TPC) is a cylindrical chamber with a pseudorapidity of ± 0.9. It is the main tracking detector of the central barrel and it measures the energy loss of charged particles to track and identify them. The chamber filled with a gas mixture of Ne-CO_2-N_2 (90:10:5) [198] surrounds the ITS and has a size of 5 m long with an inner and outer diameter of 85 and 247 cm, respectively. A cathode membrane, supplied with a high

voltage of 100 kV is placed in the middle of the chamber. The end plates of the cylinder have 18 sectors of multi-wire proportional read-out chambers. The TPC is illustrated in Figure 3.8.

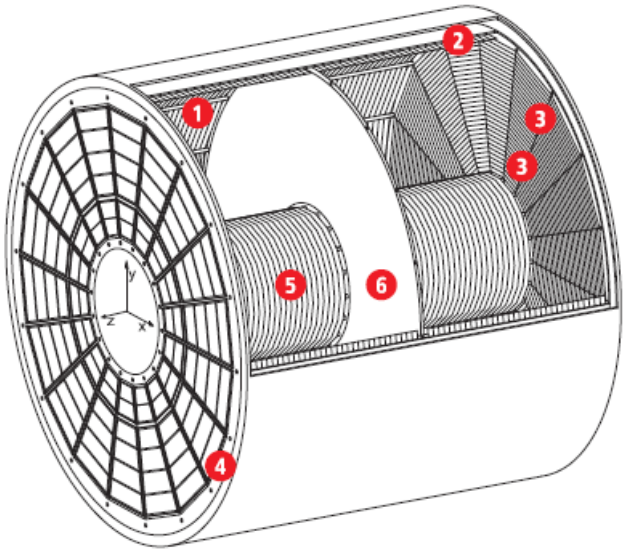

Figure 3.8: View of the TPC of ALICE. The numbers specify the inner structure of the TPC. 1: outer field cage, 2: CO_2 gap, 3: read-out chambers, 4: end-plates, 5: inner field cage, 6: central HV electrode.

The Transition-Radiation Detector (TRD) [199] identifies electrons especially with momenta larger than 1 GeV/c by measuring the transition radiation of the charged particles crossing the detector. Figure 3.9 shows the geometry of the TRD in the ALICE central barrel. The TRD detector has an inner and outer diameter w.r.t the beam axis of 290 cm and 368 cm repectively, enclosing the TPC. Its pseudorapidity is for $|\eta| < 0.84$ and it consists of 18 modules. Every module is equipped with a radiator and a drift chamber. The charged particles produced from a collision pass through the radiator and then enter in the drift chamber. Photons from the transition radiation are emitted by the charged particles at the boundary of the radiator and the chamber because of two different dielectric constants. The energy loss of the charged particles can be measured in the drift chamber. This allows to identify electrons in combination with the measurement of the transition radiations.

The Time-Of-Flight detector (TOF) determines the velocities of charged particles and its main task is to identify charged particles at low and intermediate momentum by measuring the time of flight over a given distance. The time measurement, in conjunction with the momentum and track length measured by the tracking detectors is used to calculate the particle mass. The TOF shape is cylindrical and is shown in the left panel of Figure 3.10 with the inner and outer radius of 370 and 399 cm, respectively. The TOF pseudorapidity range covers $|\eta| < 0.9$. The TOF consists of 1593 Multigap Resistive Plate Chambers (MRPC) distributed in 18 azimuthal sectors. The MRPC

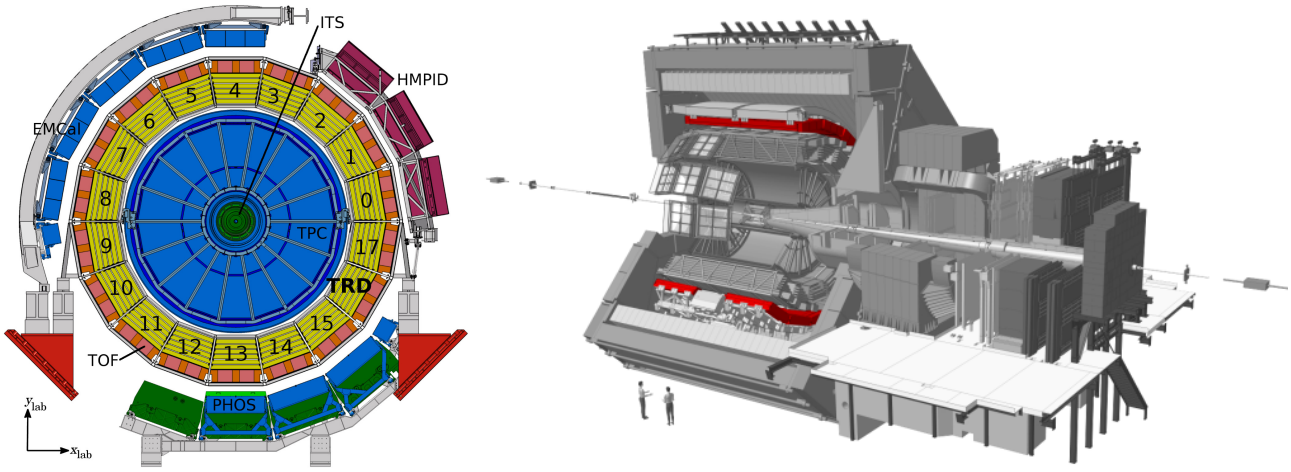

Figure 3.9: Left: schematic cross-section of the ALICE central barrel detector perpendicular to the LHC beam direction. Figure from [199]. Right: EMCal and DCal detectors are highlighted in red.

is a chamber containing a stack of resistive plates with multiple gaps. The stack is embedded by the cathode pickup electrodes which is applied with a high voltage. The anode pickup electrode penetrates the middle of the stack. The chamber is filled by the gas mixture $C_2H_2F_4$-SF_6 (93:7) [200]. If a charged particle passes through the MRPC, it causes an electron avalanche in the gas. The pickup electrodes stop the avalanche and send the signal that gives the time of traveling. The start time is measured by the T0 detector, which will be described in section 3.3.2. With the time information specified above and the track length measured by the tracking detectors, the velocity of a charged particle is then determined. Along with the momentum information measured by the ITS and the TPC, the particles produced from the collisions can be identifed. The right panel of Figure 3.10 shows the TOF velocity as a function of momentum. The electrons, pions, kaons, proton and deuterium particles are visible in the plot.

The High-Momentum Particle Identification Detector (HMPID) identifies charged particles, such as pions, kaons and protons of large momenta, with Ring Imaging Cherenkov (RICH) technology. Seven RICH counters are installed on the support cradle inside the ALICE solenoid at 5 m from the beam line. The acceptance η of the HMPID is $|\eta| < 0.6$ and the angular coverage of the HMPID is $1.2 < \phi < 58.8°$. In general the HMPID is a RICH detector which consists of two main parts: a radiator medium and a photon detector. The charged particles that move faster than the speed of light emit the Cherenkov radiations. The Cherenkov radiations are emitted in the form of a cone along the trajectory of charged particles. The angle between the trajectory of a charged particle and the edge of the cone is the Cherenkov ring angle. From the Cherenkov ring angles and the momenta measured by the ITS and the TPC, the identification of the charged particles can be determined. Figure 3.11 shows the Cherenkov angle of charged particles as a function of their momenta. The pions, kaons and protons are visible in the plot. For the π / K and K / p discrimination, the HMPID extends the p_{T} range of the particle identification up to 3 and 5 GeV/c on a track-by-track basis, respectively.

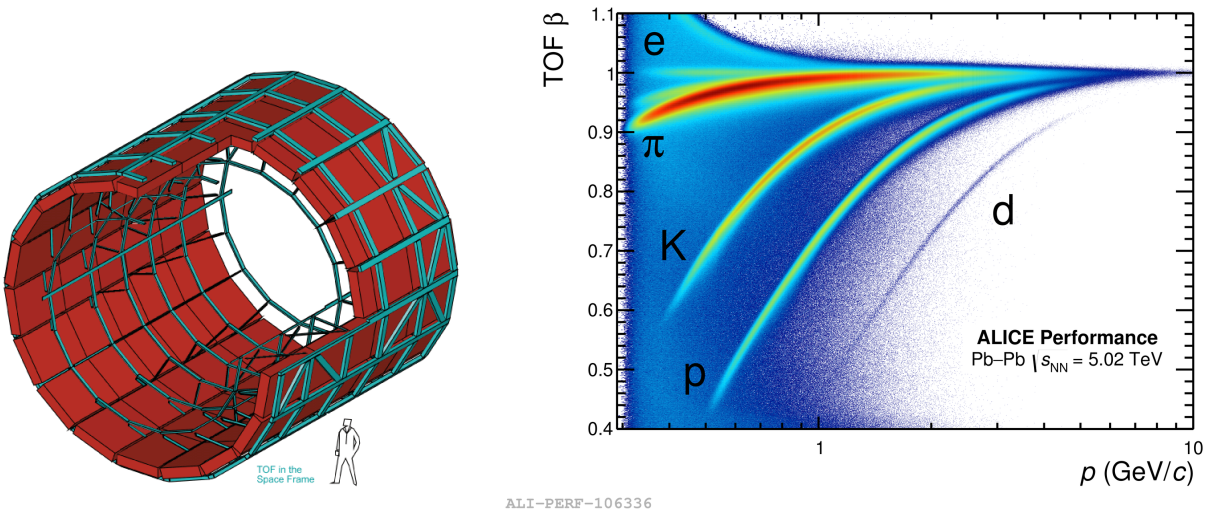

Figure 3.10: Left: illustration of the TOF detector. Right: the TOF velocity β as a function of the particle momentum in heavy-ion collisions at $\sqrt{s_{\rm NN}} = 5.02$ TeV.

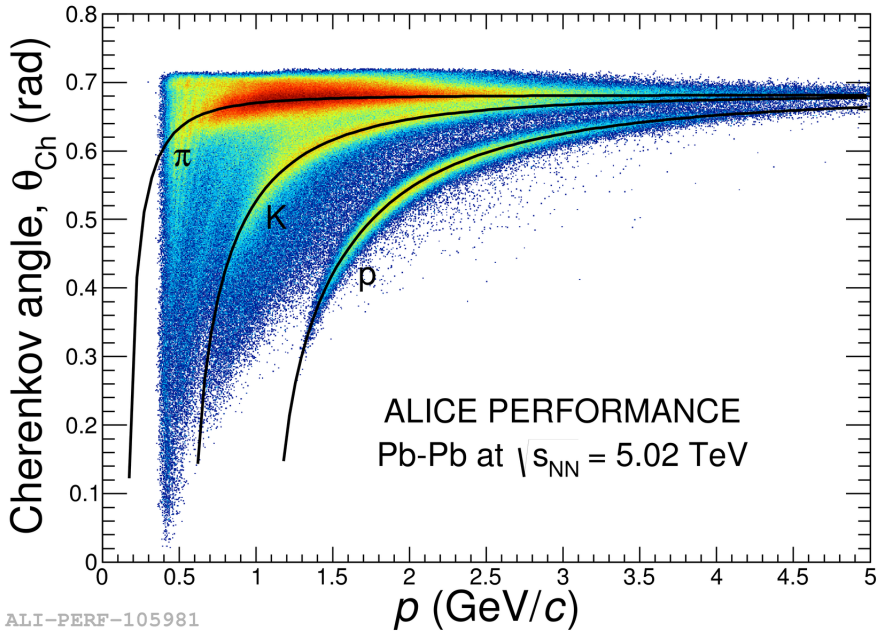

Figure 3.11: The Cherenkov angle θ_{ch} as a function of the particle momentum in heavy-ion collisions at $\sqrt{s_{\rm NN}} = 5.02$ TeV. Continuous lines represent theoretical Cherenkov angle values.

The ElectroMagnetic Calorimeter (EMCal) is a Pb-scintillator sampling calorimeter installed inside the ALICE solenoid at 4.5 m from the beamline. Its geometry in ALICE central barrel is shown in Figure 3.9. It covers the azimuthal angle of 107 degrees and the pseudorapidity range is $|\eta| < 0.7$. Its length in the longitudinal direction

is 700 cm. The EMCal measures the energy of charged particles, photons and the photonic decays of neutral mesons to study jet quenching. Another calorimeter is installed, which is the Di-jet Calorimeter (DCal) to complement the EMCal. The azimuthal coverage of the DCal is 70 degrees and the DCal is placed in front of the EMCal. This configuration allows back-to-back jet measurements.

The Photon Spectrometer (PHOS) is an electromagnetic calorimeter, made of lead-tungstate ($PbWO_4$) crystal and shown in Figure 3.12. It is capable of high spatial and energy resolution. The PHOS covers 60 degrees in azimuth and the pseudorapidity range $|\eta| < 0.12$. It was designed to measure photons and the photonic decays of neutral mesons to test the thermal and dynamical properties of the initial phase of the collision [201].

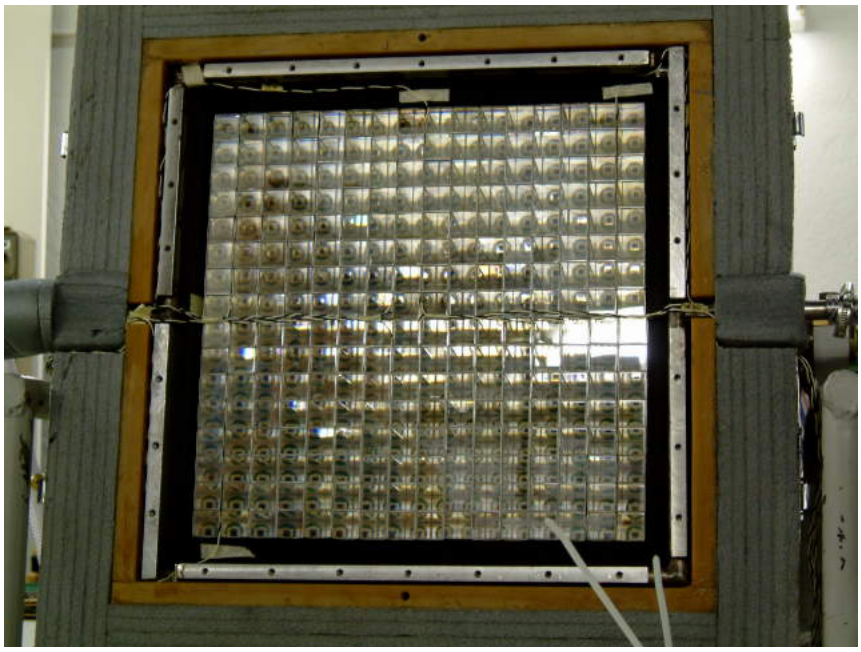

Figure 3.12: Front view of the PHOS prototype. The lead-tungstate crystals are shown.

3.3.2 The forward detectors

The V0 detector consists of two arrays of scintillator counters. One is placed at 340 cm from the interaction point in the A-side of the ALICE detectors. It is called V0-A and is shown in Figure 3.13. Its pseudorapidity range is for $2.8 < \eta < 5.1$. Another one is located at 90 cm from the IP in the C-side, and is known as V0-C. It covers the pseudorapidity range of $-3.7 < \eta < -1.7$. Each V0 has 32 segments of scintillators connecting to a Photo-Multiplier Tube (PMT) by Wave-Length-Shifting (WLS) optical fibers as shown in Figure 3.13.
When a charged particle crosses the scintillator, the atoms are excited along the incident track. The de-excitation of atoms emits photons which are then guided by WLS fibers to reach PMT and generate the electronic signals.

The V0 detector provides the Minimum Bias trigger and is also used to distinguish the beam-gas background from the beam interaction. The V0 detector is also used as a collision centrality estimator by summing up the energy deposited in the two arrays of scintillators. Figure 3.14 shows a typical distribution of the V0 amplitudes (the summed deposited energy of V0-A and V0-C) in heavy-ion collisions [202]. The areas below the distribution represent the different centrality classes defined for physics analyses. The Glauber model fit [29] describes the amplitude distribution correctly. The details of the Glauber model can be found in appendix A.

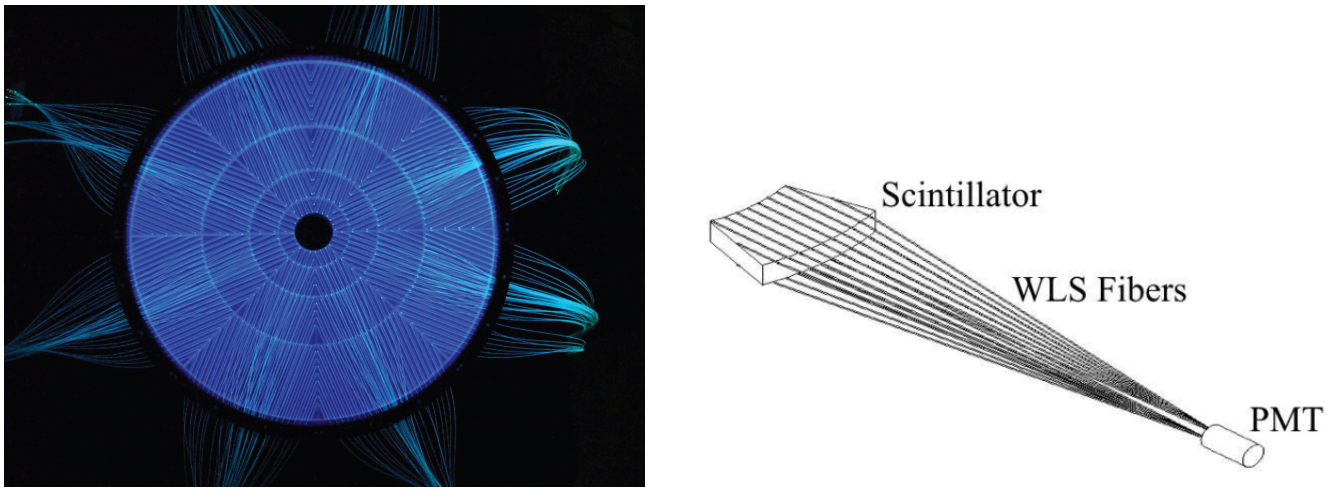

Figure 3.13: Front view of the V0-A (left). Schematic drawings of the design for the V0-A (right).

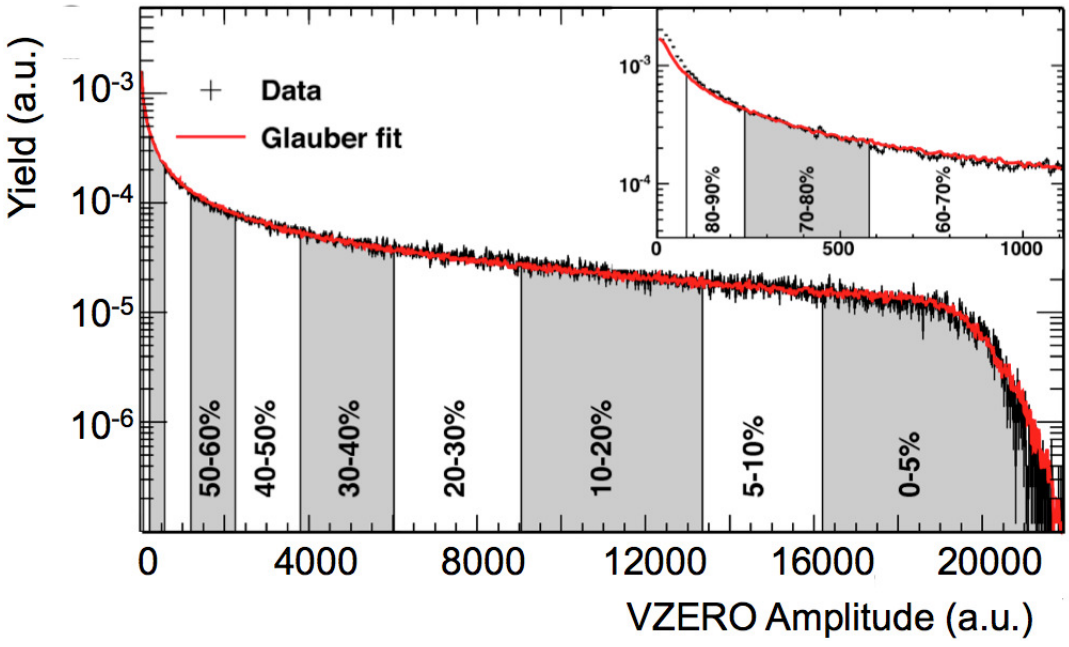

Figure 3.14: Distribution of the sum of amplitudes in the two V0 arrays in Pb-Pb collisions at $\sqrt{s_{\mathrm{NN}}} = 2.76$ TeV [202] with the Glauber model fit [29]. The insert shows the most peripheral centrality classes.

The T0 detector [1] [203] is made of two arrays (T0-A and T0-C) of Cherenkov counters connected to fast photomultipliers. The T0-A is located at 3.6 m from the IP in the A-side and its pseudorapidity range is $4.61 < \eta < 4.92$. In the opposite direction, the T0-C is located at 70 cm from the IP and it covers the pseudorapidity range $-3.28 < \eta < -2.97$.

The T0 detector, with its time resolution of 25 ps, is able to provide a precise start-up time of a collision. It measures the vertex position online and determines the multiplicity of charged particles produced in hadron collisions. Furthermore, it serves as an alternative Minimum Bias trigger detector.

The Zero-Degree Calorimeter (ZDC) [204] measures the energy of the spectator nucleons with two sets of neutron (ZN) and proton (ZP) calorimeters. These calorimeters are located at 114 m away from the IP on both sides of the ALICE detector. ZN and ZP cover the pseudorapidity range of $|\eta| < 8.8$ and $6.5 < |\eta| < 7.5$, respectively. They are quartz-fiber spaghetti calorimeters with sliced optical fibers embedded in an absorber. It is shown in Figure 3.15. The ZDC is used in heavy-ion collisions to estimate the centrality of the event. It also serves to remove debunched heavy-ion collisions and to reject electromagnetic Pb-Pb interactions.

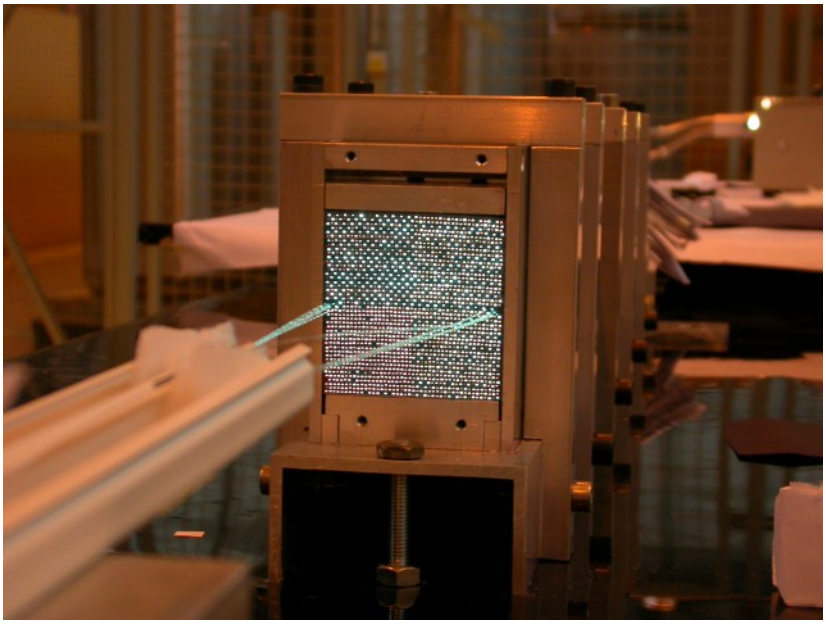

Figure 3.15: ZDC Calorimeter for spectator neutrons. The quartz fibers are placed in an absorber.

3.4 The muon spectrometer

The muon spectrometer [205] is a forward detector and is designed to detect muons. It is useful to measure particles that decay into dimuons, such as the low-mass mesons (ρ, ω, ϕ), quarkonia and Z bosons. Open heavy flavor and $W^{\pm}$

[1] For T0 and V0 as trigger detector, the important characteristic is the time resolution.

bosons are also measured by reconstucting single muons from semi-leptonic decays. The layout of the spectrometer is shown in Figure 3.16. The spectrometer is composed of an absorbing system, a dipole magnet, a tracking and trigger system. The muon spectrometer covers the pseudorapidity range of -4 < η < -2.5. Each part of the muon spectrometer is described in the following.

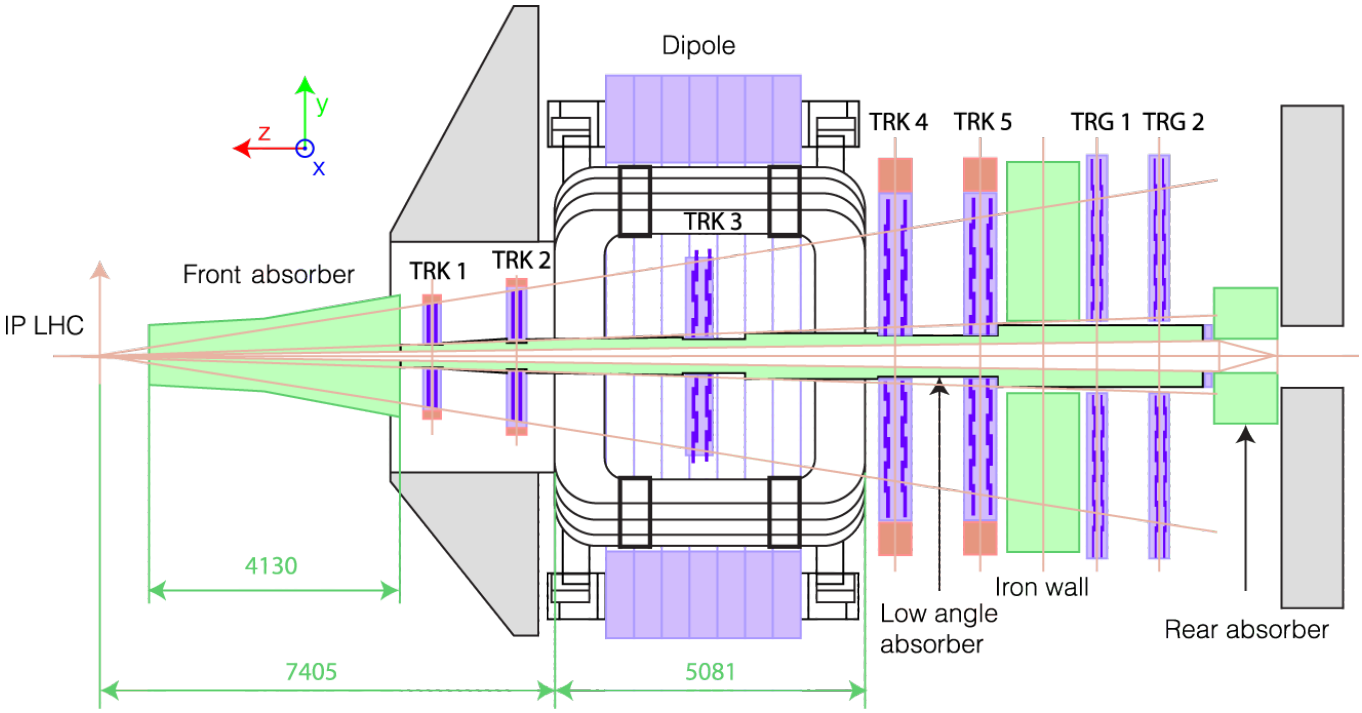

Figure 3.16: View of the muon spectrometer [196].

3.4.1 Absorber

The system of absorbers [205] suppress hadrons, mainly pions and kaons, to decrease the background for single muon and dimuon measurements. The first component of the absorbers is the front absorber which has a conical structure with a length of 4.13 m and located at 90 cm from the interaction point on the C-side. The front absorber is shown in Figure 3.17 with the light to dense materials that compose it. The carbon and concrete are adopted to lower down the effect of multiple scatterings and energy loss by traversing muons. The rear end of the front absorber are W, Pb and stainless steel in order to attenuate low energy photons, neutrons and secondary particles produced in the front absorber.

The small-angle beam shield covers the beam pipe along the length of the muon spectrometer. The shield is made of W, Pb and stainless steel to protect the muon spectrometer from particles produced by beam-gas interaction in the beam pipe and by interaction of large rapidity particles with the beam pipe.

An additional protection for the trigger chambers is provided by the muon filter which is an iron wall with a thickness of 1.2 m. The front absorber and the iron wall can stop muons with a total momentum below 4 GeV/c. Besides, a

rear absorber sits at the back of the second trigger chambers to prevent from beam-gas interactions produced in the beam pipe in the C-side.

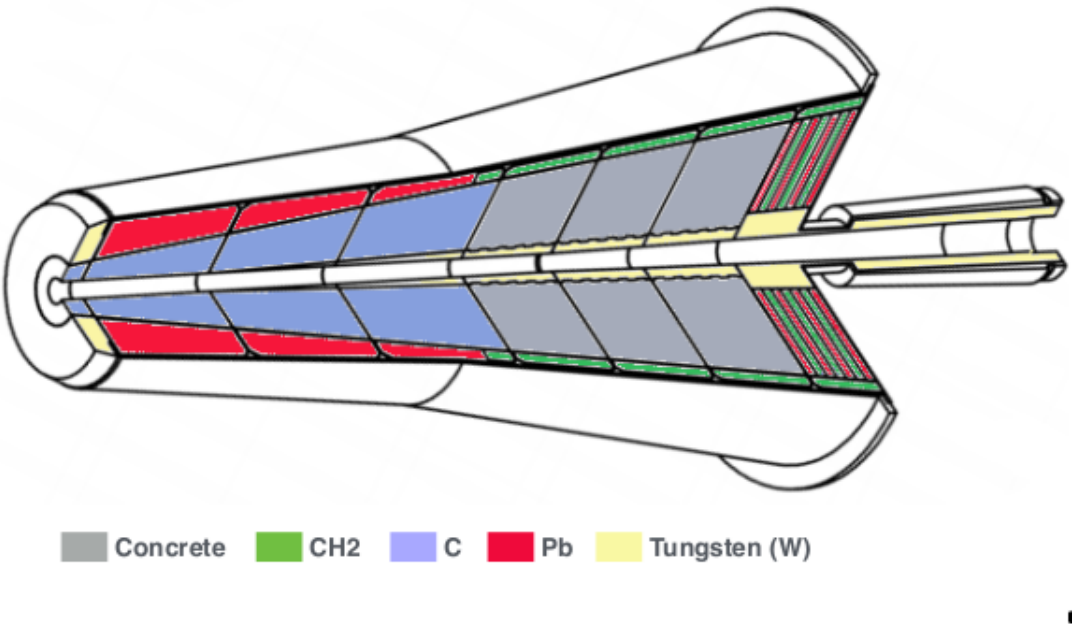

Figure 3.17: Front absorber of the muon spectrometer with details on its inner structure. Figure from [162]

3.4.2 Dipole magnet

The dipole magnet [205] provides an integral field of 3 Tm to deflect charged particles. Associated to the particle trajectory reconstructed by the tracking chambers, the magnetic field allows one to determine the particle momentum and electric charge. The magnetic field from the dipole is perpendicular to the beam pipe in the horizontal plane. The charged particle is therefore deviated in the vertical plane. The plane perpendicular to the magnetic field is referred to as "bending plane", while the one parallel to the magnetic field is referred as "non-bending plane". The volume of the magnet is of $5 \times 6.6 \times 8.6$ m^3 and is placed at 7 m from the interaction point.

3.4.3 Muon tracking chambers (MCH)

The tracking system was designed to record the three-dimensional information of muon particles. The system consists of five tracking stations. A tracking station has two planes of Multi-Wire Proportional Chambers (MWPC) with two cathode planes readout. The first two tracking stations, called Station 1 and 2 are located right after the front

absorber. The third tracking station, called Station 3 is inside the dipole magnet. The last two tracking stations, called Station 4 and 5 are placed between the dipole magnet and the muon filter. Two different geometries were designed for the chambers. As shown in Figure 3.18, Station 1 and 2 have a quadrant structure while Station 3, 4 and 5 have a slat structure.

The MWPC is made of a central plane of anode wires which are sandwiched between two cathode planes. Those two cathode planes are segmented into many pads as shown in Figure 3.20. The magnetic field follows the x-axis. The upper plane called the non-bending cathode has finer segmentations in x-direction. The bottom plane has finer segmentations in y-direction and corresponds to the bending plane. The wires are supplied by a high voltage of 1600 - 1650 V and the cathode planes are grounded. Hence the electric field is formed with a strongest field near the wires. The space between the two cathode planes is filled with a gas mixture of Argon (80%) and CO_2 (20%).

In Figure 3.19, when a charged particle goes through the chamber, the gas is ionized and produce ions and electrons. Due to the electric field, the ions move to the cathode plane and the electrons drift to the nearest anode wire. An avalanche is produced by the drifted electrons, resulting into secondary electrons. This gives an ion-cloud inducing a charge distribution on the cathode pads close to the avalanche location. The information provided by the pads of the cathode planes determines the x-y positions of the charged particles in a given chamber.

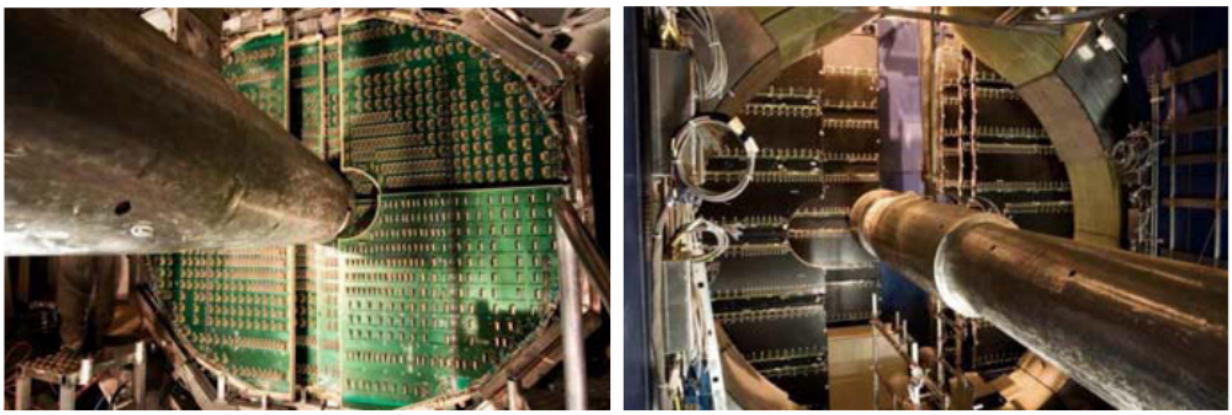

Figure 3.18: Picture of Station 2 with a quadrant structure (left) and of Stations 4 and 5 with a slat structure (right) [196].

The relative momentum resolution $\delta p/p$ as a function of p, for tracks reconstructed in the MUON spectrometer, is shown in 3.21. In the plot, $\delta p/p$ increases with decreasing momentum for $p <$ 6-8 GeV/c, which is mainly due to the multiple scatterings in the absorber. In the high momentum region, $\delta p/p$ increases with increasing momentum because of the size of the muon tracking chamber pads.

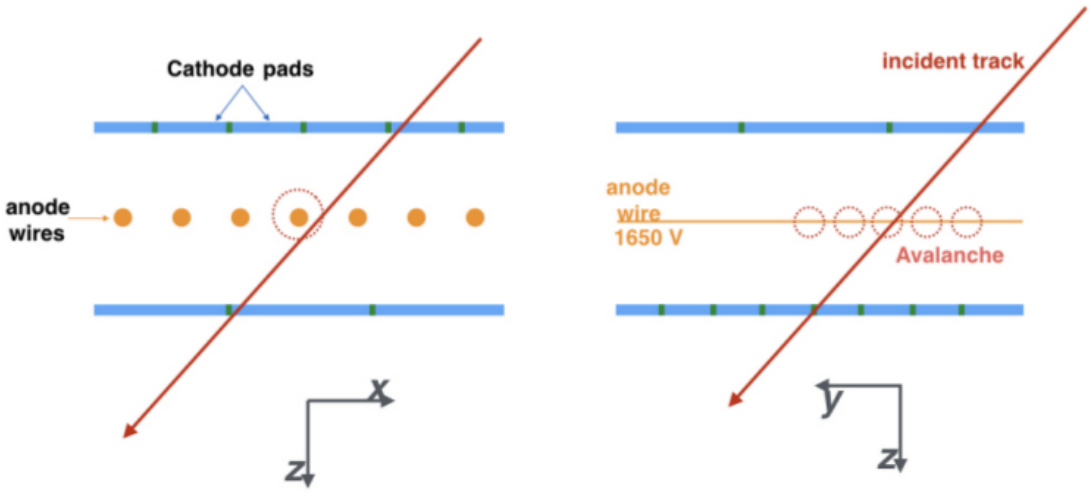

Figure 3.19: The layout of a MWPC viewed from two cathode planes. Figure from [205].

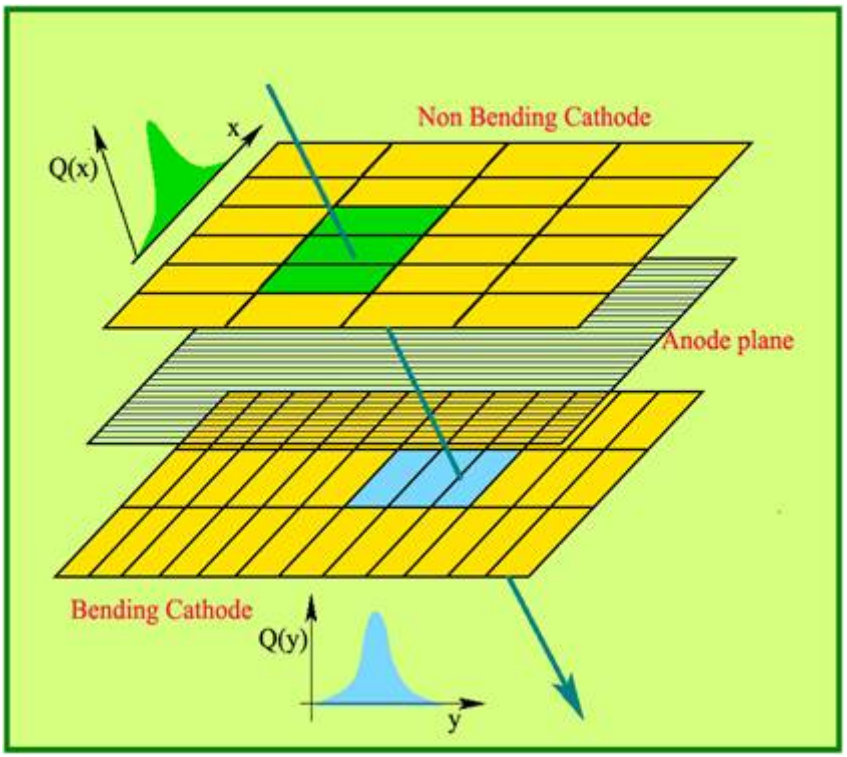

Figure 3.20: Working principle of a MWPC of the muon tracking chambers. Figure from [206].

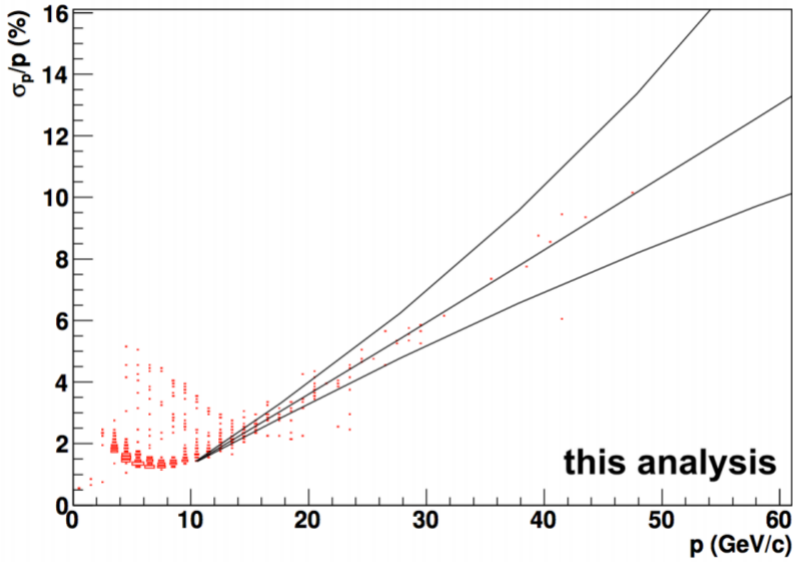

Figure 3.21: Relative momentum resolution $\delta p/p$ as a function of p of the tracks reconstructed in the muon spectrometer. Results are obtained from pp collisions at $\sqrt{s} = 900$ GeV. Figure from [207].

3.4.4 Muon trigger chambers (MTR)

The trigger system was designed to reduce the number of recorded events without a muon, or with only a low p_{T} muon [2]. The system has two trigger stations (MT1 and MT2) located after the iron wall, around 16 meters away from the IP. Besides, the two stations are separated by 1 meter. Each station has two chamber planes. Two planes (bending and non-bending) with 18 Resistive Plate Chambers (RPC) are in the front and back sides of each chamber.

The structure of one RPC is displayed in Figure 3.22. Two resistive electrode plates are separated by 2 mm-long spacers. The space inside the two plates is filled with a gas mixture Ar + $C_2H_2F_4$ + i-butane + SF_6 (50.5/41.3/7.2/1). One of the plates painted with graphite is supplied by high voltage while the other one is grounded. Those two plates are covered by two insulating films. The pick-up strips are attached to the insulating films. The two sets of strips are perpendicular to another two sets of strips.

When a charged particle passes through the gas, an avalanche of secondary electrons is produced and causes the signals. The signals, transmitted by the strips, give the spatial information of the traveling particle. From the position of the track in the two trigger stations, the p_{T} of the particle is estimated as illustrated in Figure 3.23. A muon which is produced at the IP is bent by the dipole magnetic field ($\vec{B}$) and traverse the muon triggers at (Y_1, Z_1) in MT1 and (Y_2, Z_2) in MT2. The transverse position of the track is recalculated assuming a straight track with infinite momentum (Y_∞, Z_2). The deviation $\delta_Y = Y_2$ - Y_∞, the distance from the muon track to the infinite momentum track position in MT2 is inversely proportional to the muon p_{T}. The muon track is discarded if δ_Y is larger than a given value, corresponding to a p_{T} higher than a threshold value. The muon triggers are programmed

[2] The muons of low p_{T} that reach the trigger chambers are usually not a muon decay candidate for heavy-flavour, electroweak bosons or quarkonium.

with selections depending on the p_{T} threshold, a low and a high p_{T} thresholds. The trigger decision is taken according to the transverse momentum of particles p_{T}^{μ}. The low and high p_{T} thresholds are usually set at $p_{\mathrm{T}}^{\mu} \approx 0.5$ or 1 GeV/c and p_{T}^{μ} of 4.2 GeV/c, respectively. The δ_Y sign represents the charge of the muon track. The trigger inputs are usually defined for the muon data taking as follows:

- at least one muon satisfying the low p_{T} threshold (0MSL),
- at least one muon satisfying the high p_{T} threshold (0MSH),
- at least one unlike-sign muon pair satisfying the low p_{T} threshold (0MUL),
- at least one like-sign muon pair satisfying the low p_{T} threshold (0MLL).

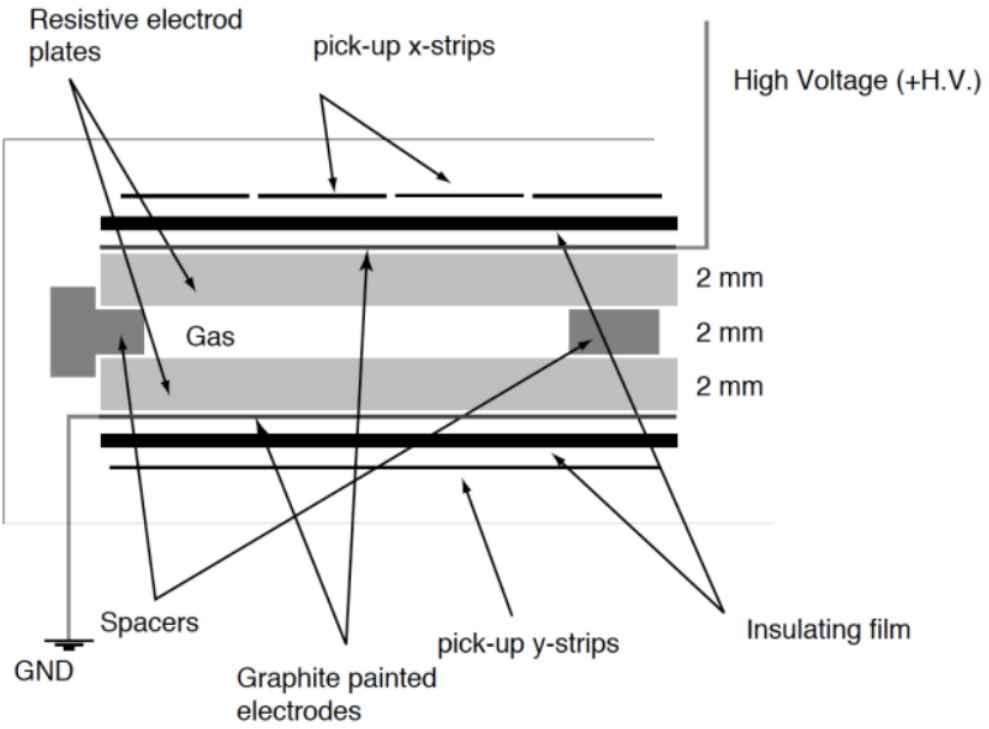

Figure 3.22: The Structure of the RPC of the muon trigger system. Figure from [205].

3.5 Trigger classes and data acquisition system

3.5.1 Trigger classes

The Central Trigger Processor (CTP) is a hardware trigger system. It was designed to combine and synchronize information from all the triggering detectors and to send the correct sequences of trigger signals to all detectors in

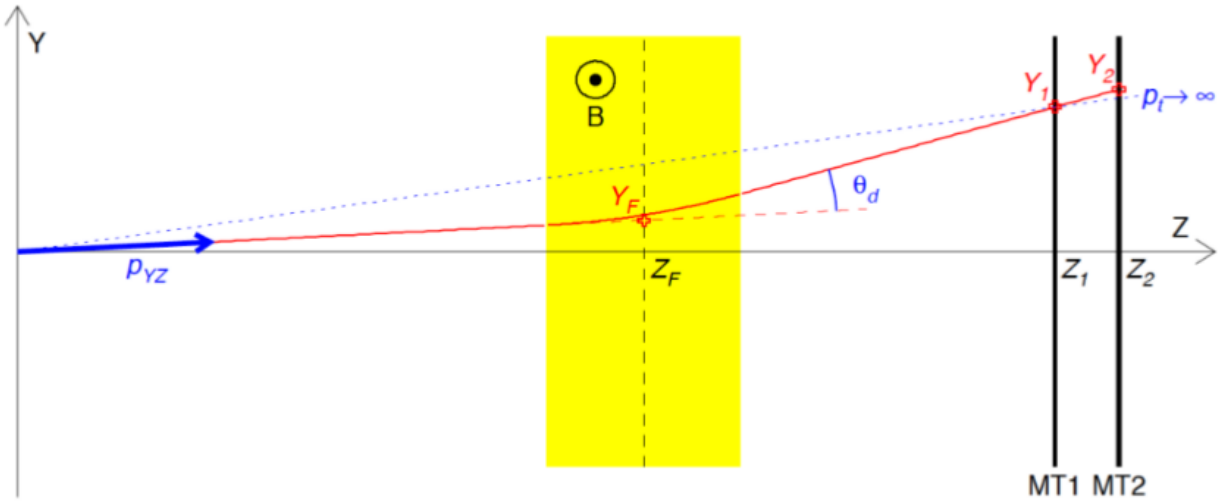

Figure 3.23: The principle of the muon trigger with the estimation of the particle track p_{T}. Figure from [205].

order to make them read out correctly [208]. Besides, the outputs of the CTP are organized into trigger classes. One trigger class has a trigger cluster with the information from group of trigger detectors along with the trigger level decisions of the CTP. The CTP was designed to have three trigger levels to read-out an event according to the response time of the sub-detectors. The first level is the fastest trigger, named L0. It allows the CTP to send the signals to the cluster of detectors with a response time of 1.2 μs. For example, V0, T0, SPD, EMCAL, PHOS and MTR can send back the L0 trigger signals within the required time. The next level trigger is L1 with a response time of 6.5 μs, which are sent by EMCAL, TRD and ZDC. The slowest level trigger is called L2 with a response time of 100 μs corresponding to the drift time of electrons in the TPC. The number of counts of all trigger classes before (L0b) and after (L0a) the CTP decision is also stored in the so-called trigger scalers.

The High-Level Trigger (HLT), a software trigger, helps the CTP in the implementation of complex logic for finer event selection to reduce the size of recorded data for the detectors which generate large volume of data [209].

The trigger classes are defined by the trigger input combinations usually via logical connectors (AND, OR), such as the minimum bias (MB) trigger, CINT7-B-NOPF-MUFAST, which is defined by a coincidence of signals from the two V0 arrays, V0-A and V0-C. Another MB trigger, known as C0TVX-B-NOPF-CENTNOTRD, is defined by the conjunction signals of T0-A and T0-C and the requirement of an interaction vertex within $|z| < 30$ cm as measured by the T0. The trigger classes which combines the V0 and MTR trigger inputs in muon data taking are the following:

- CMSL7-B-NOPF-MUFAST, the low p_{T} threshold single muon trigger, which is the combination of 0MSL, V0-A and V0-C triggers,
- CMSH7-B-NOPF-MUFAST, the high p_{T} threshold single muon trigger, which is the combination of 0MSH,

V0-A and V0-C triggers,

- CMUL7-B-NOPF-MUFAST, the unlike-signed dimuon trigger, which is the combination of 0MUL, V0-A and V0-C triggers,

- CMLL7-B-NOPF-MUFAST, the like-signed dimuon trigger, which is the combination of 0MLL, V0-A and V0-C triggers.

The names of the above trigger classes are defined according to the trigger and readout detectors for instance, CMUL7 indicates the trigger detectors and MUFAST the readout detector cluster that includes the SPD, MCH, MTR, T0, V0, and ZDC. Besides, the names also contains the information on the bunch condition and on the online timing vetoes. For example, B indicates that bunches from both beams collide in the interaction point, and NOPF means there is no past future protection on the event timing. .

3.5.2 Data acquisition system (DAQ)

The ALICE DAQ system [210] handles with data stream from sub-detectors to data storage. The process of data flow is described briefly in the following. The data produced by sub-detectors are called event fragments. They are read out by the Local Data Concentrators (LDCs). The LDCs assemble the event fragments into a sub-event. Next, the sub-events are transferred to the Global Data Collectors (GDCs) which build up the sub-events into a full event. The GDCs write the outcomes in the Transient Data Storage (TDS), a temporary buffer. The data files in the TDS are migrated to the Permanent Data Storage (PDS) at CERN and accessible via the GRID, which is a global collaboration of computering centers. Note that the maximum rate for the muon tracking readout system is 1 kHz in the Run 2 period and the DAQ system for the muon cluster is limited by the muon tracking readout system.
On the other hand, the conditions of the data including the calibration and alignment information are produced during the data-taking running. A system called Shuttle [211] handles the condition data online. The data files are stored in the Offline Condition Database (OCDB). All collected OCDB files are pushed on the Grid for the reconstruction and the analysis tasks.
The recorded events read out by the DAQ need a couple of reconstruction cycles for physics analyses. One reconstruction cycle is called a pass and it is completed offline with the ALICE offline framework. The outcomes of a pass are stored in Event Summary Data (ESD) files. The ESDs save many information recorded by the detectors for general physics analyses but usually the files are massive. The quality assurance analysis is performed on ESDs and will be detailed in the following sections. Analysis Object Data (AOD) files, obtained by filtering the ESDs contain less and essential information dedicated to specific analyses.

3.6 Data quality assurance

The data quality assurance (QA) provides a quality check of the data. It monitors as a function of time (run number), some observables and compare them to a reference for the ALICE sub-detectors in every data taking periods. The run number is the basic unit of the data taking. If there are problems in the sub-detectors during data taking or in the data reconstruction process, the monitored observables are likely different from the reference. If problems are found in some runs, we have to understand whether those runs have to be labeled as bad. Through this QA check performed by experts of sub-detectors, we provide the lists of good runs in every reconstruction passes for physics analyses. Note that a good run for muon physics depends on the data quality of the six detectors belonging to the muon cluster read-out: MCH, MTR, SPD, V0, ZDC and T0 (only for pp collisions).

3.6.1 Data quality assurance for the muon spectrometer

To determine the data quality, each sub-detector has its own observables to monitor. This section focuses on the observables of the tracking and trigger chambers for the muon QA in order to understand their performances. The usual way to start is to select a list of runs with pre-selections: the run should be of physics type, the read-out detectors are at least the muon tracking and trigger chambers, the global quality for read-out detectors are good and the beam mode should be stable. The next step is to calculate some observables from those runs.
The ratio of the number of reconstructed trigger, L2A, from QA and from the OCDB scalers for a given trigger, as shown in Figure 3.24, which is an indicator of the efficiency of the reconstruction. If the ratio is equal to one, this means that the data are fully reconstructed. Otherwise, all the events are not reconstructed [3].

Another observable is the efficiency of the muon trigger chambers which is defined as the ratio between the number of triggerable tracks and the total number of tracks which cross the muon trigger. As discussed earlier, each muon trigger chamber has two read-out planes: the bending and non-bending planes. A track is considered as triggerable when it gives a hit in at least three planes on both chambers. Figure 3.25 shows the 18 RPC efficiencies as a function of run number for the bending and non-bending plane of the muon trigger chamber. The efficiency values are above 0.9 in most RPCs and constant over run number (time) which means that the trigger chambers work as expected.

Likewise, an example of observables for accessing the quality of the data recorded by the muon tracking chambers are the number of various track types normalised by the number of triggers as a function of run number in a given chamber. The top panel of Figure 3.26 shows the number of reconstructed tracks in the muon tracking chambers for various types of tracks for the CMUL7-B-NOPF-MUFAST trigger class. The label, "Tracking (only) tracks" belongs to tracks reconstructed only in the tracking chambers. The label "Matched tracks" indicates tracks which

[3] It is not an issue not to have all the data reconstructed

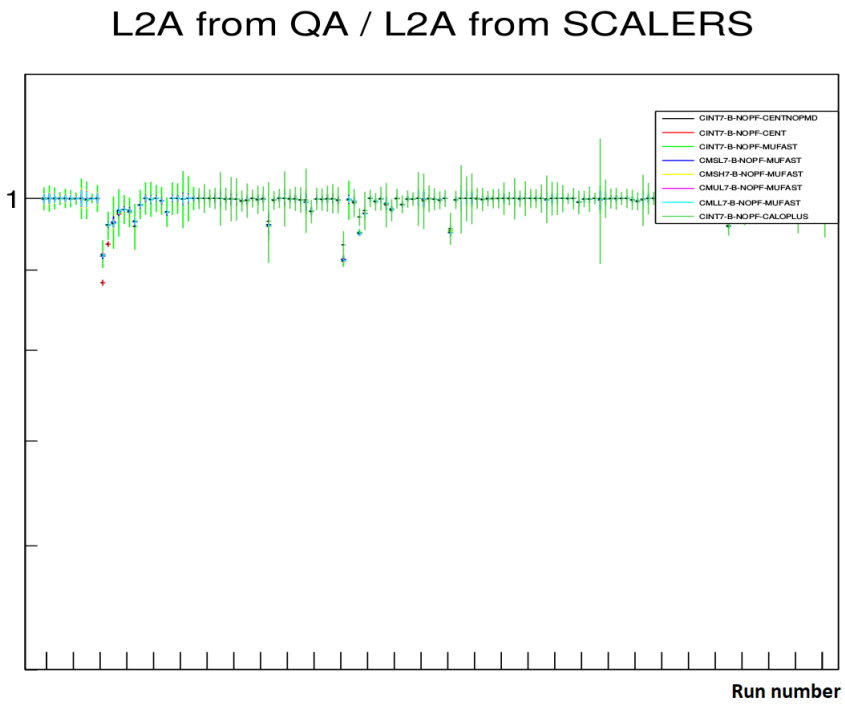

Figure 3.24: Reconstructed triggers in QA w.r.t. number of L2A from OCDB scalers in the third reconstruction pass of LHC18q.

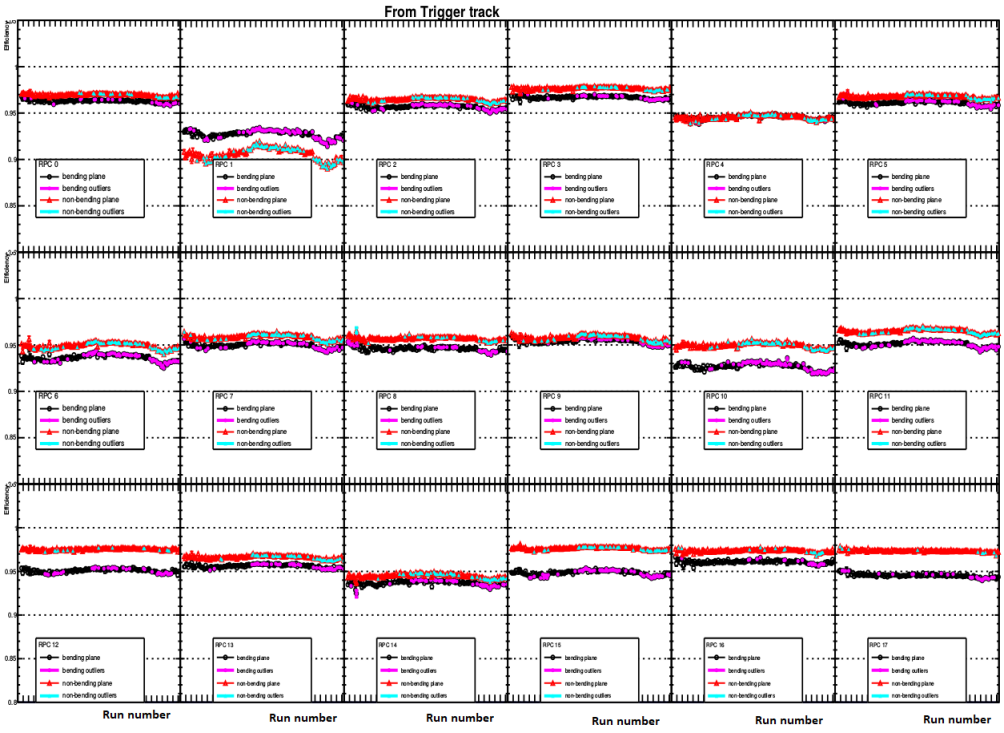

Figure 3.25: The efficiency of RPCs as a function of the run number in the muon trigger chamber in the third reconstruction pass of LHC18q.

are reconstructed both in the trigger and the tracking chambers, and the label "Trigger (only) tracks" is for tracks reconstructed only by the trigger chambers. The trending of the number of reconstructed tracks normalized by the number of triggers should be flat during the data-taking time. However, the counts drop in some runs and it is usually related to inefficiencies of reconstructing tracks in the tracking chambers.

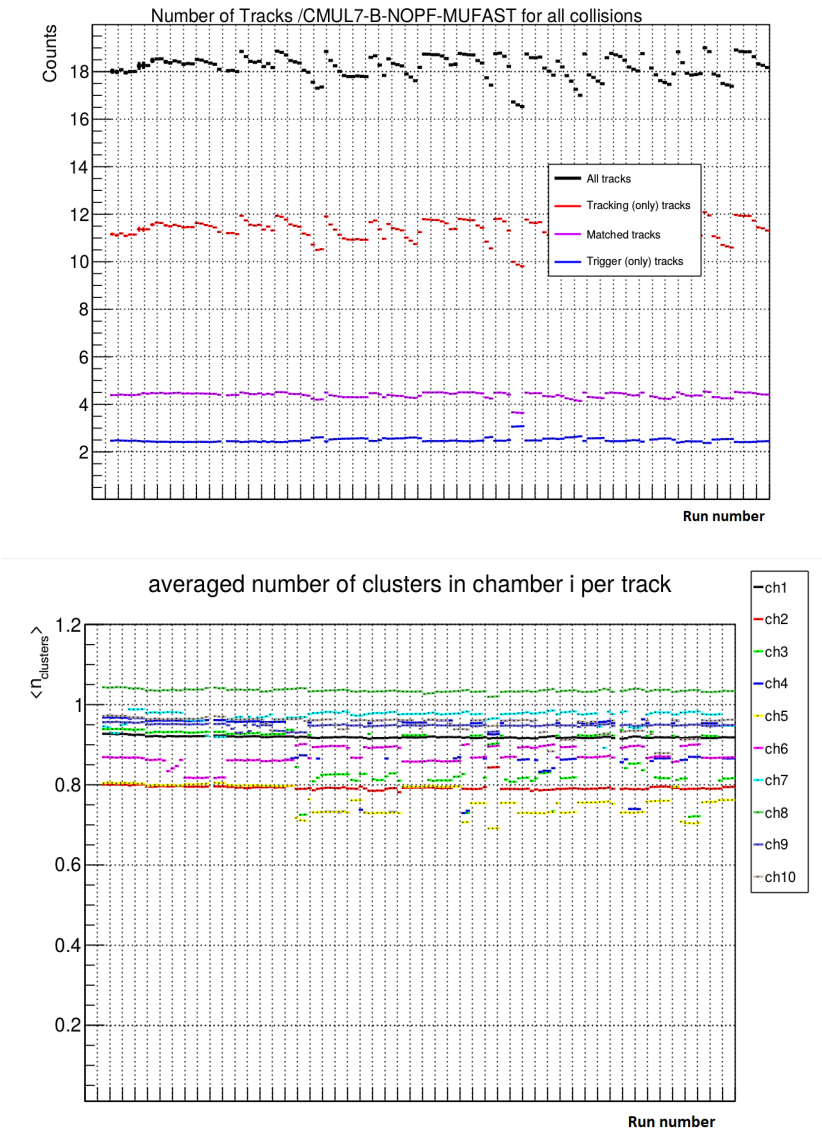

Figure 3.26: Graphs for the number of tracks in CMUL7-B-NOPF-MUFAST trigger class for all types of collisions (top) and the averaged number of clusters in a given chamber per track (bottom) in muon_calo_pass3 of LHC18q.

Moreover, the efficiency of the tracking chambers is an important observable which is related to the average number of reconstructed clusters per track, and that can be obtained for each tracking chamber. The bottom panel of Figure 3.26 displays this observable as function of the data-taking time for the ten chambers. The observables for some chambers are closed to one that indicates the high performance of the tracking chambers. However, for several

chamber, the average number of cluster per track is below 0.8, which indicates hardware problems, for instance high voltage trips in a sector of the chamber. Once suspicious runs are spotted, one can visualize in more details the muon tracking chamber conditions in those runs. For example, Figure 3.27 shows the mean of the high voltage applied to the muon tracking chambers in run 297595, showing few sectors with lower high voltage values w.r.t nominal value.

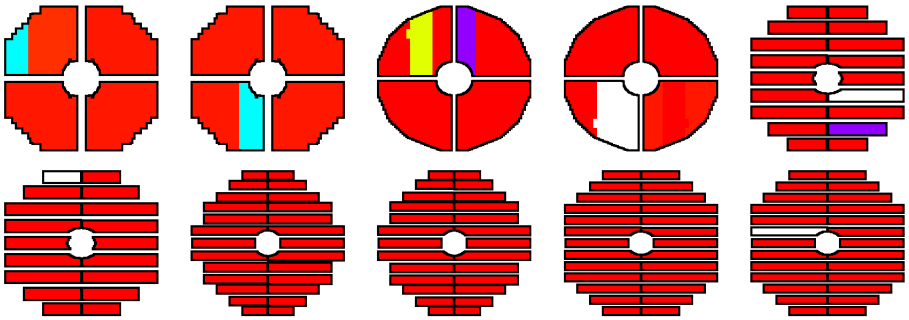

Figure 3.27: View of the average high voltage value in the high-voltage sectors of the muon tracking chambers in the run 297595 of LHC18r. The red color corresponds to normal high voltage value while other colors indicate that the voltage conditions are not normal.

3.6.2 Run condition of 2017 pp and 2015+2018 Pb-Pb collisions

The proton-proton (pp) and lead-lead (Pb-Pb) collisions at a collision energy per nucleon pair of 5.02 TeV correspond to the data sample analyzed in this thesis. The pp collisions were completed in around one month in 2017. The Pb-Pb collisions were collected in November-December, 2015 and November, 2018.

The beam energy and the integrated luminosity of pp collisions in 2017 and Pb-Pb collisions in 2015 + 2018 are tabulated in Table 3.1. These periods correspond to LHC Run 2, the LHC operation schedule lasting four years from 2015 to 2018. ALICE has recorded an integrated luminosity of 1.2 pb^{-1} in pp collisions in 2017 and of 787 $\mu\mathrm{b}^{-1}$ of Pb-Pb collisions in Run 2. Figure 3.28 shows the accumulated luminosity as a function of time. Since the integrated luminosity in 2015 collisions is lower than 2017 by about a factor of 10, this thesis only used the 2017 pp data sample. In the case of Pb-Pb collisions, the integrated luminosity in 2018 was greater than the 2015 Pb-Pb one by a factor of 3. In order to increase the statistics, both Pb-Pb data samples were merged in the analysis presented in this thesis. Note that the integrated luminosity corresponds to the luminosity integrated over Muon QA checked runs.

beam	2017 pp	Pb-Pb Run 2
$\sqrt{s_{\mathrm{NN}}}$	5.02 TeV	5.02 TeV
Integrated luminosity	1.3 pb^{-1}	787 $\mu\mathrm{b}^{-1}$
Muon QA L_{int}	1219 nb^{-1}	712 $\mu\mathrm{b}^{-1}$

Table 3.1: Beam conditions of pp and Pb-Pb collisions in LHC Run 2.

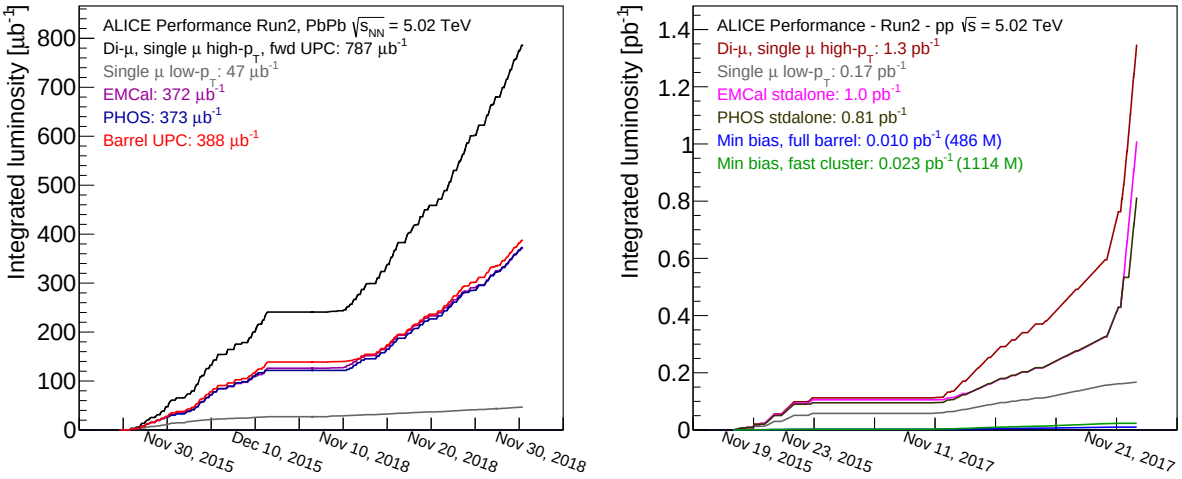

Figure 3.28: The recorded luminosity of Pb-Pb (left) and pp (right) collisions in Run 2.

Chapter 4

Inclusive J/ψ production in pp collisions

The inclusive J/ψ production cross section measurements in pp collisions are useful to investigate the J/ψ production mechanism. Besides, they are important references for the charmonium studies in heavy-ion collisions (see chapter 5). This chapter details the analysis procedure for the measurement of the inclusive J/ψ production cross section at forward rapidity in pp collisions at $\sqrt{s}$ = 5.02 TeV with the data collected in 2017. We have measured the J/ψ production cross section integrated over p_{T} and the J/ψ differential cross section as a function of p_{T}, rapidity and the rapidity-differential cross section for four different p_{T} intervals. The forward rapidity corresponds to the rapidity range $2.5 < y < 4$.

The inclusive differential J/ψ production cross section is defined as:

$$\frac{d^2\sigma}{dp_{\mathrm{T}}dy} = \frac{N_{\mathrm{J}/\psi\to\mu\mu}(\Delta y, \Delta p_{\mathrm{T}})}{BR(\mathrm{J}/\psi \to \mu\mu) \times \mathrm{L_{int}} \times (\mathrm{A} \times \epsilon)(\Delta \mathrm{y}, \Delta \mathrm{p_T}) \times \Delta \mathrm{p_T} \times \Delta \mathrm{y}}, \tag{4.1}$$

where BR is the J/ψ to dimuon branching ratio and amounts to $(5.961 \pm 0.033)\%$ [18], L_{int} is the integrated luminosity, $N_{\mathrm{J}/\psi\to\mu\mu}(\Delta y, \Delta p_{\mathrm{T}})$ is the inclusive J/ψ yield for a given range in p_{T} and y and $(A \times \epsilon)(\Delta y, \Delta p_{\mathrm{T}})$ is the acceptance times efficiency of the detector for a given range in p_{T} and y.

In this analysis, I contributed to the extraction of the p_{T} dependence J/ψ yield and to the computation of the realistic acceptance times efficiency. I also estimated the systematic uncertainties on the signal extraction, the MC input parametrisation and intrinsic efficiencies of the muon trigger chambers. Other analysis ingredients, such as the luminosity and several systematic uncertainties (on the luminosity, tracking efficiency, trigger response functions and matching efficiency) are taken from the results completed by other analysers. Consequently, I obtain the J/ψ production cross sections integrated over p_{T} and the J/ψ differential cross section as a function of p_{T}. The rapidity dependence of the J/ψ cross section and the rapidity-differential cross section for four p_{T} intervals are obtained by another analyser.

In the following, section 4.1 describes the data analysis procedure. In section 4.1.1 and 4.1.2, event and track selec-

tions that are applied to select the dimuon candidates in the data sample are described. In section 4.1.3, the inclusive J/ψ signal extraction in different p_{T} and y bins is presented. In section 4.1.4, the estimation of the acceptance and efficiency of the detector by using an official Monte Carlo (MC) simulation is detailed. In section 4.1.5, the evaluation of the integrated luminosity by using a minimum bias (MB) trigger is explained. The estimation of systematic uncertainties on the J/ψ cross section measurement. They are described in section 4.1.6. Finally the inclusive J/ψ cross section results are presented in section 4.2 and are compared to the published results from the 2015 data sample [125] and to theoretical calculations.

4.1 Data analysis

4.1.1 Data sample and event selection

The analyzed data are the pp collisions at $\sqrt{s}$ = 5.02 TeV, recorded in 2017. The sample consists of 51 good runs passing the QA selection during the first reconstruction production. The MB events, triggered by the CINT7-B-NOPF-MUFAST (V0) and the C0TVX-B-NOPF-CENTNOTRD (T0) triggers are analyzed for estimating the integrated luminosity. The CMUL7-B-NOPF-MUFAST (CMUL7) triggered events are analyzed as well to extract the J/ψ signal. The triggered events can be polluted by beam-gas interactions. A physics selection (PS) is applied to rejects physics events from the beam-gas interactions by performing timing cuts on signals in V0A and V0C and in T0A and T0C. Table 4.1 shows the 51 run numbers and the numbers of CMUL7 triggered events before and after PS for the two periods of data taking. The physics selection rejects about 3% of the events.

LHC17p				LHC17q	
282008	282118	282224	282309	282365	282439
282016	282119	282227	282312	282366	282440
282021	282120	282229	282313	282367	282441
282025	282122	282230	282314	282391	
282031	282123	282247	282340	282392	
282050	282126	282302	282341	282398	
282051	282127	282304	282342	282402	
282078	282146	282305	282343	282411	
282098	282147	282306		282415	
282099	282206	282307		282437	
CMUL7 triggered events before PS				CMUL7 triggered events before PS	
6.716×10^6				1.217×10^7	
CMUL7 triggered events after PS				CMUL7 triggered events after PS	
6.650×10^6				1.175×10^7	

Table 4.1: List of QA-checked runs during the first reconstruction production for LHC17p and LHC17q data taking periods and total number of CMUL7 triggered events before and after physics selection.

4.1.2 Track selection

Hadrons produced in the collisions and escaping the front absorber can enter in the acceptance of the muon spectrometer. In order to improve the purity of the analyzed events and to select the muon candidates in the forward rapidity region, the following track selections are applied to each individual track:

- pseudo-rapidity in the range -4 $< \eta_\mu <$ -2.5 to reject tracks outside of the geometrical acceptance of the Muon Spectrometer;

- $2 < \theta_{\rm abs} < 10$ degree, where $\theta_{\rm abs}$ is the polar angle between the beam axis and the track at the end of the absorber, in order to exclude the tracks crossing the thicker part of the absorber. An equivalent selection can be done by using the radial transverse position $R_{\rm abs}$ of the track in the transverse plane. By considering the small angle approximation, $\theta_{\rm abs} = R_{\rm abs}/L$ where L is the distance from the vertex to the end of the absorber, the equivalent selection is therefore $17.6 < R_{\rm abs} < 89.5$ cm;

- tracking track should match a trigger track, whose $p_{\rm T}$ is required to be above the low $p_{\rm T}^{\rm trig}$ trigger threshold, i.e. $p_{\rm T}^{\rm trig} > 0.5$ GeV/c in this data sample. It reduces the background from pion and kaon decays;

- $p \times$ DCA cut within 6σ, where $p \times$ DCA is the product of the track momentum and the Distance of Closest Approach (DCA). The DCA is the distance in the transverse plane between the interaction point (IP) and the straight extrapolation of the muon track from the front absorber to the IP transverse plane. This cut removes the tracks which do not originate from the interaction point.

Furthermore, the following dimuon selections are applied:

- the two muons must have opposite electric charges;

- the rapidity of the dimuon must be in the range: $2.5 < y < 4.0$;

- the $p_{\rm T}$ of the dimuon must be in the range: $0 < p_{\rm T} < 20$ GeV/c.

4.1.3 Signal extraction

The J/ψ is a resonance particle and its physical width is narrow. The J/ψ mass peak is at around 3.1 GeV/c^2 in the opposite-charge dimuon invariant-mass spectrum. To calculate the dimuon invariant-mass, the following formula is used:

$$m_{\mu^+\mu^-} = \sqrt{2m_{\mu^\pm}^2 + 2(E_{\mu^+}E_{\mu^-} - \vec{p}_{\mu^+} \cdot \vec{p}_{\mu^-})}, \tag{4.2}$$

where $m_{\mu^{\pm}}$ is the mass of muon particles, E_{μ^+} and E_{μ^-} are the energies of the positive-charge and the negative-charge muon particles and $\vec{p}_{\mu^+}$ and $\vec{p}_{\mu^-}$ are the momenta carried by the positive-charge and the negative-charge muon particles. Figure 4.1 shows a typical invariant mass spectrum of dimuon pairs measured by ALICE for pp collisions at $\sqrt{s} = 7$ TeV. It shows the low mass resonances (ω, ϕ) and the quarkonium states (J/ψ, ψ(2S), Υ) at high mass. The quarkonium peaks stand on top of a significant and complex background.
In the invariant mass region $2 < m_{\mu^+\mu^-} < 5$ GeV/c^2, the background can come from different sources:

- the correlated background in which the muon pair originates the same initial hard scattering and is produced via the semi-leptonic decay of open charm or open beauty hadrons.
- the uncorrelated background in which the muon pair come muons belonging to completely different physics processes. For instance, one muon can originate from the decay of a kaon and the other muon from the decay of a pion. This type of background is also known as the combinatorical background.

The ALICE muon spectrometer can only measure inclusive J/ψ at forward rapidity in Run 1 and Run 2. Inclusive J/ψ production includes the contributions from prompt and non-prompt J/ψ productions (see section 2.2.2). Ideally, the J/ψ peak would be a narrow Breit–Wigner function. However, the detector resolution smears the J/ψ peak. Two effects, responsible for the left tail of the signal peak, are the energy loss fluctuations and radiative decays in the front absorber. The muon tracking chamber misalignment affects the left and right tails of the signal, together with the multi-Coulomb scattering in the absorber.

In order to extract the J/ψ signal from the invariant mass spectra, a fit method is adopted and performed in several p_{T} and rapidity bins. The ψ(2S) signal is also extracted. The global fit function is a sum of three functions including two signal functions for the J/ψ as well as for the ψ(2S) and a background function. Various choices of signal and background functions are performed in two different fitting ranges to estimate the associated systematic uncertainty. The J/ψ peak is fitted with:

- an extended Crystal Ball (CB2) function (see Appendix B),
- a function developed by the NA60 experiment (NA60) (see Appendix B).

These two functions are based on a Gaussian core with two additional tails at low and high masses. The mean and the width of the Gaussian core of the two functions correspond to the J/ψ mass pole and the muon spectrometer resolution in the J/ψ mass region, respectively. These two parameters are left free during the fitting process. Concerning the ψ(2S) fitting, the mass of the ψ(2S), $m_{\psi(2S)}$, is bounded to the J/ψ mass, $m_{J/\psi}$, by the mass difference between the two states. It can be expressed as:

$$m_{\psi(2S)} = m_{J/\psi} + (m^{PDG}_{\psi(2S)} - m^{PDG}_{J/\psi}),$$

where the PDG in the superscript means that the mass value is taken from the Particle Data Group [18]. The ratio of the ψ(2S) to the J/ψ width is fixed to 1.01 according to the study performed with high statistics pp data at $\sqrt{s} = 13$

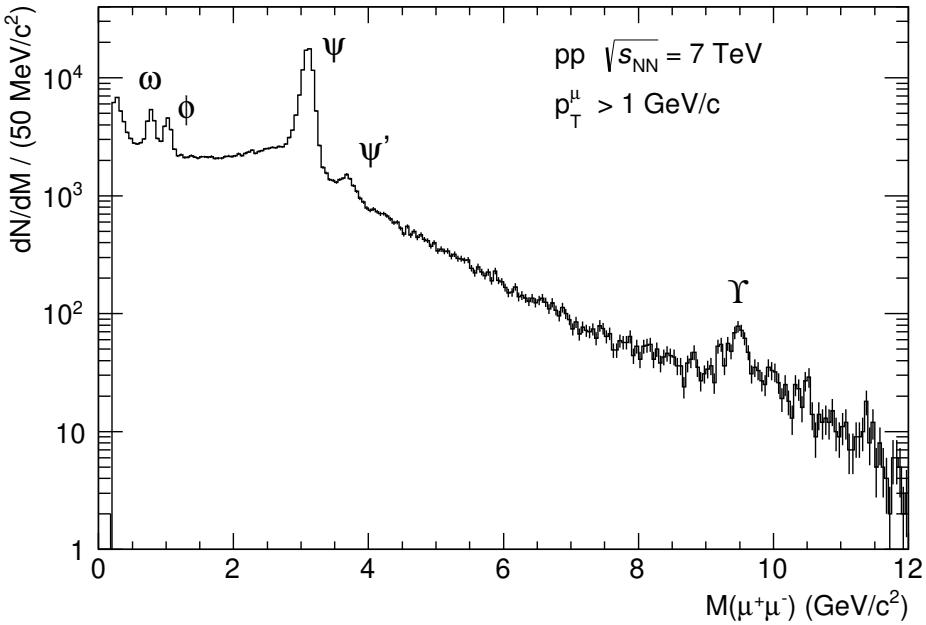

Figure 4.1: Invariant mass distribution of dimuon pairs measured by the ALICE muon spectrometer for $2.5 < y < 4$ for pp collisions at $\sqrt{s} = 7$ TeV. Figure from [212].

TeV[1]. The extended CB2 function and the NA60 function have four and eight parameters, respectively, to describe the left and right signal tails. For the signal extractions in pp collisions at $\sqrt{s} = 5.02$ TeV, the fits cannot converge if all the parameters of the functions are left free. Therefore the tail parameters of the J/ψ signal functions are fixed to the tail values obtained with the high-statistics pp data sample (CB2 function) or in MC simulations (CB2 and NA60 functions). The left panel of Figure 4.2 shows an example of the tail parameter extraction for the extended CB2 function by using a MC simulation production which uses the Geant4 transport code [213]. In total, three sets of tails are considered:

- tails extracted by fitting the hadronic J/ψ MC production with the Geant4 simulation [213] (CB2 and NA60 functions),
- tails extracted by fitting the hadronic J/ψ MC production with the Geant3 simulation [214] (CB2 and NA60 functions),
- tails extracted by fitting the hadronic J/ψ production in the pp data analysis at $\sqrt{s} = 13$ TeV [125] (CB function only [2]).

[1]The ratio of ψ(2S) to J/ψ width was also varied from 1.01 to 1.05. This variation corresponds to the difference between the ratio obtained from MC simulations at $\sqrt{s} = 13$ TeV and from a fit of the $\sqrt{s}$ =13 TeV data in which the ψ(2S) width is left free. The number of J/ψ was found to vary at the permil level on the integrated $p_{\rm T}$ / y spectra, while varying the width ratio. This effect was therefore neglected in the systematic uncertainty evaluation.

[2]The NA60 fit does not converge with all the parameters being free.

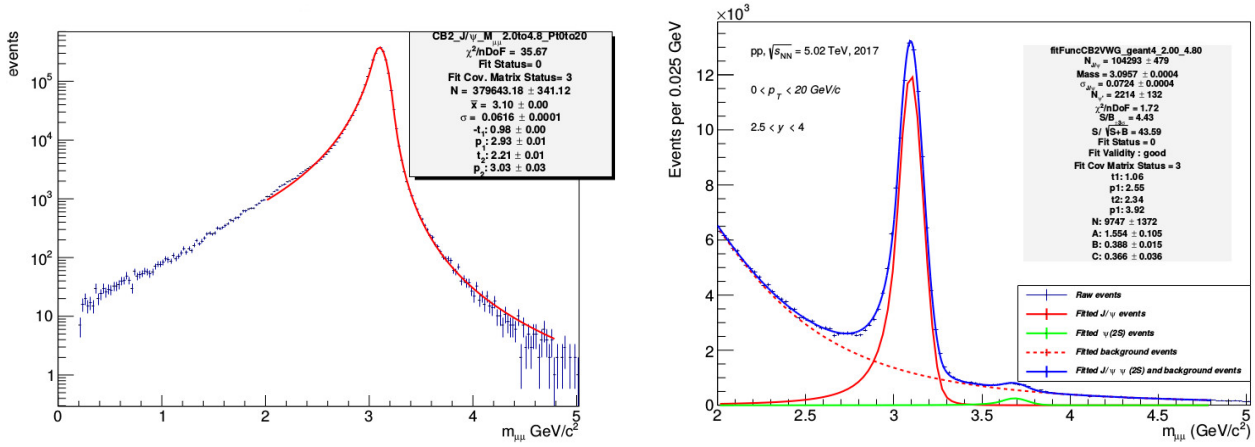

Figure 4.2: Left: example of extraction of the extended CB2 function tail parameters by using Geant4 MC simulation in the J/ψ mass region, for $p_{\mathrm{T}} < 20$ GeV/c and $2.5 < y < 4$. Right: Example of fit performed on the opposite-sign dimuon invariant mass spectrum for $0 \leq p_{\mathrm{T}} < 20$ GeV/c and $2.5 < y < 4$. The fit result in blue is the global fitting describing the J/ψ and ψ(2S) signals as well as the background. The red dashed line represents the background only. The solid red and the green lines are the J/ψ and ψ(2S) signals, respectively. The upper insert shows the values of the fitting results.

The following background functions are used to fit the mass spectra:

- a variable width Gaussian (VWG),
- a ratio of a first order polynomial over a second order polynomial (POL1/POL2).

The function descriptions and their formulae can be found in Appendix B. Then, two fitting ranges in invariant mass are considered for the global fitting:

- $2 < m_{\mu^+\mu^-} < 4.8$ GeV/c^2,
- $2.2 < m_{\mu^+\mu^-} < 4.4$ GeV/c^2.

In order to judge the goodness of the fits, several variables can be considered. A χ^2/ndf of 1 indicates that the fit describes well the data distribution. In this analysis, we accept a fit if $\chi^2/ndf < 3$. We also check that the fit has converged and that the fit parameter covariance is accurately determined. The right panel of Figure 4.2 shows an example of the invariant mass spectrum fit integrated over p_{T} and y. The global fit function contains two extended CB functions (using Geant4 tail parameters) to describe the J/ψ as well as ψ(2S) signals and a VWG function to describe the background. The fit is performed over $2 < m_{\mu^+\mu^-} < 4.8$ GeV/c^2. This fit fulfills the above criteria. The global fit in blue shows a good description of the charmonium signals and of the background shape. The numbers of J/ψ and ψ(2S) are obtained from the integrals of the signal functions in red and green. S/B$_{\pm 3\sigma}$ and S/$\sqrt{S+B}$ are the signal over background ratio and the significance, respectively, determined in a 3σ interval from the mean values. In total, 20 fit tests are performed for the signal systematic study for each p_{T} / y bin. The combination of tests

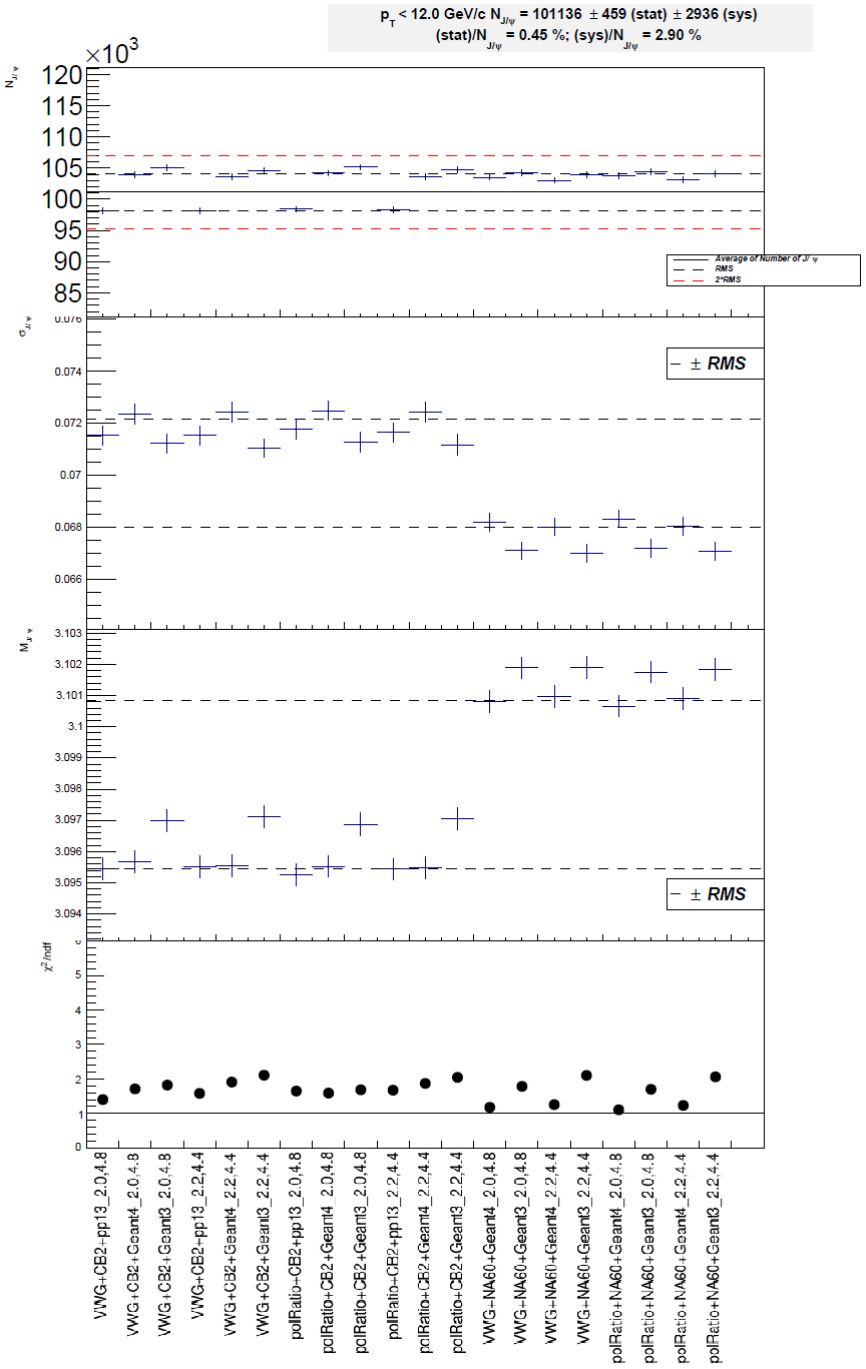

Figure 4.3: Raw number of J/ψ, the J/ψ mass, the J/ψ width and the χ^2/ndf of the fits as a function of the various tests for $0 \leq p_{\mathrm{T}} < 12$ GeV/c. The black solid line in the upper plot is the average number of J/ψ over the tests, while the black and red dashed lines correspond to $\pm$ one and two RMS of the average number of J/ψ, respectively. The black dashed line in the two middle plots correspond to the mean values of the J/ψ width and mass $\pm$ one RMS.

includes the two different background functions, the two different fitting ranges, the two sets of tail parameters from MC for both CB and NA60 functions, and one set extracted from the data for the extended CB function. Figure 4.3 shows an example of the raw number of J/ψ, the J/ψ mass, the J/ψ width and the χ^2/ndf of the fits as a function

of the fit tests for $0 \leq p_{\rm T} < 12$ GeV/c. The systematic study has been performed as well for 16 $p_{\rm T}$ and 7 rapidity bins. In each $p_{\rm T}$ / y bin, the average number of J/ψ, $< N_{J/\psi} >$, is calculated as the weighted mean of all the tests as follows:

$$< N_{J/\psi} >= \frac{\sum_{i=0}^{N_{test}} \omega^i N^i_{J/\psi}}{\sum_{i=0}^{N_{test}} \omega^i}, \tag{4.3}$$

where $N^i_{J/\psi}$ is the raw number of J/ψ extracted from the fit test i, ω^i is the weight and N_{test} is the total number of tests. The weights are used to balance the fact that there are more fits performed with tails from MonteCarlo (MC) than tails from data, since the tail variation is one of the dominant source of systematic uncertainty. The combined statistical uncertainty on the average number of J/ψ, $\sigma^{stat}_{N_{J/\psi}}$, is calculated as the linear weighted average of the statistical uncertainties of all the tests:

$$\sigma^{stat}_{N_{J/\psi}} = \frac{\sum_{i=0}^{N_{test}} \omega^i \sigma^{i,stat}_{N_{J/\psi}}}{\sum_{i=0}^{N_{test}} \omega^i}, \tag{4.4}$$

where $\sigma^{i,stat}_{N_{J/\psi}}$ is the statistical uncertainty on the raw number of J/ψ for the fitting test i. The systematic uncertainty on signal extraction, $\sigma^{syst}_{N_{J/\psi}}$, is defined as the Root Mean Square (RMS) of the raw number of J/ψ:

$$\sigma^{syst}_{N_{J/\psi}} = \sqrt{\frac{\sum_{i=0}^{Ntest} \omega^i N^{2,i}_{J/\psi}}{\sum_{i=0}^{Ntest} \omega^i} - \left(\frac{\sum_{i=0}^{Ntest} \omega^i N^i_{J/\psi}}{\sum_{i=0}^{Ntest} \omega^i} \right)^2} \tag{4.5}$$

The uncertainty on the J/ψ signal extraction varies from 1.9% to 4.4% in the different $p_{\rm T}$ and rapidity bins. The detailed values of the number of J/ψ and associated statistical and systematic uncertainties can be found in Table 4.2, 4.3, 4.4, 4.5, 4.6, 4.7, 4.8, and 4.9 for the various $p_{\rm T}$ and y intervals.

4.1.4 Acceptance efficiency

The J/ψ detection is affected by the acceptance and efficiency ($A \times \epsilon$) of the detector during the data taking. To properly estimate the correction to apply, MonteCarlo (MC) simulations are used. The same Geant3 MC simulations as the ones used for the extraction of the tail parameters are used. Note that for the calculation of the $A \times \epsilon$, the J/ψ production is assumed to be unpolarised. For more details about quarkonium polarisation, one can refer to section 2.3.4. The ALICE offline framework provides an event generator that generates the J/ψ kinematics according to input $p_{\rm T}$ and rapidity distributions which are expressed as:

$$\frac{dN}{dp_{\rm T}} = \frac{p_{\rm T}}{\left[1 + \alpha \times (\frac{p_{\rm T}}{k_{p_{\rm T}0}})^2\right]^{k_{xn}}}, \tag{4.6}$$

p_{T} (GeV/c)	$< N_{\mathrm{raw}}^{J/\psi} >$ ± stat. (%) ± syst. (%)
0–0.3	1731 ± 59 (3.4) ± 77 (4.4)
0.3–1	14788 ± 186 (1.3) ± 574 (3.9)
1–2	29693 ± 262 (0.9) ± 927 (3.1)
2–3	22189 ± 215 (1.0) ± 591 (2.7)
3–4	13985 ± 165 (1.2) ± 367 (2.6)
4–5	8110 ± 120 (1.5) ± 207 (2.6)
5–6	4711 ± 87 (1.8) ± 111 (2.4)
6–7	2730 ± 67 (2.5) ± 61 (2.2)
7–8	1479 ± 50 (3.4) ± 37 (2.5)
8–9	841 ± 37 (4.4) ± 16 (1.9)
9–10	510 ± 30 (5.9) ± 12 (2.4)
10–11	294 ± 21 (7.1) ± 6 (2.0)
11–12	183 ± 19 (10.4) ± 8 (4.4)
12–15	261 ± 21 (8.0) ± 6 (2.3)
15–20	82 ± 12 (14.6) ± 2 (2.4)
4–12	18908 ± 186 (0.98) ± 526 (2.8)
0–12	101136 ± 459 (0.5) ± 2936 (2.9)
0–20	101285 ± 452 (0.4) ± 3012 (3.0)

Table 4.2: Raw number of J/ψ in $\mathrm{p_T}$ intervals for $2.5 < y < 4$.

y	$< N_{\mathrm{raw}}^{J/\psi} >$ ± stat. (%) ± syst. (%)
2.5 – 2.75	6831 ± 124 (1.8) ± 301 (4.4)
2.75 – 3	21505 ± 207 (1.0) ± 646 (3.0)
3 – 3.25	27234 ± 225 (0.8) ± 740 (2.7)
3.25 – 3.5	23857 ± 207 (0.9) ± 504 (2.1)
3.5 – 3.75	16596 ± 169 (1.0) ± 381 (2.3)
3.75 – 4	5480 ± 99 (1.8) ± 177 (3.2)
2.5–4	102135 ± 436 (0.4) ± 2856 (2.8)

Table 4.3: Raw number of J/ψ in y intervals for $0 \leq p_{\mathrm{T}} < 12$ GeV/c.

$2.5 < y < 2.75$	$< N_{\mathrm{raw}}^{J/\psi} >$ ± stat. (%) ± syst. (%)
0.3 – 2 GeV/c	2604 ± 82 (3.1) ± 34 (1.3)
2 – 4 GeV/c	2620 ± 72 (2.7) ± 104 (4.0)
4 – 6 GeV/c	1117 ± 47 (4.2) ± 22 (2.0)
6 – 12 GeV/c	624 ± 31 (5.0) ± 27 (4.3)

Table 4.4: Raw number of J/ψ in p_{T} intervals for $2.5 < y < 2.75$.

$2.75 \leq y < 3$	$< N_{\mathrm{raw}}^{J/\psi} >$ ± stat. (%) ± syst. (%)
0.3 – 2 GeV/c	9069 ± 150 (1.7) ± 251 (2.8)
2 – 4 GeV/c	7974 ± 127 (1.6) ± 113 (1.4)
4 – 6 GeV/c	3005 ± 70 (2.3) ± 30 (1.0)
6 – 12 GeV/c	1563 ± 45 (2.9) ± 31 (2.0)

Table 4.5: Raw number of J/ψ in p_{T} intervals for $2.75 \leq y < 3$.

$3 \leq y < 3.25$	$< N_{\rm raw}^{J/\psi} >$ ± stat. (%) ± syst. (%)
0.3 – 2 GeV/c	12219 ± 169 (1.4) ± 339 (2.8)
2 – 4 GeV/c	9581 ± 135 (1.4) ± 276 (2.9)
4 – 6 GeV/c	3567 ± 74 (2.1) ± 44 (1.2)
6 – 12 GeV/c	1586 ± 46 (2.9) ± 14 (0.9)

Table 4.6: Raw number of J/ψ in $p_{\rm T}$ intervals for $3 \leq y < 3.25$.

$3.25 \leq y < 3.5$	$< N_{\rm raw}^{J/\psi} >$ ± stat. (%) ± syst. (%)
0.3 – 2 GeV/c	11273 ± 145 (1.3)± 107 (0.9)
2 – 4 GeV/c	8417 ± 132 (1.6) ± 89 (1.1)
4 – 6 GeV/c	2976 ± 70 (2.4) ± 28 (0.9)
6 – 12 GeV/c	1257 ± 44 (3.5) ± 19 (1.5)

Table 4.7: Raw number of J/ψ in $p_{\rm T}$ intervals for $3.25 \leq y < 3.5$.

$3.5 \leq y < 3.75$	$< N_{\rm raw}^{J/\psi} >$ ± stat. (%) ± syst. (%)
0.3 – 2 GeV/c	7913 ± 113 (1.4) ± 63 (0.8)
2 – 4 GeV/c	5984 ± 112 (1.9) ± 68 (1.1)
4 – 6 GeV/c	1877 ± 56 (3.0) ± 19 (1.0)
6 – 12 GeV/c	857 ± 34 (4.0) ± 16 (1.9)

Table 4.8: Raw number of J/ψ in $p_{\rm T}$ intervals for $3.5 \leq y < 3.75$.

$3.75 \leq y < 4$	$< N_{\rm raw}^{J/\psi} >$ ± stat. (%) ± syst. (%)
0.3 – 2 GeV/c	2451 ± 62 (2.5) ± 73 (3.0)
2 – 4 GeV/c	2176 ± 68 (3.1) ± 61 (2.8)
4 – 6 GeV/c	610 ± 32 (5.2) ± 7 (1.1)
6 – 12 GeV/c	249 ± 19 (7.6) ± 6 (2.4)

Table 4.9: Raw number of J/ψ in $p_{\rm T}$ intervals for $3.75 \leq y < 4$.

where $\alpha = 0.363$, k_{xn}=3.9 and $k_{p_{\rm T0}} = 1.04 \times E^{0.101}$ with E being the collision energy. And the rapidity distribution of the input function in the J/ψ event generator is:

$$\frac{dN}{dy} = exp\left[-\frac{x^2}{0.4 \times 0.4 \times 2}\right], \tag{4.7}$$

where $x = \frac{y}{log(E/3.097)}$ with E being the collision energy. Eq. 4.7 is valid only if $x \leq 1$. The parameters in both Eq. 4.6 and 4.7 were obtained by fitting the data from RHIC, CDF and LHC [215]. The J/ψ particle then decays to dimuons using EVTGEN [216]. The dimuons are then fed in the transport code (Geant3) which encodes the geometry and materials of the detectors. The muon particles travel through the detector and encounter different physics processes. Finally, the particles that hit the detectors are reconstructed. The MC productions are performed on a run by run basis to mimic the same detector conditions versus time as in data. In the MC, the same QA-checked runs as in Table 4.1 are analyzed. Events from the MULU trigger[3] are used. The background events induced by the gas do not exist in the MC simulation so the PS is not applied. The same track selections as described in section 4.1.2 are used to select the reconstructed muon tracks and dimuons in the MC simulation. The generated J/ψ are within $2.5 < y < 4$ and $p_{\rm T} < 20$ GeV/c. Additionally, for the generated J/ψ, the PDG [18] code should be equal to the J/ψ one. For the reconstructed J/ψ, the muons' mother should have the same MC label as the generated J/ψ. Then one can extract the number of generated and reconstructed J/ψ.

The $A \times \epsilon$ is calculated in a given $p_{\rm T}$ or y bin as:

$$A \times \epsilon = \frac{N_{\rm rec}(p_{\rm T}^{\rm rec},\ y^{\rm rec})}{N_{\rm gen}(p_{\rm T}^{\rm gen},\ y^{\rm gen})}, \tag{4.8}$$

where $N_{\rm gen}$ is the number of generated J/ψ and $N_{\rm rec}$ is the number of reconstructed J/ψ which fulfill the track selections described in section 4.1.1. $p_{\rm T}^{\rm rec}$ and $y^{\rm rec}$ ($p_{\rm T}^{\rm gen}$ and $y^{\rm gen}$) are the transverse momentum and rapidity, respectively, of reconstructed (generated) J/ψ. Furthermore, the acceptance and efficiency is defined run per run since the detector efficiency varies depending on the data-taking time. Therefore, the $A \times \epsilon$ must be calculated on a run-by-run basis. In order to compute the $A \times \epsilon$ integrated over runs, a weight is applied to the single-run $A \times \epsilon$. This weight is proportional to the number of CMUL7 triggered events analysed per run. Figure 4.4 shows the $A \times \epsilon_0$ as a function of the run numbers for the 2017 pp data in the range $2.5 < y < 4$ and $0 \leq p_{\rm T} < 20$ GeV/c. The $A \times \epsilon_0$ is stable for most of the runs but it decreases because of inefficiencies in the tracking chambers at the end of the data taking period[4]. The $A \times \epsilon$ calculated with the original MC input functions from Eqs. 4.6 and 4.7 is labeled as $A \times \epsilon_0$.

In order to obtain the most realistic input MC distributions, an iterative procedure is implemented to tune the

[3]MULU is an emulated trigger in the MC simulation, which is fired by opposite-sign dimuon events.

[4]According to muon QA, there are many HV trips in the end of the 2017 pp period. The HV trips appear after an increasing current in the high-voltage power supply. After investigation, it was understood that this high current was due to default in the tracking chamber (the main issue was the presence of very thin layer of glue on pads). During LS2, we consolidated the detector to ensure a better stability of the detector and its efficiency during data taking.

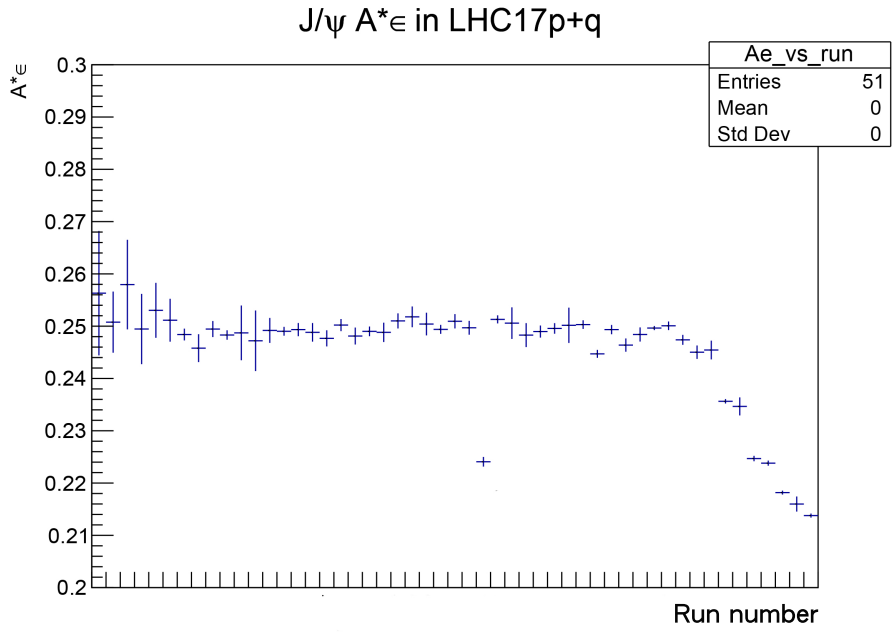

Figure 4.4: $A \times \epsilon_0$ (where the subscript refers to the original MC input functions) as a function of runs for the 2017 pp data and for $2.5 < y < 4$ and $0 \leq p_{\mathrm{T}} < 20$ GeV/c.

original input shapes to the raw J/ψ corrected distributions. The corrected J/ψ yield, $N_{J/\psi}/(A \times \epsilon_0)$ as a function of p_{T} is fitted by:

$$f^{\mathrm{corr.}}(p_{\mathrm{T}}) = p_0 \times \frac{p_{\mathrm{T}}}{\left[1 + \left(\frac{p_{\mathrm{T}}}{p_1}\right)^{p_2}\right]^{p_3}}, \tag{4.9}$$

and as a function of rapidity by the following function:

$$f^{\mathrm{corr.}}(y) = p_4 \times \exp^{-0.5\left(\frac{y}{p_5}\right)^2}, \tag{4.10}$$

where p_0, p_1, p_2, p_3, p_4 and p_5 are free parameters. The resulted fit functions $f^{\mathrm{corr.}}(p_{\mathrm{T}})$ and $f^{\mathrm{corr.}}(y)$ along with the original input shapes are used to compute a weight for each J/ψ candidate in the MC at the generated and reconstructed levels. The weight can be calculated as follows:

$$w_n(p_{\mathrm{T}}^{\mathrm{gen}}, y^{\mathrm{gen}}) = w_n(p_{\mathrm{T}}^{\mathrm{gen}}) \times w_n(y^{\mathrm{gen}}) \tag{4.11}$$

where

$$w_n(p_{\mathrm{T}}^{\mathrm{gen}}) = \frac{f_{n-1}^{\mathrm{corr.}}(p_{\mathrm{T}}^{\mathrm{gen}})}{f_{n-1}^{\mathrm{MC}}(p_{\mathrm{T}}^{\mathrm{gen}})}, \tag{4.12}$$

and

$$w_n(y^{\mathrm{gen}}) = \frac{f_{n-1}^{\mathrm{corr.}}(y^{\mathrm{gen}})}{f_{n-1}^{\mathrm{MC}}(y^{\mathrm{gen}})}, \tag{4.13}$$

where $f_i^{\text{corr.}}$ and f_i^{MC} are the functions fitted to the data corrected yield and the generated MC, at the n^{th} iteration step, respectively. The detector acceptance and efficiency $A \times \epsilon_n$ is recomputed with the weighted MC distributions at each iteration step n. The above procedure is repeated using the new $A \times \epsilon_n$ until the weighted input shapes match within uncertainties with the J/ψ yield corrected by $A \times \epsilon_n$. The procedure has therefore converged.

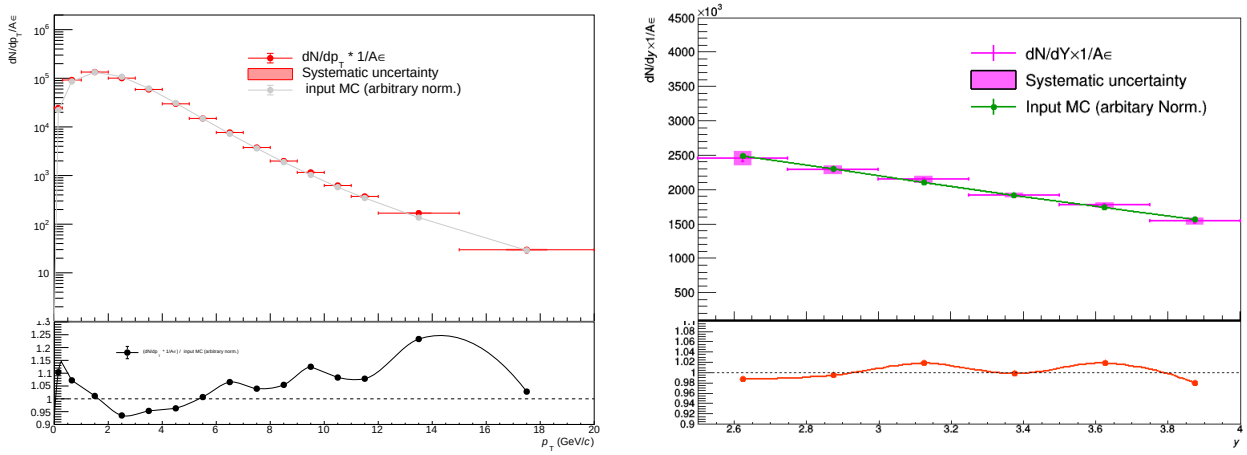

Figure 4.5: Top panel: J/ψ differential $A \times \epsilon_0$ corrected distribution as a function of p_{T} for $2.5 < y < 4$ (left) and as a function of rapidity for $0 \leq p_{\text{T}} < 12$ GeV/c (right). The corrected distributions are compared to the MC generated distribution shapes, before the iterative procedure. The vertical error bar is the statistical uncertainty. The systematic uncertainty (box) is from the signal extraction. Bottom panel: ratio of the data corrected yield over the original MC input shape.

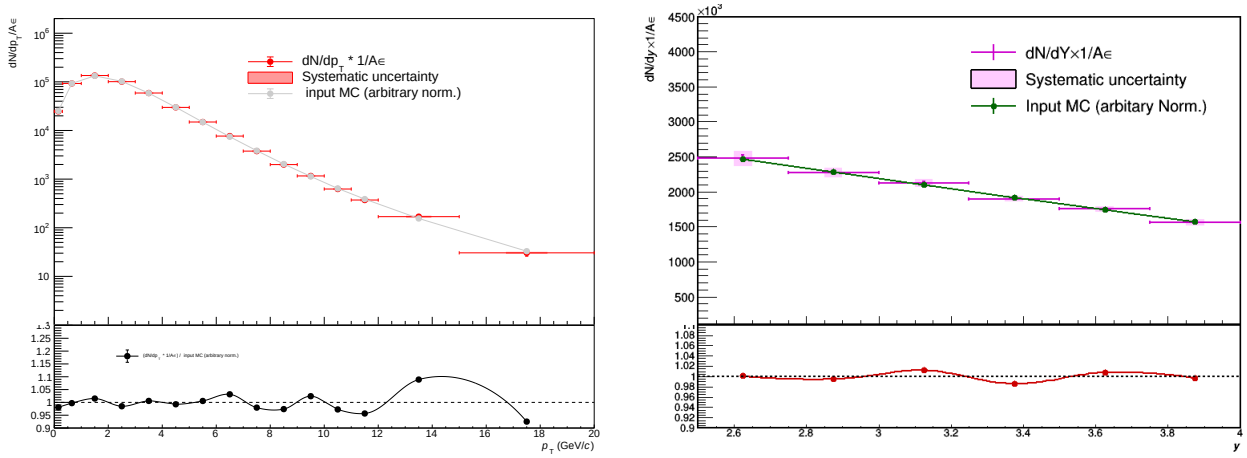

Figure 4.6: Top panel: J/ψ differential $A \times \epsilon$ corrected distribution as a function of p_{T} for $2.5 < y < 4$ (left) and as a function of rapidity for $0 \leq p_{\text{T}} < 12$ GeV/c (right). The corrected distributions are compared to the MC generated distribution shapes. The vertical error bar is the statistical uncertainty. The systematic uncertainty (box) is from the signal extraction. Bottom panel: ratio of the data corrected yield over the original MC input shape.

In this study, two iterations are performed and a convergence is already obtained after one step. Figure 4.5 and 4.6 show the J/ψ differential $A \times \epsilon$ corrected distributions as a function of p_{T} (left), and rapidity (right) before and

at the end of the iterative procedure, respectively. The ratios of the corrected J/ψ yield to the original input MC are also shown at the bottom of each plot. Before the iterative procedure, the disagreement between the generated and corrected shapes is beyond 20% at high p_{T}. At the end of the iterative procedure, the agreement between the shapes is at the few percent level in most of the p_{T} and rapidity bins.

p_{T} (GeV/c)	$A \times \epsilon \pm$ stat. (%)
0–12	0.2368 ± 0.0001 (0.04)
0–20	0.2372 ± 0.0001 (0.04)

Table 4.10: J/ψ $A \times \epsilon$ integrated over a given p_{T} range and for $2.5 < y < 4$.

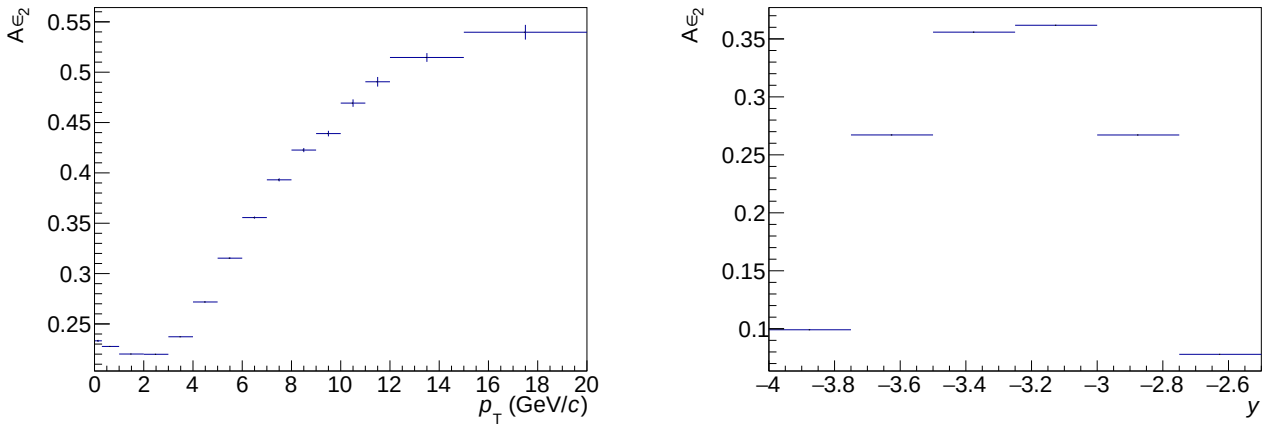

Figure 4.7: J/ψ $A \times \epsilon$ as a function of p_{T} (left) and rapidity (right) in 2017 pp collisions at $\sqrt{s} = 5.02$ TeV.

Table 4.10 shows the $A \times \epsilon$ after the iterative procedure for $0 \leq p_{\mathrm{T}} < 12$ GeV/c and $0 \leq p_{\mathrm{T}} < 20$ GeV/c at forward rapidity. Figure 4.7 and 4.8 show the p_{T} dependence, the y dependence and the p_{T} / y dependence of the $A \times \epsilon$. The $A \times \epsilon$ reaches a minimum value for $1 < p_{\mathrm{T}} < 3$ GeV/c where the J/ψ p_{T} close to the J/ψ mass. In this p_{T} region, the decay muons of the J/ψ carry rather low transverse momentum and are more sensitive to trigger inefficiencies. Therefore there is a higher probability of not detecting one (or both) muons from the J/ψ decay. The $A \times \epsilon$ rises for $p_{\mathrm{T}} > 3$ GeV/c with increasing p_{T}. At the edges of rapidity, the $A \times \epsilon$ decreases because it can happen that one of the muons falls outside of the detector acceptance. A similar trend is found in the double-differential bins. The $A \times \epsilon$ values as a function of p_{T} or y, and in double differential bins are given in Table 4.11, and 4.12, respectively. The estimation of the systematic uncertainty on the input MC will be discussed in section 4.1.6.

p_{T} (GeV/c)	$A \times \epsilon \pm$ stat. (%)
0–0.3	0.2332 ± 0.0009 (0.4)
0.3–1	0.2276 ± 0.0003 (0.1)
0–1	0.2293 ± 0.0005 (0.2)
1–2	0.2201 ± 0.0002 (0.1)
2–3	0.2199 ± 0.0002 (0.1)
3–4	0.2372 ± 0.0003 (0.1)
4–5	0.2718 ± 0.0005 (0.2)
5–6	0.3153 ± 0.0007 (0.2)
6–7	0.3556 ± 0.0010 (0.3)
7–8	0.3931 ± 0.0015 (0.4)
8–9	0.4227 ± 0.0021 (0.5)
9–10	0.4390 ± 0.0028 (0.6)
10–11	0.4693 ± 0.0037 (0.8)
11–12	0.4905 ± 0.0048 (1.0)
10–12	0.4799 ± 0.0043 (0.9)
12–15	0.5146 ± 0.0044 (0.9)
15–20	0.5397 ± 0.0073 (1.4)

y	$A \times \epsilon \pm$ stat.(%)
2.5 – 2.75	0.0780 ± 0.0002 (0.3)
2.75 – 3	0.2671 ± 0.0003 (0.1)
3 – 3.25	0.3618 ± 0.0003 (0.1)
3.25 – 3.5	0.3558 ± 0.0003 (0.1)
3.5 – 3.75	0.2672 ± 0.0003 (0.1)
3.75 – 4	0.0991 ± 0.0002 (0.2)

Table 4.11: Left: J/ψ $A \times \epsilon$ as a function of p_{T} for $2.5 < y < 4$. The statistical uncertainties from the MC statistics are shown. Right: J/ψ $A \times \epsilon$ as a function of y for $0 \leq p_{\mathrm{T}} < 12$ GeV/c.

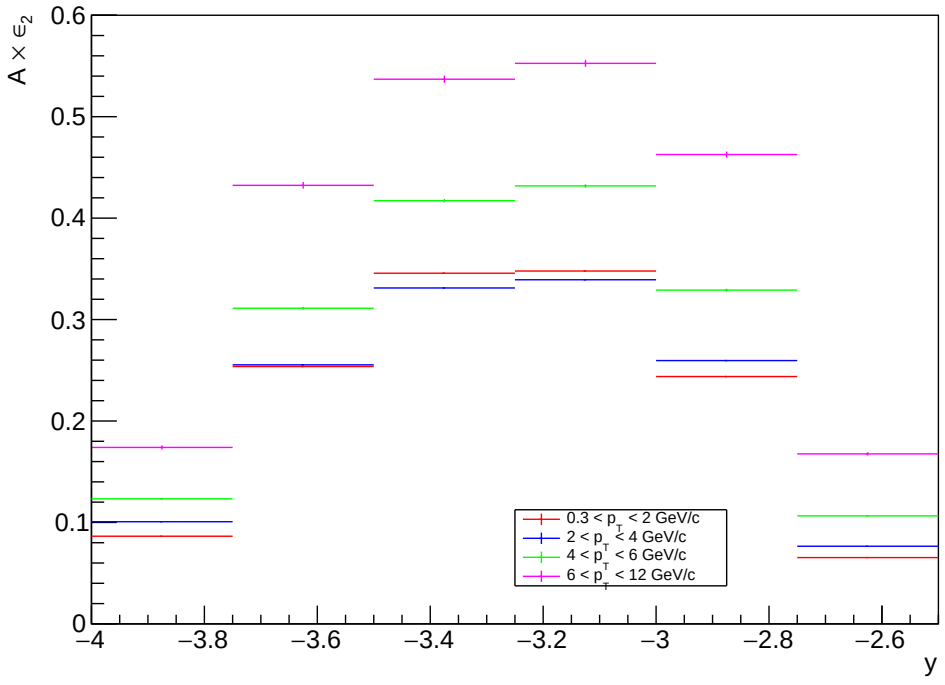

Figure 4.8: J/ψ $A \times \epsilon$ as a function of rapidity in four p_{T} intervals in 2017 pp collisions at $\sqrt{s} = 5.02$ TeV.

4.1.5 Integrated luminosity

The J/ψ raw yield is obtained from dimuon triggered events (CMUL7). In order to evaluate the yield per MB events, it is essential to evaluate the normalisation factor F_{norm}.

	$A \times \epsilon \pm$ stat. (%)			
y	$0.3 \leq p_{\rm T} < 2$ GeV/c	$2 \leq p_{\rm T} < 4$ GeV/c	$4 \leq p_{\rm T} < 6$ GeV/c	$6 \leq p_{\rm T} < 12$ GeV/c
2.5 – 2.75	0.0653 ± 0.0002 (0.3)	0.0765 ± 0.0003 (0.4)	0.1065 ± 0.0006 (0.6)	0.1676 ± 0.0012 (0.7)
2.75 – 3.	0.2438 ± 0.0004 (0.2)	0.2596 ± 0.0005 (0.2)	0.3290 ± 0.0010 (0.3)	0.4627 ± 0.0017 (0.4)
3. – 3.25	0.3479 ± 0.0005 (0.1)	0.3392 ± 0.0005 (0.1)	0.4318 ± 0.0011 (0.3)	0.5526 ± 0.0018 (0.3)
3.25 – 3.5	0.3457 ± 0.0005 (0.1)	0.3311 ± 0.0006 (0.2)	0.4172 ± 0.0011 (0.3)	0.5369 ± 0.0019 (0.4)
3.5 – 3.75	0.2537 ± 0.0005 (0.2)	0.2554 ± 0.0005 (0.2)	0.3112 ± 0.0011 (0.4)	0.4323 ± 0.0020 (0.5)
3.75 – 4	0.0864 ± 0.0003 (0.3)	0.1007 ± 0.0004 (0.4)	0.1233 ± 0.0008 (0.6)	0.1739 ± 0.0016 (0.9)

Table 4.12: J/ψ $A \times \epsilon$ as a function of y in four different $p_{\rm T}$ bins. The statistical uncertainties from the MC are shown.

There are two methods, described below, to compute the normalisation factor on a run-by-run basis by using the T0 and V0 detectors that serves as MB triggers, described below. The method which uses the V0 trigger is considered as a cross-check of the other method. The two methods take into account a pile-up correction factor, PU, since pile-up events, which contain at least two independent interactions in the same proton bunch collision, can present. The PU factor is defined for each run i as:

$$PU^i = \frac{\mu^i}{1 - e^{-\mu^i}}. \tag{4.14}$$

μ^i is defined as:

$$\mu^i = -\ln\left(1 - \frac{F^{\rm MB,i}_{\rm purity} \times L0b^i_{\rm MB}}{D^i \times N^i_{\rm colliding} \times f_{\rm LHC}}\right), \tag{4.15}$$

where:

- $F^{MB,i}_{\rm purity}$ is the purity factor of the considered MB trigger which is either a V0 or a T0 trigger,
- $L0b^i_{\rm MB}$ is the MB trigger scaler of the level 0 before the CTP decision,
- D^i is the run duration,
- $N^i_{\rm colliding}$ is the number of colliding bunches,
- $f_{\rm LHC} = 11245$ Hz is the revolution frequency of the LHC.

The purity factor for a given trigger is defined as the ratio of the number of physics selected events to the total number of events recorded with that trigger:

$$F^{trigger,i}_{\rm purity} = \frac{N^i_{trigger,\rm PS}}{N^i_{trigger,\rm ALL}} \tag{4.16}$$

The purity factors for CINT7 (V0) and CMUL7 can be computed because those triggers are not reconstructed. However, the purity factor for the C0TVX (T0) trigger cannot be estimated since this triggered events are not reconstructed in all the runs. The purity factor is taken to be 100% for C0TVX trigger. This assumption is verified in

the few runs in which this trigger is reconstructed. This verification will be discussed in this section later.

First method to compute $F_{\mathbf{norm}}$: the offline method. It uses the offline counters from reconstructed data. The V0 triggered events are used in this method. The normalisation factor $F_{\rm norm}^{\rm offline,i}$ in a given run, i, is computed by using the following formula:

$$F_{\rm norm}^{\rm offline1,i} = PU^i \times \frac{MB^i}{MB\&0MUL^i} \tag{4.17}$$

where:

- MB is the number of physics selected MB events,
- $MB\&0MUL$ is the subsample of the MB events in which the $0MUL$ trigger input is also fired,
- PU is the pile-up correction factor for MB triggerred events as given by Eq. 4.14.

However, this normalisation factor has a large statistical uncertainty since the MB trigger is heavily downscaled, so an intermediate trigger with a higher rate than CMUL7 is used to improve the statistical precision. That intermediate trigger is the CMSL trigger. As a result, Eq. 4.17 becomes:

$$F_{\rm norm}^{\rm offline2,i} = PU^i \times \frac{MB^i}{MB\&0MSL^i} \times \frac{MSL^i}{MSL\&0MUL^i} \tag{4.18}$$

where:

- MSL is the number of physics selected CMSL7 (CMSL7-B-NOPF-MUFAST) triggered events,
- $MB\&0MSL$ is the subsample of CINT7 (CINT7-B-NOPF-MUFAST) events in which the 0MSL trigger input is also fired,
- $MSL\&0MUL$ is the subsample of CMSL7 events in which the 0MUL trigger input is also fired.

The details of the trigger input definitions can be found in chapter 2.

Second method to compute $F_{\mathbf{norm}}$: the online/scaler method. It uses the *L0b* scalers saved in the OCDB files which contain the online information (see details in chapter 2). The T0 detector is used as a luminometer in this method. The normalisation factor $F_{\rm norm}^{scaler,i}$ is written as:

$$F_{\rm norm}^{\rm scaler,i} = PU^i \times \frac{F_{\rm purity}^{\rm MB,i} \times L0b_{\rm MB}^i}{F_{\rm purity}^{\rm CMUL7,i} \times L0b_{\rm CMUL7}^i} \tag{4.19}$$

where:

- $F^{\mathrm{MB}}_{\mathrm{purity}}$ and $F^{\mathrm{CMUL7}}_{\mathrm{purity}}$ are the purity factors for MB (C0TVX) and CMUL7 triggers, respectively,
- $L0b^{i}_{\mathrm{MB}}$ and $L0b^{i}_{\mathrm{CMUL7}}$ are the scalers of MB (C0TVX) and CMUL7 triggers, respectively.

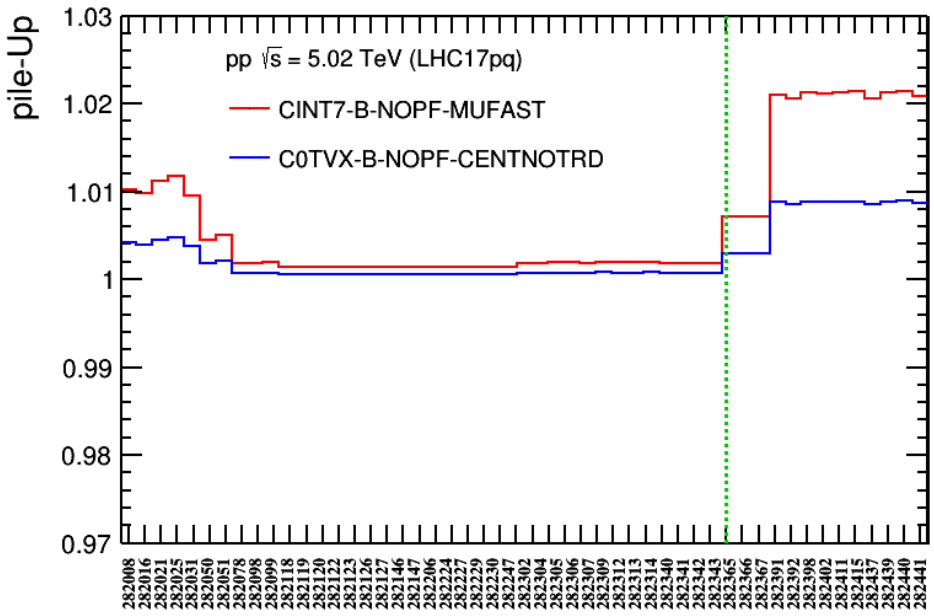

Figure 4.9: Pile-up correction factors as a function of the run number for CINT7 and C0TVX triggers for 2017 pp collisions at $\sqrt{s} = 5.02$ TeV.

The pile-up correction factors for CINT7 and C0TVX triggers as a function of the run number are shown in Figure 4.9. The pile-up factor is larger for the first five runs (small number of proton bunches with 5 kHz interaction rate), as well as for the 13 runs after the vertical dashed green line (corresponding to two fills with an interaction rate of 200 kHz for the first three runs and 600 kHz for the last ten runs, respectively).

The purity factors for CINT7 and CMUL7 triggers are computed from the reconstructed data. The left panel of Figure 4.10 shows the purity factor as a function of the run number for CINT7 and CMUL7 triggers for 2017 pp data. In the first five runs, corresponding to a low interaction rate (5 kHz CINT7), the beam-gas contribution is very small. The beam-gas contribution is larger in other runs, in particular in the last ten runs, leading to a decrease of the purity factor. The right panel of Figure 4.10 shows the purity factor as a function of run number for the C0TVX trigger in the 41 over 51 runs in which the trigger is reconstructed. The C0TVX purity factor over more than half of the 2017 pp runs is 100%. Therefore the purity factor is taken as 100% for the full 2017 pp data at $\sqrt{s} = 5.02$ TeV.

The normalisation factors for each run are computed by using the offline and the scaler methods as described above. To compare the results obtained with the two methods, the CMUL7 cross section is calculated for each run i by using:

$$\sigma^{i}_{\mathrm{CMUL7}} = \frac{\sigma_{\mathrm{VdM}}}{F^{i}_{\mathrm{norm}}} \tag{4.20}$$

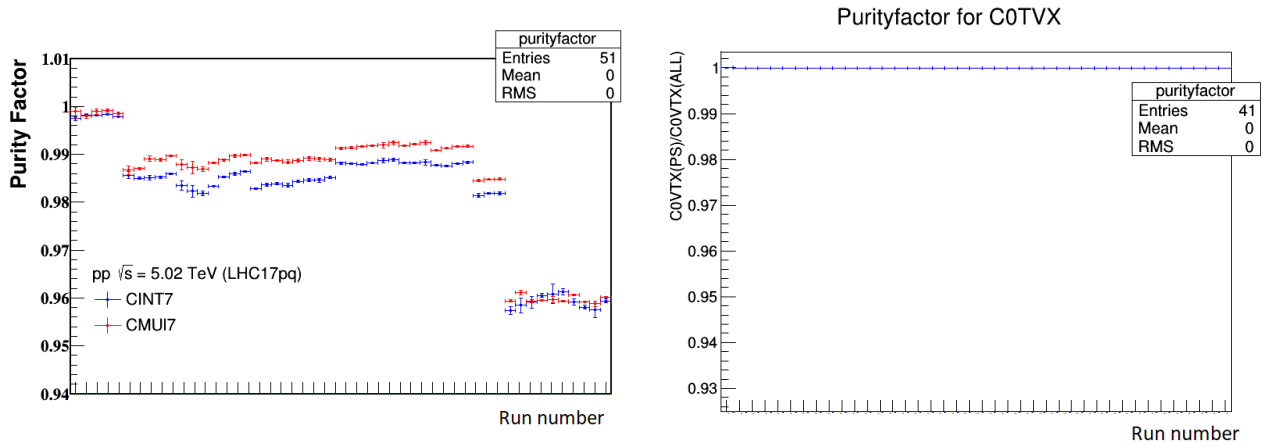

Figure 4.10: Left: purity factor as a function of the run number for CINT7 and CMUL7 triggers for 2017 pp collisions at $\sqrt{s_{\rm NN}} = 5.02$ TeV. Right: purity factor as a function of the run number for the C0TVX trigger for some runs of the 2017 pp collisions at $\sqrt{s} = 5.02$ TeV.

where $\sigma_{\rm VdM}$ is either the V0 or the T0 cross section measured with the Van der Meer scan technique [217]: $\sigma^{\rm V0}_{\rm VdM} = 50.87 \pm 0.04$ (stat) ± 1.07 (syst) mb and $\sigma^{\rm T0}_{\rm VdM} = 20.82 \pm 0.01$ (stat) ± 0.37 (syst) mb.

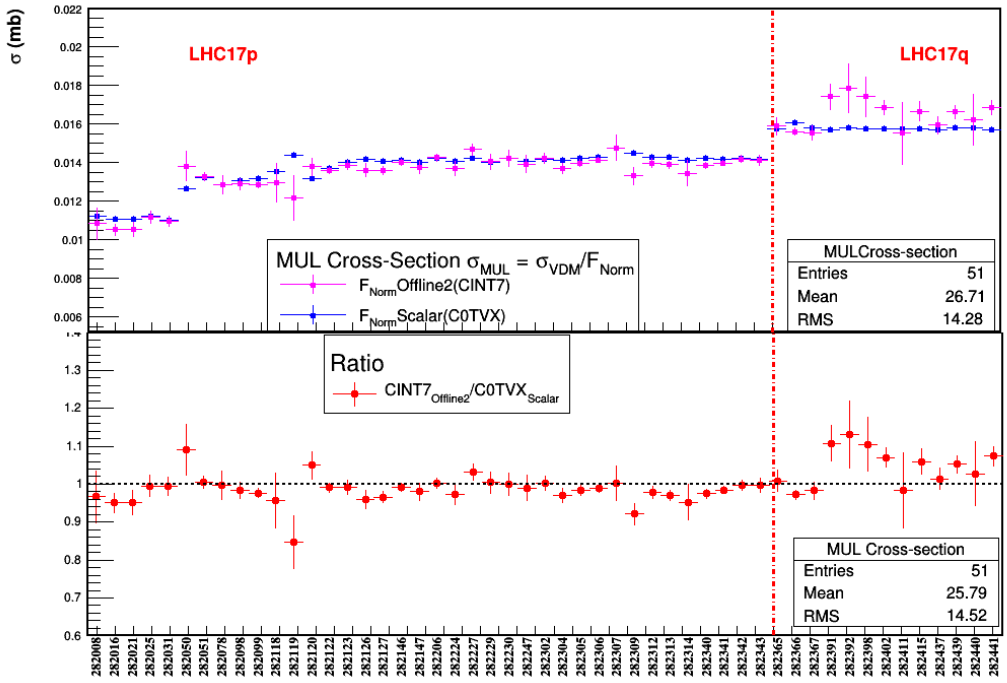

Figure 4.11: Top: CMUL7 cross sections computed by using the offline CINT7 (pink square) and the online C0TVX (blue square) methods. Bottom: ratio of the CMUL7 cross sections obtained with the two different methods.

Figure 4.11 shows the CMUL7 cross sections as a function of run number for the two methods, and the ratio of the CMUL7 cross section determined with the offline method to the one obtained with the online method as a function

of the run number. In the LHC17p period, the CMUL7 cross section increases starting from the sixth run for the two methods. The CMUL7 cross sections are overall higher in the LHC17q period than in the LHC17p one. These two steps correspond to modification in the filling scheme and/or interaction rate and such modifications could lead to an increase of the beam-gas track contribution to the CMUL7 trigger. The ratios of CMUL7 cross section obtained by the offline method to the one obtained by the scalar method is close to unity for most of runs. The scaler method gives a better precision on the normalisation factors with respect to the one obtained from the offline method. Hence, in this study the normalisation factor obtained from the scaler method are used to compute the weighted average over the runs of the normalisation factor. The weights are taken as the number of CMUL7 triggered events per run i. The average $F_{\rm norm}$ is written as:

$$F_{\rm norm} = \frac{\sum_i N^i_{\rm CMUL7,PS} \times F^i_{\rm norm}}{\sum_i N^i_{\rm CMUL7,PS}} \tag{4.21}$$

Note that the CMUL7 purity factor in Eq. 4.19 cancels out in the numerator of Eq. 4.21 which becomes:

$$F_{\rm norm} = \frac{\sum_i N^i_{\rm CMUL7,ALL} \times PU^i \times \frac{F^{\rm MB,i}_{\rm purity} \times L0b^i_{\rm MB}}{L0b^i_{\rm CMUL7}}}{\sum_i N^i_{\rm CMUL7,PS}} \tag{4.22}$$

Equation 4.22 is finally used to compute the average normalisation factor.
The integrated luminosity corresponding to our analyzed data is then calculated with:

$$L_{\rm int} = \frac{N_{\rm CMUL7,PS} \times F_{\rm norm}}{\sigma_{\rm VdM}} \tag{4.23}$$

where $N_{\rm CMUL7,PS}$ is the total number of CMUL7 events analyzed and is taken from Table 4.1, $F_{\rm norm}$ is the weighted average normalisation factor and $\sigma_{\rm VdM}$ is the T0 cross section measured with the Van der Meer scan [217]. The resulting integrated luminosity is:

$$L_{\rm int} = 1219 \pm 0 \text{ (stat.)} \pm 22 \text{ (syst.) nb}^{-1}.$$

The systematic uncertainty on the luminosity is 1.8% coming from the uncertainty on $\sigma^{\rm T0}_{\rm VdM}$.

4.1.6 Systematic uncertainties

All the systematic uncertainties in the analysis are discussed in this section. Some of the systematic uncertainties which have been described in previous sections will be shortly mentioned.

The systematic uncertainty on the branching ratio of the J/ψ dimuon decay channel amounts to 0.55% [18] and is correlated over $p_{\rm T}$ and y. The systematic uncertainty on the luminosity is 1.8% from the uncertainty on $\sigma^{\rm T0}_{\rm VdM}$

[217]. It is considered as correlated over p_{T} and/or rapidity. The systematic uncertainty on the signal extraction has been discussed in section 4.1.3. The variations of the signal tail parameters, signal functions, background functions and the fitting ranges give the systematic uncertainty with Eq. 4.5. The values for different p_{T} and rapidity bins are written in Table 4.2 and 4.3 and are all within 4.4%. The larger systematic uncertainty is obtained at the edges of the rapidity and in the high-p_{T} region.

The systematic uncertainty on the MC input parametrisation, for the determination of the $A \times \epsilon$, has two sources:

- the limited statistics of the data sample used to tune the MC input shapes.
- the correlations in p_{T} and rapidity of the MC input shapes which are not taken into account in the MC.

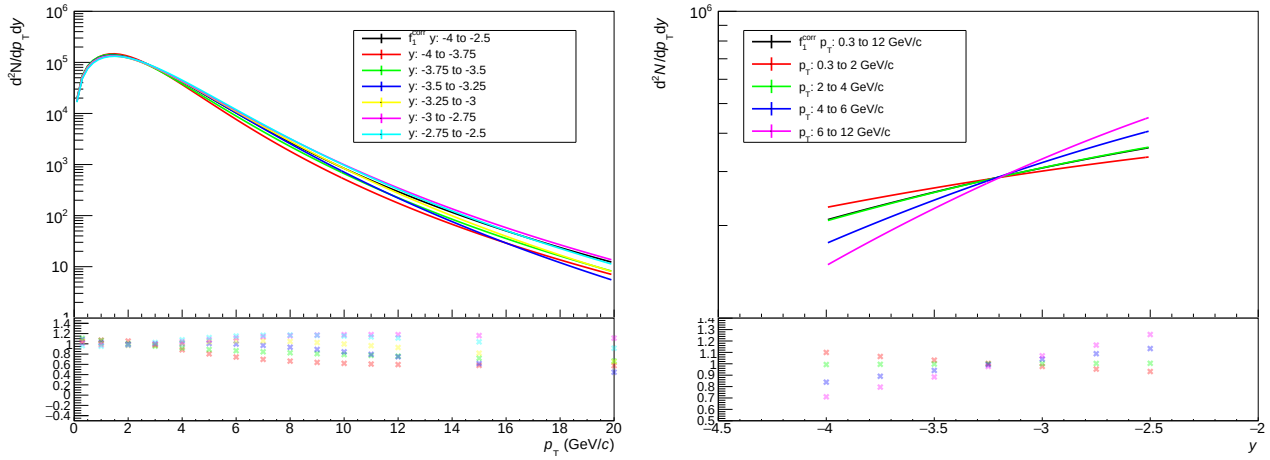

Figure 4.12: Input MC shapes used for the evaluation of the $A \times \epsilon$ systematic uncertainty as a function of p_{T} in rapidity bins (left) and as a function of rapidity in p_{T} bins (right).

The first source gives rise to a small uncertainty (< 0.1 %) according to the published result on the 2015 pp data [125] and they should be even smaller than the 2017 pp data since the luminosity is higher. Therefore, we concentrated on the second source which is related to the correlations in p_{T} and rapidity of the MC input shapes. The original input p_{T} shape is integrated over rapidity. Moreover, the original input rapidity shape is integrated over p_{T}. They neglect the correlations in p_{T} and rapidity. To study these correlations, one can extract the input shapes as a function of p_{T} in rapidity bins and as a function of rapidity in p_{T} bins, from data. Indeed, in section 4.1.4, six rapidity bins and four p_{T} bins are used in the double-differential (p_{T} / y dependence) study. All the possible shape combinations are considered to define 24 different input MC shapes by using Eq. 4.9 and 4.10. Figure 4.12 shows the input shapes as a function of p_{T} in rapidity bins and as a function of rapidity in p_{T} bins together with their ratios to the tuned p_{T} or y MC shapes. Those 24 input shapes are used to estimate a new acceptance and efficiency $A \times \epsilon^{\mathrm{corr.}}$. The systematic uncertainty is taken as the maximum relative difference between the $A \times \epsilon^{\mathrm{corr.}}$ and the $A \times \epsilon$ obtained after the iterative procedure with the tuned input shapes. Figure 4.13 shows the p_{T} and rapidity dependence of the relative differences between the $A \times \epsilon^{\mathrm{corr.}}$ and the $A \times \epsilon$. Tables 4.13 and 4.14 summarise the systematic uncertainty

on $A \times \epsilon$ in the corresponding kinematic region. The systematic uncertainty on the MC input parametrisation is uncorrelated as a function of p_{T} and rapidity.

p_{T} (GeV/c)	$\sigma_{A\times\epsilon}$ (%)
0–12	3.23
0–20	3.24

p_{T} (GeV/c)	$\sigma_{A\times\epsilon}$ (%)
0–0.3	1.94
0.3–1	1.74
0–1	2.19
1–2	1.79
2–3	1.81
3–4	1.79
4–5	1.69
5–6	1.44
6–7	1.32
7–8	1.17
8–9	1.12
9–10	0.89
10–11	0.75
11–12	0.67
10–12	1.32
12–15	0.32
15–20	1.0

y	$\sigma_{A\times\epsilon}$ (%)
2.5 – 2.75	4.93
2.75 – 3	2.42
3 – 3.25	1.55
3.25 – 3.5	1.36
3.5 – 3.75	1.68
3.75 – 4	2.96

Table 4.13: Left: $A \times \epsilon$ input MC systematic uncertainty integrated over the given p_{T} range and for $2.5 < y < 4$. Middle: $A \times \epsilon$ input MC systematic uncertainty as a function of p_{T} for $2.5 < y < 4$. Right: $A \times \epsilon$ input MC systematic uncertainty as a function of y for $0 \leq p_{\mathrm{T}} < 12$ GeV/c.

	$\sigma_{A\times\epsilon}$ (%)			
y	$0.3 \leq p_{\mathrm{T}} < 2$ GeV/c	$2 \leq p_{\mathrm{T}} < 4$ GeV/c	$4 \leq p_{\mathrm{T}} < 6$ GeV/c	$6 \leq p_{\mathrm{T}} < 12$ GeV/c
2.5 – 2.75	1.63	2.46	2.49	3.31
2.75 – 3.	0.50	0.89	1.12	1.46
3. – 3.25	0.16	0.54	0.77	0.91
3.25 – 3.5	0.14	0.43	0.71	0.84
3.5 – 3.75	0.41	0.49	0.88	1.19
3.75 – 4	1.84	2.05	1.93	2.34

Table 4.14: $A \times \epsilon$ input MC systematic uncertainty as a function of y in different p_{T} bins.

The systematic uncertainty on the tracking efficiency is evaluated by comparing single muon distributions in data and simulations [218]. The systematic uncertainty on the tracking efficiency is estimated by using the CMSL7 and CMSH7 triggered events. We first describe the principle for the evaluation of the tracking efficiency and then we show how to estimate the corresponding systematic uncertainty. The tracking efficiency for a give chamber ϵ_{ch} is estimated starting from the clusters formed by a track in the MCH station. Figure 4.14 illustrates the possible clusters formed by a track in the chamber 1 and 2. N_{1-1} is the number of tracks whose cluster information is reconstructed by both chambers in Station 1, while N_{0-0} indicates the number of tracks whose cluster information is not reconstructed by both chambers in the same station. N_{1-0} and N_{0-1} are the number of tracks whose cluster information is reconstructed by either chamber 1 or chamber 2 only. The total number of tracks N_{tot} that cross a

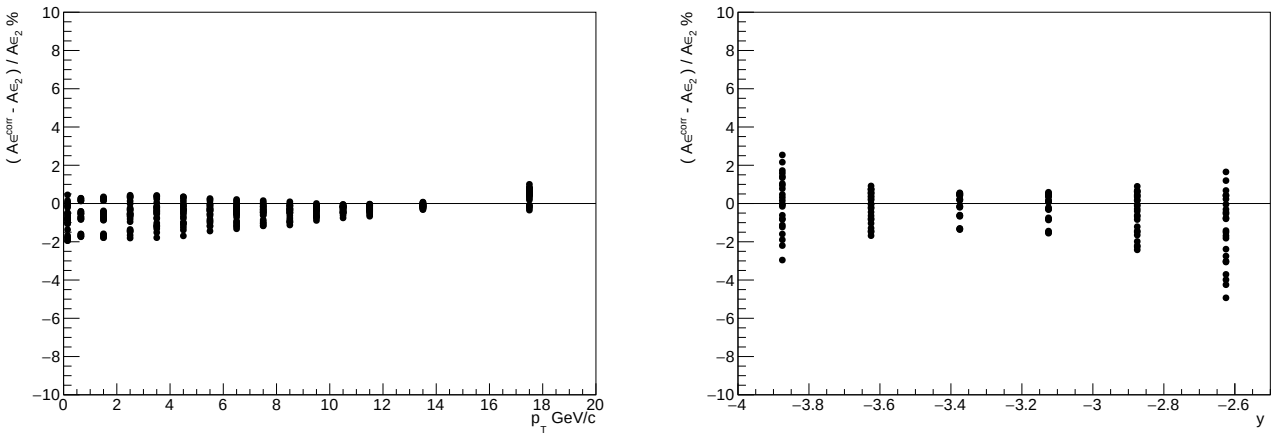

Figure 4.13: Relative difference of the $A \times \epsilon$ between the various input MC shapes used for the evaluation of the systematic uncertainty and the tuned MC shapes, as a function of p_{T} (left) and rapidity (right). $A \times \epsilon_2$ have been computed with the iterative procedure and their values are listed in section 4.1.4.

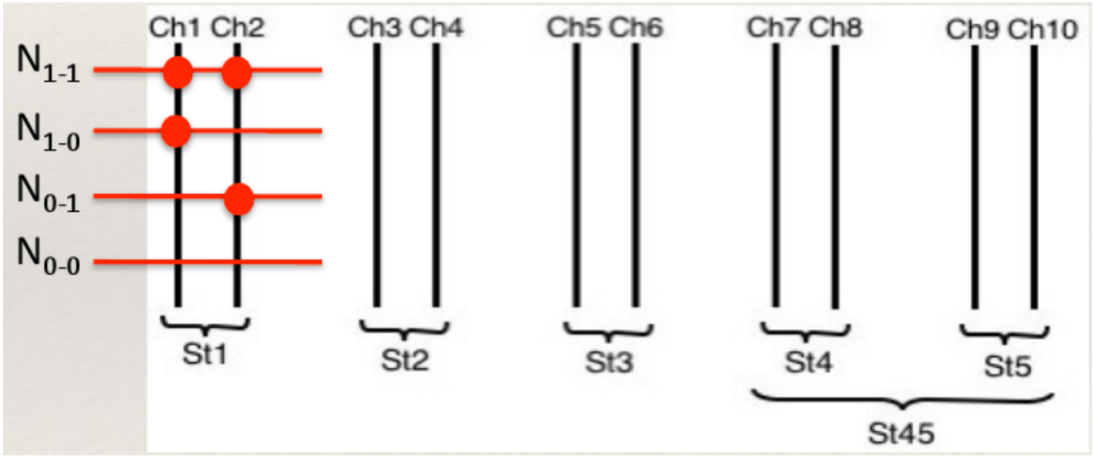

Figure 4.14: Diagram of five stations in the MCH and possible clusters formed by a track in the chamber 1 and 2. Figure from [219].

tracking station is the sum of all the above tracks for a given station:

$$N_{\mathrm{tot}} = N_{1-1} + N_{1-0} + N_{0-1} + N_{0-0}$$

Assuming that the efficiency of chamber 1 is independent of the efficiency of chamber 2 ($N_{1-1} = \epsilon_{\mathrm{ch1}}\epsilon_{\mathrm{ch2}}N_{\mathrm{tot}}$), one can define the efficiency for the chamber 1 and chamber 2 as follows:

$$\epsilon_{\mathrm{ch1}} = \frac{N_{1-1} + N_{1-0}}{N_{\mathrm{tot}}} \quad \text{leading to} \quad \epsilon_{\mathrm{ch1}} = \frac{N_{1-1}}{N_{1-1} + N_{0-1}} \tag{4.24}$$

and

$$\epsilon_{\rm ch2} = \frac{N_{1-1} + N_{0-1}}{N_{\rm tot}} \quad \text{leading to} \quad \epsilon_{\rm ch2} = \frac{N_{1-1}}{N_{1-1} + N_{1-0}} \tag{4.25}$$

The efficiency of a station is estimated according to the tracking reconstruction algorithm, that demands at least one cluster in each of the first three stations. The efficiency for station 1 is therefore defined as:

$$\epsilon_{\rm station1} = 1 - (1 - \epsilon_{\rm ch1}) \cdot (1 - \epsilon_{\rm ch2}) \tag{4.26}$$

The efficiencies for station 2 (and 3) have the same definition as Eq. 4.26 considering chambers 3 and 4 (5 and 6), respectively. For station 4 and 5, their efficiencies are considered all together, since the tracking algorithm requires at least three clusters among the last four chambers:

$$\epsilon_{\rm station4,5} = \prod_{i=1}^{4} \epsilon_i + \sum_{i=1}^{4} (1 - \epsilon_i) \cdot \prod_{j \neq i} \epsilon_j \tag{4.27}$$

The global efficiency for the muon tracking system is the products of all station efficiencies and it is defined as:

$$\epsilon_{\rm MCH} = \epsilon_{\rm station1} \cdot \epsilon_{\rm station2} \cdot \epsilon_{\rm station3} \cdot \epsilon_{\rm station4,5} \tag{4.28}$$

Figure 4.15 shows the single muon tracking efficiency in data (blue) and MC (red) as a function of the run number, $p_{\rm T}$, rapidity, and ϕ for the CMSL7 triggered events. The corresponding efficiency ratio data/MC is also shown at the bottom of each plot. The ratio data/MC versus run number, $p_{\rm T}$, rapidity and ϕ is close to unity within 1%. Similar conclusion is obtained for the CMSH7 events. Therefore, we conclude that the systematic uncertainty on the tracking efficiency is 1% for the single muon and therefore 2% for the dimuons. It is assumed to be uncorrelated versus $p_{\rm T}$ and rapidity.

The systematic uncertainty on the trigger efficiency is from two sources:

- the difference in shape of the trigger response between data and MC in the $p_{\rm T}$ region close to the trigger threshold,
- the intrinsic efficiencies of the muon trigger chambers.

The muon triggers are programmed with selections depending on a low $p_{\rm T}$ (L$p_{\rm T}$) or a high $p_{\rm T}$ (H$p_{\rm T}$) threshold (see section 2). The minimum $p_{\rm T}$ trigger threshold (A$p_{\rm T}$) for which a muon is firing the trigger is equal to 0.5 GeV/c. The trigger response function, $RF^{pp}_{\rm MC}$ = L$p_{\rm T}$/A$p_{\rm T}$ is defined as the ratio of muons matching the L$p_{\rm T}$ threshold to muons matching the A$p_{\rm T}$ threshold [220]. A fitting function is used to describe the RF function such as:

$$RF = \frac{Lp_{\rm T}}{Ap_{\rm T}} = p_0 + p_1 * (1 + erf(\frac{p_{\rm T} - {p_{\rm T}}^{\rm mean}}{\sqrt{2} \times \sigma})) \tag{4.29}$$

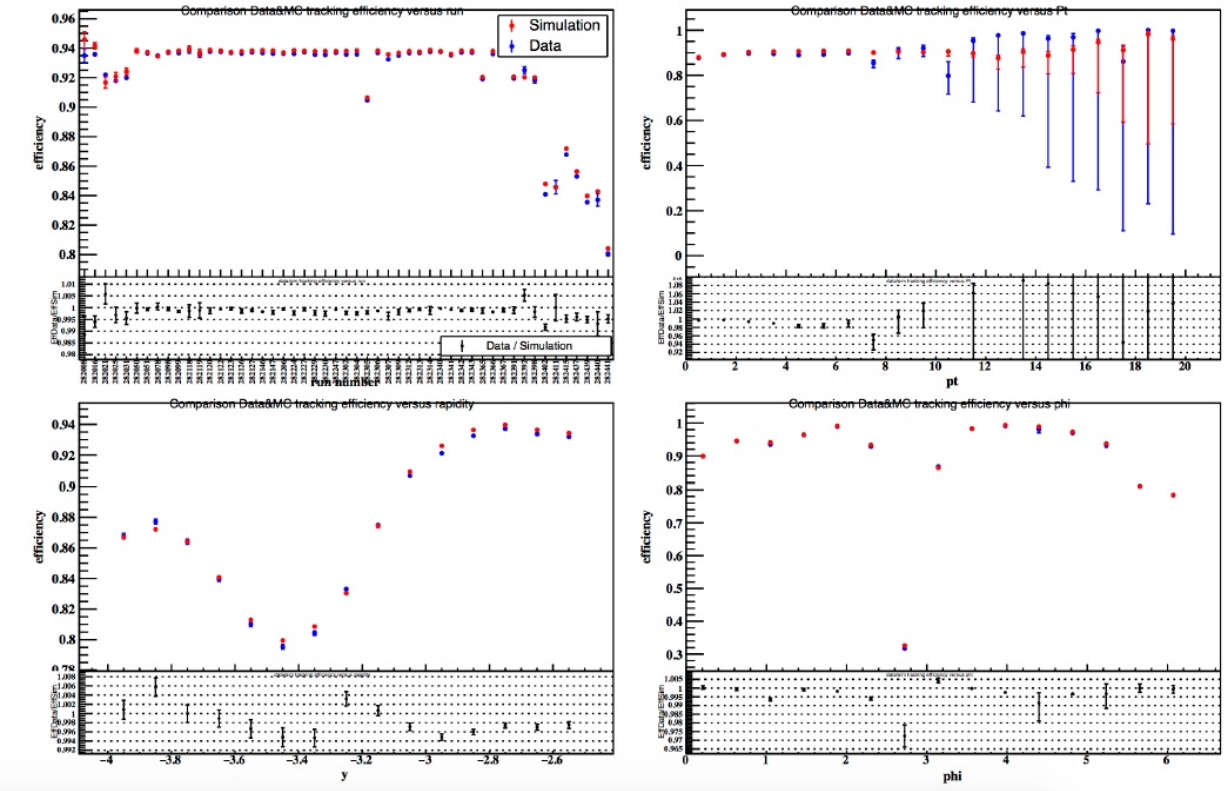

Figure 4.15: Single muon tracking efficiency in data (blue) and MC (red) as a function of the run number (top left), p_{T} (top right), rapidity (bottom left), and ϕ (bottom right) for CMSL7 triggered events. The ratio of data to MC is shown in the bottom panel of each plot.

with p_0 in the range [0, 0.5]. Note that p_0, p_1, $p_{\mathrm{T}}^{\mathrm{mean}}$ and σ are free parameters of the fit. The function erf is the error function. The fits are done in data and MC on single muon distributions. The two sets of fit parameters are used to weight the single muons passing the Ap_{T} threshold in the MC simulation. The difference on the numbers of simulated J/ψ obtained with the two weighting procedures is taken as systematic uncertainty.

In this pp study, the p_{T} threshold for Ap_{T} and Lp_{T} are the same and equal to 0.5 GeV/c. The regular trigger response function is not calculable, hence an alternative method is introduced. The trigger response function in the MC simulation is redefined as RF^{pp}_{MC} = Lp_{T} / Tp_{T} where Tp_{T} is the single muon p_{T} distribution without any trigger matching requirement. RF^{pp}_{MC} is then fitted with Eq. 4.29. However for the data, the trigger matching condition is required in order to remove hadronic contamination. So, we used the 2015 Pb-Pb data sample at $\sqrt{s_{\mathrm{NN}}}$ = 5.02 TeV in which Lp_{T} = 1 GeV/c and Ap_{T} = 0.5 GeV/c to estimate RF^{pp}_{data}. The underlying hypotheses to do so is that the trigger response does not change with time and that it is similar for Lp_{T} =0.5 GeV/c or Lp_{T} =1 GeV/c. From the Pb-Pb data, $RF^{PbPb}_{\mathrm{data}}$ and RF^{PbPb}_{MC} are extracted in terms of ratios of Lp_{T} to Ap_{T} and then fitted with Eq. 4.29. The relative difference between the resulted fit parameters ($p_{\mathrm{T}}^{\mathrm{mean}}$ and σ) is computed and then is applied to the fit parameters obtained from the fitting of RF^{pp}_{MC}. As a result, RF^{pp}_{data} is estimated. In Figure 4.16, the RF function of the data and MC for pp collisions is shown.

Then the muons passing the A$p_{\rm T}$ threshold in the MC are selected. Single muon histograms are then filled either unweighted or with a weight computed as:

$$w = \frac{w_{\rm MC}}{w_{\rm data}}, \tag{4.30}$$

where

$$w_{data} = RF_{\rm data}(p_{\rm T}^{\mu 1}) \times RF_{\rm data}(p_{\rm T}^{\mu 2}), \tag{4.31}$$

and

$$w_{MC} = RF_{\rm MC}(p_{\rm T}^{\mu 1}) \times RF_{\rm MC}(p_{\rm T}^{\mu 2}). \tag{4.32}$$

Finally the number of J/ψ is evaluated in the two cases and the relative difference in the number of J/ψ is taken as the systematic uncertainty.

The systematic uncertainty on the trigger efficiency integrated over $p_{\rm T}$ and rapidity is 1.7%. The corresponding results for $p_{\rm T}$, y and in double-differential bins are written in Table 4.15 and 4.16. In general, the systematic uncertainty is smaller at high $p_{\rm T}$ or in the most forward-rapidity region.

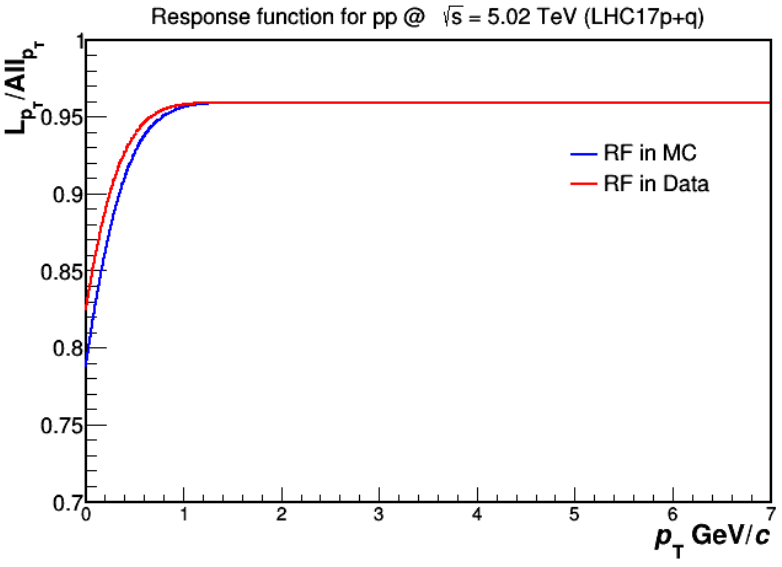

Figure 4.16: Trigger responses of data and MC as a function of $p_{\rm T}$ for pp collisions at $\sqrt{s}$ = 5.02 TeV.

The second source of systematic uncertainty is from the intrinsic efficiency of the muon trigger chambers. Each trigger chamber contains 234 local boards. The values of the trigger board efficiency, estimated during the data taking, are introduced in the MC simulation. In order to estimate the uncertainty in data, the trigger efficiency of local boards is evaluated for different muon $p_{\rm T}$ selections. A new efficiency map is thereafter built up and it is used to run a new MC simulation. The difference between the J/ψ $A \times \epsilon$ obtained from the new MC simulation and the one obtained with the standard efficiency map is taken as the systematic uncertainty. Figure 4.17 shows the $A \times \epsilon$ as a function of the run number. It is estimated by using the MC productions with the standard efficiency map (red)

p_{T} (GeV/c)	syst. unc. (%)
0 – 0.3	1.0
0.3 – 1	1.3
0 – 1	1.2
1 – 2	2.0
2 – 3	1.6
3 – 4	1.3
4 – 5	1.2
5 – 6	1.1
6 – 7	1.0
7 – 8	0.97
8 – 9	0.93
9 – 10	0.80
10 – 11	0.64
11 – 12	0.58
10 – 12	0.75
12 – 15	0.32
15 – 20	0.28

y	syst. unc. (%)
2.5 – 2.75	2.4
2.75 – 3	1.7
3 – 3.25	1.1
3.25 – 3.5	0.8
3.5 – 3.75	0.5
3.75 – 4	0.3

Table 4.15: Left: the J/ψ systematic uncertainty on the trigger efficiency associated to the trigger response as a function of p_{T}, for $2.5 < y < 4$. Right: the J/ψ systematic uncertainty on the trigger efficiency associated to the trigger response as a function of y , for $0 \leq p_{\mathrm{T}} < 12.0$ GeV/c.

	syst. unc. (%)			
y	$0.3 \leq p_{\mathrm{T}} < 2$ GeV/c	$2 \leq p_{\mathrm{T}} < 4$ GeV/c	$4 \leq p_{\mathrm{T}} < 6$ GeV/c	$6 \leq p_{\mathrm{T}} < 12$ GeV/c
2.5 – 2.75	2.9	2.1	1.5	1.0
2.75 – 3.	2.2	1.5	1.2	0.9
3. – 3.25	1.9	1.0	0.7	0.5
3.25 – 3.5	1.6	0.7	0.3	0.2
3.5 – 3.75	1.0	0.3	0.1	0.1
3.75 – 4	0.7	0.1	0.1	0.0

Table 4.16: The J/ψ systematic uncertainty on the trigger efficiency in double-differential p_{T}/y bins.

and the modified efficiency map (blue).

The relative difference between the two integrated $A \times \epsilon$ is around 0.7% for $0 < p_{\mathrm{T}} < 20$ GeV/c. Given the fact that the method for the efficiency calculation has a small correlation bias between chambers that is not fully accounted for in the efficiency variation considered, the systematic uncertainty was rounded to 1%. Figure 4.18 and 4.19 show the p_{T} and y dependences of the $A \times \epsilon$ estimated by using the two MC productions. The relative difference for most of the p_{T} and rapidity bins are within 1%. For $15 < p_{\mathrm{T}} < 20$ GeV/c, it is around 1.6% which is attributed to the lack of statistic in the MC for that p_{T} bin. Indeed, the intrinsic trigger systematic uncertainty is not expected to be strongly p_{T} or y dependent. The total systematic uncertainty on the trigger efficiency is assumed to be uncorrelated as a function of p_{T} and y.

The systematic uncertainty on the trigger-track matching is taken from the published result (see section 3.4 in [125]). At reconstruction level, the muon tracks are reconstructed independently in the muon tracking and in the

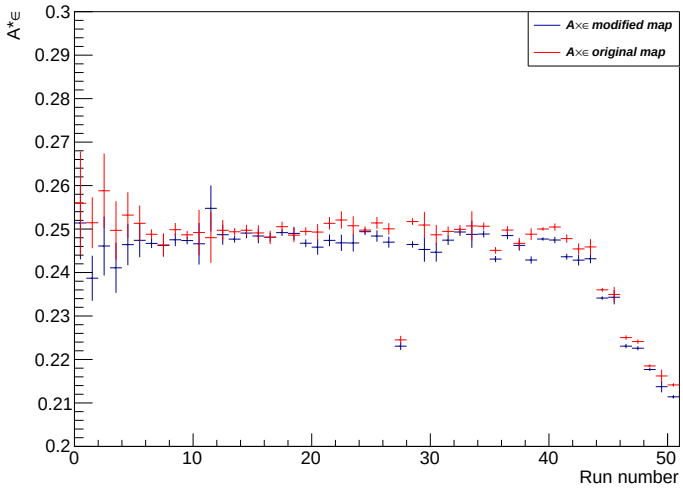

Figure 4.17: J/ψ $A\times\epsilon$ as a function of the run number in the official MC simulation and with the modified simulations using a blurred trigger response at the local board level.

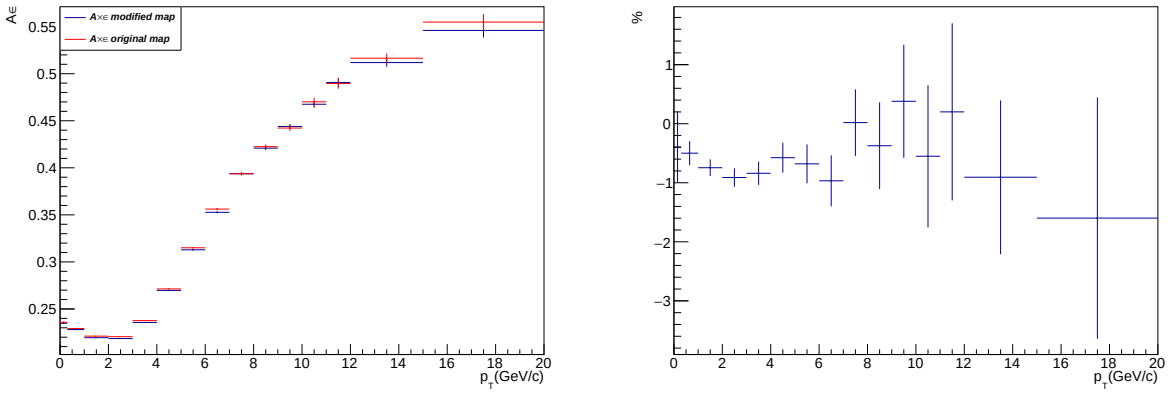

Figure 4.18: Left: J/ψ $A\times\epsilon$ as a function of p_{T} in the MC productions with the standard efficiency map (red) and the modified efficiency map (blue). Right: relative difference of the two AxEff (in %) versus p_{T}.

muon trigger systems. The reconstructed tracks in both systems are matched thereafter. The matching efficiency for the matched tracks depends on their χ^2 matching cut related to the track fit and matching goodness. The systematic uncertainty on the trigger-tracking matching efficiency is evaluated by varying the χ^2 cut in the data and MC. The difference between the loss of efficiency in data and simulations is about 0.5% when the χ^2 cut is varied between 4σ and 6σ. The systematic uncertainty is then taken as 0.5% at the single muon level. It is therefore 1% for the dimuon and is considered as uncorrelated versus p_{T} and rapidity. Note that the χ^2 cut is the same during the reconstruction of the Run 2 data so the systematic uncertainty on the trigger-track matching is the same for all the Run 2 data taking periods.

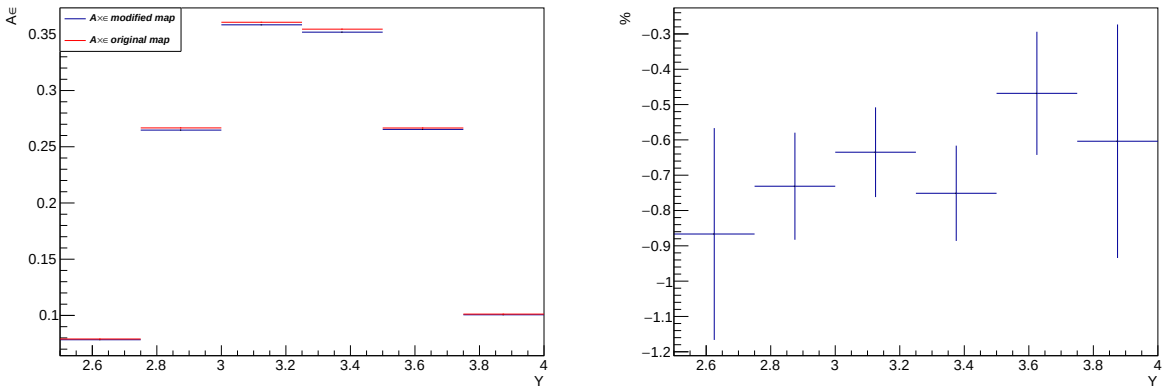

Figure 4.19: Left: J/ψ $A \times \epsilon$ as a function of y in MC productions with the standard efficiency map (red) and the modified efficiency map (blue). Right: relative difference of the two AxEff (in %) versus y.

The summary of all the systematic uncertainty contributions is tabulated in Table 4.17. The larger systematic uncertainties come from the signal extraction, and the MC input. Since large p_T up to 20 GeV/c is achieved in this analysis with respect to the 2015 analysis which reaches $p_{\rm T}$ of 12 GeV/c, the range of variation of the uncertainty can be bigger because of the high $p_{\rm T}$ signal extraction. Concerning the MC input, the 2015 analysis used the 13 TeV data sample to vary the input shapes in the MC. In our analysis, we used our 2017 pp data at $\sqrt{s}$ = 5.02 TeV to estimate the corresponding uncertainty on input MC. The 13 TeV data sample has smaller statistical uncertainties than the 2017 data at $\sqrt{s}$ 5.02 TeV.

source	integrated (%)	vs $p_{\rm T}$ (%)	vs y (%)	vs $p_{\rm T}$ and y (%)
Branching ratio	0.5	0.5*	0.5*	0.5*
Luminosity	1.8	1.8*	1.8*	1.8*
Signal extraction	3	1.9 – 4.4	2.1 – 4.4	0.8 – 4.4
MC input	3.2	0.3 – 2.2	1.4 – 4.9	0.1 – 3.3
MCH efficiency	2	2	2	2
MTR efficiency	2	1.0 – 2.2	1.0 – 2.6	1.0 – 3.1
Matching	1	1	1	1

Table 4.17: Summary of the systematic uncertainties on the J/ψ cross section measurements. The integrated values correspond to the result for $0 < p_{\rm T} < 20$ GeV/c. Values marked with an asterisk correspond to uncertainties correlated over $p_{\rm T}$ and/or rapidity.

4.2 J/ψ cross section

The inclusive J/ψ differential production cross section is computed by using Eq. 4.1. The cross sections integrated over two $p_{\rm T}$ intervals, $0 \leq p_{\rm T} < 12$ GeV/c and $0 \leq p_{\rm T} < 20$ GeV/c, for $2.5 < y < 4$ are given in Table 4.18.

The differential cross sections as a function of $p_{\rm T}$ and y are shown in Figure 4.20 and reported in Table 4.19

p_{T} (GeV/c)	$\sigma\pm$ stat. (%) $\pm$ syst. (%) (μb)
0–12	5.88 $\pm$ 0.03 (0.5) $\pm$ 0.33 (5.6)
0–20	5.88 $\pm$ 0.03 (0.4) $\pm$ 0.34 (5.7)

Table 4.18: p_{T}-integrated cross sections for inclusive J/ψ, in pp collisions at $\sqrt{s}$ = 5.02 TeV, for $2.5 < y < 4$, and two p_{T} intervals.

and 4.20. The double-differential cross sections as a function of y for four p_{T} intervals are shown in Figure 4.21 and reported in 4.21.

p_{T} (GeV/c)	$\frac{\mathrm{d}^2\sigma}{\mathrm{d}p_{\mathrm{T}}\mathrm{d}y}\pm$ (stat.) $\pm$ (syst.) (μb/(GeV/c))
0–0.3	2.27e-01 $\pm$ 7.79e-03 (3.4)$\pm$ 1.26e-02 (5.5)
0.3–1	8.52e-01 $\pm$ 1.08e-02 (1.3) $\pm$ 4.33e-02 (5.1)
1–2	1.24e+00 $\pm$ 1.10e-02 (0.9) $\pm$ 5.93e-02 (4.8)
2–3	9.26e-01 $\pm$ 9.02e-03 (1.0) $\pm$ 4.03e-02 (4.4)
3–4	5.41e-01 $\pm$ 6.42e-03 (1.2) $\pm$ 2.28e-02 (4.2)
4–5	2.74e-01 $\pm$ 4.08e-03 (1.5) $\pm$ 1.12e-02 (4.1)
5–6	1.37e-01 $\pm$ 2.55e-03 (1.9) $\pm$ 5.28e-03 (3.9)
6–7	7.05e-02 $\pm$ 1.74e-03 (2.5) $\pm$ 2.61e-03 (3.7)
7–8	3.45e-02 $\pm$ 1.17e-03 (3.4) $\pm$ 1.32e-03 (3.8)
8–9	1.83e-02 $\pm$ 8.08e-04 (4.4) $\pm$ 6.26e-04 (3.4)
9–10	1.07e-02 $\pm$ 6.31e-04 (5.9) $\pm$ 3.84e-04 (3.6)
10–11	5.75e-03 $\pm$ 4.13e-04 (7.2) $\pm$ 1.92e-04 (3.3)
11–12	3.42e-03 $\pm$ 3.57e-04 (10.4) $\pm$ 1.74e-04 (5.1)
12–15	1.55e-03 $\pm$ 1.26e-04 (8.1) $\pm$ 5.26e-05 (3.4)
15–20	2.79e-04 $\pm$ 4.10e-05 (14.7) $\pm$ 1.01e-05 (3.6)

Table 4.19: Inclusive J/ψ differential cross section in various p_{T} intervals for $2.5 < y < 4$. The global uncertainty (not included) is 1.9%.

y	$\frac{\mathrm{d}\sigma}{\mathrm{d}y}\pm$ (stat.) $\pm$ (syst.) (μb)
$2.5 < y < 2.75$	4.779 $\pm$ 0.088 (1.8) $\pm$ 0.356 (7.4)
$2.75 \leq y < 3.$	4.394 $\pm$ 0.043 (1.0)$\pm$ 0.214 (4.9)
$3. \leq y < 3.25$	4.108 $\pm$ 0.034 (0.8)$\pm$ 0.169 (4.1)
$3.25 \leq y < 3.5$	3.659 $\pm$ 0.032 (0.9) $\pm$ 0.132 (3.6)
$3.5 \leq y < 3.75$	3.389 $\pm$ 0.035 (1.0) $\pm$ 0.128 (3.8)
$3.75 \leq y < 4$	3.018 $\pm$ 0.055 (1.8) $\pm$ 0.152 (5.0)

Table 4.20: Inclusive J/ψ differential cross section in various y intervals for $0 < p_{\mathrm{T}} < 12$ GeV/c. The global uncertainty (not included) is 1.9%.

4.3 Discussion

We have measured the inclusive J/ψ production cross section for $2.5 < y < 4$ in pp collisions at $\sqrt{s}$ = 5.02 TeV. The inclusive J/ψ production cross section measured at forward-rapidity is the sum of the prompt and non-prompt J/ψ contributions. In this section, we compare the inclusive J/ψ cross sections with previous ALICE measurements

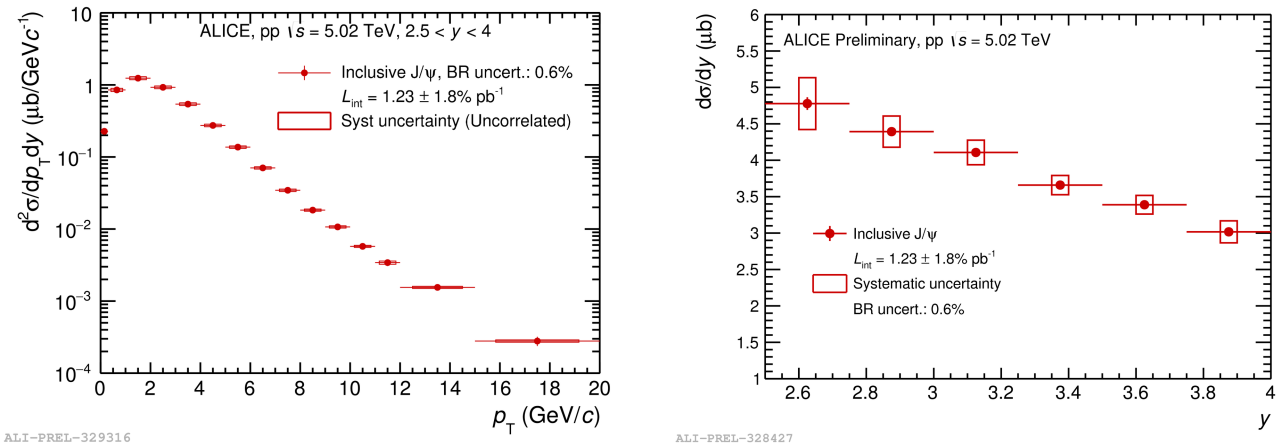

Figure 4.20: Left: inclusive J/ψ differential cross section as a function of p_{T} at forward rapidity in pp collisions at $\sqrt{s}$ = 5.02 TeV. Right: inclusive J/ψ differential cross section as a function of y for $0 < p_{\mathrm{T}} < 12$ GeV/c in pp collisions at $\sqrt{s}$ = 5.02 TeV.

y	$\mathrm{d}^2\sigma/\mathrm{d}p_{\mathrm{T}}\mathrm{d}y$ (μb/(GeV/c))	
	$0.3 \leq p_{\mathrm{T}} < 2$ GeV/c	$2 \leq p_{\mathrm{T}} < 4$ GeV/c
2.5 – 2.75	1.2801 ± 0.0405 (3.2) ± 0.0555 (4.3)	0.9345 ± 0.0259 (2.8) ± 0.0530 (5.7)
2.75 – 3.	1.1941 ± 0.0199 (1.7) ± 0.0517 (4.3)	0.8381 ± 0.0134 (1.6) ± 0.0279 (3.3)
3. – 3.25	1.1274 ± 0.0157 (1.4) ± 0.0469 (4.2)	0.7707 ± 0.0109 (1.4) ± 0.0304 (3.9)
3.25 – 3.5	1.0467 ± 0.0136 (1.3) ± 0.0322 (3.1)	0.6936 ± 0.0110 (1.6) ± 0.0194 (2.8)
3.5 – 3.75	1.0012 ± 0.0144 (1.4) ± 0.0280 (2.8)	0.6393 ± 0.0120 (1.9) ± 0.0176 (2.8)
3.75 – 4	0.9106 ± 0.0233 (2.6) ± 0.0394 (4.3)	0.5896 ± 0.0186 (3.2) ± 0.0251 (4.3)
	$4 \leq p_{\mathrm{T}} < 6$ GeV/c	$6 \leq p_{\mathrm{T}} < 12$ GeV/c
2.5 – 2.75	0.2862 ± 0.0121 (4.2) ± 0.0123 (4.3)	0.0339 ± 0.0017 (5.0) ± 0.0021 (6.1)
2.75 – 3.	0.2492 ± 0.0059 (2.3) ± 0.0078 (3.1)	0.0307 ± 0.0009 (2.9) ± 0.0011 (3.6)
3. – 3.25	0.2254 ± 0.0047 (2.1) ± 0.0066 (2.9)	0.0261 ± 0.0008 (2.9) ± 0.0007 (2.8)
3.25 – 3.5	0.1946 ± 0.0046 (2.4) ± 0.0053 (2.7)	0.0213 ± 0.0007 (3.5) ± 0.0006 (3.0)
3.5 – 3.75	0.1646 ± 0.0049 (3.0)± 0.0046 (2.8)	0.0180 ± 0.0007 (4.0) ± 0.0006 (3.3)
3.75 – 4	0.1350 ± 0.0071 (5.3) ± 0.0045 (3.3)	0.0130 ± 0.0010 (7.7) ± 0.0005 (4.2)

Table 4.21: Inclusive J/ψ double differential cross section in various p_{T} and y intervals. The global uncertainty (not included) is 1.9%.

at various energies and with theoretical models.

4.3.1 Comparison with ALICE published results

Previous measurements were performed with a low luminosity at $\sqrt{s}$ = 5.02 TeV in 2015 [125]. Therefore, it is important to compare carefully the two cross sections obtained at the same energy. Figure 4.22 shows the p_{T}-differential J/ψ cross section at $\sqrt{s}$ = 5.02 TeV for the 2017 (this result) and the 2015 pp data taking. The new measurement extends the p_{T} reach to 20 GeV/c thanks to the larger recorded luminosity in 2017. The two measurements are compatible for most of the p_{T} bins. For $4 \leq p_{\mathrm{T}} < 5$ GeV/c, $6 \leq p_{\mathrm{T}} < 9$ GeV/c and $10 \leq p_{\mathrm{T}} < 12$

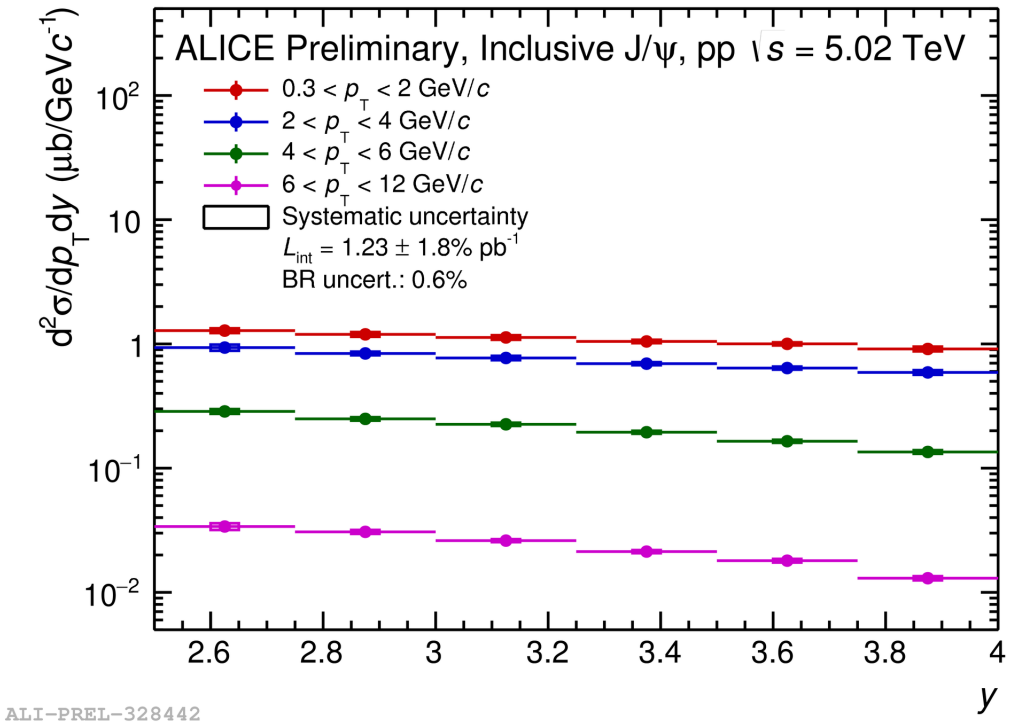

Figure 4.21: Inclusive J/ψ differential cross section as a function of y for four $p_{\rm T}$ intervals for $2.5 < y < 4$ in pp collisions at $\sqrt{s} = 5.02$ TeV.

GeV/c, the deviations are found to be 1.9σ, less than 1.4σ and 1.5σ, respectively.

Figure 4.23 shows the y-differential J/ψ cross section at $\sqrt{s} = 5.02$ TeV for the 2017 and the 2015 pp data taking. The agreement is good for most of the y bins. For $3.5 < y < 3.75$ and $3.75 < y < 4.0$, the differences are 1.3σ and 1.8σ, respectively, when considering the statistical and systematic uncertainties. The deviations between the 2017 and 2015 results are given in Table 4.23 for all the $p_{\rm T}$ and y bins. To investigate the deviation between the 2015 and 2017 results, several checks were performed and they are listed below. It was decided to:

	$\sigma^{J/\psi}$ (μb/(GeV/c)) $\pm$ stat. $\pm$ syst.		
$p_{\rm T}$ (GeV/c)	LHC15n	LHC17p	LHC17q
0–12	5.61 $\pm$ 0.08 $\pm$ 0.28	6.03 $\pm$ 0.04 $\pm$ 0.32	5.76 $\pm$ 0.03 $\pm$ 0.31
4–12	0.72 $\pm$ 0.03 $\pm$ 0.03	0.85 $\pm$ 0.01 $\pm$ 0.04	0.83 $\pm$ 0.01 $\pm$ 0.04

Table 4.22: The J/ψ cross-sections as a function of the pp period, for $2.5 < y < 4$, and integrated over a given $p_{\rm T}$ range. The first row shows the cross sections integrated over $0 \leq p_{\rm T} < 12$ GeV/c. The second row shows the cross sections integrated over $4 \leq p_{\rm T} < 12$ GeV/c. The data taking periods corresponding to the 2015 data (the 2017 data) are called LHC15n (LHC17p and LHC17q).

- Compare the J/ψ cross section in the high-$p_{\rm T}$ region ($4 \leq p_{\rm T} < 12$ GeV/c) between the 2015 and 2017 data samples. The deviation between the two cross section results is 1.8σ.

- Measure the cross-sections separately for the two data-taking periods of 2017, in order to cross check the

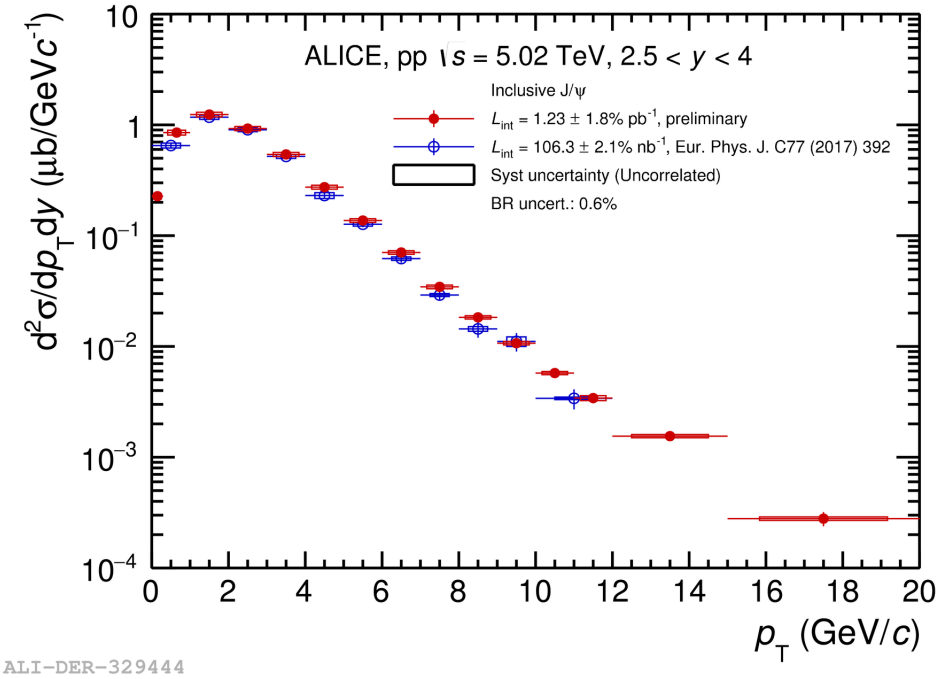

Figure 4.22: Inclusive J/ψ differential cross section as a function of p_{T} at forward rapidity in pp collisions at $\sqrt{s}$ = 5.02 TeV. The new measurement with the 2017 data is shown (red) and compared to the published results [125] (blue).

normalisation. Purity and pile-up correction factors were quite different for the two periods, the difference being attributed to some changes in the filling scheme and/or interaction rate between the two periods. Comparing the cross-sections obtained in both cases would ensure that these changes have no unaccounted impact on the ingredients that enter the cross section measurement. In addition the cross section was also extracted in the high p_{T} ($4 \leq p_{\mathrm{T}} < 12$ GeV/c) region for both periods separately. Table 4.22 shows the cross section integrated over p_{T} and at high p_{T}. The deviations between the cross sections integrated over p_{T} in 2015 and 2017 data are less than one sigma. The deviations between cross sections at high p_{T} in 2015 and the two periods of 2017 are within two sigma. The deviation between the cross sections in the two 2017 periods is found to be 0.6σ for $0 \leq p_{\mathrm{T}} < 20$ GeV/c and 0.3σ for $4 \leq p_{\mathrm{T}} < 12$ GeV/c. This cross-check confirms that the cross-sections remain consistent and stable between the two 2017 data taking periods, despite the fact that the beam conditions were different.

- Re-check the signal extraction for the 2015 dataset (not shown). The same fit method as for the 2017 analysis is applied to the 2015 data. The number of J/ψ extracted from the two datasets were compared. The bin sizes of the dimuon mass spectra were set to 25 MeV/c^2 and 50 MeV/c^2. In most of the p_{T} and y bins, the relative difference between the two independent checks on the number of J/ψ is below one percent. The largest relative difference (6%) is observed for $9 < p_{\mathrm{T}} < 10$ GeV/c. The limited statistics at high p_{T} and the different mass

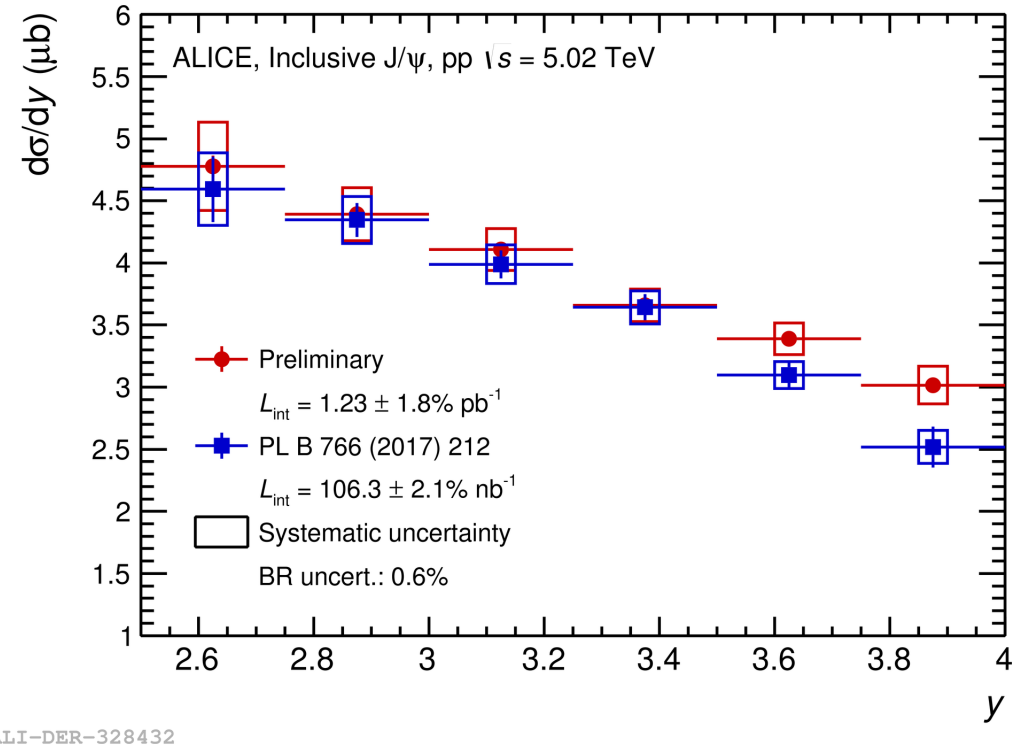

Figure 4.23: Inclusive J/ψ differential cross section as a function of y for $0 \leq p_{\mathrm{T}} < 12$ GeV/c in pp collisions at $\sqrt{s}$ = 5.02 TeV. The new measurement with the 2017 data is shown (red) and compared to the published results [125] (blue).

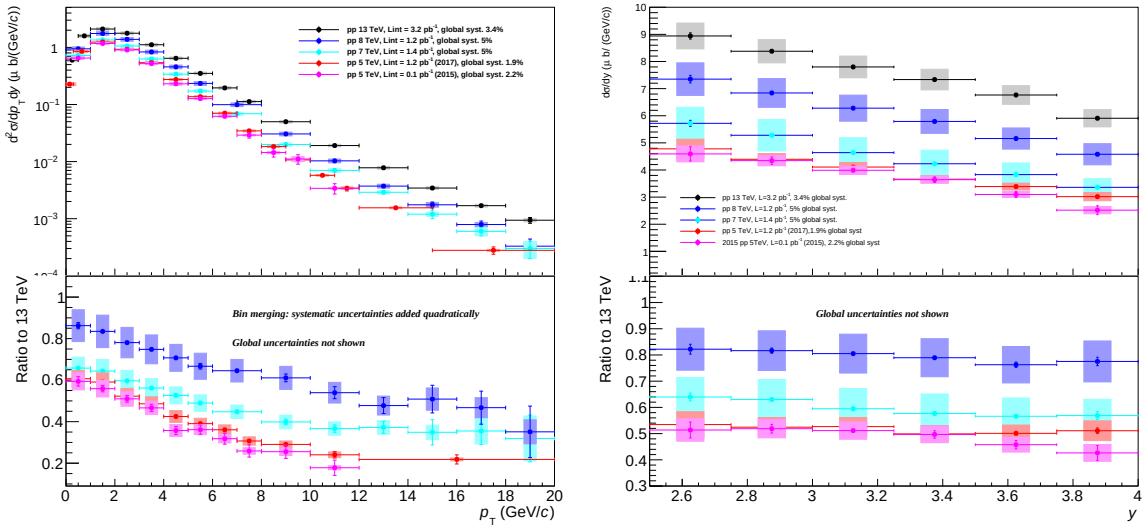

Figure 4.24: Differential J/ψ production cross section as a function of p_{T} (left) and y (right) at $\sqrt{s}$ = 5.02, 7, 8 and 13 TeV. The cross-section ratios to the 13 TeV data are shown in the bottom panels [This thesis].

binning could explain the observed statistical fluctuation.

- Similar signal extraction checks were performed on the J/ψ width from the 2017 and 2015 data samples. The

larger relative difference within about 2% between the J/ψ widths measured in 2015 and 2017 is observed at high $p_{\rm T}$ and for $2.5 < y < 3$. Those kinematic regions are not the ones for which we observe a larger deviation between the 2015 and 2017 cross sections. Hence the different signal widths that are observed cannot explain the deviation.

- Update the alignment for the 2015 and 2017 data by taking into account the presence of a residual misalignment between the tracking stations before and after the dipole magnet in the bending plane, then compare the signal extraction before and after the correction of the alignment. The effect of the residual misalignment on the J/ψ yield is small and the relative difference between the yield before and after alignment correction is covered by the systematic uncertainty on the signal extraction.

- Compare the $p_{\rm T}$ and rapidity distributions of the 5 TeV cross section obtained from the 2015 and 2017 data samples to the ALICE published results at 7 [221], 8 [222] and 13 [125] TeV. The comparison is shown in Figure 4.24, as a function of $p_{\rm T}$ (left panel) and y (right panel). The bottom panels of Figure 4.24 show the ratios to the 13 TeV data. The ratio of the 2015 to the 13 TeV data shows more fluctuations as a function of $p_{\rm T}$ than the 2017 data, which are attributed to the lower statistics of the 2015 data. On the other hand, the rapidity distributions of the ratios do not show any obvious bias both in the 2015 and 2017 data.

The checks described above, especially the last one suggest that the differences observed between the 2015 and 2017 cross section results can be attributed to statistical fluctuations in the 2015 data.

$p_{\rm T}$ (GeV/c)	$\frac{\sigma_{2017}-\sigma_{2015}}{\sqrt{\delta^2_{2017}+\delta^2_{2015}}}$
0–1	0.2σ
1–2	0.7σ
2–3	0.3σ
3–4	0.5σ
4–5	1.9σ
5–6	0.9σ
6–7	1.3σ
7–8	1.4σ
8–9	1.4σ
9–10	-0.2σ
10–12	1.5σ

y	$\frac{\sigma_{2017}-\sigma_{2015}}{\sqrt{\delta^2_{2017}+\delta^2_{2015}}}$
$2.5 < y < 2.75$	0.34σ
$2.75 \leq y < 3.$	0.14σ
$3. \leq y < 3.25$	0.42σ
$3.25 \leq y < 3.5$	0.07σ
$3.5 \leq y < 3.75$	1.32σ
$3.75 \leq y < 4$	1.80σ

Table 4.23: Deviations between the differential inclusive J/ψ cross sections in the 2017 and in the 2015 data samples as a function of $p_{\rm T}$ (left) and rapidity (right). The total uncertainties (δ_{2017} and δ_{2015}) are considered (apart from the branching ratio uncertainties which are correlated among the samples). The global uncertainty is 1.9% and 2.2% for the 2017 and 2015 dataset, respectively, and it is only included in the computation of the deviation.

The integrated J/ψ cross section for $p_{\rm T} < 12$ GeV/c written in Table 4.18 is now compared to the interpolated J/ψ cross section integrated over $p_{\rm T}$ and y [223]. The interpolated value at $\sqrt{s} = 5.02$ TeV, which is equal to 5.28 ± 0.42 μb, was estimated by fitting the ALICE experimental points at $\sqrt{s} = 2.76$ and 7 TeV and using phenomenological

functions. The ratio of the two cross sections is about 1.11 ± 0.08, which shows good compatibility. The interpolated J/ψ cross section at $\sqrt{s}$ = 5.02 TeV, integrated over p_{T} and y, is also obtained by fitting the LHCb experimental points at $\sqrt{s}$ = 2.76, 7 and 8 TeV and using phenomenological functions and is equal to 5.27 ± 0.28 μb [223]. The ratio of the ALICE data to the interpolated LHCb value is about 1.12 ± 0.05, where the ALICE data is slightly above the LHCb interpolated value. Furthermore, the y dependence of the J/ψ cross section is also compared to the interpolated values, estimated by using the ALICE experimental points at $\sqrt{s}$ = 2.76 and 7 TeV [223]. The comparison is shown in Figure 4.25. The ratio of the two y-differential cross sections is between 1.03 ± 0.14 (total unc.) and 1.13 ± 0.13 (total unc.) where the total uncertainty is the quardratic sum of the statistical, uncorrelated systematic and global systematic uncertainties. The ratio gives a nice agreement in the full y range.

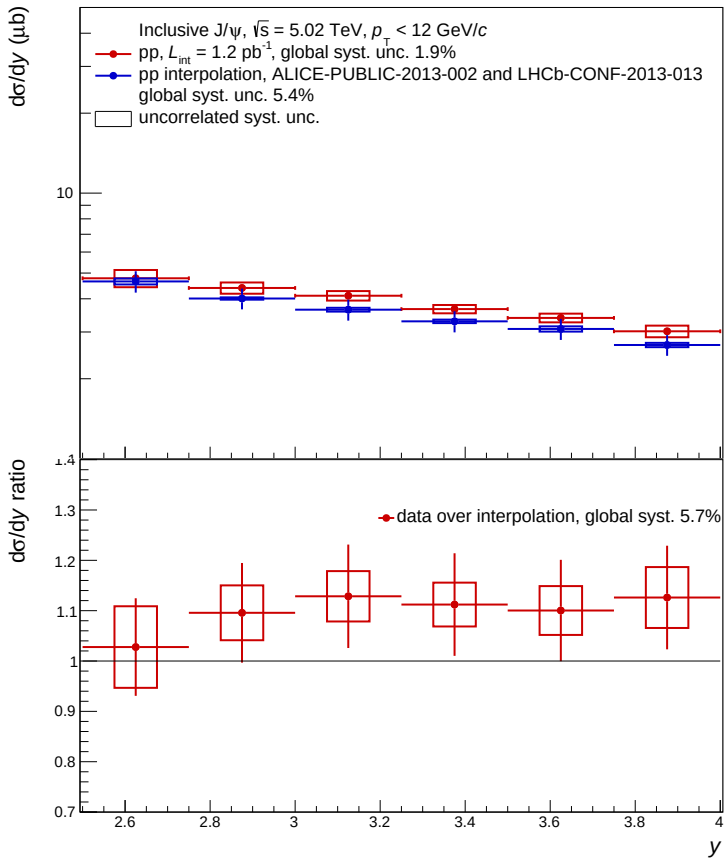

Figure 4.25: Top panel: inclusive J/ψ differential cross section as a function of y for $0 \leq p_{\mathrm{T}} < 12$ GeV/c in pp collisions at $\sqrt{s}$ = 5.02 TeV. The new measurement with the 2017 data is shown (red) and compared to the interpolated values [223] (blue). Bottom panel: the ratio of the data to the interpolated values. [This thesis].

4.3.2 Comparison with models

In the previous section, we have seen that the inclusive J/ψ production cross section in pp collisions at $\sqrt{s} = 5.02$ TeV measured in 2017 is compatible with the one measured in 2015. In this section, we compare the 2017 measurements with existing theoretical calculations. Non-relativistic quantum chromodynamics (NRQCD) models [3, 4] consider color-octet diagrams which dominate at high p_{T} and color-singlet diagrams which dominate at low p_{T} for prompt J/ψ production. The difference between the two NRQCD calculations is in the treatment of the color octet long distance matrix elements (LDME). The calculation by Ma *et al.* [4] uses two linear combinations of three matrix elements while the calculation by Butenschoen *et al.* [3] uses three different matrix elements. For both models, the NLO calculations are not valid in the low-p_{T} region ($p_{\mathrm{T}} \leq m_{c\bar{c}}$). Color glass condensate (CGC) model describes the saturation of the small-x gluon in the proton [5]. In particular, using NRQCD in combination with CGC model allows one to compute the cross secion down to low p_{T}. Two theoretical calculations of an improved CEM (ICEM) [2] and a NLO CEM [1] are also compared to the data. Fixed-order next-to-leading logarithm (FONLL) [126] model describes the non-prompt J/ψ contribution from the B meson decay. The contributions of J/ψ from B meson calculated by FONLL are added to each theoretical calculations.

The top panel of Figure 4.26 shows the p_{T}-differential inclusive J/ψ production cross section in pp collisions together with the comparison to theoretical calculations. The non-prompt J/ψ contribution (orange) from FONLL is also shown separately. This contribution increases with increasing p_{T} from 7% at p_{T} about 1 GeV/c to 42% in the largest p_{T} interval. The theoretical calculation of NRQCD by Butenschoen *et al.* combined with the FONLL estimation reproduces the data for $p_{\mathrm{T}} > 3$ GeV/c. The NRQCD model by Ma *et al.* combined with the FONLL estimation gives a good agreement with the data for $p_{\mathrm{T}} > 5$ GeV/c. The FONLL calculation together with the model including the NRQCD calculations coupled to CGC description by Ma *et al.* are compatible with the data for $p_{\mathrm{T}} <$ 8 GeV/c. A good description by the ICEM+FONLL model for the measured cross-section is obtained over the full p_{T} range. The NLO CEM+FONLL calculation describes the data for $p_{\mathrm{T}} \geq 10$ GeV/c while it underestimates the data for $4 < p_{\mathrm{T}} < 10$ GeV/c. The model comparison with the p_{T}-differential J/ψ cross sections at different $\sqrt{s}$ is shown in the bottom panel of Figure 4.26. The bottom panel of the figure shows the p_{T}-differential J/ψ cross-section ratio of the 5.02 (this results), 7 [221], or 8 [222] TeV over 13 TeV data [125]. The J/ψ p_{T}-differential cross section values enhance with increasing collision energy. A stronger hardening of the p_{T} spectra is observed in the collisions at $\sqrt{s}$ =13 TeV with respect to the 5.02, 7 and 8 TeV data, as it can be seen in the ratio. This hardening can be explained by the increase of the prompt J/ψ mean p_{T} with increasing energy, and by the increasing contribution from non-prompt J/ψ with increasing energy, at high p_{T}. The NRQCD calculation by Butenschoen *et al.* combined with the FONLL estimation within the theoretical uncertainties successfully describe the 5.02-to-13 TeV and 8-to-13 TeV ratios in the whole p_{T} range of validity of the model while it overestimates the cross-section ratio of the 7 over

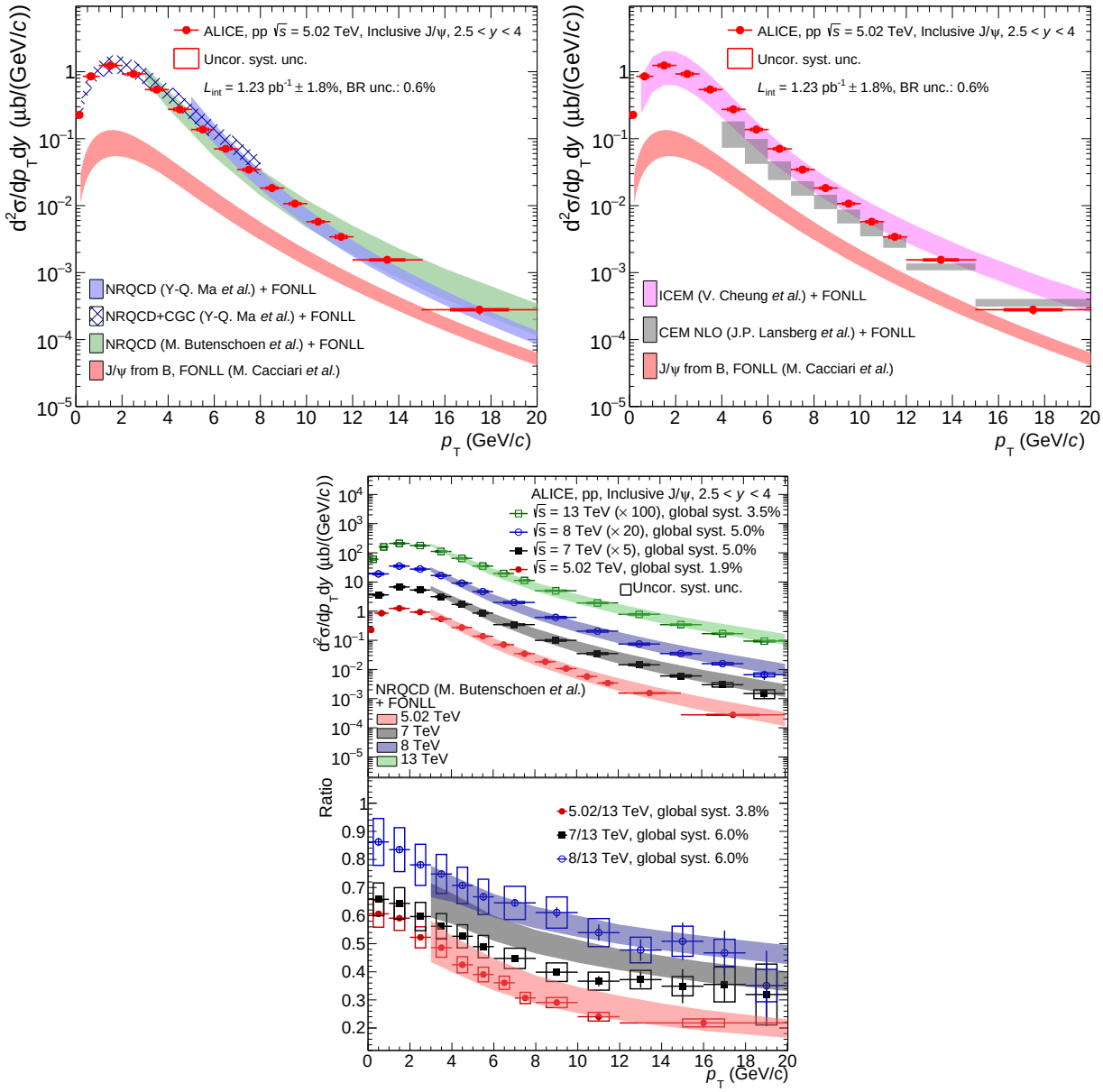

Figure 4.26: Top: inclusive J/ψ differential cross section as a function of p_{T} at forward rapidity in pp collisions at $\sqrt{s} = 5.02$ TeV. The data are compared to theoretical calculations based on CEM [1] (right), ICEM [2] (right), NRQCD [3, 4] (left), CGC coupled to NRQCD [5] (left) for the prompt contribution and summed with FONLL [126] calculations for the non-prompt contributions. Bottom: inclusive J/ψ differential cross section as a function of p_{T} at forward rapidity in pp collisions at $\sqrt{s} = 5.02$, 7 [221], 8 [222], and 13 [125] TeV (top panel). Ratio of the measurements at $\sqrt{s} = 5.02$, 7, 8 TeV to the 13 TeV data (bottom panel). The theoretical calculation based on NRQCD from Butenschoen *et al.* [3] at the four energies are compared with the corresponding data.

13 TeV data for $8 < p_{\mathrm{T}} < 12$ GeV/c, otherwise it gives a good description of the ratio.

The left panel of Figure 4.27 shows the y-differential inclusive J/ψ production cross section in pp collisions at $\sqrt{s} = 5.02$ TeV, compared to two theoretical calculations based on NRQCD coupled to CGC and on ICEM, combined with FONLL. Both two calculations are compatible with the data, within the large theoretical uncertainties. In the right panel of Figure 4.27, the J/ψ y-differential cross section is displayed for several collision energies. It shows a

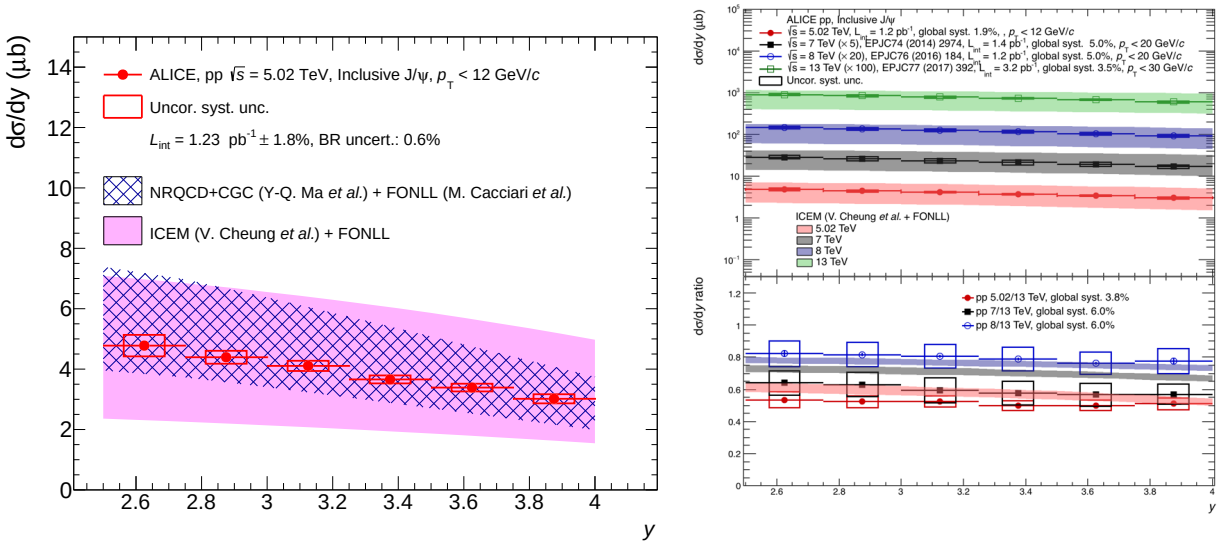

Figure 4.27: Left: inclusive J/ψ differential cross section as a function of y at forward rapidity in pp collisions at $\sqrt{s}$ = 5.02 TeV. The data are compared to theoretical calculations based on CEM [1], ICEM [2], CGC coupled to NRQCD [5] for the prompt contribution and are summed with FONLL [126] calculations for the non-prompt contributions. Right: y-differential cross section for inclusive J/ψ measured in pp collisions at $\sqrt{s}$ = 5.02, 7 [221], 8 [222] and 13 [125] TeV (top panel), and ratio of the measurements at $\sqrt{s}$ = 5.02, 7, 8 TeV to that at $\sqrt{s}$ = 13 TeV (bottom panel). The ALICE data are compared to the theoretical calculation based on ICEM coupled to FONLL.

slight decrease with increasing rapidity at all the energies. The ratio of the lower energy data to the 13 TeV data exhibits a flat behaviour within the experimental uncertainties for the data at the three energies. The y-differential cross sections are also compared to the theoretical model based on ICEM [2] coupled to FONLL. The model within its large theoretical uncertainty reproduces the measurement at all energies for $2.5 < y < 4$. The cross-section ratios among energies, shown in the bottom right panel of Figure 4.27, is compared to the ICEM model calculations as well. The model successfully describes the 8-to-13 TeV ratio over the entire y range, but overestimates or is at the edge of the 5.02-to-13 and 7-to13 TeV cross-section ratios.

The double-differential cross sections as a function of y for four $p_{\rm T}$ intervals are also compared to the theoretical calculations in Figure 4.28. Note that the cross section for $0.3 < p_{\rm T} < 2$ GeV/c is multiplied by a factor of ten in order to appreciate more the comparison of the data with the models. For $0.3 < p_{\rm T} < 6$ GeV/c, the calculation based on NRQCD+CGC by Ma *et al.*, combined with FONLL describes the data well. At high $p_{\rm T}$, the formalism of CGC is not available, so the data comparison is restricted to the intermediate $p_{\rm T}$ region [5]. At high $p_{\rm T}$, for $6 < p_{\rm T} <$ 12 GeV/c, the theoretical calculation based on NRQCD [4] combined with FONLL reproduces the data. The NLO NRQCD calculation by Butenschoen *et al.* [3] is compatible with the data for $4 < p_{\rm T} < 12$ GeV/c. The data over the full measured $p_{\rm T}$ and y ranges are reproduced by the ICEM [2] calculation. The NLO CEM [1] underestimates the data as a function of rapidity for $4 < p_{\rm T} < 12$ GeV/c.

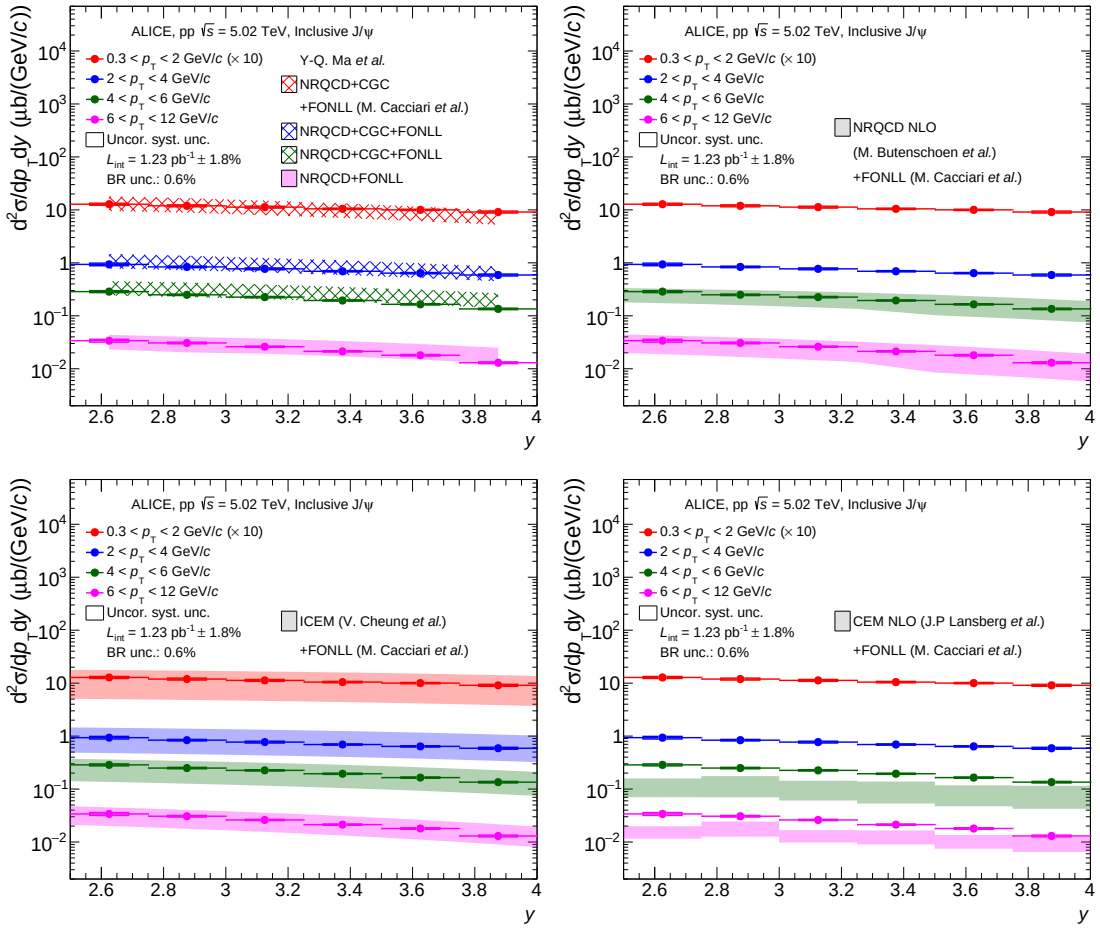

Figure 4.28: Inclusive J/ψ differential cross section as a function of y for four $p_{\rm T}$ intervals in pp collisions at $\sqrt{s}$ = 5.02 TeV. The differential cross section for $0.3 < p_{\rm T} < 2$ GeV/c is multiplied by a factor of ten. The data are compared to theoretical calculations based on CEM [1], ICEM [2], NRQCD [3, 4], CGC coupled to NRQCD [5] for the prompt contribution and summed with FONLL calculations for the non-prompt contributions.

Chapter 5

Inclusive J/ψ production in Pb-Pb collisions

The nuclear modification factor $R_{\rm AA}$ is a useful observable to probe the quark-gluon plasma (QGP) expected to be formed in ultra-relativistic Pb-Pb collisions. The J/ψ $R_{\rm AA}$ describes the J/ψ yield in Pb-Pb collisions with respect to the scaled one in pp collisions. In this chapter, the J/ψ $R_{\rm AA}$ analysis at forward rapidity with the full statistics of the Run 2 Pb-Pb collisions at $\sqrt{s_{\rm NN}} = 5.02$ TeV is presented. The J/ψ $R_{\rm AA}$ is defined as:

$$R_{\rm AA} = \frac{N_{\rm AA}}{\sigma^{pp}_{\rm J/\psi} \times < T_{\rm AA} >}, \tag{5.1}$$

where $\sigma^{\rm pp}_{\rm J/\psi}$ is the J/ψ cross section in pp collisions at $\sqrt{s} = 5.02$ TeV (see chapter 4) and $< T_{\rm AA} >$ is the average nuclear overlap function. The J/ψ invariant yield $N_{\rm AA}$ is expressed as:

$$N_{\rm AA} = \frac{N_{\rm J/\psi \to \mu\mu}(\Delta y, \Delta p_{\rm T})}{BR(\rm J/\psi \to \mu\mu) \times N_{\rm MB} \times A \times \epsilon(\Delta y, \Delta p_{\rm T})}, \tag{5.2}$$

where BR is the J/ψ to dimuon branching ratio and amounts to $(5.96 \pm 0.03)\%$ [18], $N_{\rm MB}$ is the number of minimum bias events, $N_{\rm J/\psi}(\Delta y, \Delta p_{\rm T})$ is the inclusive J/ψ yield for a given range in $p_{\rm T}$ and y, and $A \times \epsilon(\Delta y, \Delta p_{\rm T})$ is the acceptance times efficiency of the detector.

In this analysis, I contributed to the extraction of the J/ψ yields, to the computation of the realistic acceptance times efficiency and to the estimation of the systematic uncertainties on, for example, signal extraction, MC input, trigger efficiency and pp cross section reference. Other analysis ingredients, such as the number of minimum bias events and some systematic uncertainties (on normalization factor, tracking efficiency, matching efficiency, nuclear overlap function and centrality limit), are obtained based on the results from other analysers. As a result, I obtain the J/ψ $R_{\rm AA}$ by using the full data samples of Run 2 while the previously published results were using the 2015 data samples only.

In sections 5.1.1 and 5.1.2, the event and track selections for the Pb-Pb data samples are described. In section

5.1.3, the J/ψ signals are extracted in various p_{T} and centrality intervals at forward rapidity. In section 5.1.4, the J/ψ acceptance and efficiency of the detector is estimated by using MC simulations. In section 5.1.5, the normalization factor for the dimuon triggerred events is evaluated and consequently the equivalent number of minimum bias events is estimated. Besides, the systematic uncertainties on the J/ψ R_{AA} are computed and shown in section 5.1.6. The J/ψ invariant yields and R_{AA} results are presented in section 5.2 and 5.3, respectively. The R_{AA} results are compared to the earlier published results at the same energy and to theoretical computations in section 5.4.

5.1 Data analysis

5.1.1 Data samples and event selection

The analyzed data samples are the data recorded in the 2015 and 2018 Pb-Pb collisions at $\sqrt{s_{\mathrm{NN}}} = 5.02$ TeV. They consist of 365 runs passing the QA selection. Tab. 5.1 shows the list of runs analyzed. In this analysis, the invariant mass fits are built from events firing the unlike-sign dimuon trigger CMUL7-B-NOPF-MUFAST (CMUL7) for direct fit or firing either CMUL7 or the like-sign dimuon trigger CMLL7-B-NOPF-MUFAST (CMLL7) for event mixing fit (see section 5.1.3). Such selection, including CMUL7 or CMLL7, is less biased than selecting the CMUL7 triggered events when one wants to use the event mixing technique[1] to subtract the uncorrelated background, as we will see later. For event-mixing purpose, another trigger is used. It is the single low-p_{T} muon trigger CMSL7-B-NOPF-MUFAST (CMSL7) which is used to build the uncorrelated dimuon pairs. Besides, the physics selection (PS) criterion is applied to remove the beam induced background events by using the VZERO and the ZDC timing information to perform timing cuts on signals. The physics selection rejects about 0.3% of the events in the Pb-Pb data of Run 2. Centrality percentile in Pb-Pb collisions is determined based on a fit of the VZERO amplitude distribution as described in appendix A. The centrality class of collisional events are calibrated up to 90% centrality. As described in section 3.3.2, the minimum bias (MB) trigger used in Pb-Pb analyses requires a signal in both V0-A and V0-C. In addition, the number of MB events is flat as a function of centrality.

5.1.2 Track selection

Many particles are produced in a Pb-Pb collision and some of them will go through the muon spectrometer at forward rapidity. In order to select muon candidates, the following track selections are applied:

- -4 $< \eta_\mu <$ -2.5 to reject tracks at the edges of the Muon Spectrometer acceptance;
- 2$< \theta_{\mathrm{abs}} < 10^\circ$, where θ_{abs} is the angle between the beam axis and the track at the end of the absorber, in order to exclude the tracks crossing the thickest part of the absorber;

[1]For more detail of the event mixing technique, see section 5.1.3.

LHC15o				LHC18q				LHC18r		
244918	245705	246222	246859	295584	295829	296197	296550	296690	296975	297442
244980	245729	246225	246864	295585	295831	296198	296551	296691	296976	297446
244982	245731	246272	246865	295586	295854	296241	296552	296694	296979	297450
244983	245738	246275	246867	295587	295855	296242	296553	296749	297029	297451
245064	245752	246276	246871	295588	295856	296243	296615	296750	297031	297452
245066	245759	246390	246930	295589	295859	296244	296616	296752	297035	297479
245068	245766	246391	246937	295612	295860	296246	296618	296781	297085	297481
245145	245775	246392	246942	295615	295861	296247	296619	296784	297117	297483
245146	245785	246424	246945	295665	295863	296269	296622	296785	297118	297512
245151	245793	246428	246948	295666	295881	296270	296623	296786	297119	297537
245152	245829	246431	246949	295667	295908	296273		296787	297123	297540
245231	245831	246433	246980	295668	295909	296279		296791	297124	297541
245232	245833	246434	246982	295671	295910	296280		296793	297128	297542
245233	245949	246487	246984	295673	295913	296303		296794	297129	297544
245253	245952	246488	246989	295675	295936	296304		296799	297132	297558
245259	245954	246493	246991	295676	295937	296307		296836	297133	297588
245343	245963	246495	246994	295677	295941	296309		296838	297193	297590
245345	245996	246675		295714	295942	296312		296839	297194	297595
245346	246001	246676		295716	295943	296376		296848	297196	
245347	246003	246750		295717	295945	296377		296849	297218	
245353	246012	246751		295718	295947	296378		296850	297219	
245401	246036	246755		295719	296061	296379		296851	297221	
245407	246037	246757		295723	296062	296380		296852	297222	
245409	246042	246758		295725	296063	296381		296890	297278	
245410	246048	246759		295753	296065	296383		296894	297310	
245446	246049	246760		295754	296066	296414		296899	297312	
245450	246053	246763		295755	296068	296419		296900	297315	
245496	246087	246765		295758	296123	296420		296903	297317	
245501	246089	246804		295759	296128	296423		296930	297363	
245504	246113	246805		295762	296132	296424		296931	297366	
245505	246115	246806		295763	296133	296433		296932	297367	
245507	246148	246807		295786	296134	296472		296934	297372	
245535	246151	246808		295788	296135	296509		296935	297379	
245540	246152	246809		295791	296142	296510		296938	297380	
245542	246153	246844		295816	296143	296511		296941	297405	
245543	246178	246845		295818	296191	296514		296966	297408	
245554	246181	246846		295819	296192	296516		296967	297413	
245683	246182	246847		295822	296194	296547		296968	297414	
245692	246217	246851		295825	296195	296548		296969	297415	
245700	246220	246855		295826	296196	296549		296971	297441	
CMUL7 triggered events before PS				CMUL7 triggered events before PS				CMUL7 triggered events before PS		
1.269×10^8				1.112×10^8				1.634×10^8		
CMUL7 triggered events after PS				CMUL7 triggered events after PS				CMUL7 triggered events after PS		
1.266×10^8				1.108×10^8				1.630×10^8		

Table 5.1: List of QA checked runs in the first reconstruction production of LHC15o, and the third reconstruction production of LHC18q and LHC18r, along with the total CMUL7 triggered events in the centrality class 0–90% before and after physics selections.

- tracking track which matches a trigger track, whose p_{T} is required to be above the low trigger p_{T} threshold, $p_{\mathrm{T}}^{\mathrm{trig}}$, with $p_{\mathrm{T}}^{\mathrm{trig}} \approx 1$ GeV/c. It reduces the background from π and K decays.

- $p \times$ DCA cut within 6 σ is applied, where $p \times$ DCA is the product of the track momentum with the Distance of Closest Approach (DCA). The DCA is the distance in the transverse plane between the interaction point and the extrapolated muon track. This cut removes the tracks which do not originate from the interaction point.

The selected muons are then combined to form muon pairs. Further selections are applied to the muon pairs (dimuons):

- the two muons must have charges of opposite sign (OS dimuon),

- the dimuon satisfies the following rapidity cut: $2.5 < y < 4.0$,

- the dimuon p_{T} cut: $p_{\mathrm{T}} < 20$ GeV/c.

Note that the track selections in Pb-Pb collisions are the same as the ones in pp collisions, as indicated in section 4.1.2.

5.1.3 Signal extraction

As in section 4.1.3, the OS dimuon invariant mass spectrum is used to extract the J/ψ yield. The formula for the dimuon invariant mass can be found in Eq. 4.2. The signal extraction is first performed with a direct fit of the OS dimuon invariant mass spectra with a sum of two functions describing the signal shapes (J/ψ and ψ(2S), see section 4.1.3) and one function describing the background shape. The event mixing method is also used to estimate the uncorrelated background which is then subtracted from the OS dimuon invariant mass spectra. The event mixing method will be detailed later in this section. The J/ψ and ψ(2S) signal shapes as well as the different categories of background are discussed in section 4.1.3. Various fitting tests are performed to extract the J/ψ signal and the associated systematic uncertainty. The tests consist of multiple choices of signal functions (and tail parameters), background functions, and fitting ranges, as explained below.

In the following, the signal functions, the tail parameters and the background functions already used for the pp analysis are only listed. However, the functions that are only used in the Pb-Pb analysis are presented in more details.

The J/ψ peak is fitted with:

- an extended Crystal Ball (CB2) function (see Appendix B),

- a function adapted from the one of the NA60 experiment (NA60) (see Appendix B).

Several hypotheses have been considered to tune the CB2 and NA60 function tail parameters either using embedded MC simulations[2] or the high-statistic pp data sample. In total, two sets of tails have been considered:

- tails obtained by fitting the hadronic J/ψ production in embedded MC simulations using the Geant3 transport code [214]. The reconstructed J/ψ mass spectra, integrated over centrality, are merged period per period with a weight corresponding to the number of CMUL7 events in data over the number of CINT7 events in the MC (CB2 and NA60 functions). Besides, tail parameters do not depend on centrality, as seen from previous studies [224] and therefore, they are extracted from the J/ψ mass spectra integrated over centrality.
- tails obtained by fitting the hadronic J/ψ production in pp data analysis at $\sqrt{s} = 13$ TeV [125] (CB2 function).

Figure 5.1 shows an example of the tail parameter extraction for the CB2 function (red) by using a MC simulation production simulated with the Geant3 transport code.

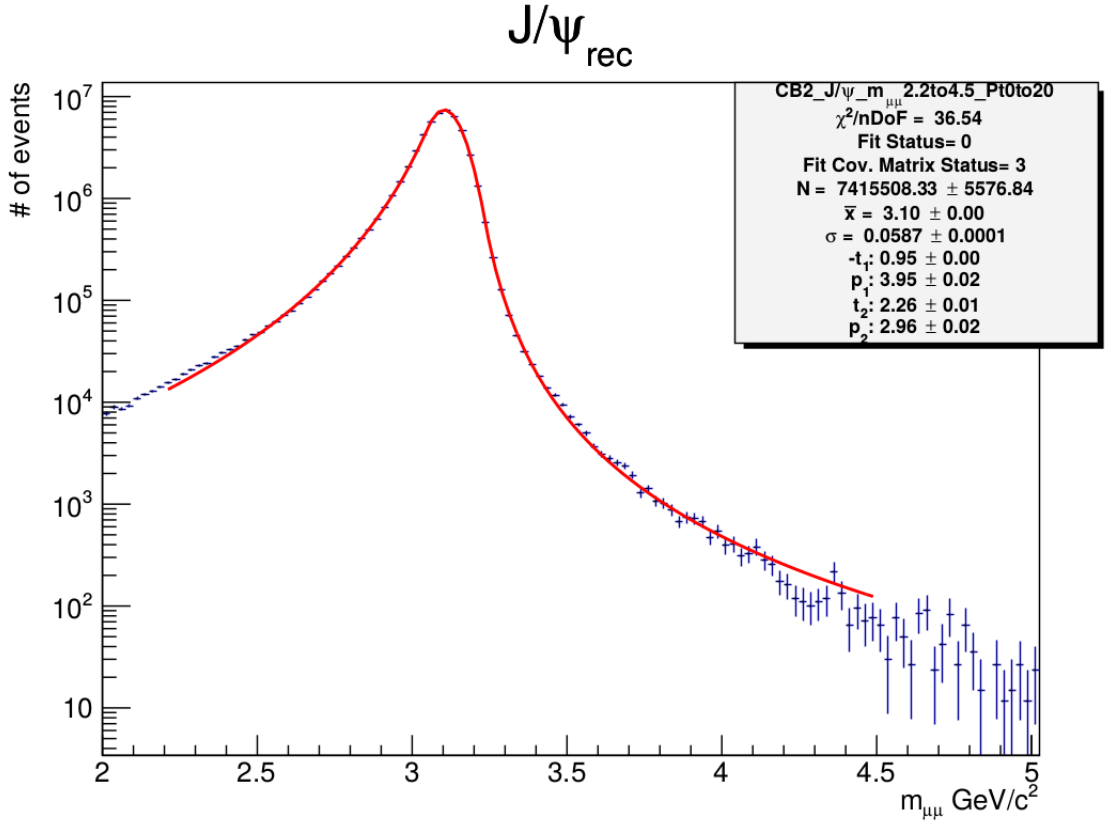

Figure 5.1: Example of extraction of the CB2 function tail parameters by using the Geant3 MC simulation in the J/ψ mass region $2.2 < m_{\mu\mu} < 4.5$ GeV/c^2, for $p_{\rm T} < 20$ GeV/c and for $2.5 < y < 4$.

For the direct fit, the background is fitted with:

- A variable width Gaussian (VWG),
- A ratio of a second order polynomial over a third order polynomial (POL2/POL3).

[2]Embedded MC simulation is detailed in section 5.1.4

In the case of the event mixing procedure, as we will see below, the remaining background is quite small and described by:

- A sum of two exponential functions.

The function descriptions and the formulas can be found in Appendix B.
Two invariant mass fitting ranges have been considered for the global fit of the invariant mass spectra:

- $2.2 < m_{\mu\mu} < 4.5$ GeV/c^2,
- $2.4 < m_{\mu\mu} < 4.7$ GeV/c^2.

To judge the fitting goodness, the same checks on variables given by the fitting process, as described in section 4.1.3, are performed in the Pb-Pb analysis.

Figure 5.2 to 5.4 show examples of the OS dimuon invariant mass distribution, at forward rapidity, for some $p_{\rm T}$ ranges and in the 0–20%, 20–40% and 40–90% centrality intervals, respectively. The spectra are fitted with two signal shapes describing the J/ψ (red solid line) as well as the ψ(2S) (green solid line), and with a background shape (dashed-red line). The global fit, which is the sum of the two signal shapes and of the background shape, is shown in blue. The ψ(2S) contribution is very small in some $p_{\rm T}$ and centrality classes.

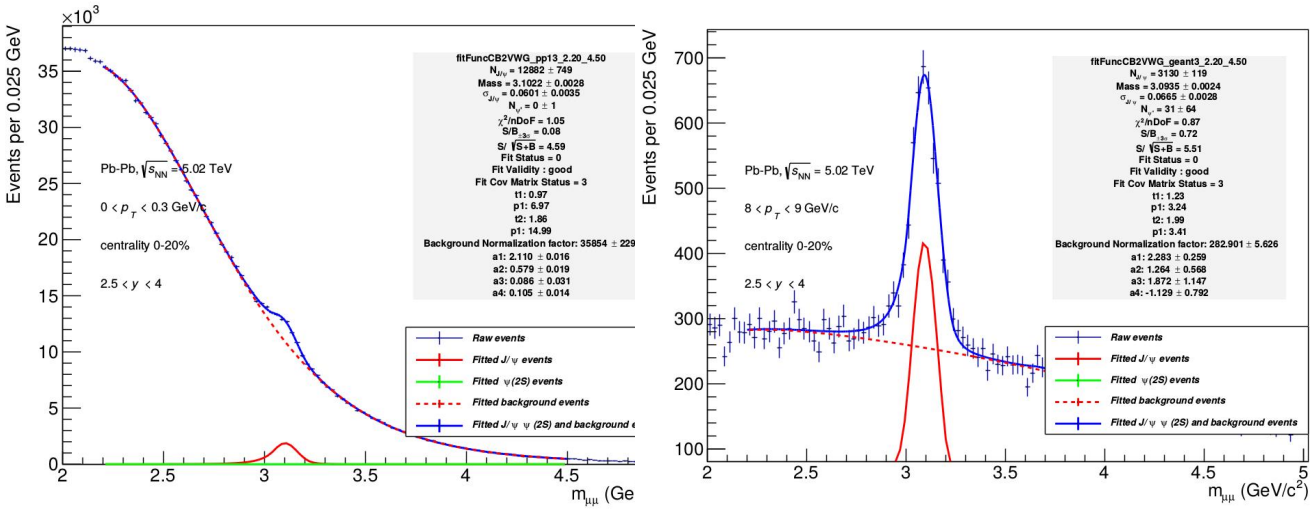

Figure 5.2: Example of J/ψ dimuon OS invariant mass spectra fits in the 0–20% centrality bin and in two $p_{\rm T}$ ranges. The upper right and left inserts show the detailed values of the fitting results and the kinematic cuts applied to the reconstructed dimuon.

Since there is a large background contribution around the J/ψ mass region particularly at low $p_{\rm T}$ and in the most central Pb-Pb collisions, the event mixing method is applied to subtract the uncorrelated OS dimuon background. The idea of this method is to mix one muon track from a given event with another one from the next events (up to the next 20 events). In this method, pools of events per centrality bin width of 10% are built in order to mix muons

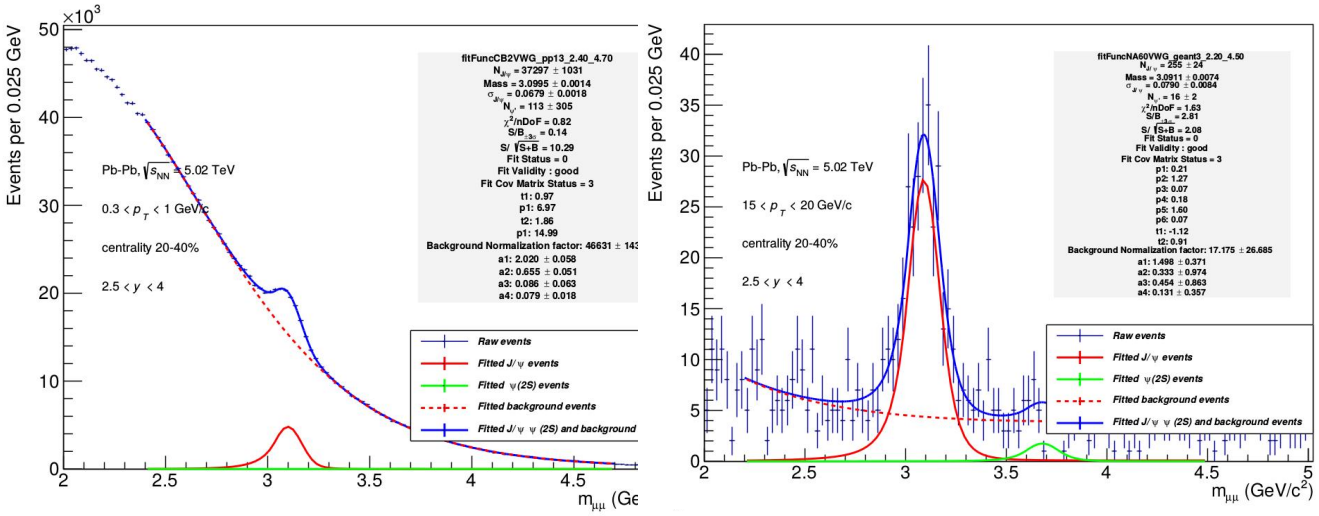

Figure 5.3: Example of J/ψ dimuon OS invariant mass spectra fits in the 20–40% centrality bin and in two p_{T} ranges. The upper right and left inserts show the detailed values of the fitting results and the kinematic cuts applied to the reconstructed dimuon.

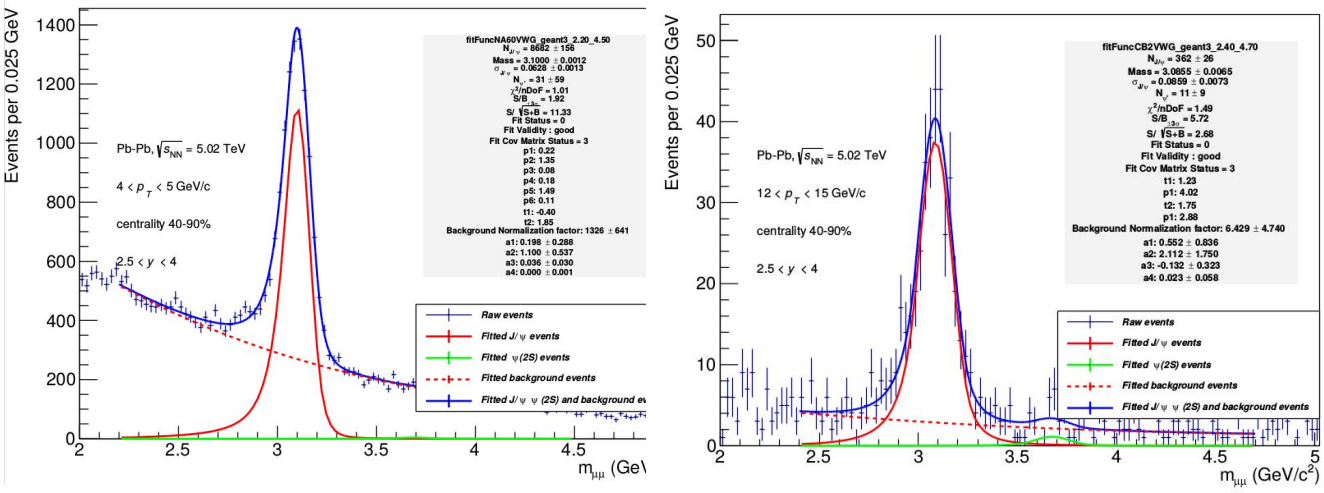

Figure 5.4: Example of J/ψ dimuon OS invariant mass spectra fits in the 40–90% centrality bin and in two p_{T} ranges. The upper right and left inserts show the detailed values of the fitting results and the kinematic cuts applied to the reconstructed dimuon.

belonging to events with a similar multiplicity. Those muon tracks are selected from CMSL triggered events as it was shown in [225] that this trigger provides a better description of the uncorrelated background for the like-sign pairs. A normalization factor is needed to normalize the mixed dimuon background events to the raw mass spectra. The normalization factor is given by:

$$F = \frac{\int_{m_1}^{m_2} 2R_{\rm acc}\sqrt{N^{++}_{\rm real}N^{--}_{\rm real}}{\rm d}m}{\int_{m_1}^{m_2} N^{+-}_{\rm mixed}{\rm d}m} \tag{5.3}$$

where m is the dimuon mass. The lower ($m_1 = 2$ GeV/c^2) and upper ($m_2 = 8$ GeV/c^2) bounds are set to exclude the regions which is close to the trigger threshold and in which bottomina exist, respectively. The acceptance factor $R_{\rm acc}$ is defined as:

$$R_{\rm acc} = \frac{N^{+-}_{\rm mixed}}{2\sqrt{N^{++}_{\rm mixed}N^{--}_{\rm mixed}}}. \tag{5.4}$$

$R_{\rm acc} \neq 1$ indicates an asymmetry in the detection of the muons with opposite charges while one can expects $R_{\rm acc} = 1$ for an ideal detector (see Appendix B in [226] for more details). The other variables in Eq. 5.3 and Eq. 5.4 are defined such as:

- $N^{++}_{\rm mixed}, N^{+-}_{\rm mixed}, N^{--}_{\rm mixed}$ are the number of dimuons obtained from the event mixing sample in the CMSL7 triggered events. The superscripts specify the electric charges of the two muons.

- $N^{++}_{\rm real}, N^{+-}_{\rm real}, N^{--}_{\rm real}$ are the number of dimuons obtained in the raw data from the CMUL7 or CMLL7 triggered events.

Note that the CMLL7 trigger is downscaled in the 2018 Pb-Pb data taking periods. In order to properly normalize the number of dimuon pairs in the CMLL7 trigger, the OS and like-sign (LS) raw data dimuon pairs from CMLL7 triggered events, which do not contain CMUL7 triggered events, are weighted by the inverse of the downscaling factor, run by run.

centrality	0–10%	10–20%	20–30%	30–40%	40–50%	50–60%	60–70%	70–80%	80–90%
F_{2018}	0.584	0.449	0.325	0.222	0.14	0.08	0.043	0.02	0.008
F_{2015}	0.199	0.153	0.111	0.075	0.047	0.027	0.015	0.007	0.003

Table 5.2: Summary of the normalization factor, F_{2018} and F_{2015} for the 2018 and 2015 Pb-Pb data samples, respectively.

Table 5.2 tabulates the normalization factor (F_{2018} and F_{2015}) for the 2018 and 2015 Pb-Pb data samples, respectively. Figure 5.5 shows the acceptance factor computed by using Eq. 5.4 for the 0–10% centrality class and for the 2015 (2018) data samples in the left (right) panels. For the 2015 and 2018 data samples, the R_{acc} values over

the mass range $2 < m_{\mu\mu} < 8$ GeV/c^2 approximate unity as expected. In order to control the event mixing method quality, the mass, rapidity and p_{T} distributions of the OS and also of the LS raw muon pairs (red) and mixed muon pairs (blue) are shown in Figure 5.6. The ratios of raw muon pair to mixed muon pair distributions are also shown below each distribution panel. The p_{T} and rapidity distributions are obtained from the muon pairs in the mass range $2 < m_{\mu\mu} < 5$ GeV/c^2. For the OS muon pairs (middle panel), the mass ratio is close to unity except in the J/ψ mass region, as expected. The rapidity ratio is within 2–4% and can reach 10% at the edges of the rapidity, and the p_{T} ratio is within 4% at low p_{T} and above 10% for $p_{\mathrm{T}} > 10$ GeV/c. As for the LS muon pairs (left and right panels), the mass, p_{T} and rapidity ratios are within about 2% except at $p_{\mathrm{T}} \approx 5$ GeV/c for the positive-positive like-sign pair and at the edges of the rapidity where it can reach up to 5%. Overall, the event mixing method demonstrates a good background description in the J/ψ mass region.

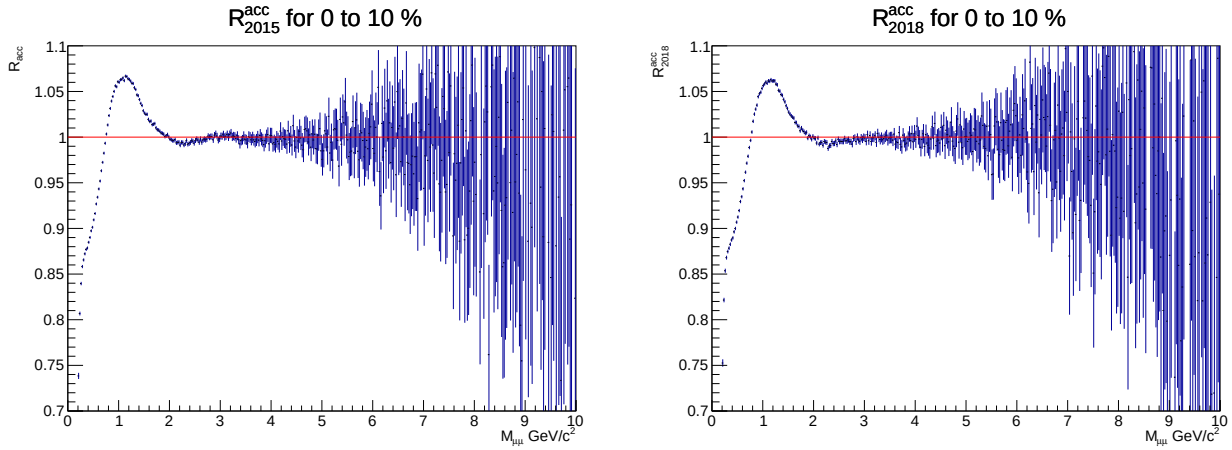

Figure 5.5: The acceptance factor R_{acc} obtained with the mixed muon pair events for the 0–10% centrality class in the 2015 (left panel) and 2018 (right panel) data samples.

Figure 5.7 shows examples of the event mixing fits. Subtracted invariant-mass spectra are obtained after the subtraction of the uncorrelated background described by the event mixing technique. The residual background, originating from correlated muon pairs, then needs to be fitted. Fit function for the residual invariant-mass spectra is a sum of two functions including a signal and a background shape. Note that only one parametrisation (a sum of two exponential functions) is used to describe the residual background because this contribution is small.

In total, 18 fits are performed for the systematic study of the signal extraction. For each bin of p_{T} and centrality, the combination of all the signal shapes, background shapes, fitting ranges and sets of tail parameters have been considered. The final number of J/ψ is calculated as the weighted mean of all the tests by using Eq. 4.3 for the average number of J/ψ and Eq. 4.4 for the statistical uncertainty. The systematic uncertainty is defined as the weighted Root Mean Square (RMS) of the results and is computed by using Eq. 4.5. The results have been weighted such that fits with pp data tail parameters have the same weight as tests with embedded MC tail parameters. Figures 5.8, 5.9, and 5.10 show the raw number of J/ψ as a function of the 18 fitting tests for $0 \leq p_{\mathrm{T}} < 20$ GeV/c and for 0–20%, 20–40%,

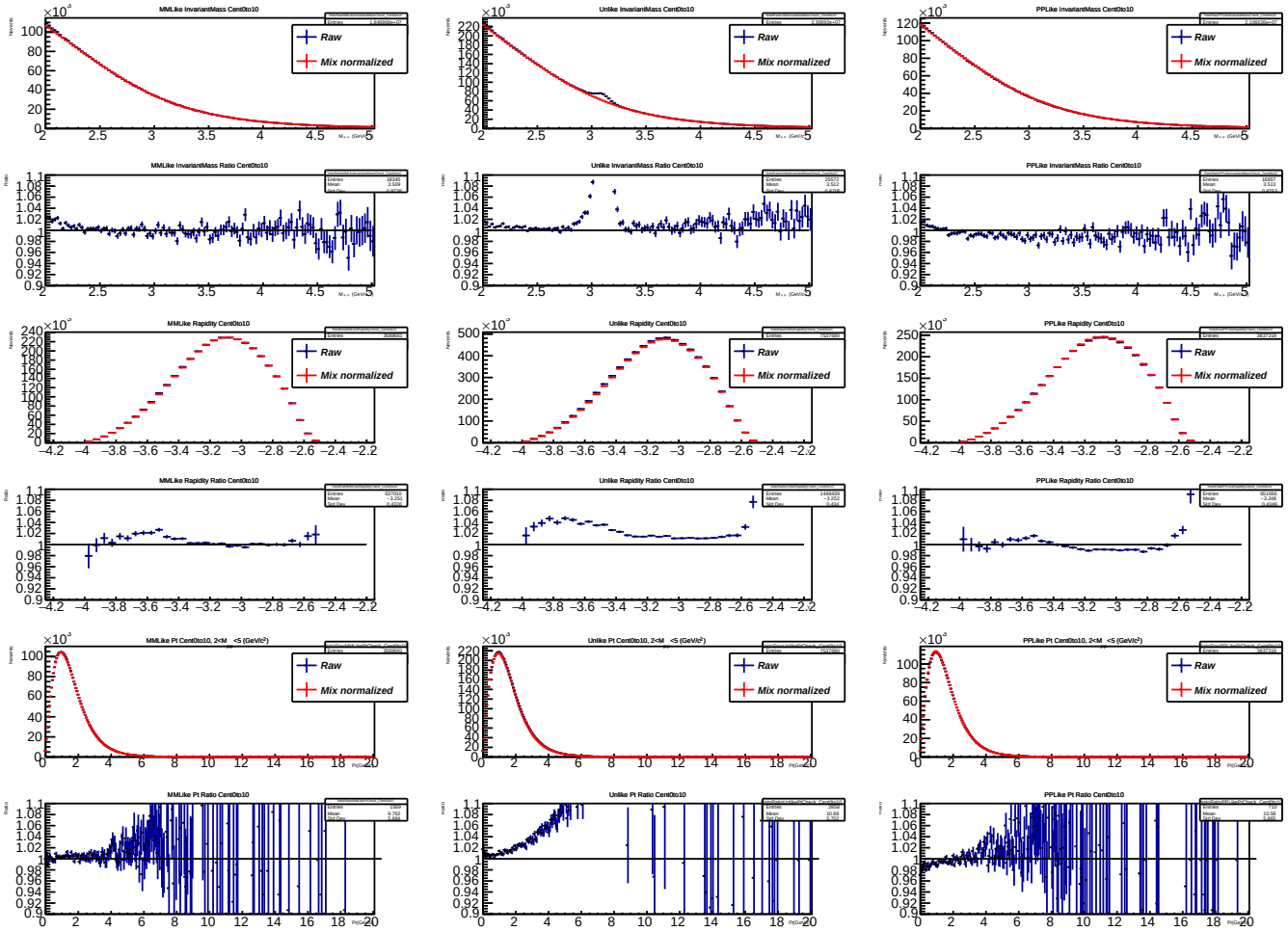

Figure 5.6: Control plots of the event-mixing method: the invariant mass (first row), rapidity (third row) and p_{T} (fifth row) spectra of the raw events (blue) and the mixed muon pair events (red) are shown for the 0–10% centrality class in the 2018 Pb-Pb data samples. Below each mass, p_{T} and rapidity spectrum, the ratios of the raw to the mixed muon pair distributions are also shown. The first (third) column corresponds to the negative-negative (positive-positive) LS pairs. The second column corresponds to the OS pairs.

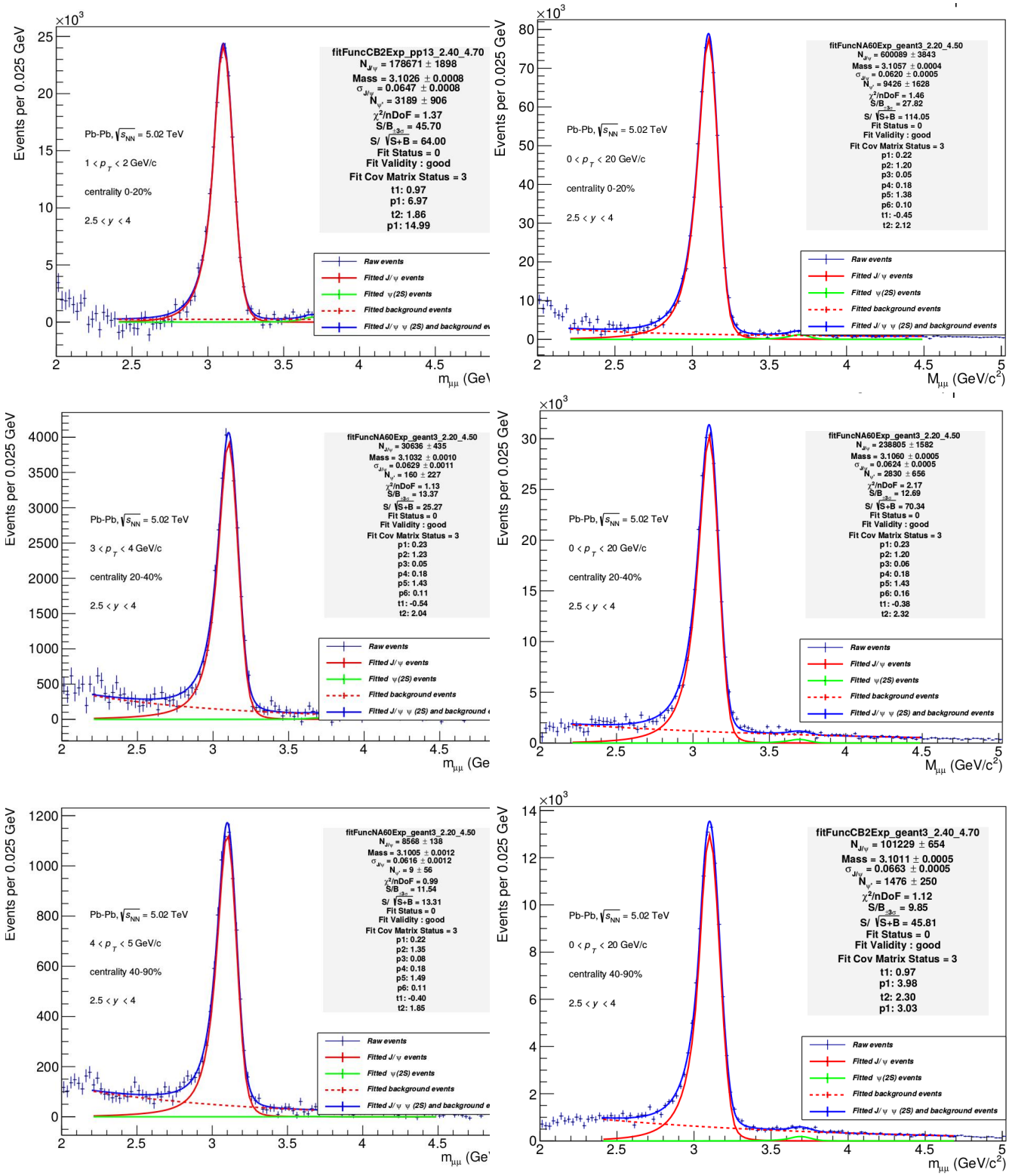

Figure 5.7: Examples of event mixing fits of the dimuon OS invariant mass spectra at forward rapidity in several p_{T} and centrality ranges in Pb-Pb collisions at $\sqrt{s_{\mathrm{NN}}} = 5.02$ TeV. The upper right and left inserts show the detailed values of the fitting results and the kinematic cuts which are applied to the dimuons.

and 40–90% centrality classes, respectively, as well as the J/ψ width, mass and χ^2/NDF of the fits. Furthermore, in order to determine the $p_{\rm T}$ dependence of the J/ψ yield, the 18 fitting tests are also performed for 15 $p_{\rm T}$ bins in three centrality ranges (0–20%, 20–40%, and 40–90%).

The systematic uncertainties on the J/ψ signal extraction vary in between 1.6–5.8%, 1.9–4.5%, and 1.6–10.7% for 0–20%, 20–40%, and 40–90% centrality classes, respectively. The number of J/ψ for various $p_{\rm T}$ intervals are given in Table 5.3 and 5.4 in the 0–20%, 20–40%, and 40–90% centrality classes. A check was performed in order to compare the sum of the J/ψ yield integrated over $p_{\rm T}$ bins with the J/ψ yield obtained from the direct fit of the invariant mass spectrum integrated over $p_{\rm T}$. This check shows that there is a very small difference in the number of J/ψ (within 1% in the three centrality bins).

$p_{\rm T}$ (GeV/c)	$N_{\rm raw}^{J/\psi}$ ± stat.(%)± syst. (%)
centrality 0 – 20%	
0–0.3	13890 ± 824 (5.9) ± 552 (4.0)
0.3–1	106158 ± 2240 (2.1) ± 2985 (2.8)
1–2	183306 ± 2389 (1.3) ± 3277 (1.8)
2–3	131450 ± 1602 (1.2) ± 3950 (3.0)
3–4	73631 ± 1340 (1.8) ± 2069 (2.8)
4–5	37874 ± 764 (2.0) ± 1064 (2.8)
5–6	20346 ± 432 (2.1) ± 329 (1.6)
6–7	10440 ± 260 (2.5) ± 188 (1.8)
7–8	5796 ± 179 (3.1) ± 99 (1.7)
8–9	3125 ± 121 (3.9) ± 46 (1.5)
9–10	1826 ± 92 (5.0) ± 70 (3.9)
10–11	1148 ± 68 (5.9) ± 34 (2.9)
11–12	701 ± 51 (7.3) ± 23 (3.3)
12–15	1050 ± 63 (6.0) ± 30 (2.9)
15–20	393 ± 37 (9.4) ± 23 (5.8)
0–20 (sum of $p_{\rm T}$ bins)	591137 ± 4803 (0.7)
0–20 (fit)	591968 ± 4294 (0.7) ± 14172 (2.4)

Table 5.3: Raw number of J/ψ in $p_{\rm T}$ intervals and in the 0–20% centrality class.

5.1.4 Acceptance efficiency

The principle of performing a MonteCarlo (MC) simulation to estimate the correction of the J/ψ yield from the acceptance and efficiency of the detector is presented in section 4.1.4. In the case of Pb-Pb, the initial J/ψ is generated according to the following input $p_{\rm T}$ shape:

$$f_{0-90\%}(p_{\rm T}) = p_0 \times \frac{p_{\rm T}}{\left[1 + \left(\frac{p_{\rm T}}{p_1}\right)^{p_2}\right]^{p_3}} \tag{5.5}$$

where $p_0 = 1.00715 * 10^6$, $p_1 = 3.50274$, $p_2 = 1.93403$ and $p_3 = 3.96363$. The J/ψ input y shape is given by:

$$f_{0-90\%}(y) = p_0 \times e^{-0.5\left(\frac{y-p_1}{p_2}\right)^2} \tag{5.6}$$

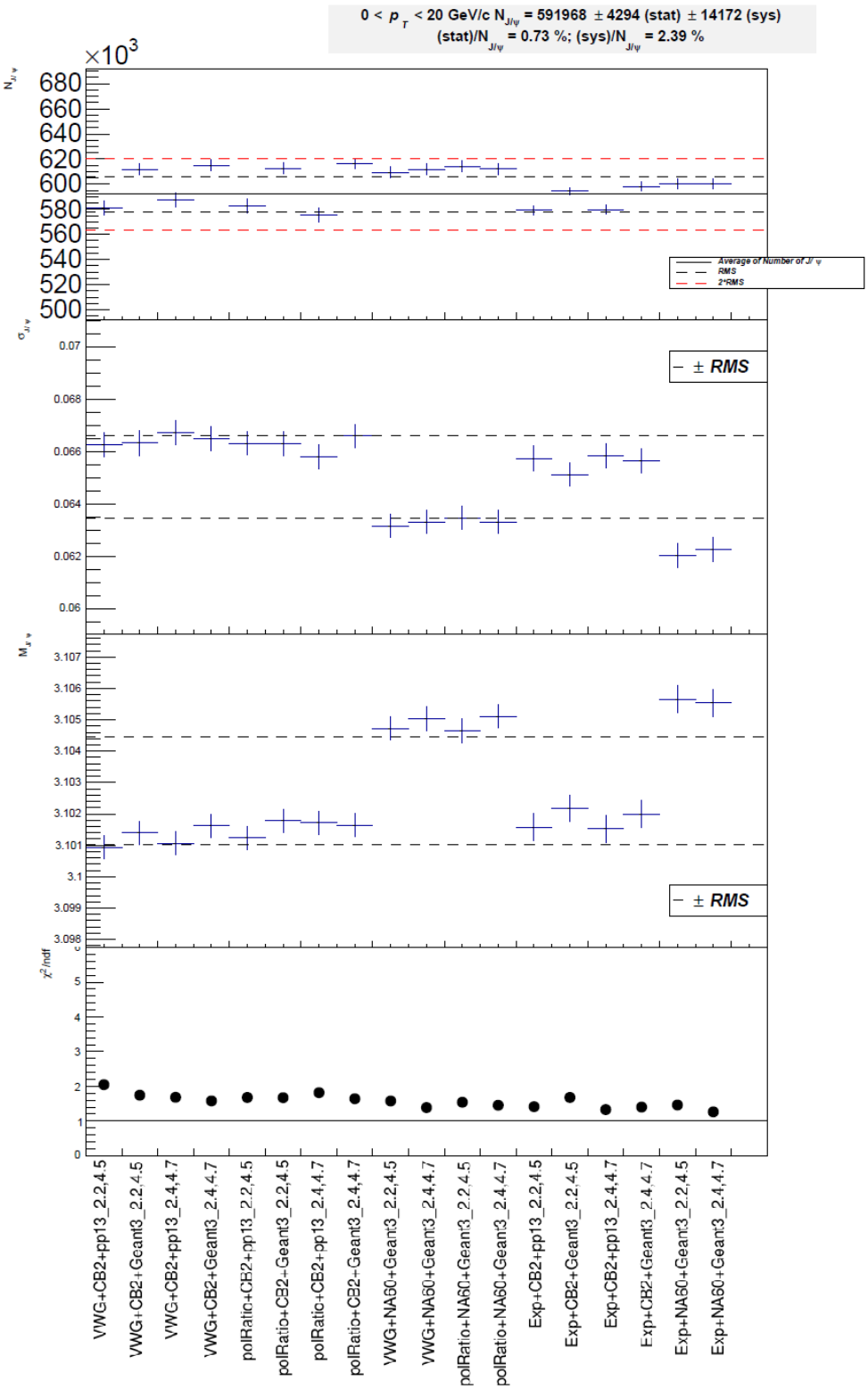

Figure 5.8: Raw number of J/ψ, J/ψ width, mass and χ^2/NDF as a function of the fitting tests for $0 \leq p_{\mathrm{T}} < 20$ GeV/c and for the 0–20 % centrality class.

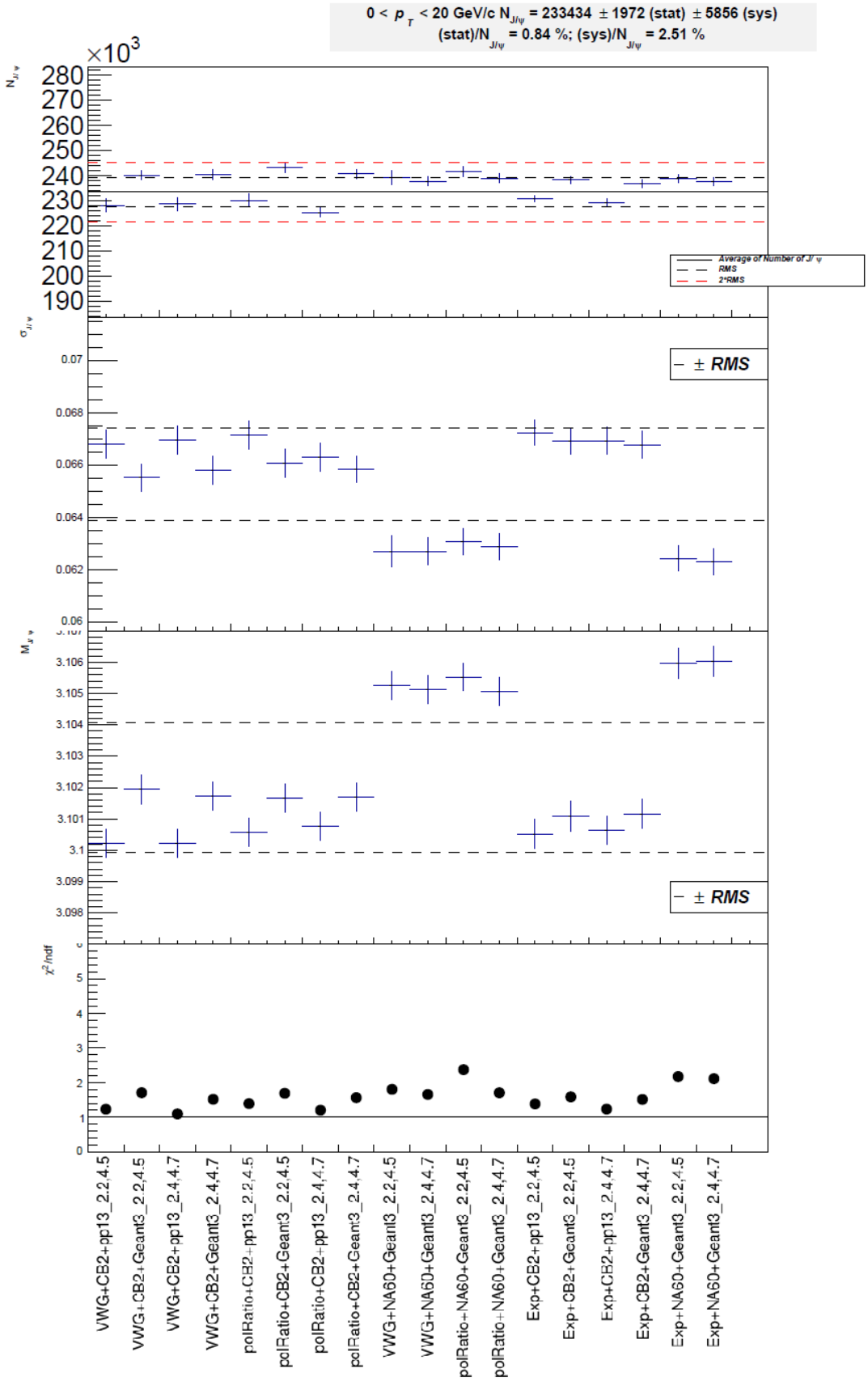

Figure 5.9: Raw number of J/ψ, J/ψ width, mass and χ^2/NDF as a function of the fitting tests for $0 \leq p_{\mathrm{T}} < 20$ GeV/c and for the 20–40 % centrality class.

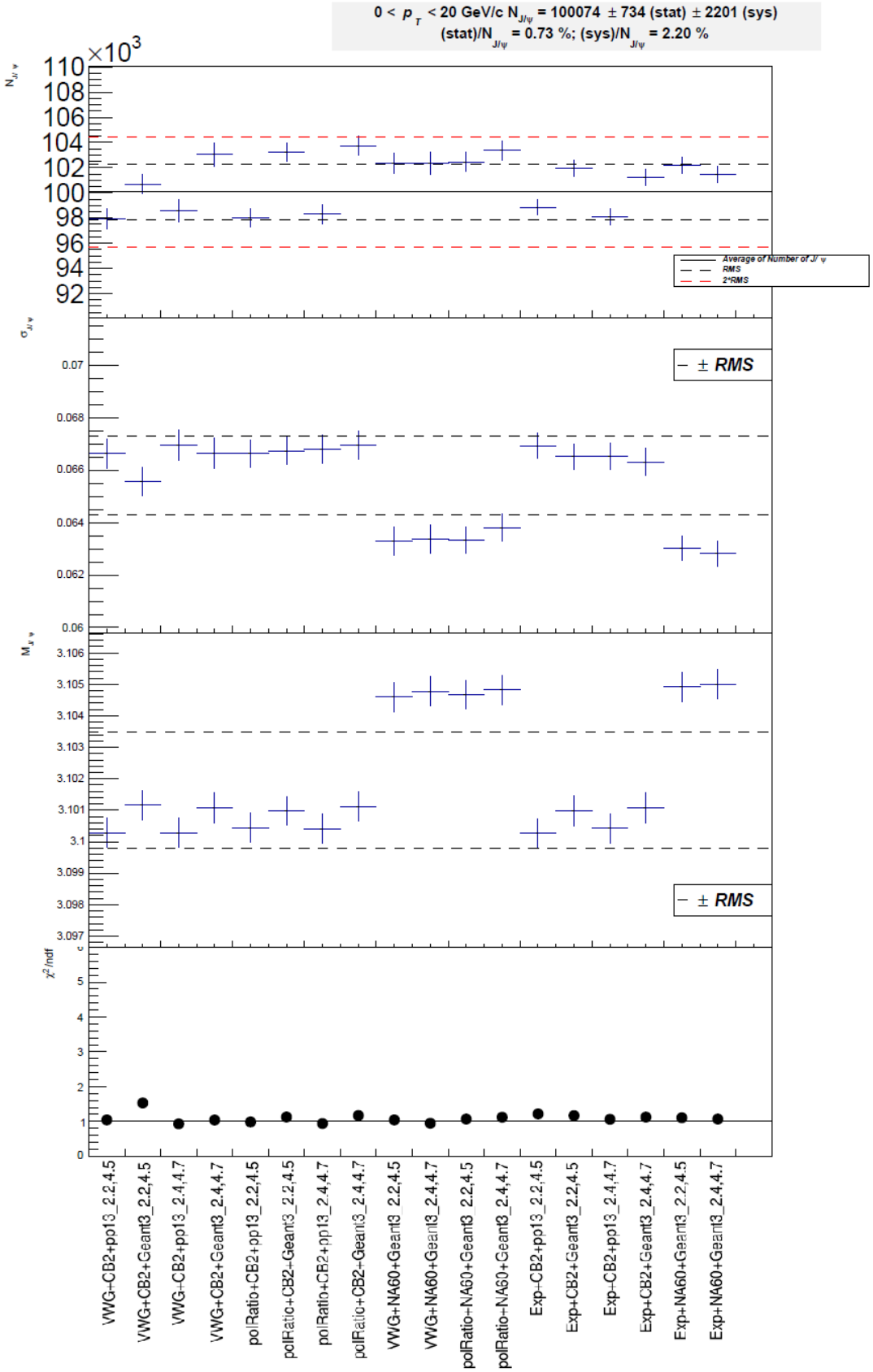

Figure 5.10: Raw number of J/ψ, J/ψ width, mass and χ^2/NDF as a function of the fitting tests for $0 \leq p_{\mathrm{T}} < 20$ GeV/c and for the 40–90 % centrality class.

p_{T} (GeV/c)	$\mathrm{N}_{\mathrm{raw}}^{J/\psi}$ ±stat. (%)±syst. (%)	p_{T} (GeV/c)	$\mathrm{N}_{\mathrm{raw}}^{J/\psi}$ ±stat. (%)±syst. (%)
centrality 20 – 40%		centrality 40 – 90%	
0–0.3	6584 ± 401 (6.1) ± 206 (3.1)	0–0.3	6379 ± 156 (2.4) ± 139 (2.2)
0.3–1	38709 ± 984 (2.5) ± 1052 (2.7)	0.3–1	14349 ± 389 (2.7) ± 416 (2.9)
1–2	66303 ± 1241 (1.9) ± 1748 (2.6)	1–2	25545 ± 436 (1.7) ± 609 (2.4)
2–3	49791 ± 972 (2.0) ± 1272 (2.6)	2–3	19354 ± 321 (1.7) ± 458 (2.4)
3–4	30467 ± 491 (1.6) ± 892 (2.9)	3–4	13759 ± 215 (1.6) ± 438 (3.2)
4–5	17566 ± 306 (1.7) ± 447 (2.5)	4–5	8491 ± 148 (1.7) ± 221 (2.6)
5–6	9805 ± 206 (2.1) ± 189 (1.9)	5–6	5252 ± 111 (2.1) ± 95 (1.8)
6–7	5789 ± 140 (2.4) ± 112 (1.9)	6–7	3151 ± 78 (2.5) ± 56 (1.8)
7–8	3203 ± 97 (3.0) ± 67 (2.1)	7–8	1743 ± 55 (3.2) ± 41 (2.4)
8–9	1781 ± 70 (4.0) ± 49 (2.8)	8–9	1062 ± 42 (3.9) ± 35 (3.3)
9–10	1023 ± 54 (5.3) ± 21 (2.1)	9–10	584 ± 31 (5.3) ± 9 (1.6)
10–11	638 ± 41 (6.4) ± 13 (2.0)	10–11	347 ± 23 (6.5) ± 21 (6.0)
11–12	457 ± 36 (7.9) ± 14 (3.0)	11–12	220 ± 18 (8.3) ± 6 (2.7)
12–15	509 ± 37 (7.3) ± 23 (4.5)	12–15	381 ± 24 (6.3) ± 31 (8.1)
15–20	249 ± 24 (9.8) ± 6 (2.4)	15–20	123 ± 15 (12.1) ± 13 (10.7)
0–20 (sum of p_{T} bins)	232874 ± 2008 (0.9)	0–20 (sum of p_{T} bins)	100740 ± 750 (0.7)
0–20 (fit)	233434 ± 1972 (0.8) ± 5856 (2.5)	0–20 (fit)	100074 ± 734 (0.7) ± 2201 (2.2)

Table 5.4: Raw number of J/ψ in $\mathrm{p_T}$ intervals and in the 20–40% (left) and 40–90% (right) centrality classes.

where $p_0 = 1.09886 * 10^6$, $p_1 = 0$, $p_2 = 2.12568$. The parameters in Eqs. 5.5 and 5.6 are obtained from the fits of the J/ψ corrected yield from the 2015 Pb-Pb data for the 0–90% centrality class, corrected by using a pure J/ψ signal MC simulation. In order to simulate realistic acceptance and efficiency of the detector, the embedding technique is employed. A J/ψ MC event is embedded into a real event triggered by CINT7 (serving as minimum bias (MB) trigger) and in centrality bin width of 10% at the hit level in the detector. The acceptance and efficiency ($A \times \epsilon$) of the detector is then estimated, according to Eq. 4.8, by reconstructing embedded events in the simulation. In the MC, the same QA-checked runs as for the data (see Table 5.1) are analyzed. The analysis cuts on the reconstructed J/ψ in the simulation are similar to the ones used for the raw data sample except for the trigger selection. The CINT7 trigger cut is used for the reconstructed simulation. Two kinematic cuts corresponding to the interval of the measurements, namely $2.5 < y < 4$ and $0 \leq p_{\mathrm{T}} < 20$ GeV/c, are applied to the generated and reconstructed opposite-sign dimuons for the $A \times \epsilon$ calculation. In order to make the number of J/ψ in the MC proportional to the number of raw J/ψ extracted from the data and to account for the evolution of the detector status with time, two weights are considered:

- a weight proportional to the number of CMUL7 triggered events in each run (the run number weighting),
- a weight proportional to the number of raw J/ψ in each centrality bin (the centrality weighting).

For the first weight, we do not consider the number of raw J/ψ per run because the statistics is scarce and choose to use the number of CMUL7 triggered events which is almost proportional to the number of raw J/ψ. The uncertainty on the $A \times \epsilon$ is computed by taking either the value of $1/N_{\mathrm{gen}}$ or a regular the binomial error when the number of generated J/ψ N_{gen} is less or equal to the number of reconstructed J/ψ N_{rec}. In the case where N_{rec} is larger than N_{gen} (this can happen because of the J/ψ kinematic smearing for low-statistic runs), the uncertainty is computed as

$1/N_{\rm gen}$. The binomial error $\sigma_{\rm bino}$ is calculated as:

$$\sigma_{\rm bino} = \sqrt{\frac{N_{\rm rec}}{N_{\rm gen}} \times (\frac{1 - N_{\rm rec}/N_{\rm gen}}{N_{\rm gen}})} \tag{5.7}$$

The $A \times \epsilon_0$ is extracted run per run for each centrality bin and $p_{\rm T}$ interval. The index "0" for $A \times \epsilon_0$ corresponds to the initial MC kinematical distributions. Note that for the calculation of the $A \times \epsilon$, the J/ψ production is assumed

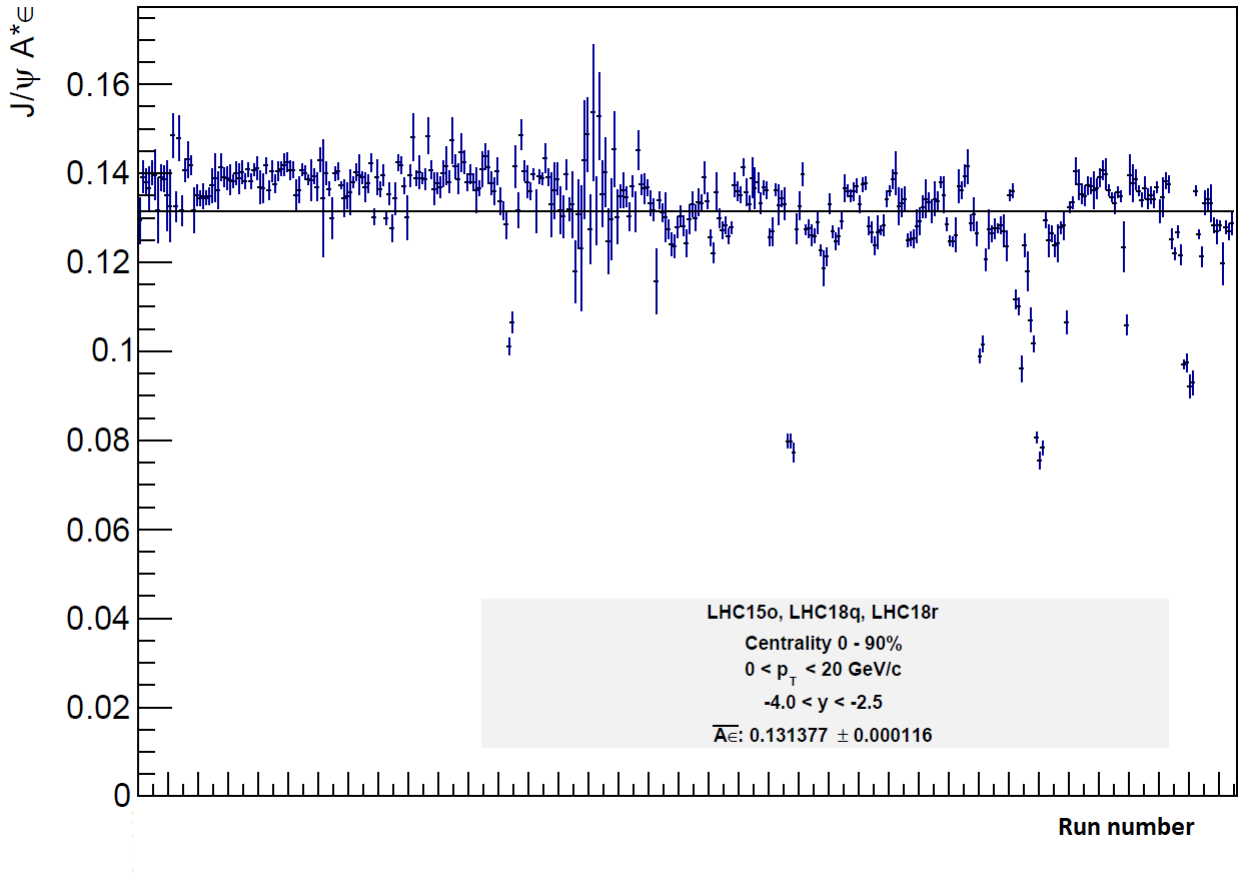

Figure 5.11: J/ψ $A \times \epsilon_0$ as a function of runs for LHC15o, 18q and 18r periods for $2.5 < y < 4$, $0 \leq p_{\rm T} < 20$ GeV/c and the 0–90% centrality class. The uncertainty corresponds to the statistical uncertainty.

to be unpolarised. Recent measurements [181] show that the J/ψ is slightly polarised within about 2.1σ at low $p_{\rm T}$ (2–4GeV/c) and for more details about quarkonium polarisation, one can refer to section 2.3.4. Figure 5.11 shows the $A \times \epsilon_0$ of the J/ψ as a function of the run number for the three Pb-Pb data-taking periods, for $2.5 < y < 4$ and for $0 \leq p_{\rm T} < 20$ GeV/c in the 0–90% centrality class. The $A \times \epsilon_0$ decreases for some runs and at the end of the LHC18r period[3]. Then in a given centrality bin, i, the $A \times \epsilon_{0,i}$ is averaged over the runs using as weight by the number of CMUL7 events. Note that the number of CMUL7 triggered events used as weight are integrated over

[3]The reason for the decrease of the acceptance and efficiency for some runs is related to high-voltage trips in muon tracking chambers and to inefficiency of some local boards in muon trigger chambers.

centrality. In this run weighting procedure, runs are discarded when $N_{\rm gen}$ is equal to 0. Such cases happen mainly in the high-$p_{\rm T}$ bins where the MC statistics can be scarce.

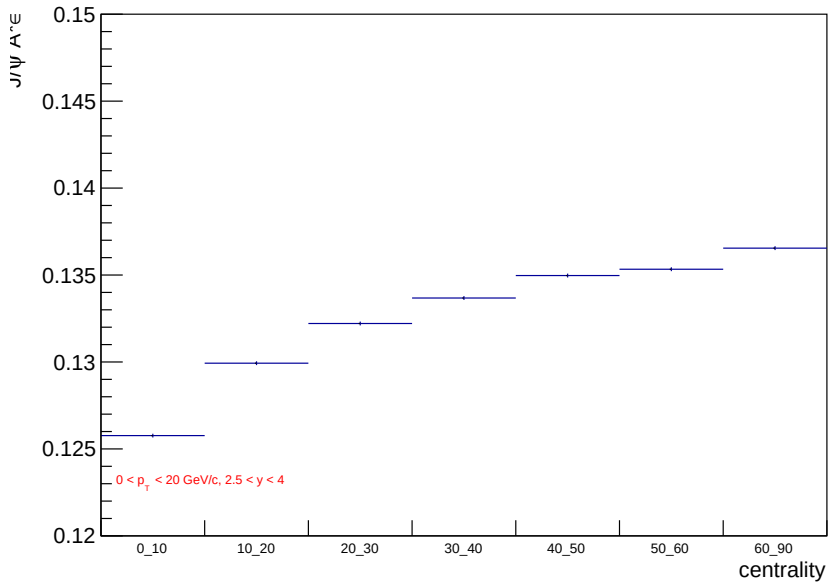

Figure 5.12: J/ψ $A\times\epsilon_0$ as a function of the centrality class in Pb-Pb collisions for $2.5 < y < 4$ and $0 \leq p_{\rm T} < 20$ GeV/c.

The embedded MC generates events according to MB events in centrality bin width of 10%. Figure 5.12 shows the $A \times \epsilon_0$ as a function of the centrality class for $0 < p_{\rm T} < 20$ GeV/c and $2.5 < y < 4$. The values of $A \times \epsilon_0$ for 40–50%, 50–60% and 60–90% are relatively close while the ones for 0–10%, 10–20%, 20–30% and 30–40% decrease when the centrality of the collision increases due to the tracking algorithm in tracking chambers and to the trigger algorithm in trigger chambers [212]. Therefore, the last three centrality classes are considered together in the MC when performing the tuning of the input shapes. For this analysis, we decided to use the following centrality classes: 0–10%, 10–20%, 20–30%, 30–40% and 40–90% for the tuning of input shape. The five panels of Figures 5.13 and 5.14 show the $p_{\rm T}$ and rapidity distributions of the J/ψ raw data corrected by $A \times \epsilon_0$ and the normalized input MC distributions for the 0–10%, 10–20%, 20–30%, 30–40% and 40–90% centrality intervals. The corrected $p_{\rm T}$ distributions depend on the centrality interval and is not in agreement with the original input MC shapes for most of the centrality intervals. One needs to tune the distributions to each centrality class in order to estimate a reliable acceptance and efficiency of the detector. For that purpose, the iterative procedure as defined in section 4.1.4 is used.

The $p_{\rm T}$ and y shapes are described by the input functions that are defined in Eqs. 5.5 and 5.6. Since the fit of the data with Eq. 5.5 is not able to describe the corrected data shape at high $p_{\rm T}$ (probably because of the non-prompt

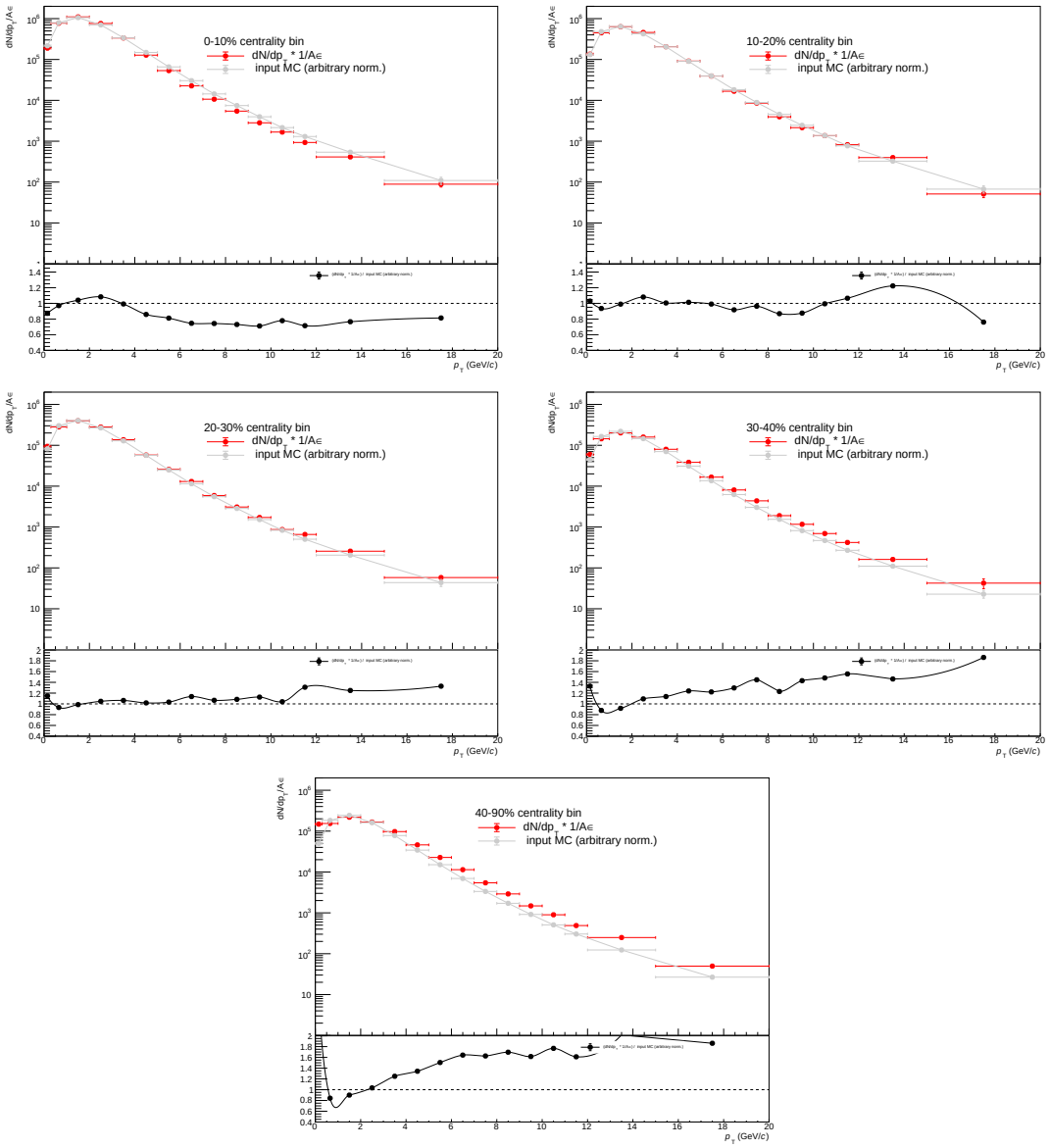

Figure 5.13: J/ψ differential $A\epsilon_0$ corrected distribution as a function of p_{T} for $2.5 < y < 4$, for the 0–10% (left top panel), 10–20% (right top panel), 20–30% (left middle panel), 30–40% (right middle panel) and 40–90% (bottom panel) centrality classes. The corrected distribution (red) are compared to the MC generated distribution (grey) before the iterative procedure.

J/ψ contribution), another empirical functional form is proposed:

$$f_i(p_{\mathrm{T}}) = p_0 \times \frac{p_{\mathrm{T}}}{\left[1 + \left(\frac{p_{\mathrm{T}}}{p_1}\right)^{p_2}\right]^{p_3}} + p_4 \times e^{-p_5 p_{\mathrm{T}}} \tag{5.8}$$

Eqs. 5.6 and 5.8 are used to fit the input MC shapes and corrected data. From the fits, new fit parameters are obtained. A weight can then be calculated with Eqs. 4.11, 4.12 and 4.13. Then the iterative procedure detailed in section 4.1.4 is performed. In this study, two iterations are performed and convergence is already obtained after

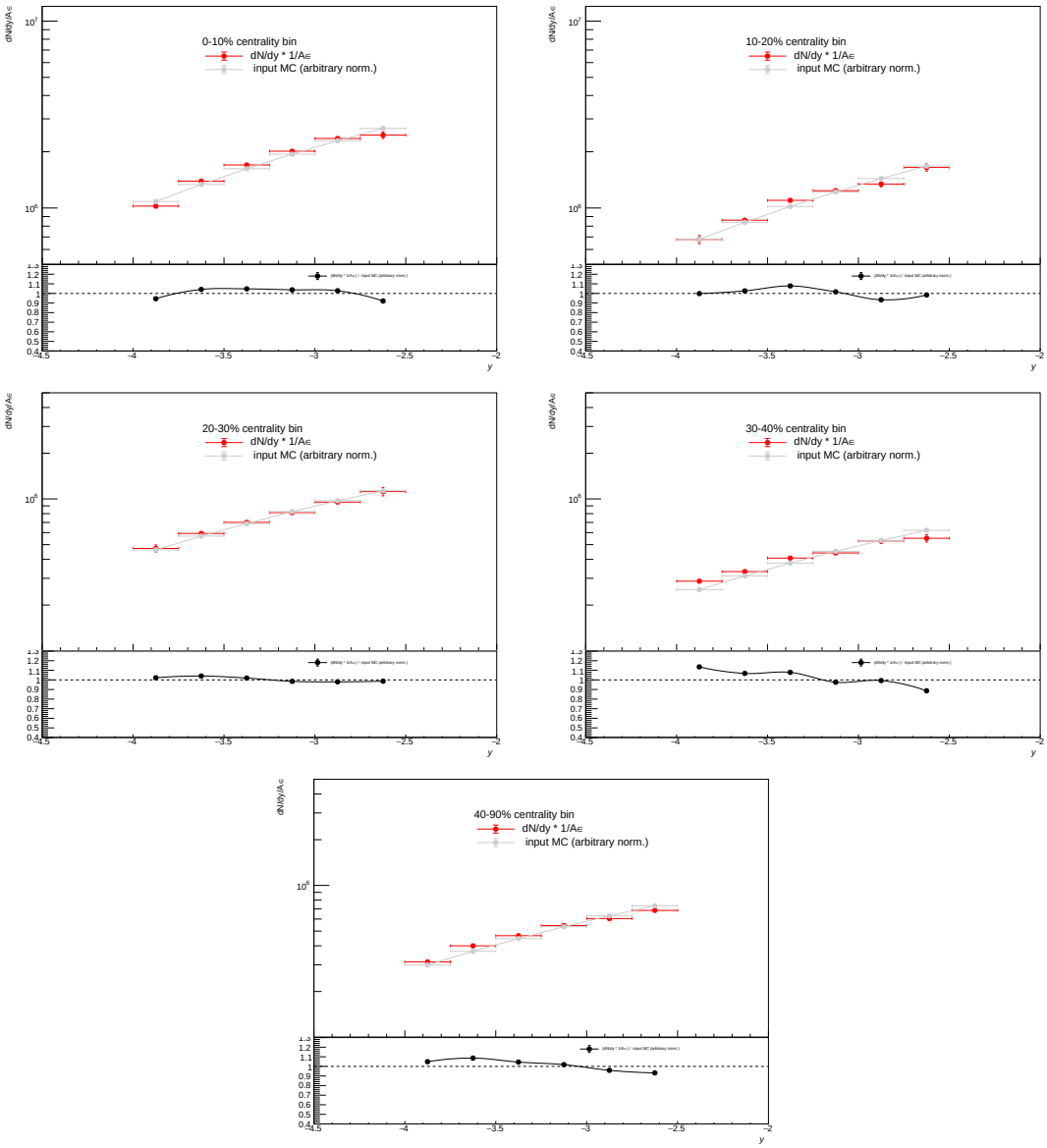

Figure 5.14: J/ψ differential $A \times \epsilon_0$ corrected distribution as a function of y for $0 \leq p_{\mathrm{T}} < 20$ GeV/c and for the 0–10% (left top panel), 10–20% (right top panel), 20–30% (left middle panel), 30–40% (right middle panel) and 40–90% (bottom panel) centrality classes. The corrected distribution (red) is compared to the MC generated distribution (grey) before the iterative procedure.

one iteration. Therefore, the new $A \times \epsilon$ is taken from the first iterative step, $A \times \epsilon_1$, where the index "1" of $A \times \epsilon_1$ specifies the iteration step. The p_{T} and y dependence of $A \times \epsilon_1$ and $A \times \epsilon_0$ are shown in the left panels of Figure 5.15, 5.16, 5.17, 5.18, 5.19, and 5.20 for the five centrality classes of interest. The blue points correspond to $A \times \epsilon_0$ with the original input MC shape while the green points correspond to $A \times \epsilon_1$ with the tuned input MC shape. The right panels of those six figures show the relative difference between $A \times \epsilon_1$ and $A \times \epsilon_0$. The $A \times \epsilon$ increases after the tuning for most of the measured p_{T} bins. The acceptance and efficiency decreases as a function of y for the 0–10% centrality class and increases for the other centrality classes. Figure. 5.21 and 5.22 show the p_{T} and y distributions

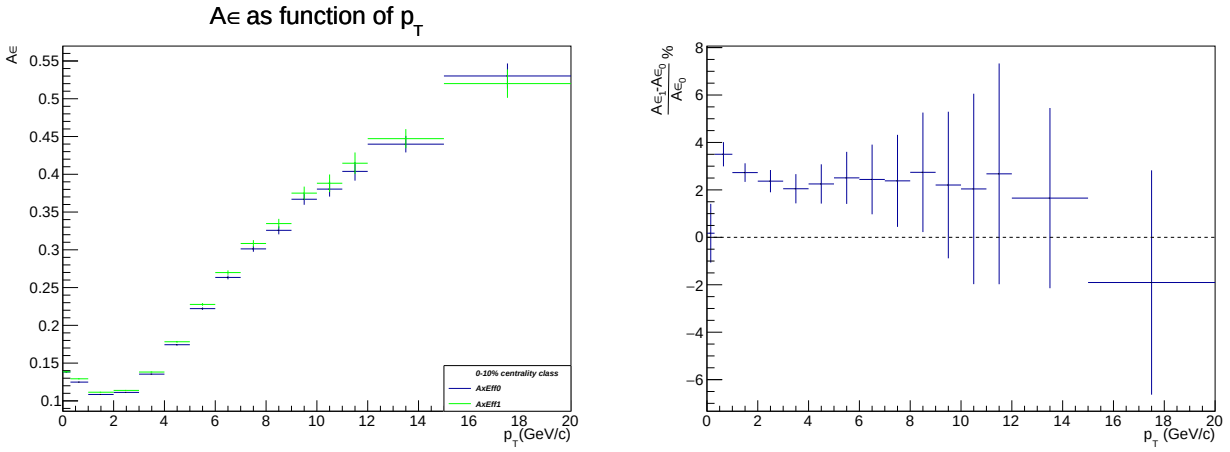

Figure 5.15: Left: J/ψ $A \times \epsilon$ as a function of p_{T} for LHC15o, 18q and 18r periods for $2.5 < y < 4$, and for the 0–10% centrality class. Right: relative difference on the J/ψ $A \times \epsilon_0$ and the $A \times \epsilon$ at the first iteration as a function of p_{T} for $2.5 < y < 4$ and for the 0–10% centrality class.

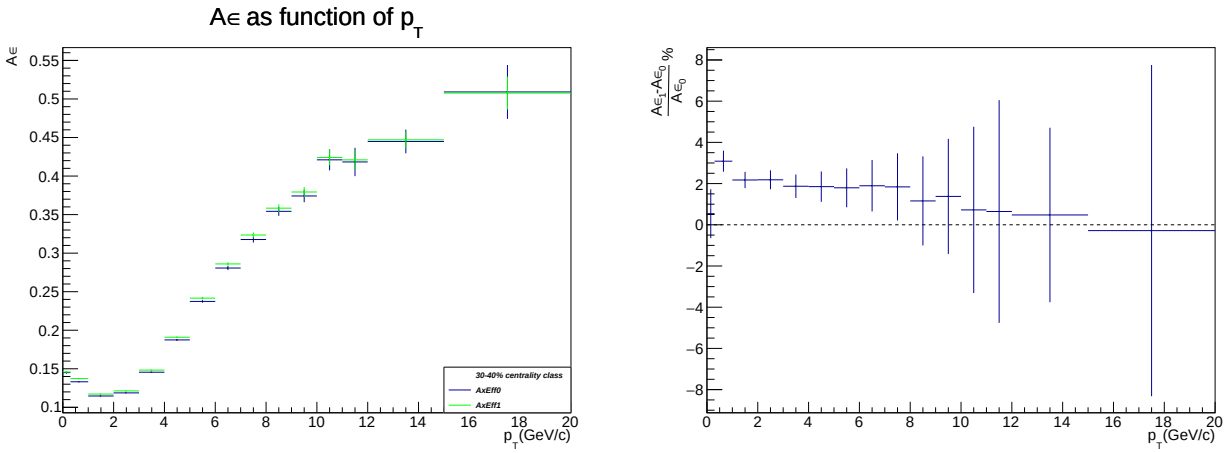

Figure 5.16: Left: J/ψ $A \times \epsilon$ as a function of p_{T} for LHC15o, 18q and 18r periods for $2.5 < y < 4$, and for the 30–40% centrality class. Right: relative difference on the J/ψ $A \times \epsilon_0$ and the $A \times \epsilon$ at the first iteration as a function of p_{T} for $2.5 < y < 4$ and for the 30–40% centrality class.

of the raw data corrected by $A \times \epsilon_1$, of the tuned normalized input MC distributions, and their ratios, for 0-10%, 10-20%, 20-30%, 30-40% and 40-90% centrality intervals. The ratio is close to unity in most of the p_{T} and y bins. Notice that the first p_{T} bin is excluded from the tuning procedure because of the contamination from photoproduced J/ψ events in particular in peripheral collisions. As a result the ratio is not close to unity for that bin. The effect of the second iteration is checked in the centrality range 0–10% and 10–20%. The weights for the second iteration are obtained as described in section 4.1.4. The results show that the $A \times \epsilon_2$ obtained from the second iterative step is similar to $A\epsilon_1$ within 1% in most of the p_{T} and y bins (up to about 2.5% at high p_{T}). Hence $A \times \epsilon_1$ is used in the analysis. In the following, the acceptance efficiency after the first iterative procedure is denoted as $A \times \epsilon$.

Table 5.5 gives the values of $A \times \epsilon$ in different p_{T} intervals for the 0–20%, 20–40% and 40–90% centrality classes.

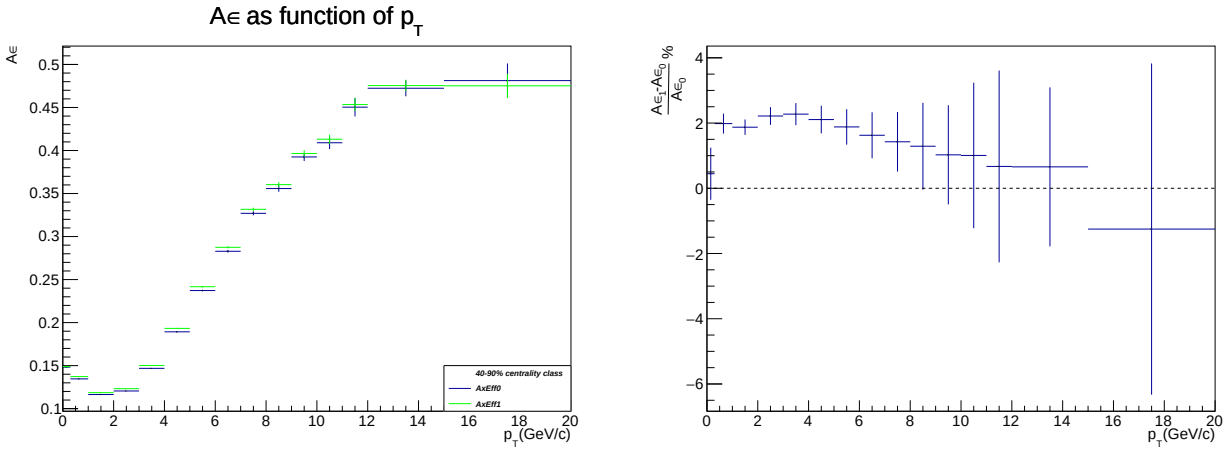

Figure 5.17: Left: J/ψ $A \times \epsilon$ as a function of p_{T} for LHC15o, 18q and 18r periods for $2.5 < y < 4$, and for the 40–90% centrality class. Right: relative difference on the J/ψ $A \times \epsilon_0$ and the $A \times \epsilon$ at the first iteration as a function of p_{T} for $2.5 < y < 4$ and for the 40–90% centrality class.

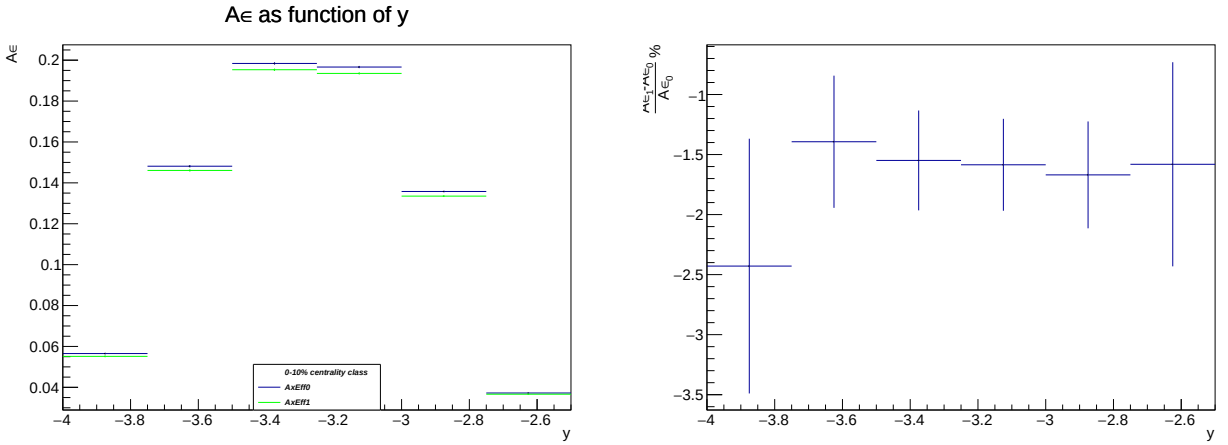

Figure 5.18: Left: J/ψ $A \times \epsilon$ as a function of y for LHC15o, 18q and 18r periods for $0 \leq p_{\mathrm{T}} < 20$ GeV/c, and for the 0–10% centrality class. Right: relative difference on the J/ψ $A \times \epsilon_0$ and the $A \times \epsilon$ at the first iteration as a function of y for $0 \leq p_{\mathrm{T}} < 20$ GeV/c, and for the 0–10% centrality class.

The $A \times \epsilon$ reaches a minimum value for $1 < p_{\mathrm{T}} < 3$ GeV/c in the three centrality ranges. The $A \times \epsilon$ then rises with increasing p_{T} but the $A \times \epsilon$ is not smooth for $p_{\mathrm{T}} > 10$ GeV/c, especially in peripheral collisions. An independent cross-check is performed and reproduces a similar phenomenon at high p_{T}. Besides, another cross-check on the p_{T} dependence of the $A \times \epsilon$ prior to any run number or centrality weighting is also performed. The discrete step is spotted at high p_{T} in that case as well and is attributed to the low MC statistics in this region. Those checks suggest that the embedded MC needs more statistics to avoid the discrete steps at high p_{T}, and a new embedded MC production is under preparation in view of the publication of those results.

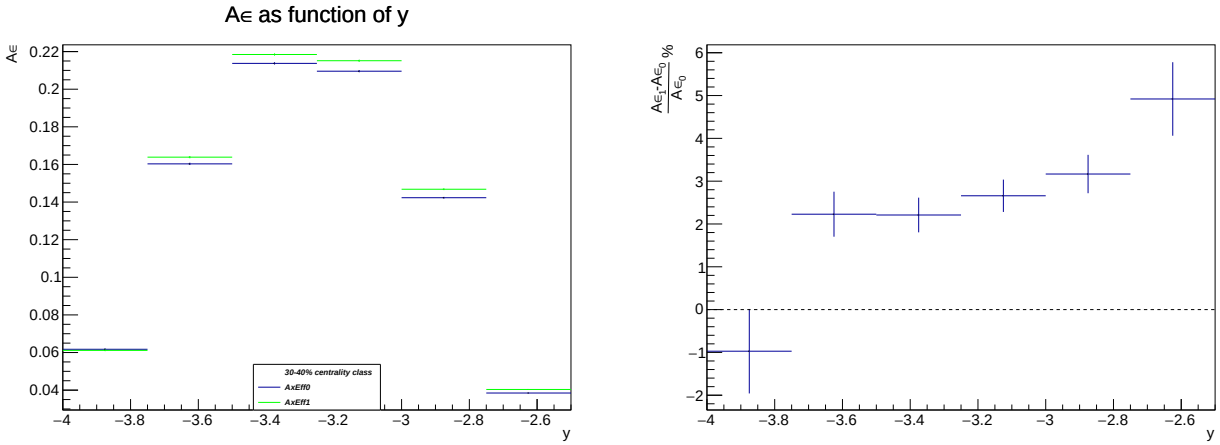

Figure 5.19: Left: J/ψ $A \times \epsilon$ as a function of y for LHC15o, 18q and 18r periods for $0 \leq p_{\mathrm{T}} < 20$ GeV/c, and for the 30–40% centrality class. Right: relative difference on the J/ψ $A \times \epsilon_0$ and the $A \times \epsilon$ at the first iteration as a function of y for $0 \leq p_{\mathrm{T}} < 20$ GeV/c, and for the 30–40% centrality class.

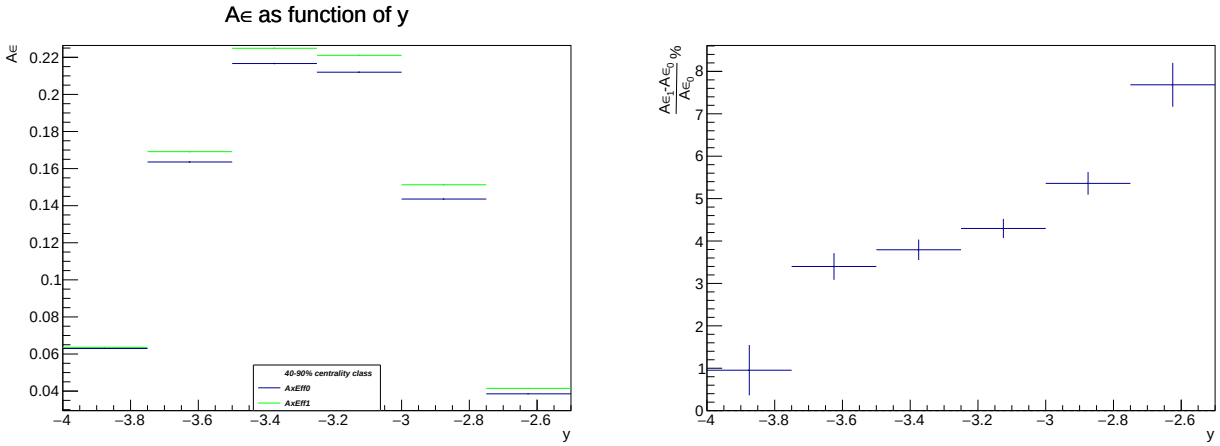

Figure 5.20: Left: J/ψ $A \times \epsilon$ as a function of y for LHC15o, 18q and 18r periods for $0 \leq p_{\mathrm{T}} < 20$ GeV/c, and for 40–90% centrality class. Right: relative difference on the J/ψ $A \times \epsilon_0$ and the $A \times \epsilon$ at the first iteration as a function of y for $0 \leq p_{\mathrm{T}} < 20$ GeV/c, and for the 40–90% centrality class.

centrality 0 – 20 %	
p_{T}(GeV/c)	$A \times \epsilon \pm$ stat. (%)
0–0.3	0.139 ± 0.0008 (0.58)
0.3–1	0.130 ± 0.0003 (0.23)
1–2	0.113 ± 0.0002 (0.18)
2–3	0.116 ± 0.0003 (0.26)
3–4	0.140 ± 0.0004 (0.29)
4–5	0.181 ± 0.0007 (0.39)
5–6	0.228 ± 0.0012 (0.53)
6–7	0.275 ± 0.0020 (0.73)
7–8	0.312 ± 0.0029 (0.93)
8–9	0.339 ± 0.0041 (1.21)
9–10	0.370 ± 0.0056 (1.51)
10–11	0.389 ± 0.0073 (1.88)
11–12	0.414 ± 0.0092 (2.22)
12–15	0.447 ± 0.0082 (1.83)
15–20	0.492 ± 0.0114 (2.32)

centrality 20 – 40 %	
p_{T}(GeV/c)	$A \times \epsilon \pm$ stat. (%)
0–0.3	0.141 ± 0.0008 (0.59)
0.3–1	0.134 ± 0.0004 (0.26)
1–2	0.115 ± 0.0002 (0.20)
2–3	0.119 ± 0.0003 (0.23)
3–4	0.145 ± 0.0004 (0.29)
4–5	0.188 ± 0.0007 (0.38)
5–6	0.236 ± 0.0012 (0.50)
6–7	0.278 ± 0.0018 (0.65)
7–8	0.319 ± 0.0027 (0.86)
8–9	0.353 ± 0.0039 (1.09)
9–10	0.372 ± 0.0053 (1.41)
10–11	0.424 ± 0.0077 (1.82)
11–12	0.426 ± 0.0112 (2.64)
12–15	0.429 ± 0.0095 (2.21)
15–20	0.493 ± 0.0182 (3.70)

centrality 40 – 90 %	
p_{T}(GeV/c)	$A \times \epsilon \pm$ stat. (%)
0–0.3	0.149 ± 0.0009 (0.58)
0.3–1	0.137 ± 0.0003 (0.23)
1–2	0.119 ± 0.0002 (0.17)
2–3	0.123 ± 0.0002 (0.19)
3–4	0.150 ± 0.0003 (0.23)
4–5	0.193 ± 0.0005 (0.28)
5–6	0.242 ± 0.0008 (0.35)
6–7	0.287 ± 0.0013 (0.45)
7–8	0.332 ± 0.0019 (0.57)
8–9	0.360 ± 0.0029 (0.81)
9–10	0.397 ± 0.0037 (0.93)
10–11	0.413 ± 0.0054 (1.32)
11–12	0.453 ± 0.0077 (1.70)
12–15	0.475 ± 0.0068 (1.42)
15–20	0.475 ± 0.0141 (2.97)

Table 5.5: J/ψ acceptance times efficiency as a function of p_{T} for $2.5 < y < 4$ and several centrality classes.

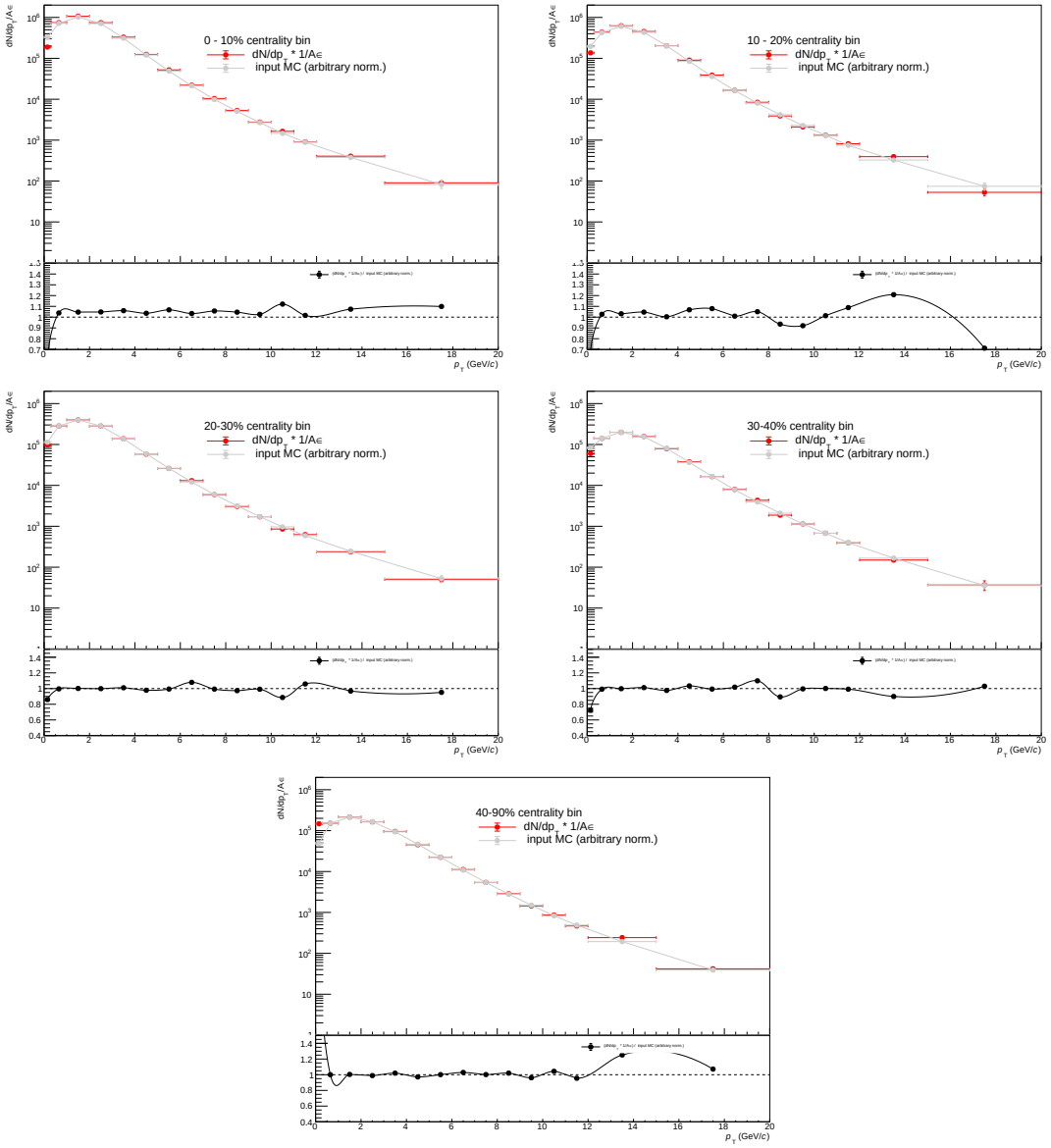

Figure 5.21: J/ψ differential $A \times \epsilon_1$ corrected distribution as a function of p_{T} for $2.5 < y < 4$, in 0–10% (left of top panel), 10–20% (right of top panel), 20–30% (left of middle panel), 30–40% (right of middle panel) and 40–90% (bottom panel) centrality classes. The corrected distribution (red) are compared to the MC generated distribution (grey) after the first step of the iterative procedure.

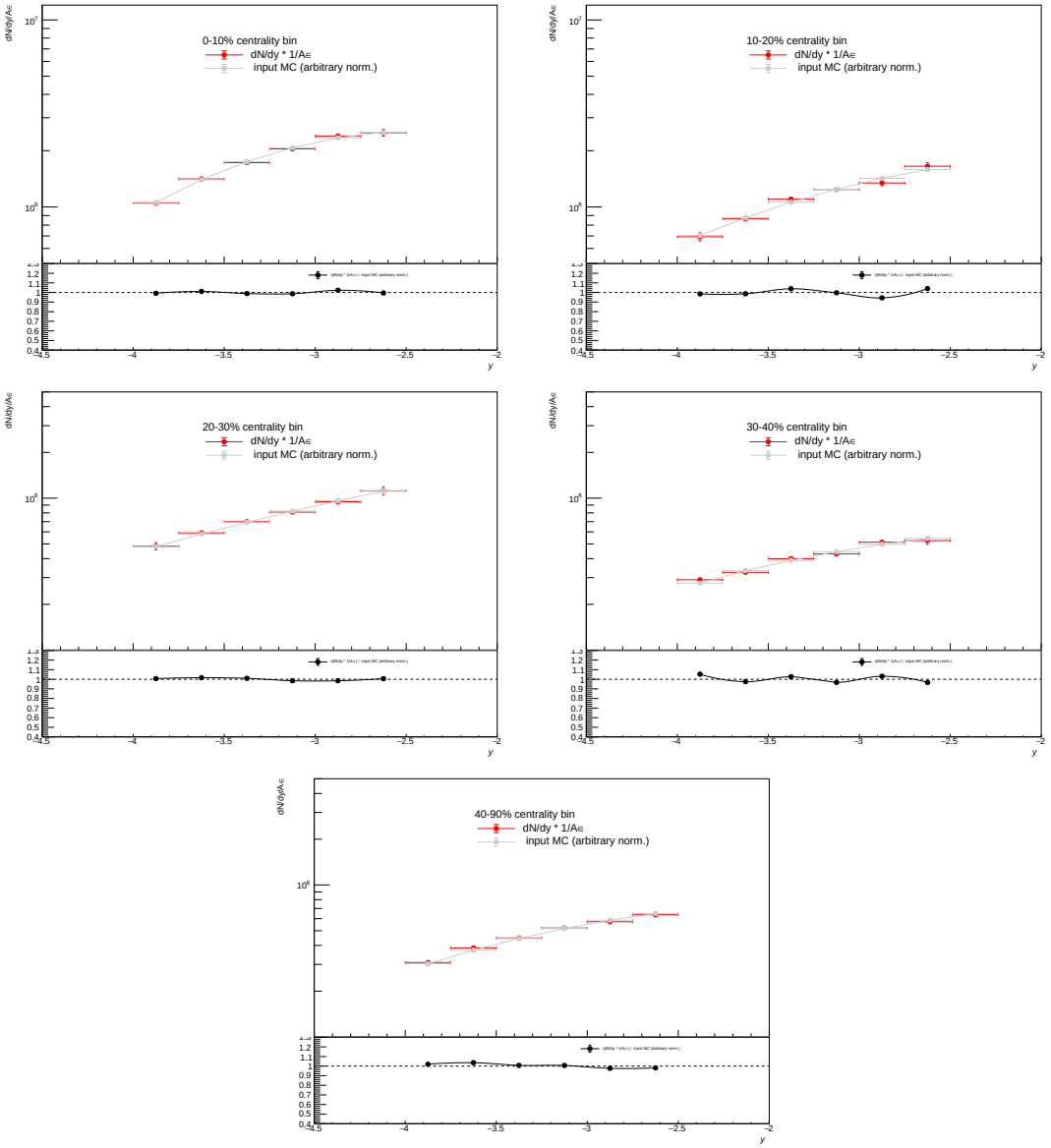

Figure 5.22: J/ψ differential $A \times \epsilon_1$ corrected distribution as a function of y for $0 \leq p_{\mathrm{T}} < 20$ GeV/c in 0–10% (left of top panel), 10–20% (right of top panel), 20–30% (left of middle panel), 30–40% (right of middle panel) and 40–90% (bottom panel) centrality classes. The corrected distribution (red) are compared to the MC generated distribution (grey) after the first step of the iterative procedure.

5.1.5 Normalization factor

In order to compute the number of minimum bias (MB) events, N_{MB}, equivalent to the number of CMUL7 events in the analysed data sample N_{CMUL7}, the evaluation of the normalization factor F_{norm} has been completed. In this study, the values of $F_{\mathrm{norm},i}$, in which i is the run number, are taken from [227] to compute the average normalization factor, F_{norm}. The number of CMUL7 events analyzed in this work run per run is taken into account for evaluating the final F_{norm}.

The number of MB events, $N_{\mathrm{MB},i}$, in the 0–90% centrality class in a given run i is defined as:

$$N_{\mathrm{MB},i} = F_{\mathrm{norm},i} \times N_{\mathrm{CMUL7},i}, \tag{5.9}$$

where $N_{\mathrm{CMUL7},i}$ is the number of CMUL7 triggered events in the same centrality class and $F_{\mathrm{norm},i}$ is the normalization factor which can be calculated with two different methods (offline and online methods) as described in section 4.1.5. Two minimum bias triggers have been considered for the calculation of the normalization factor: CINT7 for the offline method and C0V0M[4] for the online method. C0V0M triggers on the sum of the V0-A and V0-C detectors, together with a threshold on the signal. Hence, C0V0M covers the centrality range of about 0–60% and serves as a mid-central MB trigger. However, the normalization factor over the 0–90% centrality range is desired, so a scaling is needed for the C0V0M trigger. In LHC15o, the C0V0M triggered event distribution is flat as a function of the collision centrality up to 60% while in LHC18q and LHC18r, the centrality distribution is flat up to the 50%. So the number of C0V0M events are scaled according to $9/6 \times N_{\mathrm{LHC15o}}(0-60\%)$ and $9/5 \times N_{\mathrm{LHC18q;18r}}(0-50\%)$ for the 2015 and the 2018 data samples, respectively. After applying the centrality scaling, the normalization factor to the MB events in the 0–90% centrality class can be calculated. Note that the pile-up factor PU, which corrects for pile-up events in the collisions has also been defined in Eqs. 4.14 and 4.15. The pile-up factor correction should be applied to both offline and online methods since the pile-up offline selection is not applied in both cases. According to [227], the average pileup correction for the Run 2 data is around 1.0004 which is a tiny correction. The pileup correction is therefore finally neglected in both methods.

The $F_{\mathrm{norm},i}$ as a function of the run number, obtained from the offline method, is shown in Figure 5.23 for LHC15o and in Figure 5.24 for LHC18q and LHC18r.

The $F_{\mathrm{norm},j,k}$ factor, for a given method j and a given period k is obtained as an average over the run number, i, weighted by the number of CMUL7 triggered events:

$$F_{\mathrm{norm},j,k} = \frac{\sum_i F_{\mathrm{norm},i} \times N_{\mathrm{CMUL7},i}}{\sum_i N_{\mathrm{CMUL7},i}} \tag{5.10}$$

[4]There are actually two C0V0M triggers depending on the run number: CINT7ZAC-B-NOPF-CENTNOPMD and C0V0M-B-NOPF-MUFAST. In the 2015 Pb-Pb data sample, the C0V0M-B-NOPF-CENTNOTRD trigger is considered. The same trigger is still used until run 295725 in the 2018 Pb-Pb data sample. However, from run 295725, the C0V0M-B-NOPF-MUFAST trigger is considered.

and its uncertainty is obtained as:

$$F^{\rm err}_{{\rm norm},j,k} = \frac{\sqrt{\sum_i (\delta F_{{\rm norm},i})^2 \times (N_{{\rm CMUL7},i})^2}}{\sum_i N_{{\rm CMUL7},i}}, \tag{5.11}$$

where $\delta F_{{\rm norm},i}$ is the statistical uncertainty on $F_{{\rm norm},i}$. The results of the average normalization factors, for the three values obtained from the (in)direct offline and the online methods, are shown in Table 5.6. In a given period, the average $F_{{\rm norm},k}$ over the three methods is obtained by taking into account the statistical uncertainty on $F_{{\rm norm},j,k}$ as a weight (see Eq. 5.12):

$$F_{{\rm norm},k} = \frac{\sum_j \frac{F_{{\rm norm},j,k}}{\left(F^{\rm err}_{{\rm norm},j,k}\right)^2}}{\sum_j \frac{1}{\left(F^{\rm err}_{{\rm norm},j,k}\right)^2}}, \tag{5.12}$$

The uncertainty $F^{\rm err}_{{\rm norm},k}$ on the average $F_{{\rm norm},k}$ over the three methods can be calculated as:

$$F^{\rm err}_{{\rm norm},k} = \sqrt{\frac{1}{\sum_j (F_{{\rm norm},j,k})^{-2}}}. \tag{5.13}$$

Furthermore, the average of the three periods, $F_{\rm norm}$, is obtained by considering as a weight the number of CMUL7 triggered events per period $N_{{\rm CMUL7},k}$ such as:

$$F_{\rm norm} = \frac{\sum_k F_{{\rm norm},k} \times N_{{\rm CMUL7},k}}{\sum_k N_{{\rm CMUL7},k}}$$

In addition, the largest relative difference between the online method using C0V0M (i.e. the one with the highest statistical precision) and the values obtained from other methods is taken as systematic uncertainty.

In order to calculate the number of minimum bias events in the 0–90% centrality class, we use:

$$N^{0-90\%}_{\rm MB} = F^{0-90\%}_{\rm norm} \times N^{0-90\%}_{\rm CMUL7}. \tag{5.14}$$

Since the MB events are distributed equally in each centrality bin, we can derive the number of MB events in each centrality bin by dividing by a factor 90/Δcent, where Δcent is the centrality bin width. One could also compute the normalization factor directly in each centrality bin. In that case, larger statistical uncertainty will be obtained, therefore this method is not used.

	$F_{\rm norm} \pm$ stat. Offline direct CINT7	$F_{\rm norm} \pm$ stat. Offline indirect CINT7	$F_{\rm norm} \pm$ stat. Online C0V0M	Avg.
LHC15o	11.84 ± 0.012	11.85 ± 0.007	11.88 ± 0.001	11.87 ± 0.01 (%)
LHC18q	13.59 ± 0.026	13.59 ± 0.013	13.56 ± 0.001	13.56 ± 0.01 (%)
LHC18r	13.75 ± 0.022	13.72 ± 0.012	13.65 ± 0.001	13.65 ± 0.01 (%)
Results				13.06 ± 0.73% (syst.)

Table 5.6: Normalization factors in the three periods obtained with three different methods and the average values.

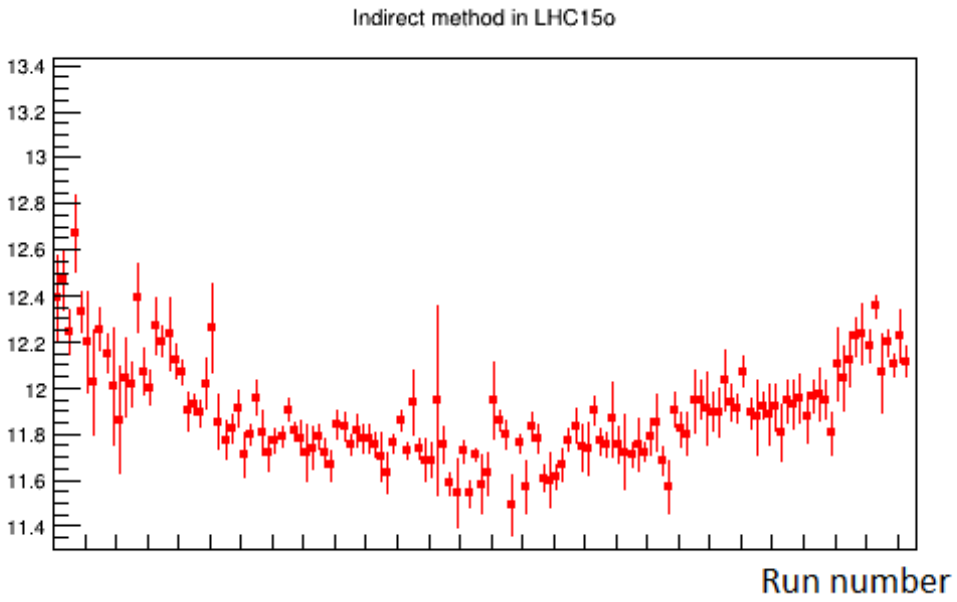

Figure 5.23: The normalization factor as a function of the run number in LHC15o obtained with the indirect offline method.

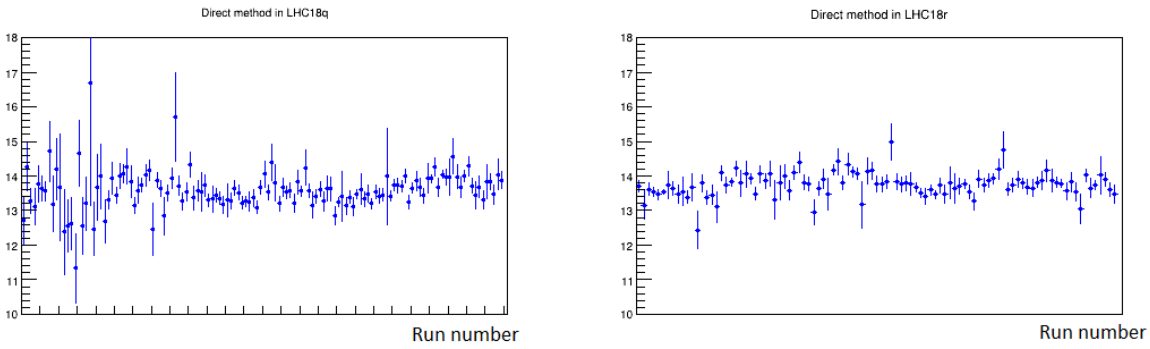

Figure 5.24: The normalization factor as a function of the run number obtained with the direct offline method in LHC18q (left) and LCH18r (right).

The integrated luminosity of the analyzed data sample is calculated as:

$$L_{\text{int}} = \frac{N_{\text{MB}}^{0-90\%} \times 10/9}{\sigma_{\text{PbPb}}}, \tag{5.15}$$

where σ_{PbPb} is the total hadronic Pb-Pb cross section at $\sqrt{s_{\text{NN}}} = 5.02$ TeV and is equal to 7.67 $\pm$ 0.16 (syst.)b [228]. Appendix A discusses how σ_{PbPb} is obtained. The total number of MB events in the 0–100% centrality class is obtained by multiplying the number of MB events in the 0–90% centrality class by a factor of 10/9. The integrated luminosity of the analyzed data sample corresponds to about 750 μb^{-1} while the integrated luminosity of the full Run 2 Pb-Pb data is 787 μb^{-1} (see Table 3.1).

5.1.6 Systematic uncertainties

In this section, the systematic uncertainties on the J/ψ invariant yield (see Eq. 5.2) and $R_{\rm AA}$ (see Eq. 5.1) as a function of $p_{\rm T}$ are discussed. The values of the systematic uncertainty are summarized in Table 5.9. Some of the systematic uncertainty sources, which have been presented in the previous sections, are shortly mentioned in this section.

The systematic uncertainty on the branching ratio of the J/ψ decaying into dimuons amounts to 0.55% [18] and is correlated over $p_{\rm T}$ and centrality. Note that this systematic uncertainty contributes to the J/ψ invariant yield, but not to the J/ψ $R_{\rm AA}$ because this term cancels out in the $R_{\rm AA}$ equation (see Eq. 5.1). **The systematic uncertainty on** $F_{\rm norm}$ has been presented in section 5.1.5 and is correlated over $p_{\rm T}$ and centrality.

The systematic uncertainty on the signal extraction is discussed in section 5.1.3. The variations of the signal tail parameters, the signal functions, the background functions and the fitting ranges give the systematic uncertainty. The numbers for each $p_{\rm T}$ interval are given in Table 5.3 and Table 5.4 for the 0–20%, 20–40% and 40–90% centrality classes. It ranges from 1.5 to 10.7%. The larger systematic uncertainty is found at high $p_{\rm T}$ and in the 40–90% centrality class where the statistics is the lowest.

The systematic uncertainty on the MC parametrisation is taken from the largest relative difference between $A \times \epsilon_0$ and $A \times \epsilon$, the latter being obtained after applying the iterative procedure. For example, the left panel of Figure 5.15 shows the comparison of $A \times \epsilon_0$ (blue) and $A \times \epsilon$ (green) in the 0–10% centrality range. The right panel of Figure 5.15 shows the relative difference between $A \times \epsilon_0$ and $A \times \epsilon$, which shows the largest difference of 3.5% in the second $p_{\rm T}$ bin in the 0–10% (as well as in the 10–20%) centrality class (with respect to all other $p_{\rm T}$ bins). This largest difference is taken as the systematic uncertainty on the MC parametrisation in the 0–20% centrality range. For the 20–40% and 40-90% centrality classes, the largest difference taken as systematic uncertainty is found to be 3% (from the second $p_{\rm T}$ bin in Figure 5.16) and 2.3% (the fifth $p_{\rm T}$ bin in 5.17).

The systematic uncertainty on the tracking efficiency is from two sources in Pb-Pb collisions:

- the difference in the tracking efficiency between data and MC,
- the loss of tracking efficiency at high event centrality.

The difference in the tracking efficiency between data and MC has been evaluated for the 2015 [145] and the 2018 [229] Pb-Pb data samples. The method for calculating the tracking efficiency is presented in section 4.1.6. Figure 5.25 shows the single muon tracking efficiency in data and embedded MC as a function of run number, $p_{\rm T}$, y, and ϕ for the CMSL7 triggered events in the 2018 periods. The efficiency ratio of data to MC is also shown at the bottom of each plot. The ratio varies from 0 to about 3% depending on the muon kinematics. In order to check the comparison data/MC for various $p_{\rm T}$ and centrality (since the tracking efficiency depends on $p_{\rm T}$ and centrality), various $p_{\rm T}$ and centrality selections are further applied in the data and the embedded MC [145]. Based on those studies, the tracking efficiency systematic uncertainty is found to be 1.5% at the single muon level, with variations

depending on the kinematics, the maximum being always within 2 to 3σ of the considered systematic values. Hence a systematic uncertainty of 3% is taken for the J/ψ, and is assumed uncorrelated versus p_{T}, however, correlated as a function of centrality. The same tracking efficiency systematic uncertainty is also found in the 2015 Pb-Pb data. The systematic uncertainty is therefore 3% for the full Pb-Pb data sample of Run 2.

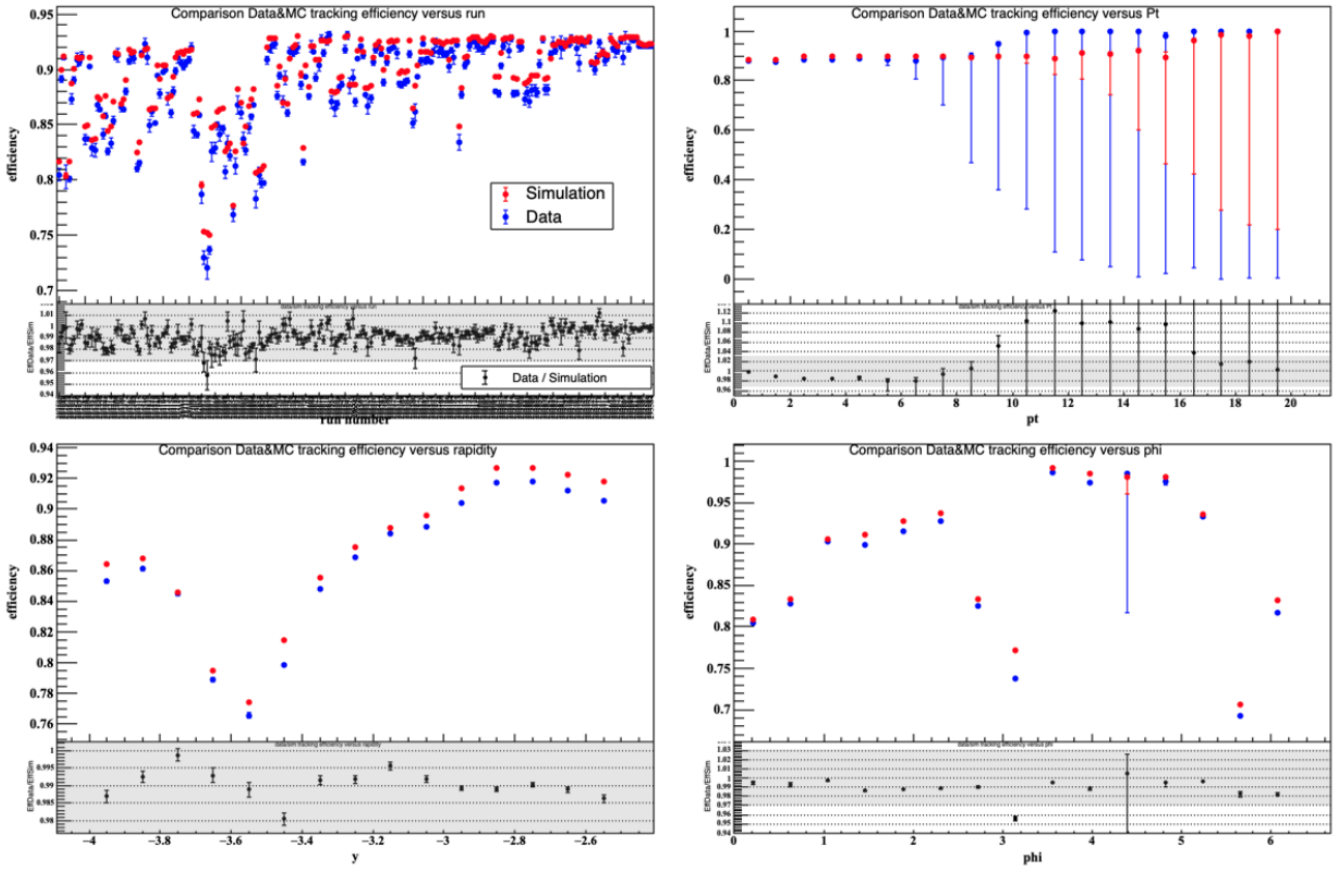

Figure 5.25: Single muon tracking efficiency obtained from data (blue) and from the corresponding embedded MC simulation (red) as a function of the run number (top left), p_{T} (top right), y (bottom left), and ϕ (bottom right) for CMSL7 triggered events and for the 2018 periods. Figure from [229].

The second source of systematic uncertainty comes from the loss of tracking efficiency with increasing centrality, which is because of the tracking algorithm [145, 229]. The loss of tracking efficiency as a function of centrality is reproduced in embedded MC simulation and measured in data. The difference in the efficiency between data and MC drops in most central collisions and it amounts to 0.5% for single muon, as a consequence, assuming that the muons are uncorrelated, to 1% for dimuons. Besides, this additional systematic uncertainty decreases with decreasing centrality, down to zero in peripheral collisions. This uncertainty is considered as fully correlated over p_{T}.

The systematic uncertainty on trigger efficiency is associated with two components:

- the uncertainty on the trigger chambers efficiency maps (intrinsic trigger efficiency),

- the differences in the shapes of the trigger response between data and MC.

The principle and the analysis procedure for estimating the uncertainty on the intrinsic trigger efficiency is presented in section 4.1.6. The same procedure is adopted in the analysis of the Pb-Pb data. According to [145], the systematic uncertainty on the intrinsic trigger efficiency is 1.5% for the 2015 Pb-Pb data sample. The same value is taken in this thesis based on the stability of the J/ψ invariant yield values in the 2015 and in the full Run 2 Pb-Pb data (see section 5.2). Indeed, the two invariant yields do not vary significantly and give confidence that the trigger efficiency is similar in the two data taking periods. This contribution is uncorrelated versus p_{T} and y, and is correlated versus centrality.

The systematic uncertainty on the trigger response is performed with the full Pb-Pb data of Run 2. The procedure to evaluate this systematic uncertainty is detailed in section 4.1.6. However, a different fitting trigger response function (RF) is adopted for the Pb-Pb data sample, in contrast to Eq. 4.29, to better reproduce the RF shape. If the single muon p_{T} is below 2 GeV/c, the following RF fitting function is considered:

$$RF = \frac{L_{p_{\mathrm{T}}}}{A_{p_{\mathrm{T}}}} = p_7 + p_0 \times erf\Big[\frac{max(p_{\mathrm{T}}, p_6)}{\sqrt{2}p_2} - 1\Big], \text{ if } p_{\mathrm{T}} > p_6. \tag{5.16}$$

In addition, an extra term is added to the previous RF fitting function if $p_{\mathrm{T}} < p_6$. The extra term is defined as:

$$p_3 \times erf\Big[\frac{-1 \times max(p_{\mathrm{T}}, p_6) - p_4}{\sqrt{2}p_5} - erf\big(\frac{p_6 + p_4}{\sqrt{2}p_5}\big)\Big]. \tag{5.17}$$

If $p_{\mathrm{T}} \geq 2$ GeV/c, another fitting function is considered, such as:

$$RF = p_0 + \frac{p_1}{1 + exp[-p_2(p_{\mathrm{T}} - p_3)]}. \tag{5.18}$$

Note that p_0, p_1, p_2,..., p_7 are the free parameters. The function max returns the largest value of its two arguments and the function erf is the error function [230]. Fits of the RF functions obtained from data and MC are performed. In the muon trigger system, there are 234 local boards. The local boards with similar geometry are expected to have the same performances. Figure 5.26 shows the six groups of local boards considered in the study of the muon trigger chamber systematic uncertainty. The RF functions of the six groups are obtained for each centrality class. Asymmetric uncertainties on the RF functions as a function of p_{T} are considered by using binomial errors. The fits in red solid line (see for instance Figure 5.27) describe well the RF functions of data in the whole p_{T} range. However in the MC, since the fit fails at describing the rising of the RF functions with decreasing p_{T} for $p_{\mathrm{T}} < 0.3$ GeV/c, the first three bins, corresponding to $p_{\mathrm{T}} < 0.3$ GeV/c, are merged to obtain a better fitting quality. The systematic uncertainty is found to be similar in all centrality classes (0–20%, 20–40%, and 40–90%) and hence for the final results, the study is carried out by integrating over centrality to benefit from an increase of the MC statistics. Figure

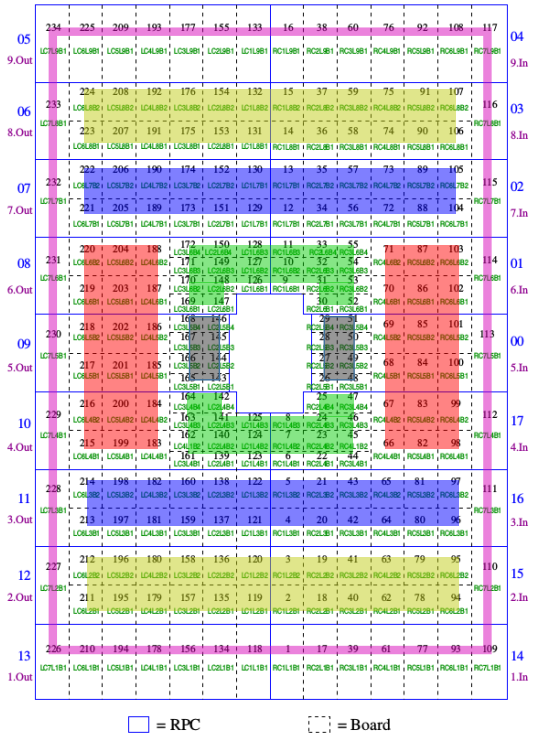

Figure 5.26: Six groups of local boards are defined per muon trigger chamber. Group one is represented in black, group two in green, group three in red, group four in blue, group five in yellow and group six in magenta.

5.27 shows the fits of the RF functions for the local board group one, integrated over centrality, in data and in MC. The fits describe well the RF functions for $0 < p_{\mathrm{T}} < 20$ GeV/c. The fit parameters of the two RF functions for the data and MC are used to extract the two weights of Eqs. 4.31 and 4.32. Then the weight, either from data or MC, is applied at the single muon level to muon matching the Ap_{T} trigger threshold from J/ψ MC simulations. The number of reconstructed J/ψ are extracted in the two cases using the two different weights. The relative difference in the number of reconstructed J/ψ gives the systematic uncertainty on the trigger response. The results in various p_{T} bins are tabulated in Table 5.7.

The range of the uncertainty on the trigger response is from 0.1 to 2.4%. Taking into account the intrinsic trigger chamber efficiency, the total uncorrelated systematic uncertainty on the trigger efficiency over p_{T} ranges from 1.5 to 2.8% for $0 < p_{\mathrm{T}} < 20$ GeV/c (1.5 to 2% for $0.3 < p_{\mathrm{T}} < 20$ GeV/c).

The systematic uncertainty on the efficiency of the matching between a trigger and a tracker track efficiency is uncorrelated over p_{T} and centrality and amounts to 1%. This uncertainty is considered similar as in previous analyses of the 2015 Pb-Pb data [231]. Indeed the reconstruction parameters do not change in Run 2 and the systematic uncertainty estimated in 2015 is expected to hold as well in 2018.

The systematic uncertainties on the reference cross sections in pp collisions are taken from 4.1.6. A 1.9%

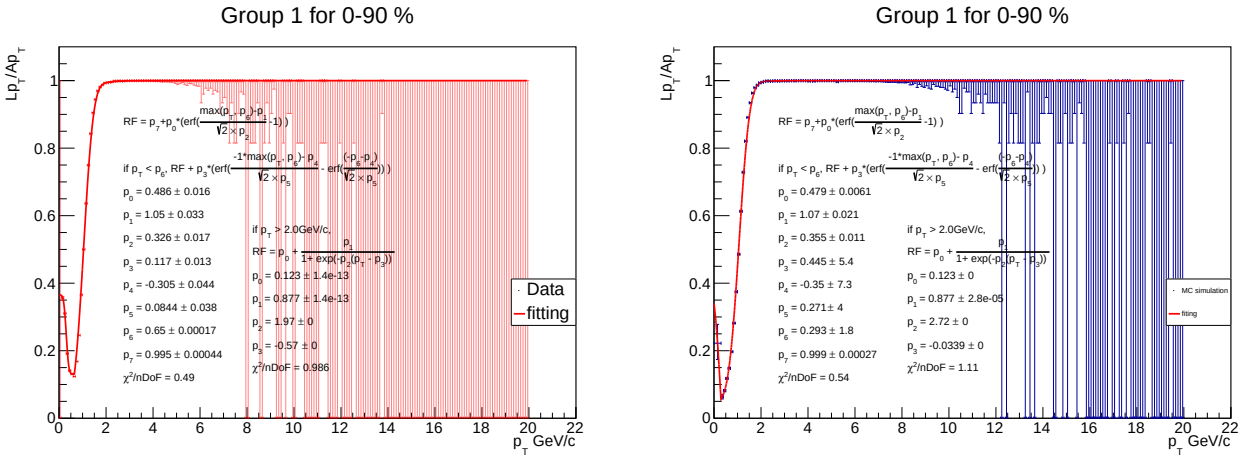

Figure 5.27: Examples of fits (red solid line) of the RF functions for group 1, integrated over centrality, in data (left in red) and MC (right in blue).

0–90% centrality	
p_{T} (GeV/c)	syst. unc. (%)
0 – 0.3	2.38
0.3 – 1	1.38
1 – 2	0.14
2 – 3	0.03
3 – 4	0.15
4 – 5	0.15
5 – 6	0.12
6 – 7	0.12
7 – 8	0.13
8 – 9	0.11
9 – 10	0.13
10 – 11	0.13
11 – 12	0.11
12 – 15	0.12
15 – 20	0.12

Table 5.7: The systematic uncertainty on the trigger efficiency associated to the J/ψ trigger response as function of p_{T} for $2.5 < y < 4$ in the 0–90% centrality range.

correlated systematic uncertainty is accounted for, while a systematic uncertainty (uncorrelated over p_{T}) ranging from 3.5 to 5.6% is also included.

The systematic uncertainty on $< T_{\mathrm{AA}} >$ is obtained from the Glauber model for several centrality bins in [228]. However, $< T_{\mathrm{AA}} >$ in centrality 40–90% is not available in [228]. In order to estimate it in this centrality bin, we take the weighted sum of $< T_{\mathrm{AA}} >$ over centrality from 40% to 90% where the weight corresponds to the bin width (of 10%). The values of $< T_{\mathrm{AA}} >$, including the central and the systematic uncertainty values, are given in Table 5.8. This systematic uncertainty is correlated over p_{T}.

The systematic uncertainty on the centrality limits has been computed in [145] for the 2015 data sample by comparing the J/ψ yield extracted by varying the definition of the centrality classes according to the uncertainty on

Centrality	T_{PbPb} ± syst. (%) (1/mbarn)
0–20%	18.83 ± 0.142 (0.75)
20–40%	6.93 ± 0.091 (1.31)
40–90%	1.00 ± 0.021 (2.04)

Table 5.8: T_{AA} and its systematic uncertainties for Pb-Pb collisions at $\sqrt{s_{\mathrm{NN}}}$ = 5.02 TeV for various centrality classes [228].

the anchor point evaluation from the Glauber fit. Events in Pb-Pb data samples are calibrated up to 90% centrality class according to this anchor point determined with an uncertainty of 1%. The centrality is evaluated with the VZERO detector (V0M centrality estimators). For the systematic study, different centrality estimators (V0Mplus05 and V0Mminus05) are used. They consider a ±0.5% shift of the anchor point with respect to the V0M estimator. The total shift between V0Mplus05 and V0Mminus05 is 1%. The uncertainty that is calculated corresponds to a shift of the anchor point of 0.5%. Therefore a normalisation factor of $\frac{1}{2}$ is taken into account when comparing the J/ψ yield obtained with V0Mplus05 and V0Mminus05. In Figure 5.28, the ratio of the number of J/ψ obtained from V0Mplus05 and V0Mminus05 and multiplied by 1/2 is shown as a function of centrality. As a result, the systematic uncertainty is taken as 0.4%, 0.2% and 1.4% for the centrality classes 0–20%, 20–40% and 40–90%, respectively. The uncertainty is correlated as function of p_{T}.

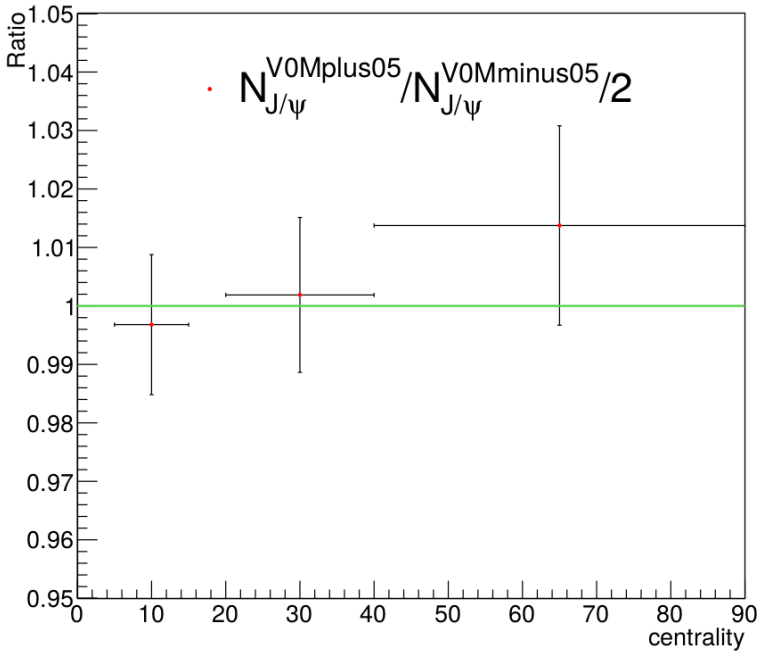

Figure 5.28: Ratio of the number of J/ψ obtained using the centrality estimators V0Mplus05 and V0Mminus05 in the 2015 analysis. The error bars represent the statistical uncertainty from the signal extraction.

The summary of all the systematic uncertainty contributions is tabulated in Table 5.9.

source	vs p_{T} (%) (0–20%)	vs p_{T} (%) (20–40%)	vs p_{T} (%) (40–90%)
Branching ratio	0.5*		
F_{norm}	0.73*		
Signal extraction	$1.6 - 5.8$	$1.9 - 4.5$	$1.6 - 10.7$
MC input	3.5	3	2.3
MCH efficiency	3.0 + 1.0*	3.0 + 0.5*	3.0
MTR efficiency	1.5–2.8	1.5–2.0	1.5–2.0
Matching	1		
T_{AA}	0.75*	1.31*	2.04*
Centrality limit	0.4*	0.2*	1.4*
pp cross section reference	3.5–5.6 + 1.9*		

Table 5.9: Summary of the systematic uncertainties. The values marked with an asterisk correspond to uncertainties correlated over p_{T}.

The uncertainties on $< T_{\mathrm{AA}} >$, centrality limit, F_{norm} and the correlated part of the pp cross section and tracking uncertainties lead to a global correlated systematic uncertainty over p_{T} on the R_{AA} of 2.4%, 2.5% and 3.2% for the 0–20%, 20–40% and 40–90% centrality intervals, respectively. Those values do not include the systematic uncertainty on the branching ratio which cancel out in the R_{AA} computation.

Comparing to the systematic uncertainties in the 2015 analysis, the systematic uncertainties on signal extraction and the MC input are larger in this analysis. In the J/ψ-signal-extraction study, the choices of the tails are the dominant source of systematic uncertainties on signal extraction. Also, at high p_{T} such as for 15$< p_{\mathrm{T}} <$20 GeV/c, the statistics is scarce, and there is a remaining statistical uncertainty component which enters the evaluation of the systematic uncertainties for such low statistics bins. Concerning the systematic uncertainty on the MC input, the values are not final and can be considered as conservative because we considered the difference between $A \times \epsilon_1$ (using MC production with the tuned input shapes) and $A \times \epsilon_0$ (using MC production with original input shapes).

5.2 Invariant yield

The J/ψ invariant yield, N_{AA}, is defined in Eq. 5.2. The invariant yield as a function of p_{T} is shown in Figure 5.29 in three centrality intervals and is tabulated in Table 5.10, 5.11 and 5.12. For each distribution, the statistical uncertainty is represented by vertical error bar while the systematic uncertainty, uncorrelated as a function of p_{T}, is shown as open box. The p_{T} correlated systematic uncertainty includes the contributions from the tracking efficiency and centrality limit. The uncertainty on the branching ratio and F_{norm} is a global systematic uncertainty correlated over the three centrality classes. The coherent J/ψ photoproduction contribution increases the yield for $p_{\mathrm{T}} < 0.3$ GeV/c in peripheral collisions. The invariant yield obtained from Run 2 statistics is compared to the results from the 2015 statistics only. The 2015 results in 0–20%, 20–40% and 40–90% centrality bins are taken from [145]. The statistical uncertainty on the ratio is calculated by considering that the two datasets are fully correlated. For the

three centrality bins, the yield ratios, shown in Figure 5.30 and 5.31 are close to unity as expected, for the whole p_{T} range.

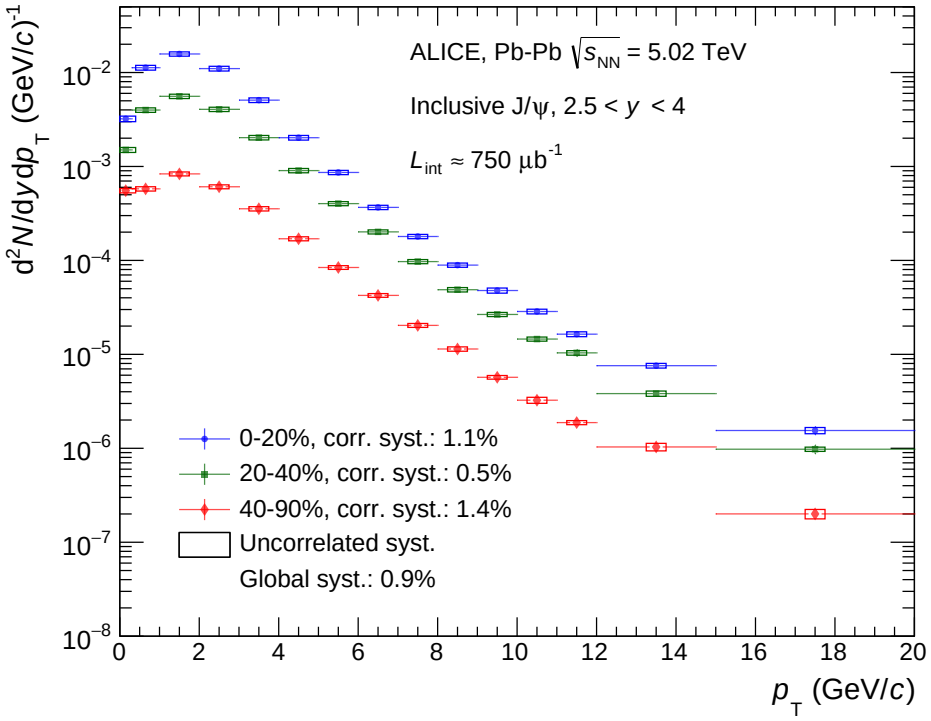

Figure 5.29: J/ψ invariant yield as a function of p_{T} for $2.5 < y < 4$ in the three centrality classes (0–20% in blue, 20–40% in green, and 40–90% in red). The statistical uncertainty is displayed as vertical error bar and the uncorrelated systematic uncertainty is represented by an open box. [This thesis].

5.3 Nuclear modification factor R_{AA}

The J/ψ nuclear modification factor is defined in Eq. 5.1. The J/ψ invariant yield is obtained in section 5.2. The reference cross-section in pp collisions is measured in section 4.2. Table 5.8 shows the values of $< T_{\mathrm{AA}} >$. In this thesis, the J/ψ R_{AA} is measured as a function of p_{T} in the centrality classes 0–20%, 20–40% and 40–90%. The R_{AA} results are shown in Figure 5.32, and 5.33. The values of the R_{AA} are given in Table 5.13 and 5.14. Note that the p_{T} dependence of the R_{AA} measurement for the 20–40% and 40–90% centrality classes excludes the p_{T} bin $0 < p_{\mathrm{T}} < 0.3$ GeV/c in order to avoid the J/ψ photoproduction contamination, which is expected to be negligible for the 0–20% centrality class.

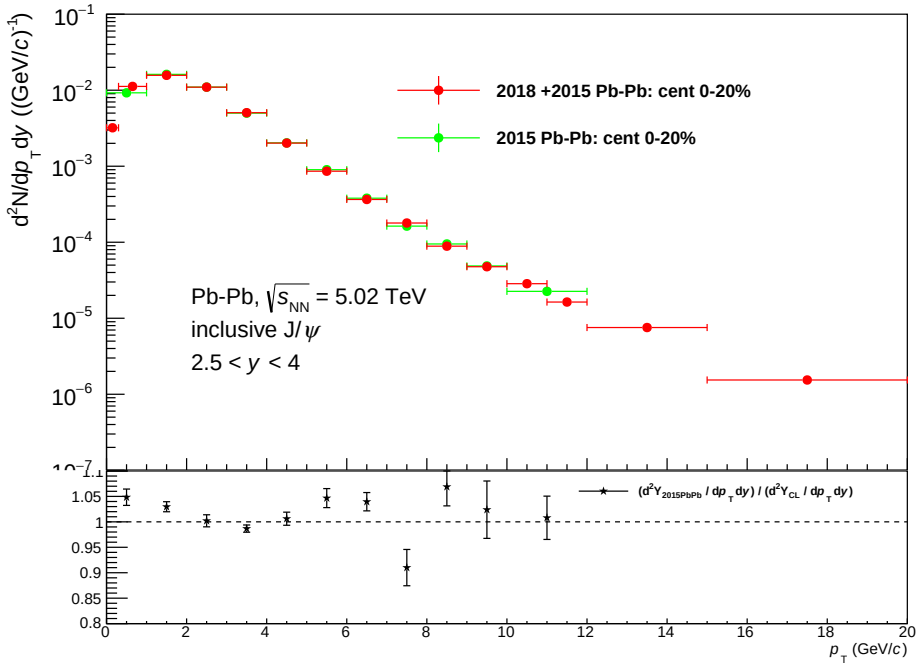

Figure 5.30: J/ψ invariant yield as a function of p_{T} for $2.5 < y < 4$ in the 0–20% centrality class, compared to the analysis of the 2015 Pb-Pb data. The statistical uncertainties are shown as vertical error bars. [This thesis].

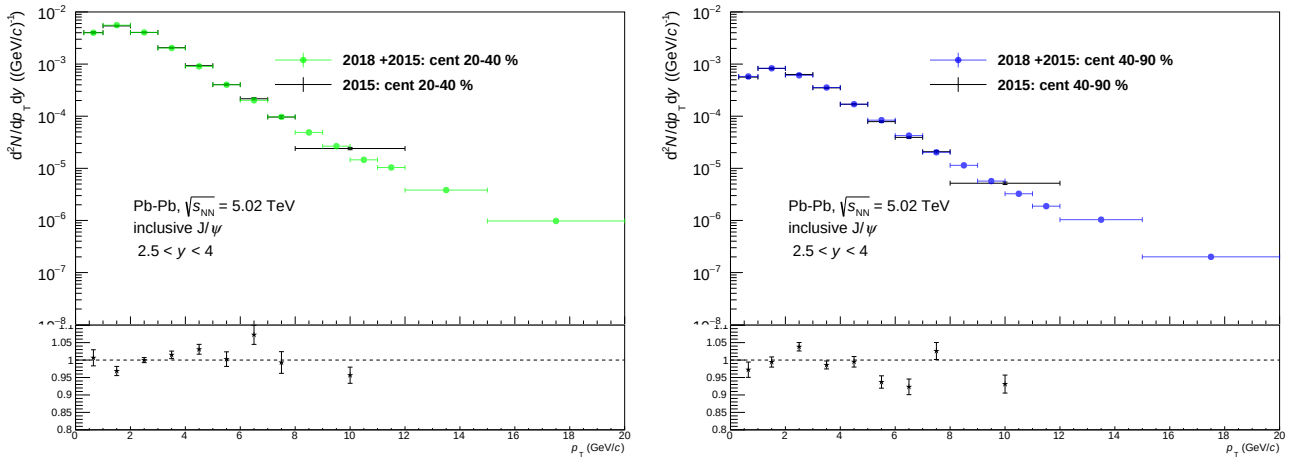

Figure 5.31: J/ψ invariant yield as a function of p_{T} for $2.5 < y < 4$ in the 20–40% (left) and 40–90% (right) centrality classes, compared to the 2015 analysis. The statistical uncertainties are shown as vertical error bars. [This thesis].

5.4 Discussion

We have measured the J/ψ R_{AA} as a function of p_{T} and centrality at forward rapidity in Pb-Pb collisions at $\sqrt{s_{\mathrm{NN}}} =$ 5.02 TeV. In this section, the results are compared to previous ALICE results at the same energy with the 2015 statistics [145] as well as the ATLAS and CMS measurements at mid-rapidity, and to the theoretical models.

p_{T} (GeV/c)	$\mathrm{d}^2N_{\mathrm{AA}}/\mathrm{d}y\mathrm{d}p_{\mathrm{T}}$ ± (stat.) (%) ± (syst.) (%) (GeV/c)$^{-1}$	2015 data ± (stat.) (GeV/c)$^{-1}$
0–0.3	3.22e-03 ± 1.92e-04 (6.0) ± 2.18e-04 (6.8)	–
0.3–1	1.13e-02 ± 2.39e-04 (2.1) ±6.59e-04 (5.9)	–
0–1	8.81e-03 ± 1.76e-04	9.24e-03 ± 3.26e-04
1–2	1.58e-02 ± 2.08e-04 (1.3) ± 8.29e-04 (5.3)	1.62e-02 ± 3.68e-04
2–3	1.10e-02 ± 1.36e-04 (1.2) ± 6.38e-04 (5.8)	1.10e-02 ± 2.66e-04
3–4	5.08e-03 ± 9.37e-05 (1.8) ± 2.89e-04 (5.7)	4.99e-03 ± 1.28e-04
4–5	2.02e-03 ± 4.16e-05 (2.1) ± 1.15e-04 (5.7)	2.03e-03 ± 6.77e-05
5–6	8.63e-04 ± 1.89e-05 (2.2) ± 4.50e-05 (5.2)	9.00e-04 ± 3.58e-05
6–7	3.67e-04 ± 9.50e-06 (2.6) ± 1.93e-05 (5.3)	3.80e-04 ± 1.64e-05
7–8	1.80e-04 ± 5.80e-06 (3.2) ± 9.42e-06 (5.2)	1.63e-04 ± 1.16e-05
8–9	8.91e-05 ± 3.61e-06 (4.1) ± 4.60e-06 (5.2)	9.49e-05 ± 7.18e-06
9–10	4.78e-05 ± 2.50e-06 (5.2) ± 3.00e-06 (6.3)	4.88e-05 ± 5.24e-06
10–11	2.86e-05 ± 1.78e-06 (6.2) ± 1.65e-06 (5.8)	–
11–12	1.64e-05 ± 1.26e-06 (7.7) ± 9.76e-07 (5.9)	–
10–12	2.24e-05 ± 1.08e-06	2.26e-05 ± 2.05e-06
12–15	7.58e-06 ± 4.73e-07 (6.2) ± 4.34e-07 (5.7)	–
15–20	1.55e-06 ± 1.49e-07 (9.7) ± 1.18e-07 (7.6)	–

Table 5.10: J/ψ invariant yield in various p_{T} intervals for $2.5 < y < 4$ in the 0–20% centrality class, compared to the results obtained from the analysis of the 2015 Pb-Pb data. The blue quantities are computed from the merging of several p_{T} bins in order to make the comparison with the 2015 data.

p_{T}(GeV/c)	$\mathrm{d}^2N_{\mathrm{AA}}/\mathrm{d}y\mathrm{d}p_{\mathrm{T}}$± (stat.) (%) ± (syst.) (%) (GeV/c)$^{-1}$	2015 data ± (stat.) ± (syst.) (GeV/c)$^{-1}$
0–0.3	1.50e-03 ± 9.18e-05 (6.1) ± 9.09e-05 (6.1)	–
0.3–1	3.99e-03 ± 1.02e-04 (2.6) ± 2.20e-04 (5.5)	4.02e-03 ± 1.95e-04 ± 2.21e-04
1–2	5.58e-03 ± 1.05e-04 (1.9) ± 2.96e-04 (5.3)	5.40e-03 ± 1.75e-04 ± 2.57e-04
2–3	4.06e-03 ± 7.97e-05 (2.0) ± 2.14e-04 (5.3)	4.05e-03 ± 1.09e-04 ± 2.11e-04
3–4	2.03e-03 ± 3.32e-05 (1.6) ± 1.11e-04 (5.5)	2.06e-03 ± 5.57e-05 ± 9.21e-05
4–5	9.04e-04 ± 1.61e-05 (1.8) ± 4.76e-05 (5.3)	9.32e-04 ± 2.93e-05 ± 4.92e-05
5–6	4.02e-04 ± 8.69e-06 (2.2) ± 2.01e-05 (5.0)	4.03e-04 ± 1.71e-05 ± 1.70e-05
6–7	2.01e-04 ± 5.04e-06 (2.5) ± 1.01e-05 (5.0)	2.16e-04 ± 1.10e-05 ± 1.04e-05
7–8	9.72e-05 ± 3.06e-06 (3.1) ± 4.92e-06 (5.1)	9.65e-05 ± 6.05e-06 ± 4.70e-06
8–9	4.88e-05 ± 1.99e-06 (4.1) ± 2.62e-06 (5.4)	–
9–10	2.66e-05 ± 1.45e-06 (5.5) ± 1.34e-06 (5.0)	–
10–11	1.45e-05 ± 9.72e-07 (6.7) ± 7.33e-07 (5.0)	–
11–12	1.04e-05 ± 8.62e-07 (8.3) ± 5.74e-07 (5.5)	–
8–12	2.51e-05 ± 6.96e-07(2.8)	2.40e-05 ± 1.25e-06 ± 1.03e-06
12–15	3.82e-06 ± 2.90e-07 (7.6) ± 2.47e-07 (6.5)	–
15–20	9.78e-07 ± 1.01e-07 (10.3) ± 5.09e-08 (5.2)	–

Table 5.11: J/ψ invariant yield in various p_{T} intervals for $2.5 < y < 4$ in the 20–40% centrality class, compared to the results obtained from the analysis of the 2015 Pb-Pb data. The blue quantities are computed from the merging of several p_{T} bins in order to make the comparison with the 2015 data.

5.4.1 Comparison with ALICE results

As described in section 2.3.1, the J/ψ mesons experience the QGP and are sensitive to nuclear matter effects. Those effects modify the J/ψ production in Pb-Pb collisions with respect to that in pp collisions. For example, the J/ψ (re)generation is expected to enhance the J/ψ yield while colour screening and energy loss are expected to suppress the J/ψ yield. As we will see below, the J/ψ R_{AA} reflects the various nuclear matter effects at play in

p_{T}(GeV/c)	$\mathrm{d}^2N_{\mathrm{AA}}/\mathrm{d}y\mathrm{d}p_{\mathrm{T}}$± (stat) (%) ± (syst.) (%) (GeV/c)$^{-1}$	2015 data ± (stat.) ± (syst.) (GeV/c)$^{-1}$
0–0.3	5.53e-04 ± 1.39e-05 (2.5) ± 2.92e-05 (5.3)	–
0.3–1	5.78e-04 ± 1.57e-05 (2.7) ± 3.05e-05 (5.3)	5.63e-04 ± 2.80e-05 ± 3.20e-05
1–2	8.34e-04 ± 1.43e-05 (1.7) ± 4.02e-05 (4.8)	8.26e-04 ± 2.63e-05 ± 4.12e-05
2–3	6.08e-04 ± 1.02e-05 (1.7) ± 2.92e-05 (4.8)	6.32e-04 ± 1.79e-05 ± 3.00e-05
3–4	3.55e-04 ± 5.60e-06 (1.6) ± 1.87e-05 (5.3)	3.50e-04 ± 9.56e-06 ± 1.74e-05
4–5	1.70e-04 ± 3.00e-06 (1.8) ± 8.39e-06 (4.9)	1.69e-04 ± 5.55e-06 ± 7.49e-06
5–6	8.41e-05 ± 1.80e-06 (2.1) ± 3.84e-06 (4.6)	7.87e-05 ± 3.17e-06 ± 3.34e-06
6–7	4.24e-05 ± 1.07e-06 (2.5) ± 1.93e-06 (4.6)	3.92e-05 ± 1.94e-06 ± 1.67e-06
7–8	2.03e-05 ± 6.52e-07 (3.2) ± 9.77e-07 (4.8)	2.08e-05 ± 1.16e-06 ± 8.77e-07
8–9	1.14e-05 ± 4.60e-07 (4.0) ± 6.08e-07 (5.3)	–
9–10	5.70e-06 ± 3.07e-07 (5.4) ± 2.54e-07 (4.5)	–
10–11	3.25e-06 ± 2.20e-07 (6.8) ± 2.39e-07 (7.4)	–
11–12	1.88e-06 ± 1.57e-07 (8.4) ± 9.39e-08 (5.0)	–
8–12	5.56e-06± 1.54e-07(2.77)	5.18e-06 ± 2.87e-07 ± 2.19e-07
12–15	1.03e-06 ± 6.68e-08 (6.5) ± 9.52e-08 (9.2)	–
15–20	2.00e-07 ± 2.51e-08 (12.6) ± 2.30e-08 (11.5)	–

Table 5.12: J/ψ invariant yield in various p_{T} intervals for $2.5 < y < 4$ in the 40–90% centrality class, compared to the results obtained from the analysis of the 2015 Pb-Pb data. The blue quantities are computed from the merging of several p_{T} bins in order to make the comparison with the 2015 data.

0–20%	
p_{T} (GeV/c)	R_{AA} ± (stat.) (%) ± (syst.) (%)
0–0.3	0.74 ± 0.05 (6.9) ± 0.07 (8.8)
0.3–1	0.70 ± 0.02 (2.5) ± 0.05 (7.8)
1–2	0.67 ± 0.01 (1.6) ± 0.05 (7.1)
2–3	0.63 ± 0.01 (1.6) ± 0.05 (7.2)
3–4	0.50 ± 0.01 (2.2) ± 0.04 (7.1)
4–5	0.39 ± 0.01 (2.5) ± 0.03 (7.0)
5–6	0.33 ± 0.01 (2.9) ± 0.02 (6.5)
6–7	0.28 ± 0.01 (3.6) ± 0.02 (6.4)
7–8	0.28 ± 0.01 (4.7) ± 0.02 (6.5)
8–9	0.26 ± 0.02 (6.0) ± 0.02 (6.2)
9–10	0.24 ± 0.02 (7.9) ± 0.02 (7.2)
10–11	0.26 ± 0.03 (9.5) ± 0.02 (6.7)
11–12	0.25 ± 0.03 (12.9) ± 0.02 (7.8)
12–15	0.26 ± 0.03 (10.2) ± 0.02 (6.7)
15–20	0.29 ± 0.05 (17.6) ± 0.02 (8.4)

Table 5.13: J/ψ R_{AA} in various p_{T} intervals for $2.5 < y < 4$ in the 0–20% centrality class with the Pb-Pb data of Run 2.

different kinematic regions. The R_{AA} results in this thesis are compared to that from 2015 Pb-Pb collisions [145]. In general the agreement between the new results and previous J/ψ R_{AA} measurements are good for the three centrality classes (as it has been seen for comparison with the J/ψ invariant yields in section 5.2). Differences between the two R_{AA} values in some p_{T} bins, such as $4 < p_{\mathrm{T}} < 5$ GeV/c, occur mainly because of the different pp cross section reference which are used. Apart from that, the measurement in this thesis is more precise and extends the p_{T} reach up to 20 GeV/c in the three centrality classes. Figure 5.34 shows the J/ψ R_{AA} measurement as a function of p_{T} at

20–40%		40–90%	
p_{T} (GeV/c)	R_{AA} ± (stat.) (%) ± (syst.) (%)	p_{T} (GeV/c)	R_{AA} ± (stat.) (%) ± (syst.) (%)
0.3–1	0.67 ± 0.02 (2.9) ± 0.05 (7.5)	0.3–1	0.67 ± 0.02 (3.0) ± 0.05 (7.3)
1–2	0.65 ± 0.01 (2.1) ± 0.05 (7.2)	1–2	0.67 ± 0.01 (1.9) ± 0.05 (6.8)
2–3	0.63 ± 0.01 (2.2) ± 0.04 (6.9)	2–3	0.65 ± 0.01 (1.9) ± 0.04 (6.5)
3–4	0.54 ± 0.01 (2.02) ± 0.04 (6.9)	3–4	0.65 ± 0.01 (2.0) ± 0.04 (6.8)
4–5	0.47 ± 0.01 (2.32) ± 0.03 (6.7)	4–5	0.61 ± 0.01 (2.3) ± 0.04 (6.4)
5–6	0.42 ± 0.01 (2.85) ± 0.03 (6.35)	5–6	0.61 ± 0.02 (2.8) ± 0.04 (6.0)
6–7	0.41 ± 0.01 (3.5) ± 0.03 (6.26)	6–7	0.60 ± 0.02 (3.5) ± 0.04 (5.9)
7–8	0.40 ± 0.02 (4.6) ± 0.03 (6.4)	7–8	0.58 ± 0.03 (4.7) ± 0.04 (6.0)
8–9	0.38 ± 0.02 (6.0) ± 0.02 (6.4)	8–9	0.62 ± 0.04 (6.0) ± 0.04 (6.4)
9–10	0.36 ± 0.03 (8.0) ± 0.02 (6.2)	9–10	0.53 ± 0.04 (8.0) ± 0.03 (5.8)
10–11	0.36 ± 0.04 (9.8) ± 0.02 (6.1)	10–11	0.56 ± 0.05 (9.8) ± 0.05 (8.1)
11–12	0.44 ± 0.06 (13.3) ± 0.03 (7.5)	11–12	0.54 ± 0.07 (13.4) ± 0.04 (7.1)
12–15	0.35 ± 0.04 (11.1) ± 0.03 (7.3)	12–15	0.66 ± 0.07 (10.4) ± 0.06 (9.8)
15–20	0.50 ± 0.09 (18.0) ± 0.03 (6.4)	15–20	0.71 ± 0.14 (19.2) ± 0.09 (12.1)

Table 5.14: J/ψ R_{AA} in various p_{T} intervals for $2.5 < y < 4$ in the 20–40% (left) and 40–90% (right) centrality classes with the Pb-Pb data of Run 2.

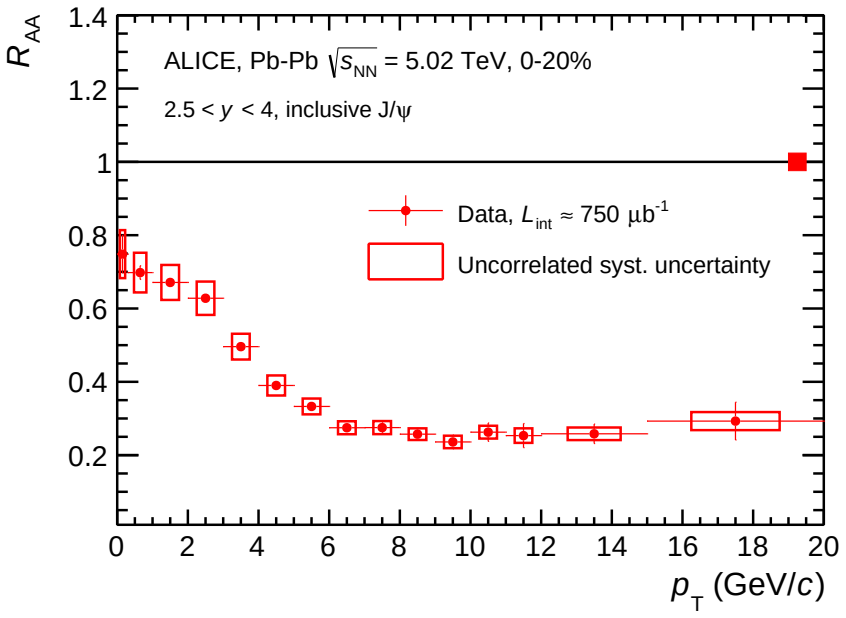

Figure 5.32: J/ψ R_{AA} as a function of p_{T} for $2.5 < y < 4$ in the 0–20% centrality class. The statistical uncertainty is displayed with vertical error bars and the uncorrelated systematic uncertainty is represented by an open box around a point. The global uncertainty is 2% [This thesis].

forward rapidity in the 0–20% centrality interval. The result in red is obtained in this thesis while the result in blue is taken from the published results from the 2015 data [145]. Both results show that R_{AA} increases with decreasing p_{T} at low p_{T} ($p_{\mathrm{T}} \leq 7$ GeV/c), which is a hint for J/ψ regeneration. For $p_{\mathrm{T}} \geq 8$ GeV/c, both R_{AA} are suppressed by about 75% and exhibit a flat p_{T} dependence.

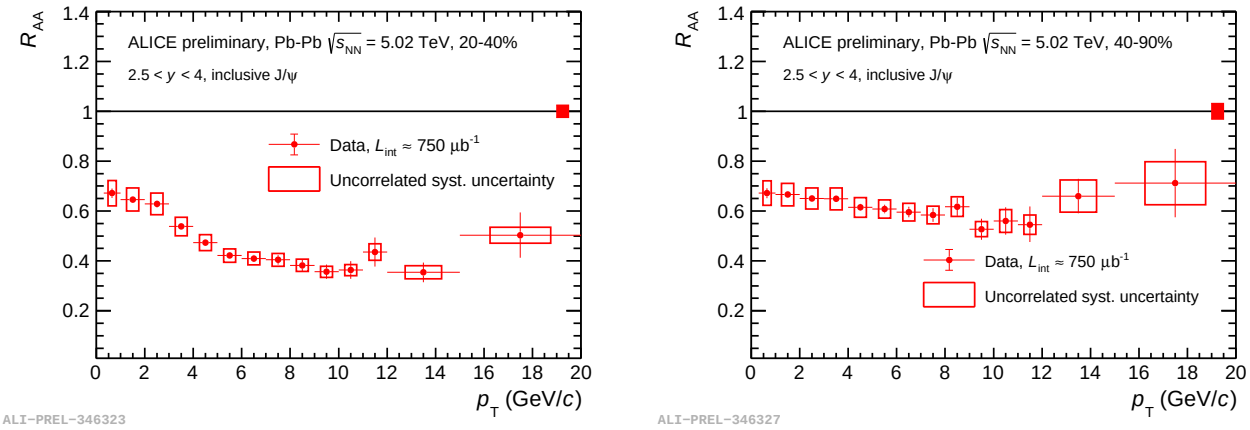

Figure 5.33: J/ψ $R_{\rm AA}$ as a function of $p_{\rm T}$ for $2.5 < y < 4$ in the 20–40% (left) and the 40–90% (right) centrality classes. The statistical uncertainty is displayed with vertical error bars and the uncorrelated systematic uncertainty is represented by open box. The global uncertainties on $R_{\rm AA}$ for centrality 20–40% and 40–90% are 2% and 3%, respectively.

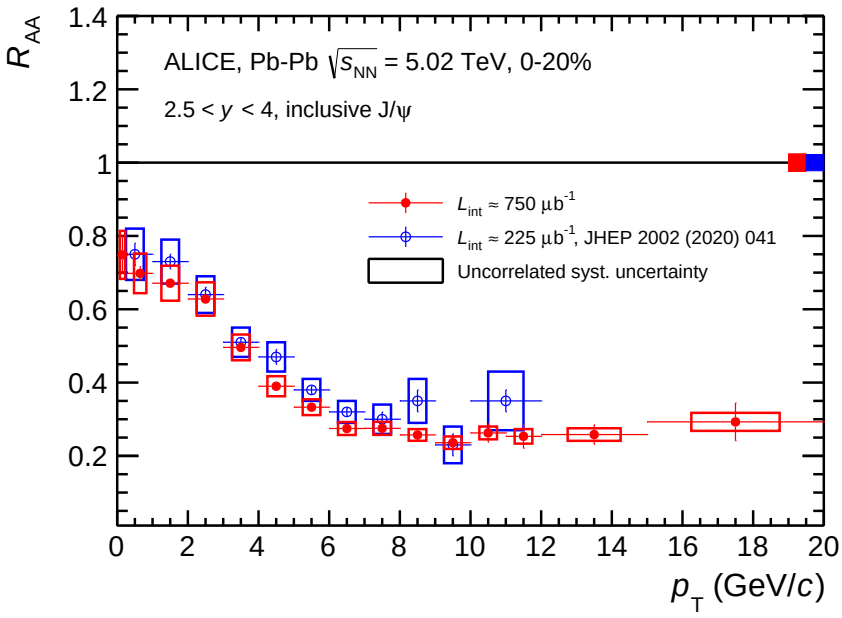

Figure 5.34: J/ψ $R_{\rm AA}$ as a function of $p_{\rm T}$ for $2.5 < y < 4$ in the 0–20% centrality class, compared to the published results from ALICE [145]. The statistical uncertainty is displayed with vertical error bars and the uncorrelated systematic uncertainty is represented by an open box around a point [This thesis].

The left panel of Figure 5.35 shows the comparison with the published results of the J/ψ $R_{\rm AA}$ in the 20–40% centrality range from ALICE [145]. For $0.3 < p_{\rm T} < 6$ GeV/c, the two J/ψ $R_{\rm AA}$ are enhanced compared to that at high $p_{\rm T}$. Both $R_{\rm AA}$ are suppressed by about 60% for $p_{\rm T} \geq 6$ GeV/c. The right panel of Figure 5.35 shows the comparison with the published results of the J/ψ $R_{\rm AA}$ in the 40–90% centrality range from ALICE [145]. Both

$R_{\rm AA}$ are flat in the full measured $p_{\rm T}$ range. In some $p_{\rm T}$ bins, such as $4 \leq p_{\rm T} < 5$ GeV/c, a slight difference between the $R_{\rm AA}$ in this thesis and in [145] is observed. It is mainly coming from the different pp reference cross-sections used.

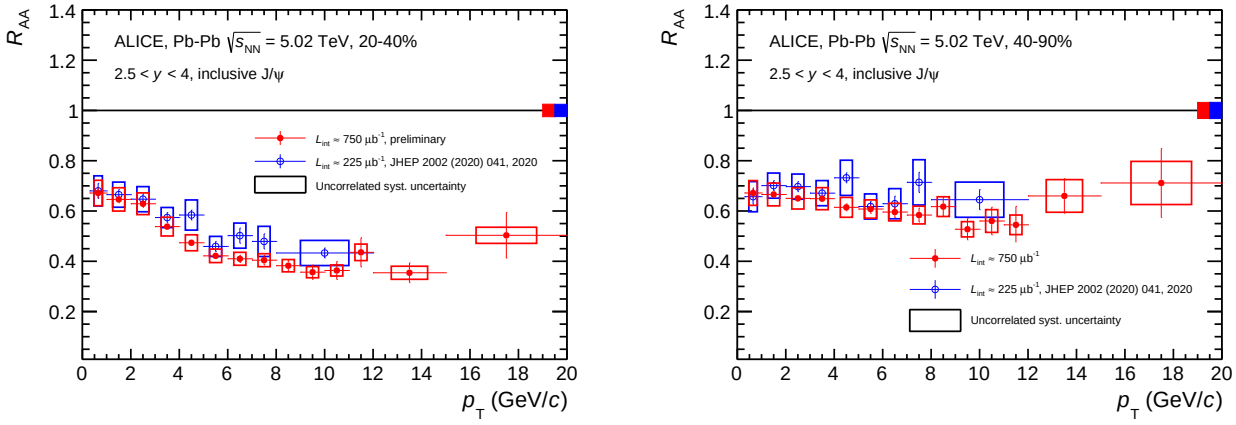

Figure 5.35: J/ψ $R_{\rm AA}$ as a function of $p_{\rm T}$ for $2.5 < y < 4$ in the 20–40% (left) and the 40–90% (right) centrality classes, compared to the published results [145]. The statistical uncertainty is displayed with vertical error bars and the uncorrelated systematic uncertainty is represented by an open box around a point [This thesis].

5.4.2 Comparison with models

The theoretical calculations based on a transport model by X. Du *et al.* [9] and on a statistic hadronisation model by A. Andronic *et al.* [10] are compared to the J/ψ $R_{\rm AA}$ measured in this thesis. The models are already presented in section 2.3.1. Figure 5.36 shows the $R_{\rm AA}$ in the 0–20% centrality class compared to the two calculations. The transport model reproduces the data in the full $p_{\rm T}$ range. In this model, the J/ψ yield is dominated by the regeneration from the $c\bar{c}$ pairs in the QGP phase for $p_{\rm T} < 6$ GeV/c. For $p_{\rm T}$ above 6 GeV/c, the J/ψ yield is dominated by primordial J/ψ that survive in the QGP. The calculation based on the statistic hadronization model is compatible with the data for $p_{\rm T} < 4$ GeV/c, within the large uncertainties from the model. In this region, the initially produced J/ψ in the nucleus core are fully suppressed and the J/ψ yield is dominated by the regeneration from the $c\bar{c}$ pairs at the phase transition. For $p_{\rm T} \geq 4$ GeV/c, the J/ψ is initially produced in the nucleus corona where the density is small and there is no QGP effect. The $R_{\rm AA}$ computed from this model is well below unity because there are few J/ψ produced in the nucleus corona with respect to the normalised pp yield. The calculation underestimates the data by about a factor of 4 in this $p_{\rm T}$ range.

The left panel of Figure 5.37 shows the $R_{\rm AA}$ in the centrality class 20–40% compared to the two theoretical calculations. The transport model underestimates the data for $3 < p_{\rm T} < 5$ GeV/c, otherwise it reproduces well the data. The statistic hadronisation model describes well the data for $p_{\rm T} \leq 4$ GeV/c because of the regeneration component from the $c\bar{c}$ pairs in this $p_{\rm T}$ interval. For $p_{\rm T} > 4$ GeV/c, the statistic hadronisation model, however, fails

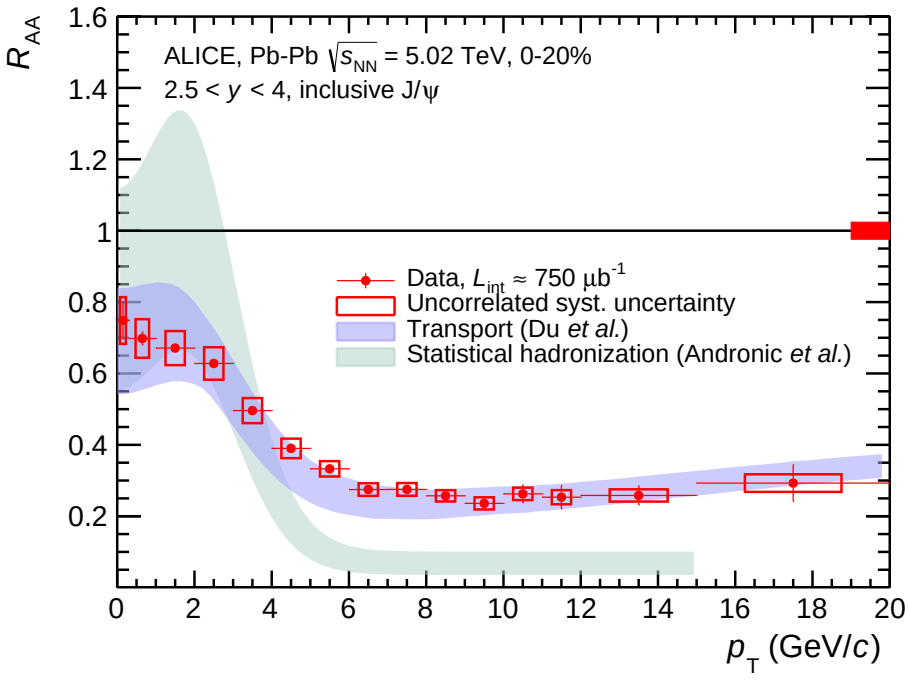

Figure 5.36: J/ψ $R_{\rm AA}$ as a function of $p_{\rm T}$ for $2.5 < y < 4$ in the 0–20% centrality class with the Pb-Pb data of Run 2, compared to theoretical calculations based on transport model [9] and on statistic hadronization model [10] [This thesis].

at describing the data as for the most central collisions.

The right panel of Figure 5.37 shows the $R_{\rm AA}$ in the centrality class 40–90%, compared to transport model. The model is in agreement with the data within uncertainties in the full $p_{\rm T}$ range. Note that the model suggests an increase of the $R_{\rm AA}$ towards unity at low $p_{\rm T}$ which is not observed in the data.

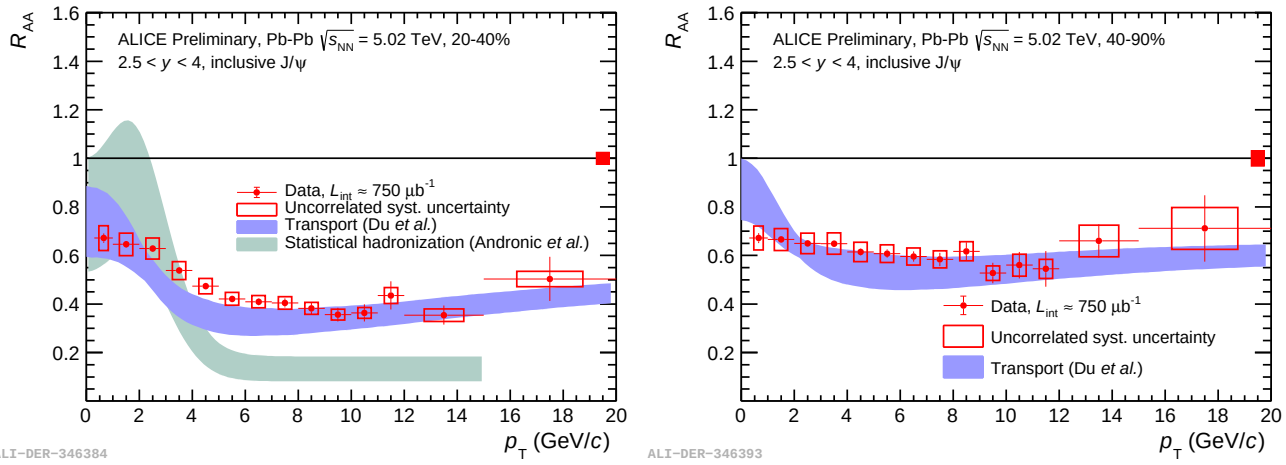

Figure 5.37: J/ψ $R_{\rm AA}$ as a function of $p_{\rm T}$ for $2.5 < y < 4$ in the 20–40% (left) and the 40–90% (right) centrality classes with the Pb-Pb data of Run 2, which are compared to theoretical calculations based on transport model [9] and on statistic hadronisation model [10].

5.4.3 Comparison with ATLAS and CMS results

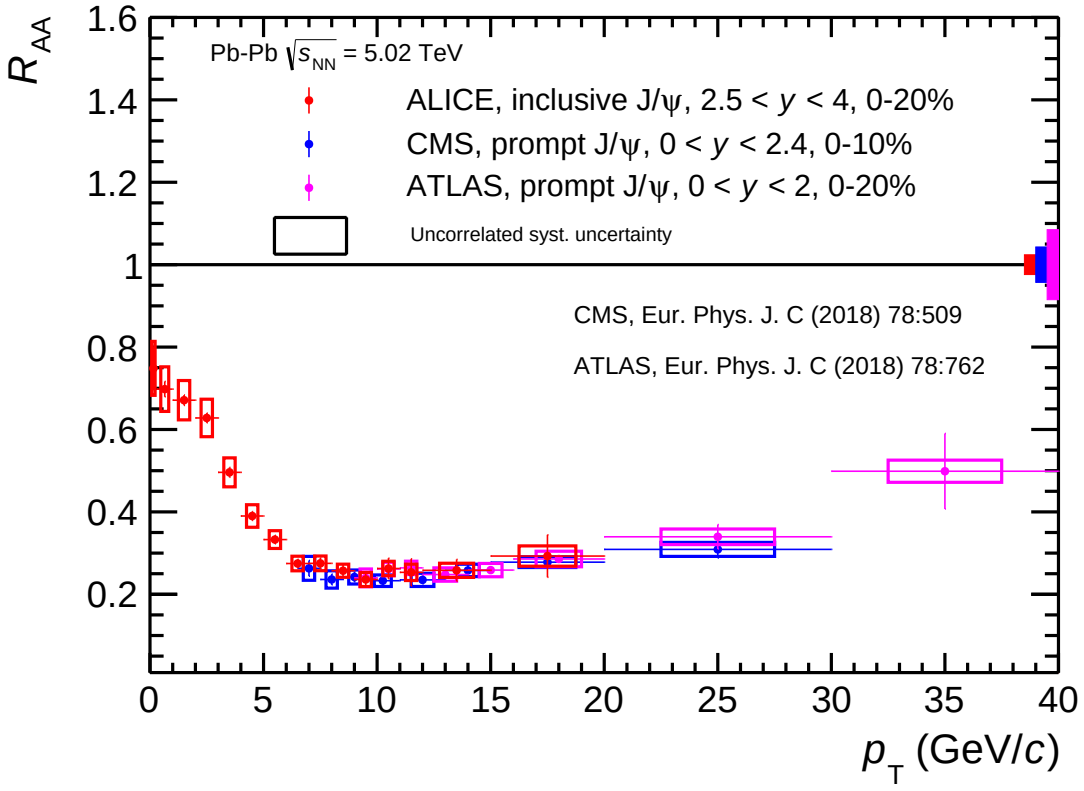

Figure 5.38: J/ψ R_{AA} as a function of p_{T} for $2.5 < y < 4$ in the 0–20% centrality class, compared to the published results from CMS [7] and ATLAS [8]. The statistical uncertainty is displayed with vertical error bars and the uncorrelated systematic uncertainty is represented by an open box around a point [This thesis].

The J/ψ R_{AA} result is also compared to the data obtained from CMS [7] and ATLAS [8]. In Figure 5.38, the CMS and ATLAS experiments measure prompt J/ψ at mid-rapidity, as a function of p_{T} in the 0–10% and 0–20% centrality ranges, respectively. The three results are compatible within uncertainty for $6 < p_{\mathrm{T}} < 20$ GeV/c although the different rapidity regions probed by the different measurements. An interplay between colour screening and energy loss is expected in this high-p_{T} region [146, 8].

Chapter 6

Conclusions and outlooks

It is important to measure J/ψ production in pp collisions in order to study the production mechanism of charmonium production. In addition, measurements of J/ψ production in pp collisions provide a reference for the study of the medium effects in heavy-ion collisions. Furthermore, measuring the J/ψ production in Pb-Pb collisions gives an opportunity to probe the QGP. At the LHC, ALICE is one of the four major experiments and it studies not only the QGP and the cold nuclear matter in heavy-ion collisions but also the particle production in hadron-hadron collisions. In this thesis, the work on the inclusive J/ψ production measurement for $2.5 < y < 4$ in pp and Pb-Pb collisions at $\sqrt{s_{\rm NN}} = 5.02$ TeV is presented. The two analyses use the dimuon decay channel to study the charmonium production with the muon spectrometer. In addition, my service task on the muon data quality assurance (QA) is also presented. The service task was performed on the data recorded in ALICE from 2017 to 2018. The data that fulfill the detector (including muon tracking and trigger chambers) QA-checks are the ones used for analysis. In particular, the 2017 pp and 2018 Pb-Pb data at $\sqrt{s_{\rm NN}} = 5.02$ TeV provide a higher luminosity with respect to the previous pp and Pb-Pb data at the same energy.

This thesis first reports on the analysis of the inclusive J/ψ production in pp collisions in ALICE. The analysis includes the J/ψ signal extraction, the calculation of the J/ψ acceptance efficiency correction of the detector, the computation of the luminosity corresponding to the analysed data samples and the estimation of the systematic uncertainties on the different sources, such as signal extraction, MC input parametrisation, luminosity, tracking, trigger and matching efficiencies. The $p_{\rm T}$- and y-differential inclusive J/ψ cross sections are obtained for $2.5 < y < 4$ and for $0 < p_{\rm T} < 12$ GeV/c at forward rapidity, respectively. The double-differential inclusive J/ψ cross sections are measured at forward rapidity for $0.3 < p_{\rm T} < 12$ GeV/c. The $p_{\rm T}$-differential cross-section increases from $p_{\rm T} = 0$ to $p_{\rm T} = 2$ GeV/c and decreases for $p_{\rm T} > 2$ GeV/c. The y-differential cross-section increases from $y = 4$ to $y = 2.5$. The double-differential cross section decreases with increasing $p_{\rm T}$ and y. Concerning the comparison with the published cross section from the 2015 pp data samples, the high statistics 2017 pp data extend the $p_{\rm T}$ reach from 12 GeV/c to 20

GeV/c and allow for more precise measurements. The agreement between the 2017 and 2015 differential cross sections are within 2σ. The larger deviations in some kinematic intervals are considered to come from statistical fluctuations in the 2015 data sample, based on the checks, for example, of the cross-section comparison to other energies, such as 7, 8 and 13 TeV. In this comparison, a stronger hardening of the $p_{\rm T}$ spectra is observed in the collisions at $\sqrt{s}$ =13 TeV with respect to the 5.02, 7 and 8 TeV data. This hardening can be explained by the increase of the prompt J/ψ mean $p_{\rm T}$ with increasing energy, and by the increasing contribution from non-prompt J/ψ with increasing energy, at high $p_{\rm T}$. The resulting cross-section is also compared to prompt J/ψ combined with non-prompt J/ψ theoretical calculations. The prompt J/ψ calculations are based on the Colour Evaporation Model (CEM), the Non-Relativistic Quantum Chromodynamics (NRQCD) model and the NRQCD coupled to the colour glass condensate (CGC) model. The non-prompt contribution ($B \rightarrow$ J/ψ) is described by a first-order-next-to-leading-logarithm (FONLL) perturbative QCD (pQCD) calculations. Most of theoretical models reproduce the data within uncertainties.

This thesis also reports on the analysis of the inclusive J/ψ production at forward rapidity in Pb-Pb collisions at $\sqrt{s_{\rm NN}}$ = 5.02 TeV in ALICE. The analysis includes the J/ψ signal extraction, the calculation of the J/ψ acceptance efficiency, the computation of the normalization factor to the analyzed data samples and the estimation of the systematic uncertainties on signal extraction, MC input parametrisation, normalisation factor, nuclear overlap function, centrality limit, reference to pp cross section, tracking, trigger and matching efficiencies. The J/ψ nuclear modification factor, $R_{\rm AA}$, as a function of $p_{\rm T}$ is measured for three different centrality intervals. The $R_{\rm AA}$ for the 0–20% centrality class is below one. It increases with decreasing $p_{\rm T}$ from 6 GeV/c to 0, but stays flat and well below unity for $p_{\rm T} > 6$ GeV/c. This measurement is found to be similar with the $R_{\rm AA}$ measured in the 2015 Pb-Pb data sample. The $R_{\rm AA}$ enhancement at low $p_{\rm T}$ is attributed to the J/ψ (re)generation since the charm quark production is large at the LHC energy. In the most central collisions, the inclusive J/ψ $R_{\rm AA}$ for $6 < p_{\rm T} < 20$ GeV/c and $2.5 < y < 4$ is compatible with the prompt-J/ψ $R_{\rm AA}$ measured at mid-rapidity by ATLAS and CMS. In ATLAS, at high $p_{\rm T}$, the prompt-J/ψ $R_{\rm AA}$ is found to be similar to the charged particle $R_{\rm AA}$ which is seen as an energy-loss signature. The J/ψ production at high $p_{\rm T}$ is probably affected by an interplay between colour screening and energy loss. The $R_{\rm AA}$ for the 20–40% centrality class is about 0.4 at large $p_{\rm T}$ and is slightly enhanced for $p_{\rm T} \leq 7$ GeV/c with respect to the values measured for $p_{\rm T} > 7$ GeV/c. The $R_{\rm AA}$ for the 40–90% centrality is about 0.5 and flat within uncertainty in the full $p_{\rm T}$ range. Theoretical calculations, based on a transport approach with primordial J/ψ affected by colour screening and including charmonium (re)generation at low $p_{\rm T}$ are compared to the data. The comparison between the data and the transport model is in good agreement in the full $p_{\rm T}$ range for the three centrality classes. Data are also compared to the calculations based on a statistical model which includes the contribution from charmonium (re)generation. Besides, it considers the J/ψ that are produced in the nucleus corona in which no QGP is expected to exist. This model calculation is compatible with the data at low $p_{\rm T}$ for the 0–20% and 20–40% centrality classes. For $p_{\rm T} \geq 4$ GeV/c, it underestimates the data by about a factor of 4.

For the completeness of this study, the inclusive J/ψ analysis at forward rapidity in Pb-Pb collisions at $\sqrt{s_{\rm NN}}$ = 5.02 TeV can be extended to more differential studies as a function of the rapidity, centrality and $p_{\rm T}$ of the J/ψ $R_{\rm AA}$. The rapidity dependence of the $R_{\rm AA}$ can also be studied with the same centrality regions that the ones at mid-rapidity for a better comparison of the rapidity dependence. For the centrality dependence of the $R_{\rm AA}$, one can also focus on the investigation of the J/ψ coherent photoproduction from central to peripheral collisions by using a $p_{\rm T}$ cut of $p_{\rm T} < 0.3$ GeV/c.

Concerning future measurements, the LHC is now in the second long shutdown (LS2) from 2019 to 2021 for experimental upgrades. In ALICE, two of the upgrades, relevant for the charmonium studies at forward rapidity, are the installation of the Muon Forward Tracker (MFT) in front of the muon spectrometer and a new readout electronics for the muon systems. The former will measure the secondary vertex for muon spectrometer analysis and will allow one to distinguish prompt and non-prompt J/ψ at forward rapidity. Then, for example, it will be possible to access the $R_{\rm AA}$ of the b (J/ψ from B) down to low $p_{\rm T}$ at forward rapidity. The latter upgrade will enhance the rate to read out events in the three systems (pp, p-Pb and Pb-Pb). After the LS2, the LHC will enter the Run 3 and 4 periods and ALICE aims at collecting a heavy-ion luminosity which is 10 times more than the collected heavy-ion luminosity in Run 2. This collected luminosity increase therefore will give opportunities to study the J/ψ production more precisely in the kinematic region where the statistics are scarce in Run 2, such as the edge of the forward rapidity, the (ultra-)peripheral collisions and the high-$p_{\rm T}$ region. The collected luminosity increase will also help to discriminate the theoretical models. Furthermore, the increase of statistics will allow for more precise and differential measurements ($R_{\rm AA}$ and flow) of other quarkonium states, like ψ(2S) and Υ(nS) which are still very limited in terms of precision in the Run 2 data. In the case of ψ(2S), the limitation of the measurement from the background will be also reduced thanks to the MFT. Besides, one can also study rare probes such as double J/ψ production or correlation of quarkonium measured at forward rapidity with other particles (J/ψ, D, hadrons) measured at mid-rapidity.

Appendix A

The Glauber model

The Glauber model has been presented in section 1.3.2. This appendix explains how the Glauber model allows to extract the centrality from experimental data in ALICE and mainly refers to [228]. In ALICE, the centrality is expressed as a percentile of the total hadronic cross section and evaluated for a given data sample, via the measurement of the charged particle multiplicity or deposited energy by the spectator nucleons. The charged particle multiplicity is measured by different detectors, for instance, the V0, SPD and/or TPC. The deposited energy by the spectator nucleons is measured by the ZDC.

The Glauber model describes the dependence of the number of participating nucleons, $N_{\rm part}$, and the number of binary nucleon-nucleon collisions, $N_{\rm coll}$, with the impact parameter $\vec{b}$ of the heavy-ion collisions (see section 1.3.2 for details). Neither $N_{\rm part}$, $N_{\rm coll}$ nor $\vec{b}$ can be measured in experiments. But mean values of such quantities can be extracted for classes of the measured events ($N_{\rm evt}$) via a mapping procedure. A measured distribution is usually mapped to the corresponding $N_{\rm part}$ or $N_{\rm coll}$ obtained from phenomenological calculations or MC simulations based on the Glauber model. Figure 3.14 shows the distribution of the sum of amplitudes in the two V0 arrays in Pb-Pb collisions at $\sqrt{s_{\rm NN}} = 2.76$ TeV in ALICE. The centrality classes are defined as the percentile of the hadronic cross section corresponding to a particle multiplicity within a lower and a higher given threshold. For each centrality class, the mean of a quantity, such as $N_{\rm part}$, is calculable from MonteCarlo (MC) events. In ALICE, the Glauber model is implemented with MC simulation. The first step in the Glauber MC is to model two nuclei by defining the position of the nucleons in each nucleus. To define the nucleon position in ^{208}Pb, a nuclear density function (a modified Woods-Saxon distribution) is used. The next step is to simulate a nuclear collision. The nucleus-nucleus collision is considered as a sequence of independent binary nucleon-nucleon collisions. The nucleons travel along straight line trajectories and two nucleons from different nuclei are assumed to collide if the relative transverse distance, d, between nucleons is less than the distance corresponding to the inelastic nucleon-nucleon cross section ($d < \sqrt{\sigma_{inel}/\pi}$). Note that the same cross section is used for all successive collisions. Then $N_{\rm coll}$ and $N_{\rm part}$ are determined, respectively, by

counting the binary nucleon collisions and the nucleons that experience at least one collision. The total Pb-Pb cross section, σ_{PbPb}, is calculated by simulating heavy-ion collisions. The result is [228]:

$$\sigma_{\mathrm{PbPb}} = (7.67 \pm 0.16 \text{ (syst.)}) \text{ b for } \mathrm{Pb}-\mathrm{Pb} \text{ at } 5.02 \text{ TeV}.$$

The Glauber MC model is then coupled to a model for particle production, based on a negative binomial distribution (NBD), to fit the charged particle multiplicity distribution. The NBD function, $P_{\mu,k}(n)$, permits to generate the number of particles produced per interaction. The NBD function gives the probability of measuring n detector hits per ancestor (defined below), where μ is the mean multiplicity per ancestor and k controls the width. In the NBD-Glauber MC model, there is the concept of "ancestors" that correspond to independent emitting sources of particles. The number of ancestors $N_{\mathrm{ancestors}}$ is assumed to be parameterised by $N_{\mathrm{ancestors}} = f \cdot N_{\mathrm{part}} + (1-f) \cdot N_{\mathrm{coll}}$ with f the proportion of "ancestors" coming from a soft interaction. Indeed, this model is inspired by two-component models, where the nucleus-nucleus collisions are decomposed into soft (N_{part} term) and hard (N_{coll} term) interactions. For each Glauber MC event, $P_{\mu,k}(n) \times N_{\mathrm{ancestors}}$ is calculated to obtain the averaged simulated V0 amplitude, which is proportional to the number of particles hitting the hodoscopes. The V0 amplitude distribution is then simulated for a set of events and for different values of μ, k and f. A fit is performed on the V0 experimental distribution by using the simulated distribution and the minimisation procedure permits to evaluate the values of μ, k and f from data. For each centrality class, distributions of quantities, such as N_{part} or N_{coll} are obtained from the MC. Therefore one can access to the means of these distributions in a given centrality interval.

Appendix B

Signal extraction functions

Two signal functions and several background functions are employed to fit the dimuon invariant mass spectra in order to extract the J/ψ and ψ(2S) signals. The analytical forms of the signal functions and of the background functions are given in this appendix. All signal functions can be found as well in [232].

B.1 The charmonium signal functions

Crystal Ball function: the extended Crystal Ball (CB2) function is defined as a Gaussian core with a variable width and non-Gaussian tails. A factor, N, is used for the normalisation. The charmonium signal mass and width are respectively described by $\bar{x}$ and σ and they define the t variable. The non-Gaussian tails have four parameters t_1, p_1 and t_2, p_2, which describe the left (low mass) and right (high mass) sides of the charmonium peak. The function is defined as:

$$f(x; N, \bar{x}, \sigma, t_1, t_2, p_1, p_2) = N \cdot \begin{cases} A \cdot (B - t)^{-p_1}, & t < -t_1 \\ \exp(-\frac{1}{2}t^2), & -t_1 \leq t < t_2 \\ C \cdot (D + t)^{-p_2}, & t \geq t_2 \end{cases}$$

where

$$t = \frac{x - \bar{x}}{\sigma}$$
$$A = (\frac{p_1}{|t_1|})^{p_1} \cdot \exp(-\frac{|t_1|^2}{2})$$
$$B = \frac{p_1}{|t_1|} - |t_1|$$
$$C = (\frac{p_2}{|t_2|})^{p_2} \cdot \exp(-\frac{|t_2|^2}{2})$$
$$D = \frac{p_2}{|t_2|} - |t_2|$$

A new CB2 function is developed in this thesis in order to describe both the J/ψ and ψ(2S) signals with a global fit. We call this new CB2 function: double extended Crystal Ball function or double CB2 function. The double CB2 function is the sum of two CB2 functions and is defined as $f + f_{\psi(2S)}$, where

$$f_{\psi(2S)}(x; N_2, \bar{x}, \sigma, t_1, t_2, p_1, p_2) = N_2 \cdot \begin{cases} A \cdot (B - z)^{-p_1}, & z < -t_1 \\ \exp(-\frac{1}{2}z^2), & -t_1 \leq z < t_2 \\ C \cdot (D + z)^{-p_2}, & z \geq t_2 \end{cases}$$

where z:

$$z = \frac{x - \left[\bar{x} + \left(m^{PDG}_{\psi(2S)} - m^{PDG}_{J/\psi}\right)\right]}{\sigma \times \frac{\sigma^{MC}_{\psi(2S)}}{\sigma^{MC}_{J/\psi}}}.$$

The ψ(2S) mass is bounded to the J/ψ mass, $\bar{x}$, by the difference of the Particle Data Group (PDG) mass ($m^{PDG}_{\psi(2S)} - m^{PDG}_{J/\psi}$). The charmonium width ratio $\frac{\sigma^{MC}_{\psi(2S)}}{\sigma^{MC}_{J/\psi}}$ is fixed to 1.01 for the double CB2 function (see section 4.1.2).

NA60 function: it is also defined as a variable width Gaussian function but with more parameters that describe the left and right tails. There are eight tail parameters $(t_1, t_2, p_1, p_2, ..., p_6)$ and the NA60 function is defined as:

$$f(x; N, \bar{x}, \sigma, t_1, t_2, p_1, ..., p_6) = N \cdot \exp\left[-\frac{1}{2}\left(\frac{t}{t_0}\right)^2 \right]$$

where

$$t = \frac{x - \bar{x}}{\sigma}$$

and

$$t_0 = \begin{cases} 1 + \left[p_1(t_1 - t)\right]^{p_2 - p_3\sqrt{t_1 - t}}, & t < t_1 \\ 1, & t_1 \leq t < t_2 \\ 1 + \left[p_4(t - t_2)\right]^{p_5 - p_6\sqrt{t - t_2}}, & t \geq t_2 \end{cases}$$

A new NA60 function is also developed in this thesis in order to describe both the J/ψ and ψ(2S) signals with a global fit. We call this new NA60 function: double NA60 function, which is the sum of two NA60 functions and is defined as $f + f_{\psi(2S)}$, where

$$f_{\psi(2S)}(x; N_2, \bar{x}, \sigma, t_1, t_2, p_1, ..., p_6) = N_2 \cdot \exp\left[-\frac{1}{2}\left(\frac{z}{z_0}\right)^2 \right],$$

where

$$z = \frac{x - \left[\bar{x} + \left(m^{PDG}_{\psi(2S)} - m^{PDG}_{J/\psi}\right)\right]}{\sigma \times \frac{\sigma^{MC}_{\psi(2S)}}{\sigma^{MC}_{J/\psi}}}$$

and

$$z_0 = \begin{cases} 1 + \left[p_1(t_1 - z)\right]^{p_2 - p_3\sqrt{t_1 - z}}, & z \leq t_1 \\ 1, & t_1 < z < t_2 \\ 1 + \left[p_4(z - t_2)\right]^{p_5 - p_6\sqrt{z - t_2}}, & z \geq t_2 \end{cases}$$

The charmonium width ratio $\frac{\sigma^{MC}_{\psi(2S)}}{\sigma^{MC}_{J/\psi}}$ is fixed to 1.01 for the double NA60 function.

B.2 The background functions

Variable width Gaussian (VWG2)

The function is defined by a normalization factor N and three parameters (A, B, C):

$$f(x; N, \bar{x}, A, B, C) = N \cdot \exp\left[- \frac{(x - \bar{x})^2}{2\sigma^2_{VWG}} \right],$$

where

$$\sigma_{VWG} = A + B \cdot \frac{(x - \bar{x})}{\bar{x}} + C \cdot \left[\frac{(x - \bar{x})}{\bar{x}}\right]^2$$

Polynomial ratio (Pol2/Pol3 or Pol1/Pol2)

The function is defined as:

$$f_{\frac{\text{POL2}}{\text{POL3}}}(x; p_0, ..., p_6) = p_0 \cdot \frac{1 + p_1 x + p_2 x^2}{p_3 + p_4 x + p_5 x^2 + p_6 x^3}, \text{ or } f_{\frac{\text{POL1}}{\text{POL2}}}(x; p_0, ..., p_4) = p_0 \cdot \frac{1 + p_1 x}{p_2 + p_3 x + p_4 x^2}$$

Double exponential sum

The function is expressed as:

$$f_{\exp}(x; p_0, ..., p_3) = p_0 e^{-x/p_1} + p_2 e^{-x/p_3}.$$

Appendix C

Non-prompt J/ψ effect on inclusive J/ψ $R_{\rm AA}$

In the Run 2 period, the ALICE muon spectrometer measures the inclusive J/ψ nuclear modification factor, $R_{\rm AA}^{\rm incl}$, and is not able to measure prompt and non-prompt J/ψ productions separately, at forward rapidity. The prompt J/ψ nuclear modification factor, $R_{\rm AA}^{\rm pro}$, can be estimated by using the measured $R_{\rm AA}^{\rm incl}$ and by making assumptions on two quantities:

- f_B the fraction of J/ψ production from B-hadron decays to the prompt J/ψ production in pp collisions, in the kinematic coverage of the muon spectrometer;
- the suppression of B-hadron production in Pb-Pb collisions due to initial- and final-state nuclear effects.

$R_{\rm AA}^{\rm pro}$ can be obtained by deriving Eq. 5.1, which is also rewritten below:

$$R_{\rm AA}^{\rm incl} = \frac{N_{\rm AA}^{\rm incl}}{\sigma_{\rm pp}^{\rm incl} \times < T_{\rm AA} >}. \tag{C.1}$$

We know that the inclusive J/ψ yield, $N_{\rm AA}^{\rm incl}$, is the sum of prompt ($N_{\rm AA}^{\rm pro}$) and non-prompt ($N_{\rm AA}^{\rm npro}$) yields and the inclusive J/ψ cross section, $\sigma_{\rm pp}^{\rm incl}$, is the sum of prompt ($\sigma_{\rm pp}^{\rm pro}$) and non-prompt ($\sigma_{\rm pp}^{\rm npro}$) cross sections in pp collisions. Eq. C.1 can be expanded into:

$$R_{\rm AA}^{\rm incl} = \frac{N_{\rm AA}^{\rm pro} + N_{\rm AA}^{\rm npro}}{(\sigma_{\rm pp}^{\rm pro} + \sigma_{\rm pp}^{\rm npro}) \times < T_{\rm AA} >}. \tag{C.2}$$

Eq. C.2 can be rewritten as:

$$R_{\rm AA}^{\rm incl}\sigma_{\rm pp}^{\rm pro} < T_{\rm AA} > + R_{\rm AA}^{\rm incl}\sigma_{\rm pp}^{\rm npro} < T_{\rm AA} > - N_{\rm AA}^{\rm npro} = N_{\rm AA}^{\rm pro}. \tag{C.3}$$

In order to obtain $R_{\rm AA}^{\rm pro}$, the above equation is divided by the product of $\sigma_{\rm pp}^{\rm pro}$ and $< T_{\rm AA} >$ and it becomes:

$$R_{\rm AA}^{\rm incl} + \frac{R_{\rm AA}^{\rm incl}\sigma_{\rm pp}^{\rm npro} < T_{\rm AA} >}{\sigma_{\rm pp}^{\rm pro} < T_{\rm AA} >} - \frac{N_{\rm AA}^{\rm npro}}{\sigma_{\rm pp}^{\rm pro} < T_{\rm AA} >} = R_{\rm AA}^{\rm pro}. \tag{C.4}$$

The third term in Eq. C.4 is then multiplied by a factor, $\frac{\sigma_{\rm pp}^{\rm npro}}{\sigma_{\rm pp}^{\rm npro}}$, and the equation becomes:

$$R_{\rm AA}^{\rm incl} + R_{\rm AA}^{\rm incl} f_B - \frac{N_{\rm AA}^{\rm npro} \sigma_{\rm pp}^{\rm npro}}{\sigma_{\rm pp}^{\rm pro} < T_{\rm AA} > \sigma_{\rm pp}^{\rm npro}} = R_{\rm AA}^{\rm pro}, \tag{C.5}$$

where f_B equals to $\frac{\sigma_{\rm pp}^{\rm npro}}{\sigma_{\rm pp}^{\rm pro}}$. Finally, $R_{\rm AA}^{\rm pro}$ can be expressed as a function of $R_{\rm AA}^{\rm incl}$, $R_{\rm AA}^{\rm npro}$ and f_B:

$$R_{\rm AA}^{\rm pro} = R_{\rm AA}^{\rm incl} + R_{\rm AA}^{\rm incl} f_B - R_{\rm AA}^{\rm npro} f_B. \tag{C.6}$$

In case $R_{\rm AA}$ prompt is found to be negative, it is set to zero. One note from Eq. C.6 is that if the non-prompt $R_{\rm AA}$ is equal to the inclusive one, then the prompt $R_{\rm AA}$ is also equal to the inclusive one, as expected. The $p_{\rm T}$-differential cross sections, in rapidity bins, of prompt and non-prompt J/ψ production at forward rapidity in pp collisions at $\sqrt{s}$ = 8 TeV have been measured by the LHCb experiment [233]. Therefore, the fraction, f_B, of non-prompt J/ψ over prompt J/ψ can be recomputed from the LHCb measurement, for the acceptance of the ALICE muon spectrometer, $2.5 < y < 4$. Figure C.1 shows the f_B measurement from LHCb as a function of $p_{\rm T}$ (blue) for $2.5 < y < 4$. The LHCb f_B values increase from about 0.1 to about 0.4 with increasing $p_{\rm T}$ for $0 < p_{\rm T} < 14$ GeV/c. The $p_{\rm T}$ dependence of the f_B fraction from LHCb can be parametrised by using a second-degree polynomial function, which is shown with a red line in Figure C.1. For $p_{\rm T} \geq 15$ GeV/c, the fit is extended and is shown with a red dashed line. The ALICE result on inclusive J/ψ production cross section measured in this thesis at $\sqrt{s}$ = 5.02 TeV and the FONLL model calculation for the non-prompt J/ψ cross section are used to extract the ALICE f_B as a function of $p_{\rm T}$ (green) for $0 < p_{\rm T} < 20$ GeV/c and $2.5 < y < 4$. The ALICE f_B values increase from about 0.08 to about 0.75 with increasing $p_{\rm T}$.

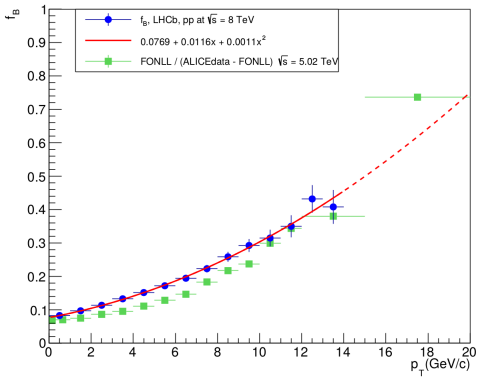

Figure C.1: Fraction of non-prompt J/ψ to prompt J/ψ contributions, $f_{\rm B}$, is obtained as a function of $p_{\rm T}$ by using the LHCb data at $\sqrt{s}$ = 8 TeV [233] and by using the FONLL model calculation and the ALICE data at $\sqrt{s}$ = 5.02 TeV [This thesis].

In this appendix, the LHCb f_B at $\sqrt{s}$ = 8 TeV is used for the estimation of $R_{\rm AA}^{\rm pro}$, in order to avoid the usage of theoretical calculations. As it can be seen in Figure C.1, the f_B fraction seems not strongly energy dependent. In

addition, two extreme assumptions on non-prompt J/ψ $R_{\rm AA}$ ($R_{\rm AA}^{\rm npro} = 0$ and $R_{\rm AA}^{\rm npro} = 1$) are considered. Figures C.2 and C.3 show $p_{\rm T}$-dependence of the inclusive J/ψ $R_{\rm AA}$ measured in this thesis and of the prompt J/ψ $R_{\rm AA}$ estimated if $R_{\rm AA}^{\rm npro} = 0$ or if $R_{\rm AA}^{\rm npro} = 1$ for the 0–20% (left panel) and 20-40% (right panel) centrality classes. For the case, $R_{\rm AA}^{\rm npro} = 0$, for both centrality intervals, the estimated prompt J/ψ $R_{\rm AA}$ is below unity and is higher than the inclusive J/ψ $R_{\rm AA}$ in the whole $p_{\rm T}$ range, especially for $p_{\rm T} \geq 12$ GeV/c where the B-contribution is the largest. If $R_{\rm AA}^{\rm npro} = 1$, for both centrality ranges, the estimated prompt J/ψ $R_{\rm AA}$ is lower than the inclusive J/ψ $R_{\rm AA}$ in the whole $p_{\rm T}$ range and can drop to zero for $p_{\rm T} > 12$ GeV/c (centrality 0–20%) and to 0.09 for $12 < p_{\rm T} < 15$ GeV/c (centrality 20–40%).

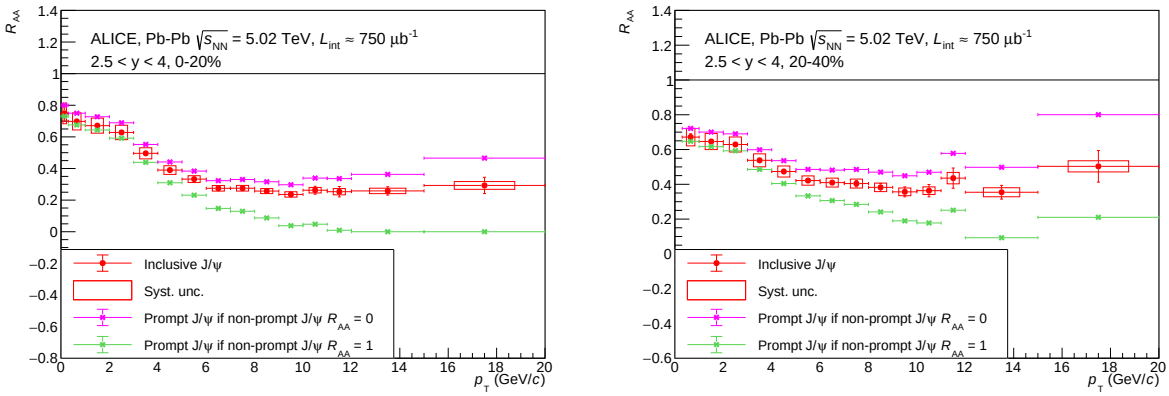

Figure C.2: $p_{\rm T}$-dependence of the inclusive J/ψ $R_{\rm AA}$ (red), prompt J/ψ $R_{\rm AA}$ if $R_{\rm AA}^{\rm npro} = 0$ (magenta) or if $R_{\rm AA}^{\rm npro} = 1$ (green) in the 0–20% (left) and 20–40% (right) centrality ranges [This thesis].

Figure C.3 shows the $p_{\rm T}$-dependence of the inclusive J/ψ $R_{\rm AA}$ measured in this thesis and of the prompt J/ψ $R_{\rm AA}$ estimated if $R_{\rm AA}^{\rm npro} = 0$ or if $R_{\rm AA}^{\rm npro} = 1$ for the 40–90% centrality class. For the case $R_{\rm AA}^{\rm npro} = 0$, the estimated prompt J/ψ $R_{\rm AA}$ is systematically higher than the inclusive one in the full $p_{\rm T}$ range and is above unity for $15 < p_{\rm T} < 20$ GeV/c. If $R_{\rm AA}^{\rm npro} = 1$, the estimated prompt J/ψ $R_{\rm AA}$ is lower by about 24% than the inclusive one.

We also use the non-prompt J/ψ $R_{\rm AA}$ measured by the ATLAS [8] and CMS [7] experiments to estimate the prompt J/ψ $R_{\rm AA}$. The f_B fraction at $\sqrt{s} = 8$ TeV from LHCb is used as well. Note that the rapidity range covered by the ATLAS ($0 < y < 2$) and CMS ($0 < y < 2.4$) experiments are different from the rapidity range of the ALICE muon spectrometer. Besides, the non-prompt J/ψ $R_{\rm AA}$ is measured by CMS in the centrality ranges, 0–10%, 10–30% and 30–100%, while ATLAS provides a measurement in the 0–20% centrality range only. We therefore assume with this choice that the non-prompt $R_{\rm AA}$ does not depend on rapidity.

Figure C.4 shows the $p_{\rm T}$-dependence of the inclusive J/ψ $R_{\rm AA}$ (red) and of the prompt J/ψ $R_{\rm AA}$ (black and green), in most central collisions, estimated by using the data from the ATLAS [8] and CMS [7] experiments, respectively. The $R_{\rm AA}^{\rm pro}$ evaluated with the $R_{\rm AA}$ non-prompt assumption from the ATLAS data is very close to the central values of the ALICE $R_{\rm AA}^{\rm incl}$. The $R_{\rm AA}^{\rm pro}$ evaluated with the $R_{\rm AA}$ non-prompt assumption from the CMS data is systematically lower than the $R_{\rm AA}^{\rm incl}$. The relative difference between the $R_{\rm AA}^{\rm incl}$ and the $R_{\rm AA}^{\rm pro}$ is within 18%.

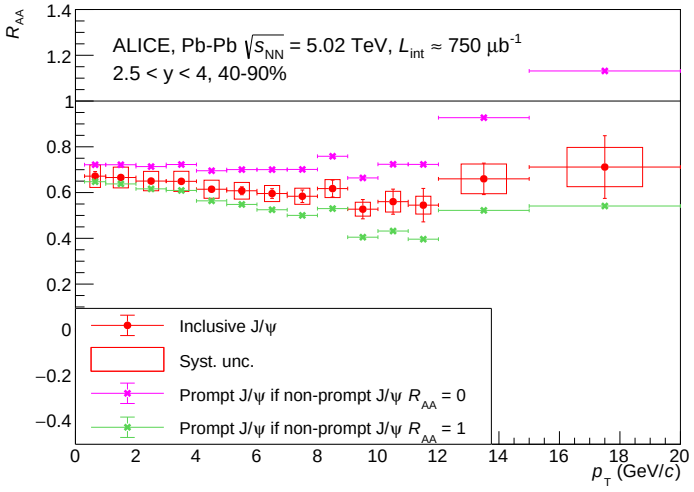

Figure C.3: p_{T}-dependence of inclusive J/ψ R_{AA} (red), prompt J/ψ R_{AA} if $R_{\mathrm{AA}}^{\mathrm{npro}} = 0$ (magenta) or if $R_{\mathrm{AA}}^{\mathrm{npro}} = 1$ (green) in the 40–90% centrality range [This thesis].

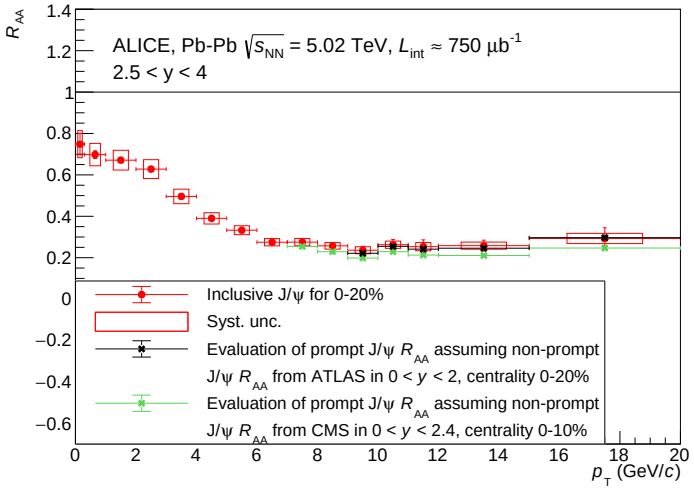

Figure C.4: p_{T}-dependence of R_{AA} of inclusive J/ψ (red) and prompt J/ψ (black and green) when the ATLAS $R_{\mathrm{AA}}^{\mathrm{npro}}$ [8] and the CMS $R_{\mathrm{AA}}^{\mathrm{npro}}$ [7], respectively, are used in most central collisions [This thesis].

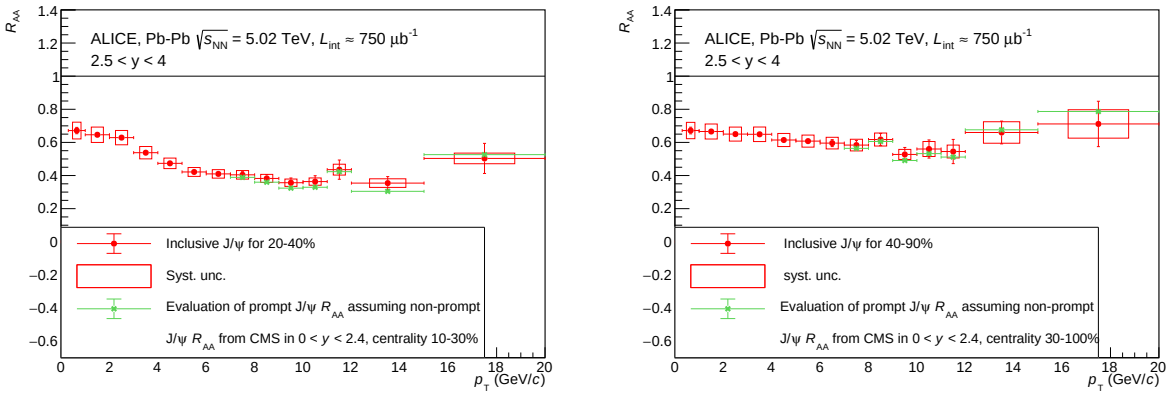

Figure C.5: p_{T}-dependence of the inclusive J/ψ R_{AA} (red) and the prompt J/ψ R_{AA} (green) when the CMS $R_{\mathrm{AA}}^{\mathrm{npro}}$ [7] is used in semi-central (left) and peripheral collisions (right) [This thesis].

The left panel of Figure C.5 shows the p_{T}-dependence of the inclusive J/ψ R_{AA} (red) and of the prompt J/ψ R_{AA} (green) estimated by using the CMS data [7] in semi-central collisions. The relative difference between the $R_{\mathrm{AA}}^{\mathrm{incl}}$ and the $R_{\mathrm{AA}}^{\mathrm{pro}}$ is within 10%, except in the range $12 < p_{\mathrm{T}} < 15$ GeV/c where it reaches 14%. Also, the $R_{\mathrm{AA}}^{\mathrm{pro}}$ is systematically lower than the $R_{\mathrm{AA}}^{\mathrm{incl}}$ for $7 < p_{\mathrm{T}} < 15$ GeV/c. The right panel of Figure C.5 shows the p_{T}-dependence of the inclusive J/ψ R_{AA} (red) and of the prompt J/ψ R_{AA} (green) estimated by using the CMS data [7] in peripheral collisions. The relative difference between the $R_{\mathrm{AA}}^{\mathrm{incl}}$ and the $R_{\mathrm{AA}}^{\mathrm{pro}}$ is within 11%. In conclusion, one can expect that inclusive J/ψ R_{AA} measurement from ALICE is not strongly affected by the B feed-down contribution (impact of 18% at maximum in central events) if the non-prompt R_{AA} does not depend on rapidity. A measurement of R_{AA} non-prompt will be carried out in Run 3 and Run 4 by using the Muon Forward Tracker.

List of Figures

List of Tables

Bibliography

[1] **Lansberg, J.-P., Shao, H.-S., Yamanaka, N., Zhang, Y.-J.** and **Noûs, C.**, *Complete NLO QCD study of single- and double-quarkonium hadroproduction in the colour-evaporation model at the Tevatron and the LHC*, Phys. Lett. B, Vol. 807, pp. 135559, 2020, doi: https://doi.org/10.1016/j.physletb.2020.135559.

[2] **Cheung, V.** and **Vogt, R.**, *Production and polarization of prompt J/ψ in the improved color evaporation model using the k_T-factorization approach*, Phys. Rev. D, Vol. 98, pp. 114029, Dec 2018, doi: https://doi.org/10.1103/PhysRevD.98.114029.

[3] **Butenschön, M.** and **Kniehl, B. A.**, *Reconciling J/ψ Production at HERA, RHIC, Tevatron, and LHC with Nonrelativistic QCD Factorization at Next-to-Leading Order*, Phys. Rev. Lett., Vol. 106, pp. 022003, Jan 2011, doi: https://doi.org/10.1103/PhysRevLett.106.022003.

[4] **Ma, Y.-Q., Wang, K.** and **Chao, K.-T.**, *$J/\psi(\psi^{'})$ Production at the Tevatron and LHC at $\mathcal{O}(\alpha_s^4 v^4)$ in Nonrelativistic QCD*, Phys. Rev. Lett., Vol. 106, pp. 042002, Jan 2011, doi: https://doi.org/10.1103/PhysRevLett.106.042002.

[5] **Ma, Y.-Q.** and **Venugopalan, R.**, *Comprehensive Description of J/ψ Production in Proton-Proton Collisions at Collider Energies*, Phys. Rev. Lett., Vol. 113, pp. 192301, 2014, doi: https://doi.org/10.1103/PhysRevLett.113.192301.

[6] **Cacciari, M., Frixione, S., Houdeau, N., Mangano, M. L., Nason, P.** and **Ridolfi, G.**, *Theoretical predictions for charm and bottom production at the LHC*, JHEP, Vol. 10, pp. 137, 2012, doi: https://doi.org/10.1007/JHEP10(2012)137.

[7] **CMS Collaboration, Sirunyan, A. M. et al.**, *Measurement of prompt and nonprompt charmonium suppression in PbPb collisions at 5.02 TeV*, Eur. Phys. J. C, Vol. 78, No. 6, pp. 509, 2018, doi: https://doi.org/10.1140/epjc/s10052-018-5950-6.

[8] **ATLAS Collaboration, Aaboud, M. et al.**, *Prompt and non-prompt J/ψ and ψ(2S) suppression at high transverse momentum in* 5.02 TeV *Pb+Pb collisions with the ATLAS experiment*, Eur. Phys. J. C, Vol. 78, No. 9, pp. 762, 2018, doi: https://doi.org/10.1140/epjc/s10052-018-6219-9.

[9] **Zhao, X.** and **Rapp, R.**, *Medium Modifications and Production of Charmonia at LHC*, Nucl. Phys. A, Vol. 859, pp. 114–125, 2011, doi: https://doi.org/10.1016/j.nuclphysa.2011.05.001.

[10] **Andronic, A., Braun-Munzinger, P., Köhler, M. K., Redlich, K.** and **Stachel, J.**, *Transverse momentum distributions of charmonium states with the statistical hadronization model*, Phys. Lett. B, Vol. 797, pp. 134836, 2019, doi: https://doi.org/10.1016/j.physletb.2019.134836.

[11] **Mertens, S.**, *Direct Neutrino Mass Experiments*, J. Phys. Conf. Ser., Vol. 718, No. 2, pp. 022013, 2016, doi: https://doi.org/10.1088/1742-6596/718/2/022013.

[12] **Feynman, R.**, Quantum Electrodynamics, Westview Press, 1998, ISBN: 9780201360752.

[13] **Sakata, S., Umezawa, H.** and **Kamefuchi, S.**, *On the structure of the interaction of the elementary particles. I: The renormalizability of the interaction*, Prog. Theor. Phys., Vol. 7, pp. 377–390, 1952, https://doi.org/10.1143/PTP.7.377.

[14] **Galileo Galilei (GG) project**, *Phase A-2 study report of the GG mission in space*, GG Phase A-2 Study Report, 2009.

[15] **Gell-Mann, M.**, *A Schematic Model of Baryons and Mesons*, Phys. Lett., Vol. 8, pp. 214–215, 1964, https://doi.org/10.1016/S0031-9163(64)92001-3.

[16] **Gross, D.** and **Wilczek, F.**, *Ultraviolet Behavior of Non-Abelian Gauge Theories*, Phys. Rev. Lett., Vol. 30, pp. 1343, 1973, https://doi.org/10.1103/PhysRevLett.30.1343.

[17] **Politzer, H. D.**, *Reliable Perturbative Results for Strong Interactions?*, Phys. Rev. Lett., Vol. 30, pp. 1346, 1973, https://doi.org/10.1103/PhysRevLett.30.1346.

[18] **Particle Data Group Collaboration, M. T. et al.**, *The Review of Particle Physics (2019)*, Phys. Rev. D, Vol. 98, pp. 030001, 2018.

[19] **S. Sarkar, H. S.** and **Sinha, B.**, *The physics of the quark-gluon plasma*, Lect. Notes Phys., Vol. 785, pp. 1–369, 2010, ISBN: 9783642022852, https://doi.org/10.1007/978-3-642-02286-9.

[20] **HotQCD Collaboration, Bazavov, A. et al.**, *Chiral crossover in QCD at zero and non-zero chemical potentials*, Phys. Lett. B, Vol. 795, pp. 15–21, 2019, https://doi.org/10.1016/j.physletb.2019.05.013.

[21] **Crkovská, J.**, Study of the J/ψ production in pp collisions at $\sqrt{s_{\rm NN}}$ = 5.02 TeV and of the J/ψ production multiplicity dependence in p-Pb collisions at $\sqrt{s_{\rm NN}}$ = 8.16 TeV with ALICE at the LHC, Theses, Université Paris-Saclay, Oct. 2018, https://cds.cern.ch/record/2651031.

[22] **NA49 Collaboration, Afanasiev, S. et al.**, *The NA49 large acceptance hadron detector*, Nucl. Instrum. Meth. A, Vol. 430, pp. 210–244, 1999, doi: https://doi.org/10.1016/S0168-9002(99)00239-9.

[23] **NA49 Collaboration, Alt, C. et al.**, *Pion and kaon production in central Pb + Pb collisions at 20-A and 30-A-GeV: Evidence for the onset of deconfinement*, Phys. Rev. C, Vol. 77, pp. 024903, 2008, doi: https://doi.org/10.1103/PhysRevC.77.024903.

[24] **Odyniec, G.**, *RHIC Beam Energy Scan Program: Phase I and II*, PoS, Vol. CPOD2013, pp. 043, 2013, doi: https://doi.org/10.22323/1.185.0043.

[25] **Harrison, M., Ludlam, T.** and **Ozaki, S.**, *RHIC project overview*, Nucl. Instrum. Meth. A, Vol. 499, No. 2, pp. 235 – 244, 2003, https://doi.org/10.1016/S0168-9002(02)01937-X.

[26] **Alford, M. G., Schmitt, A., Rajagopal, K.** and **Schäfer, T.**, *Color superconductivity in dense quark matter*, Rev. Mod. Phys., Vol. 80, pp. 1455–1515, Nov 2008, doi: https://doi.org/10.1103/RevModPhys.80.1455.

[27] **Strickland, M.**, *Anisotropic Hydrodynamics: Three lectures*, Acta Phys. Polon. B, Vol. 45, No. 12, pp. 2355–2394, 2014, doi: https://doi.org/10.5506/APhysPolB.45.2355.

[28] **Bjorken, J. D.**, *Highly Relativistic Nucleus-Nucleus Collisions: The Central Rapidity Region*, Phys. Rev. D, Vol. 27, pp. 140, 1983, https://doi.org/10.1103/PhysRevD.27.140.

[29] **Miller, M. L., Reygers, K., Sanders, S. J.** and **Steinberg, P.**, *Glauber modeling in high energy nuclear collisions*, Ann. Rev. Nucl. Part. Sci., Vol. 57, pp. 205–243, 2007, doi: https://doi.org/10.1146/annurev.nucl.57.090506.123020.

[30] **Koch, P., Müller, B.** and **Rafelski, J.**, *From strangeness enhancement to quark–gluon plasma discovery*, Int. J. Mod. Phys. A, Vol. 32, No. 31, pp. 1730024, 2017, doi: https://doi.org/10.1142/S0217751X17300241.

[31] **FOPI Collaboration, Pelte, D. et al.**, *Charged pion production in Au on Au collisions at 1 AGeV The FOPI Collaboration*, Z Phys. A, Vol. 357, pp. 215, 1997, doi: https://doi.org/10.1007/s002180050236.

[32] **E-802 Collaboration, Ahle, L. et al.**, *Particle production at high baryon density in central Au+Au reactions at 11.6A GeV/c*, Phys. Rev. C, Vol. 57, pp. R466–R470, Feb 1998, doi: https://doi.org/10.1103/PhysRevC.57.R466.

[33] **E-802 Collaboration, Ahle, L. et al.**, *Kaon production in Au+Au collisions at* 11.6AGeV/c, Phys. Rev. C, Vol. 58, pp. 3523–3538, Dec 1998, doi: https://doi.org/10.1103/PhysRevC.58.3523.

[34] **E-802 Collaboration, Ahle, L. et al.**, *Centrality dependence of kaon yields in* Si+A *and Au+Au collisions at relativistic energies*, Phys. Rev. C, Vol. 60, pp. 044904, Sep 1999, doi: https://doi.org/10.1103/PhysRevC.60.044904.

[35] **E802 Collaboration, Ahle, L. et al.**, *Proton and deuteron production in Au+Au reactions at* 11.6AGeV/c, Phys. Rev. C, Vol. 60, pp. 064901, Oct 1999, https://doi.org/10.1103/PhysRevC.60.064901.

[36] **E866 Collaboration, Ahle, L. et al.**, *Excitation function of K+ and pi+ production in Au + Au reactions at 2/A-GeV to 10/A-GeV*, Phys. Lett. B, Vol. 476, pp. 1–8, 2000, doi: https://doi.org/10.1016/S0370-2693(00)00037-X.

[37] **E866 Collaboration, Ahle, L. et al.**, *An Excitation function of K- and K+ production in Au + Au reactions at the AGS*, Phys. Lett. B, Vol. 490, pp. 53–60, 2000, doi: https://doi.org/10.1016/S0370-2693(00)00916-3.

[38] **E877 Collaboration, Barrette, J. et al.**, *Proton and pion production in Au + Au collisions at 10.8A-GeV/c*, Phys. Rev. C, Vol. 62, pp. 024901, 2000, doi: https://doi.org/10.1103/PhysRevC.62.024901.

[39] **E895 Collaboration, Klay, J. et al.**, *Longitudinal flow from 2-A-GeV to 8-A-GeV Au+Au collisions at the Brookhaven AGS*, Phys. Rev. Lett., Vol. 88, pp. 102301, 2002, doi: https://doi.org/10.1103/PhysRevLett.88.102301.

[40] **E917 Collaboration, Back, B. et al.**, *Proton emission in Au+Au collisions at 6-GeV/nucleon, 8-GeV/nucleon, and 10.8-GeV/nucleon*, Phys. Rev. C, Vol. 66, pp. 054901, 2002, doi: https://doi.org/10.1103/PhysRevC.66.054901.

[41] **E895 Collaboration, Klay, J. L. et al.**, *Charged pion production in* 2A *to* 8A *GeV central Au+Au Collisions*, Phys. Rev. C, Vol. 68, pp. 054905, Nov 2003, doi: https://doi.org/10.1103/PhysRevC.68.054905.

[42] **BRAHMS Collaboration, Bearden, I. et al.**, *Pseudorapidity distributions of charged particles from Au+Au collisions at the maximum RHIC energy*, Phys. Rev. Lett., Vol. 88, pp. 202301, 2002, doi: https://doi.org/10.1103/PhysRevLett.88.202301.

[43] **PHOBOS Collaboration, Back, B. et al.**, *Comparison of the total charged particle multiplicity in high-energy heavy ion collisions with e+ e- and p p / anti-p p data*, arXiv:nucl-ex/0301017, Jan. 2003, https://arxiv.org/abs/nucl-ex/0301017.

[44] **Velkovsky, M.** and **the PHENIX Collaboration**, *Kaon production in Au–Au collisions measured with the PHENIX experiment at RHIC*, Journal of Physics G: Nuclear and Particle Physics, Vol. 30, No. 1, pp. S187–S192, Dec. 2003, doi: https://doi.org/10.1088/0954-3899/30/1/019.

[45] **STAR Collaboration, Adler, C. et al.**, *Kaon production and kaon to pion ratio in Au+Au collisions at* $\sqrt{s_{\rm NN}}$ *= 130-GeV*, Phys. Lett. B, Vol. 595, pp. 143–150, 2004, doi: https://doi.org/10.1016/j.physletb.2004.06.044.

[46] **PHENIX Collaboration, Adler, S. S. et al.**, *Identified charged particle spectra and yields in Au + Au collisions at* $\sqrt{s_{\rm NN}}$ *= 200 GeV*, Phys. Rev. C, Vol. 69, pp. 034909, Mar 2004, doi: https://doi.org/10.1103/PhysRevC.69.034909.

[47] **PHENIX Collaboration, Adcox, K. et al.**, *Single identified hadron spectra from* $\sqrt{s_{\rm NN}}$ *= 130 GeV Au+Au collisions*, Phys. Rev. C, Vol. 69, pp. 024904, 2004, doi: https://doi.org/10.1103/PhysRevC.69.024904.

[48] **STAR Collaboration, Adams, J. et al.**, *Identified particle distributions in pp and Au+Au collisions at* $\sqrt{s_{\rm NN}}$ *= 200 GeV*, Phys. Rev. Lett., Vol. 92, pp. 112301, 2004, doi: https://doi.org/10.1103/PhysRevLett.92.112301.

[49] **BRAHMS Collaboration, Bearden, I. et al.**, *Charged meson rapidity distributions in central Au+Au collisions at* $\sqrt{s_{\rm NN}}$ *= 200 GeV*, Phys. Rev. Lett., Vol. 94, pp. 162301, 2005, doi: https://doi.org/10.1103/PhysRevLett.94.162301.

[50] **BRAHMS Collaboration, Arsene, I. et al.**, *Centrality dependent particle production at* $y = 0$ *and* $y \approx 1$ *in Au + Au collisions at* $\sqrt{s_{\rm NN}}$ *= 200 GeV*, Phys. Rev. C, Vol. 72, pp. 014908, 2005, doi: https://doi.org/10.1103/PhysRevC.72.014908.

[51] **M. Gadzicki, M. G.**, *On the early stage of nucleus-nucleus collisions*, Acta Phys. Polon. B, Vol. 30, pp. 2705, 1999, https://arxiv.org/abs/nucl-ex/0301017.

[52] **Beth, R. A.** and **Lasky, C.**, *The Brookhaven Alternating Gradient Synchrotron*, Science, Vol. 128, No. 3336, pp. 1393–1401, 1958, doi: https://doi.org/10.1126/science.128.3336.1393.

[53] **Gazdzicki, M.** and **Roehrich, D.**, *Pion multiplicity in nuclear collisions*, Z. Phys. C, Vol. 65, pp. 215–223, 1995, doi: https://doi.org/10.1007/BF01571878.

[54] **Gazdzicki, M.** and **Rohrich, D.**, *Strangeness in nuclear collisions*, Z. Phys. C, Vol. 71, pp. 55–64, 1996, doi: https://doi.org/10.1007/s002880050147.

[55] **Nouicer, R.**, *New State of Nuclear Matter: Nearly Perfect Fluid of Quarks and Gluons in Heavy Ion Collisions at RHIC Energies*, Eur. Phys. J. Plus, Vol. 131, No. 3, pp. 70, 2016, doi: https://doi.org/10.1140/epjp/i2016-16070-2.

[56] **Voloshin, S.** and **Zhang, Y.**, *Flow study in relativistic nuclear collisions by Fourier expansion of Azimuthal particle distributions*, Z. Phys. C, Vol. 70, pp. 665–672, 1996, doi: https://doi.org/10.1007/s002880050141.

[57] **Prakash, M., Prakash, M., Venugopalan, R.** and **Welke, G.**, *Nonequilibrium properties of hadronic mixtures*, Phys. Rept., Vol. 227, pp. 321–366, 1993, doi: https://doi.org/10.1016/0370-1573(93)90092-R.

[58] **Denicol, G., Monnai, A.** and **Schenke, B.**, *Moving forward to constrain the shear viscosity of QCD matter*, Phys. Rev. Lett., Vol. 116, No. 21, pp. 212301, 2016, doi: https://doi.org/10.1103/PhysRevLett.116.212301.

[59] **ALICE Collaboration, Aamodt, K. et al.**, *Higher harmonic anisotropic flow measurements of charged particles in Pb-Pb collisions at* $\sqrt{s_{\rm NN}}$ *= 2.76 TeV*, Phys. Rev. Lett., Vol. 107, pp. 032301, 2011, doi: https://doi.org/10.1103/PhysRevLett.107.032301.

[60] **ALICE Collaboration, Acharya, S. et al.**, *Measurement of* Υ(1S) *elliptic flow at forward rapidity in Pb-Pb collisions at* $\sqrt{s_{\rm NN}}$ = 5.02 *TeV*, Phys. Rev. Lett., Vol. 123, No. 19, pp. 192301, 2019, doi: https://doi.org/10.1103/PhysRevLett.123.192301.

[61] **ALICE Collaboration, Acharya, S. et al.**, *Study of J/*ψ *azimuthal anisotropy at forward rapidity in Pb-Pb collisions at* $\sqrt{s_{\rm NN}}$ = 5.02 *TeV*, JHEP, Vol. 02, pp. 012, 2019, doi: https://doi.org/10.1007/JHEP02(2019)012.

[62] **ALICE Collaboration, Acharya, S. et al.**, *Investigations of Anisotropic Flow Using Multiparticle Azimuthal Correlations in pp, p-Pb, Xe-Xe, and Pb-Pb Collisions at the LHC*, Phys. Rev. Lett., Vol. 123, No. 14, pp. 142301, 2019, doi: https://doi.org/10.1103/PhysRevLett.123.142301.

[63] **Schenke, B., Tribedy, P.** and **Venugopalan, R.**, *Multiplicity distributions in p+p, p+A and A+A collisions from Yang-Mills dynamics*, Phys. Rev. C, Vol. 89, No. 2, pp. 024901, 2014, doi: https://doi.org/10.1103/PhysRevC.89.024901.

[64] **Mäntysaari, H., Schenke, B., Shen, C.** and **Tribedy, P.**, *Imprints of fluctuating proton shapes on flow in proton-lead collisions at the LHC*, Phys. Lett. B, Vol. 772, pp. 681–686, 2017, doi: https://doi.org/10.1016/j.physletb.2017.07.038.

[65] **Sjöstrand, T., Ask, S., Christiansen, J. R., Corke, R., Desai, N., Ilten, P., Mrenna, S., Prestel, S., Rasmussen, C. O.** and **Skands, P. Z.**, *An introduction to PYTHIA 8.2*, Comput. Phys. Commun., Vol. 191, pp. 159–177, 2015, doi: https://doi.org/10.1016/j.cpc.2015.01.024.

[66] **Conesa del Valle, Z.**, *Vector bosons in heavy-ion collisions at the LHC*, Eur. Phys. J. C, Vol. 61, pp. 729–733, 2009, doi: https://doi.org/10.1140/epjc/s10052-009-0980-8.

[67] **Stocco, D.**, *Electroweak boson production in p–Pb and Pb–Pb collisions at* $\sqrt{s_{\rm NN}}$ *= 5.02 TeV with ALICE*, Nuclear Physics A, Vol. 967, pp. 309 – 312, 2017, https://doi.org/10.1016/j.nuclphysa.2017.05.051.

[68] **ATLAS Collaboration, Aad, G. et al.**, *Z boson production in p+Pb collisions at* $\sqrt{s_{NN}} = 5.02$ *TeV measured with the ATLAS detector*, Phys. Rev. C, Vol. 92, No. 4, pp. 044915, 2015, doi: https://doi.org/10.1103/PhysRevC.92.044915.

[69] **CMS Collaboration, Zsigmond, A. J.**, *Z and W boson production in pPb collisions with CMS*, Nucl. Phys. A, Vol. 931, pp. 718–723, 2014, doi: https://doi.org/10.1016/j.nuclphysa.2014.07.039.

[70] **CMS Collaboration, Zsigmond, A. J.**, *Electroweak bosons in heavy ion collisions in CMS*, Nucl. Phys. A, Vol. 926, pp. 34–40, 2014, doi: https://doi.org/10.1016/j.nuclphysa.2014.02.016.

[71] **Connors, M., Nattrass, C., Reed, R.** and **Salur, S.**, *Jet measurements in heavy ion physics*, Rev. Mod. Phys., Vol. 90, pp. 025005, 2018, https://doi.org/10.1103/RevModPhys.90.025005.

[72] **CMS Collaboration, Chatrchyan, S. et al.**, *Observation and studies of jet quenching in PbPb collisions at* $\sqrt{s_{\mathrm{NN}}} = 2.76$ *TeV*, Phys. Rev. C, Vol. 84, pp. 024906, 2011, doi: https://doi.org/10.1103/PhysRevC.84.024906.

[73] **CMS Collaboration, Tatar, K.**, *Study of Z+jet correlations in PbPb and pp collisions at* $\sqrt{s_{\mathrm{NN}}} = 5.02$ *TeV*, Nucl. Part. Phys. Proc., Vol. 289-290, pp. 321–324, 2017, doi: https://doi.org/10.1016/j.nuclphysbps.2017.05.074.

[74] **Satz, H.**, *Colour deconfinement and quarkonium binding*, J. Phys. G, Vol. 32, pp. R25, 2006, doi: https://doi.org/10.1088/0954-3899/32/3/R01.

[75] **Matsui, T.** and **Satz, H.**, J/ψ *Suppression by Quark-Gluon Plasma Formation*, Phys. Lett. B, Vol. 178, pp. 416–422, 1986, doi: https://doi.org/10.1016/0370-2693(86)91404-8.

[76] **Braun-Munzinger, P.** and **Stachel, J.**, *(Non)thermal aspects of charmonium production and a new look at* J/ψ *suppression*, Phys. Lett. B, Vol. 490, pp. 196–202, 2000, doi: https://doi.org/10.1016/S0370-2693(00)00991-6.

[77] **Thews, R. L., Schroedter, M.** and **Rafelski, J.**, *Enhanced* J/ψ *production in deconfined quark matter*, Phys. Rev. C, Vol. 63, pp. 054905, 2001, doi: https://doi.org/10.1103/PhysRevC.63.054905.

[78] **Braaten, E.** and **Thoma, M. H.**, *Energy loss of a heavy quark in the quark - gluon plasma*, Phys. Rev. D, Vol. 44, No. 9, pp. 2625, 1991, doi: https://doi.org/10.1103/PhysRevD.44.R2625.

[79] **Baier, R., Dokshitzer, Y. L., Mueller, A. H., Peigne, S.** and **Schiff, D.**, *Radiative energy loss and p(T) broadening of high-energy partons in nuclei*, Nucl. Phys. B, Vol. 484, pp. 265–282, 1997, doi: https://doi.org/10.1016/S0550-3213(96)00581-0.

[80] **Aubert, J. et al.**, *Experimental Observation of a Heavy Particle J*, Phys. Rev. Lett., Vol. 33, pp. 1404–1406, 1974, doi: https://doi.org/10.1103/PhysRevLett.33.1404.

[81] **Augustin, J. E. et al.**, *Discovery of a Narrow Resonance in e^+e^- Annihilation*, Phys. Rev. Lett., Vol. 33, pp. 1406–1408, Dec 1974, doi: https://doi.org/10.1103/PhysRevLett.33.1406.

[82] **Luth, V. et al.**, *The Quantum Numbers and Decay Widths of the psi-prime (3684)*, Phys. Rev. Lett., Vol. 35, pp. 1124–1126, 1975, doi: https://doi.org/10.1103/PhysRevLett.35.1124.

[83] **Lansberg, J.-P.**, Quarkonium production at high-energy hadron colliders: A Systematic gauge-invariant approach to relativistic effects of J/ψ, ψ' and v production, Other thesis, Liege University, Apr. 2005, arXiv:hep-ph/0507175.

[84] **Griffiths, D.**, Introduction to Elementary Particles, Wiley, 2008, ISBN: 9783527406012.

[85] **Andronic, A. et al.**, *Heavy-flavour and quarkonium production in the LHC era: from proton–proton to heavy-ion collisions*, Eur. Phys. J. C, Vol. 76, No. 3, pp. 107, 2016, doi: https://doi.org/10.1140/epjc/s10052-015-3819-5.

[86] **Halzen, F.**, *CVC for gluons and hadroproduction of quark flavours*, Physics Letters B, Vol. 69, No. 1, pp. 105 – 108, 1977, doi: https://doi.org/10.1016/0370-2693(77)90144-7.

[87] **Glück, M., Owens, J. F.** and **Reya, E.**, *Gluon contribution to hadronic J/ψ production*, Phys. Rev. D, Vol. 17, pp. 2324–2331, May 1978, doi: https://doi.org/10.1103/PhysRevD.17.2324.

[88] **Chao-Hsi, C.**, *Hadronic production of J/ψ associated with a gluon*, Nuclear Physics B, Vol. 172, pp. 425 – 434, 1980, doi: https://doi.org/10.1016/0550-3213(80)90175-3.

[89] **Berger, E. L.** and **Jones, D.**, *Inelastic photoproduction of $\frac{J}{\psi}$ and Υ by gluons*, Phys. Rev. D, Vol. 23, pp. 1521–1530, Apr 1981, doi: https://doi.org/10.1103/PhysRevD.23.1521.

[90] **Bodwin, G. T., Braaten, E.** and **Lepage, G.**, *Erratum: Rigorous QCD analysis of inclusive annihilation and production of heavy quarkonium [Phys. Rev. D 51, 1125 (1995)]*, Phys. Rev. D, Vol. 55, pp. 5853–5854, May 1997, doi: https://doi.org/10.1103/PhysRevD.55.5853.

[91] **Gunji, T.**, J/psi production in high energy heavy ion collisions at RHIC, Ph.D. thesis, Tokyo U., 2007, CNS-REP-73.

[92] **Ma, Y.-Q.** and **Vogt, R.**, *Quarkonium Production in an Improved Color Evaporation Model*, Phys. Rev. D, Vol. 94, No. 11, pp. 114029, 2016, doi: https://doi.org/10.1103/PhysRevD.94.114029.

[93] **Brodsky, S. J.** and **Lansberg, J.-P.**, *Heavy-Quarkonium Production in High Energy Proton-Proton Collisions at RHIC*, Phys. Rev. D, Vol. 81, pp. 051502, 2010, doi: https://doi.org/10.1103/PhysRevD.81.051502.

[94] **Feng, Y., Lansberg, J.-P.** and **Wang, J.-X.**, *Energy dependence of direct-quarkonium production in pp collisions from fixed-target to LHC energies: complete one-loop analysis*, Eur. Phys. J. C, Vol. 75, No. 7, pp. 313, 2015, doi: https://doi.org/10.1140/epjc/s10052-015-3527-1.

[95] **H1 Collaboration, Aaron, F. et al.**, *Inelastic Production of J/ψ Mesons in Photoproduction and Deep Inelastic Scattering at HERA*, Eur. Phys. J. C, Vol. 68, pp. 401–420, 2010, doi: https://doi.org/10.1140/epjc/s10052-010-1376-5.

[96] **CDF Collaboration, Abe, F. et al.**, *Production of J/ψ mesons from χ_c meson decays in $p\bar{p}$ collisions at $\sqrt{s} = 1.8$ TeV*, Phys. Rev. Lett., Vol. 79, pp. 578–583, 1997, doi: https://doi.org/10.1103/PhysRevLett.79.578.

[97] **Brambilla, N. et al.**, *Heavy Quarkonium: Progress, Puzzles, and Opportunities*, Eur. Phys. J. C, Vol. 71, pp. 1534, 2011, doi: https://doi.org/10.1140/epjc/s10052-010-1534-9.

[98] **Butenschoen, M.** and **Kniehl, B. A.**, *J/ψ polarization at Tevatron and LHC: Nonrelativistic-QCD factorization at the crossroads*, Phys. Rev. Lett., Vol. 108, pp. 172002, 2012, doi: https://doi.org/10.1103/PhysRevLett.108.172002.

[99] **Gong, B., Wan, L.-P., Wang, J.-X.** and **Zhang, H.-F.**, *Polarization for Prompt J/ψ and $\psi(2s)$ Production at the Tevatron and LHC*, Phys. Rev. Lett., Vol. 110, No. 4, pp. 042002, 2013, doi: https://doi.org/10.1103/PhysRevLett.110.042002.

[100] **Chao, K.-T., Ma, Y.-Q., Shao, H.-S., Wang, K.** and **Zhang, Y.-J.**, *J/ψ Polarization at Hadron Colliders in Nonrelativistic QCD*, Phys. Rev. Lett., Vol. 108, pp. 242004, 2012, doi: https://doi.org/10.1103/PhysRevLett.108.242004.

[101] **CDF Collaboration, Affolder, T. et al.**, *Measurement of J/ψ and $\psi(2S)$ polarization in $p\bar{p}$ collisions at $\sqrt{s} = 1.8$ TeV*, Phys. Rev. Lett., Vol. 85, pp. 2886–2891, 2000, doi: https://doi.org/10.1103/PhysRevLett.85.2886.

[102] **CDF Collaboration, Abulencia, A. et al.**, *Polarizations of J/ψ and $\psi(2S)$ Mesons Produced in $p\bar{p}$ Collisions at $\sqrt{s} = 1.96$ TeV*, Phys. Rev. Lett., Vol. 99, pp. 132001, 2007, doi: https://doi.org/10.1103/PhysRevLett.99.132001.

[103] **Butenschoen, M.** and **Kniehl, B. A.**, *J/ψ polarization at Tevatron and LHC: Nonrelativistic-QCD factorization at the crossroads*, Phys. Rev. Lett., Vol. 108, pp. 172002, 2012, doi: https://doi.org/10.1103/PhysRevLett.108.172002.

[104] **Iancu, E.** and **Venugopalan, R.**, *The Color glass condensate and high-energy scattering in QCD*, Quark–Gluon Plasma 3, pp. 249–363, Jan 2004, doi: https://doi.org/10.1142/9789812795533_0005.

[105] **ALICE Collaboration, Abelev, B. et al.**, *Measurement of prompt J/ψ and beauty hadron production cross sections at mid-rapidity in pp collisions at $\sqrt{s} = 7$ TeV*, JHEP, Vol. 11, pp. 065, 2012, doi: https://doi.org/10.1007/JHEP11(2012)065.

[106] **ATLAS collaboration**, *Comparison of D^* meson production cross sections with FONLL and GM-VFNS predictions*, Aug. 2011, ATL-PHYS-PUB-2011-012.

[107] **LHCb collaboration**, *Prompt charm production in pp collisions at $\sqrt{s} = 7$ TeV*, Dec. 2010, LHCb-CONF-2010-013; CERN-LHCb-CONF-2010-013.

[108] **Lourenco, C.** and **Wohri, H.**, *Heavy flavour hadro-production from fixed-target to collider energies*, Phys. Rept., Vol. 433, pp. 127–180, 2006, doi: https://doi.org/10.1016/j.physrep.2006.05.005.

[109] **STAR Collaboration, Adamczyk, L. et al.**, *Measurements of D^0 and D^* Production in $p+p$ Collisions at $\sqrt{s} = 200$ GeV*, Phys. Rev. D, Vol. 86, pp. 072013, 2012, doi: https://doi.org/10.1103/PhysRevD.86.072013.

[110] **PHENIX Collaboration, Adare, A. et al.**, *Heavy-quark production in p + p and energy loss and flow of heavy quarks in Au + Au collisions at $\sqrt{s_{NN}} = 200$ GeV*, Phys. Rev. C, Vol. 84, pp. 044905, Oct 2011, doi: https://doi.org/10.1103/PhysRevC.84.044905.

[111] **Mangano, M. L., Nason, P.** and **Ridolfi, G.**, *Heavy quark correlations in hadron collisions at next-to-leading order*, Nucl. Phys. B, Vol. 373, pp. 295–345, 1992, doi: https://doi.org/10.1016/0550-3213(92)90435-E.

[112] **ALICE Collaboration, Abelev, B. et al.**, *Measurement of charm production at central rapidity in proton-proton collisions at $\sqrt{s} = 2.76$ TeV*, JHEP, Vol. 07, pp. 191, 2012, doi: https://doi.org/10.1007/JHEP07(2012)191.

[113] **PHENIX Collaboration, Adare, A. et al.**, *Measurement of Bottom versus Charm as a Function of Transverse Momentum with Electron-Hadron Correlations in p^+p Collisions at $\sqrt{s} = 200$ GeV*, Phys. Rev. Lett., Vol. 103, pp. 082002, 2009.

[114] **Albajar, C. et al.**, *Beauty production at the CERN $p\bar{p}$ collider*, Phys. Lett. B, Vol. 256, pp. 121–128, 1991, doi: https://doi.org/10.1016/0370-2693(91)90228-I [Erratum: Phys.Lett.B 262, 497 (1991)].

[115] **CDF Collaboration, Abe, F. et al.**, *Measurement of the B Meson Differential Cross Section $d\sigma/\mathrm{dp}_T$ in $p\overline{p}$ Collisions at $\sqrt{s} = 1.8$ TeV*, Phys. Rev. Lett., Vol. 75, pp. 1451–1455, Aug 1995, doi: https://doi.org/10.1103/PhysRevLett.75.1451.

[116] **LHCb Collaboration, Aaij, R. et al.**, *Measurement of forward J/ψ production cross-sections in pp collisions at $\sqrt{s} = 13$ TeV*, JHEP, Vol. 10, pp. 172, 2015, doi: https://doi.org/10.1007/JHEP10(2015)172 [Erratum: JHEP 05, 063 (2017)].

[117] **LHCb Collaboration, Aaij, R. et al.**, *Measurement of $\psi(2S)$ meson production in pp collisions at $\sqrt{s}$= 7 TeV*, Eur. Phys. J. C, Vol. 72, pp. 2100, 2012, doi: https://doi.org/10.1140/epjc/s10052-012-2100-4 [Erratum: Eur.Phys.J.C 80, 49 (2020)].

[118] **LHCb Collaboration, Aaij, R. et al.**, *Measurement of the ratio of prompt χ_c to J/ψ production in pp collisions at $\sqrt{s} = 7$ TeV*, Phys. Lett. B, Vol. 718, pp. 431–440, 2012, doi: https://doi.org/10.1016/j.physletb.2012.10.068.

[119] **CMS Collaboration, Chatrchyan, S. et al.**, *J/ψ and ψ(2S) production in pp collisions at $\sqrt{s} = 7$ TeV*, JHEP, Vol. 02, pp. 011, 2012, doi: https://doi.org/10.1007/JHEP02(2012)011.

[120] **STAR Collaboration, Adam, J. et al.**, *J/ψ production cross section and its dependence on charged-particle multiplicity in $p + p$ collisions at $\sqrt{s} = 200$ GeV*, Phys. Lett. B, Vol. 786, pp. 87–93, 2018, doi: https://doi.org/10.1016/j.physletb.2018.09.029.

[121] **STAR Collaboration, Adamczyk, L. et al.**, *J/ψ production at high transverse momenta in $p + p$ and Au+Au collisions at $\sqrt{s_{NN}} = 200$ GeV*, Phys. Lett. B, Vol. 722, pp. 55–62, 2013, doi: https://doi.org/10.1016/j.physletb.2013.04.010.

[122] **PHENIX Collaboration, Adare, A. et al.**, *Transverse momentum dependence of J/psi polarization at midrapidity in p+p collisions at $\sqrt{s} = 200$ GeV*, Phys. Rev. D, Vol. 82, pp. 012001, 2010, doi: https://doi.org/10.1103/PhysRevD.82.012001.

[123] **Frawley, A. D., Ullrich, T.** and **Vogt, R.**, *Heavy flavor in heavy-ion collisions at RHIC and RHIC II*, Phys. Rept., Vol. 462, pp. 125–175, 2008, doi: https://doi.org/10.1016/j.physrep.2008.04.002.

[124] **Ma, Y.-Q., Wang, K.** and **Chao, K.-T.**, *Complete next-to-leading order calculation of the J/ψ and $\psi^{'}$ production at hadron colliders*, Phys. Rev. D, Vol. 84, pp. 114001, Dec 2011, doi: https://doi.org/10.1103/PhysRevD.84.114001.

[125] **ALICE Collaboration, Acharya, S. et al.**, *Energy dependence of forward-rapidity J/ψ and $\psi(\mathrm{2S})$ production in pp collisions at the LHC*, Eur. Phys. J. C, Vol. 77, No. 6, pp. 392, 2017, doi: https://doi.org/10.1140/epjc/s10052-017-4940-4.

[126] **Cacciari, M., Frixione, S., Houdeau, N., Mangano, M. L., Nason, P.** and **Ridolfi, G.**, *Theoretical predictions for charm and bottom production at the LHC*, JHEP, Vol. 10, pp. 137, 2012, doi: https://doi.org/10.1007/JHEP10(2012)137.

[127] **Abelev, B. et al.**, *Measurement of prompt J/ψ and beauty hadron production cross sections at mid-rapidity in pp collisions at $\sqrt{s} = 7$ TeV*, JHEP, Vol. 11, pp. 065, 2012, doi: https://doi.org/10.1007/JHEP11(2012)065.

[128] **Saleev, V. A., Nefedov, M. A.** and **Shipilova, A. V.**, *Prompt J/ψ production in the Regge limit of QCD: From the Tevatron to the LHC*, Phys. Rev. D, Vol. 85, pp. 074013, Apr 2012, doi: https://doi.org/10.1103/PhysRevD.85.074013.

[129] **Abachi, S. et al.**, *J/ψ production in $p\bar{p}$ collisions at $\sqrt{s} = 1.8$ TeV*, Phys. Lett. B, Vol. 370, pp. 239–248, 1996, doi: https://doi.org/10.1016/0370-2693(96)00067-6.

[130] **Abe, F. et al.**, *Production of J/ψ mesons from χ_c meson decays in $p\bar{p}$ collisions at $\sqrt{s} = 1.8$ TeV*, Phys. Rev. Lett., Vol. 79, pp. 578–583, 1997, doi: https://doi.org/10.1103/PhysRevLett.79.578.

[131] **CDF Collaboration, Acosta, D. et al.**, *Measurement of the J/ψ meson and $b-$hadron production cross sections in $p\bar{p}$ collisions at $\sqrt{s} = 1960$ GeV*, Phys. Rev. D, Vol. 71, pp. 032001, 2005, doi: https://doi.org/10.1103/PhysRevD.71.032001.

[132] **Shao, H., Han, H., Ma, Y., Meng, C., Zhang, Y.** and **Chao, K.**, *Yields and polarizations of prompt J/ψ and $\psi(2S)$ production in hadronic collisions*, JHEP, Vol. 05, pp. 103, 2015, doi: https://doi.org/10.1007/JHEP05(2015)103.

[133] **CMS Collaboration, Sirunyan, A. M. et al.**, *Measurement of prompt and nonprompt* J/ψ *production in* pp *and* pPb *collisions at* $\sqrt{s_{\mathrm{NN}}} = 5.02$ *TeV*, Eur. Phys. J. C, Vol. 77, No. 4, pp. 269, 2017, doi: https://doi.org/10.1140/epjc/s10052-017-4828-3.

[134] **ATLAS Collaboration, Aaboud, M. et al.**, *Measurement of quarkonium production in proton–lead and proton–proton collisions at* 5.02 TeV *with the ATLAS detector*, Eur. Phys. J. C, Vol. 78, No. 3, pp. 171, 2018, doi: https://doi.org/10.1140/epjc/s10052-018-5624-4.

[135] **Karsch, F., Mehr, M.** and **Satz, H.**, *Color Screening and Deconfinement for Bound States of Heavy Quarks*, Z. Phys. C, Vol. 37, pp. 617, 1988, doi: https://doi.org/10.1007/BF01549722.

[136] **Digal, S., Petreczky, P.** and **Satz, H.**, *String breaking and quarkonium dissociation at finite temperatures*, Phys. Lett. B, Vol. 514, pp. 57–62, 2001, doi: https://doi.org/10.1016/S0370-2693(01)00803-6.

[137] **Digal, S., Kaczmarek, O., Karsch, F.** and **Satz, H.**, *Heavy quark interactions in finite temperature QCD*, Eur. Phys. J. C, Vol. 43, pp. 71–75, 2005, doi: https://doi.org/10.1140/epjc/s2005-02309-7.

[138] **Grandchamp, L., Rapp, R.** and **Brown, G. E.**, *In-Medium Effects on Charmonium Production in Heavy-Ion Collisions*, Phys. Rev. Lett., Vol. 92, pp. 212301, May 2004, doi: https://doi.org/10.1103/PhysRevLett.92.212301.

[139] **Zhao, X.** and **Rapp, R.**, *Charmonium in Medium: From Correlators to Experiment*, Phys. Rev. C, Vol. 82, pp. 064905, 2010, doi: https://doi.org/10.1103/PhysRevC.82.064905.

[140] **Yan, L., Zhuang, P.** and **Xu, N.**, *J/ψ Production in Quark-Gluon Plasma*, Phys. Rev. Lett., Vol. 97, pp. 232301, Dec 2006, doi: https://doi.org/10.1103/PhysRevLett.97.232301.

[141] **Liu, Y.-p., Qu, Z., Xu, N.** and **Zhuang, P.-f.**, *J/ψ Transverse Momentum Distribution in High Energy Nuclear Collisions*, Phys. Lett. B, Vol. 678, pp. 72–76, 2009, doi: https://doi.org/10.1016/j.physletb.2009.06.006.

[142] **Andronic, A., Braun-Munzinger, P., Redlich, K.** and **Stachel, J.**, *The statistical model in Pb-Pb collisions at the LHC*, Nucl. Phys. A, Vol. 904-905, pp. 535c–538c, 2013, doi: https://doi.org/10.1016/j.nuclphysa.2013.02.070.

[143] **Andronic, A., Braun-Munzinger, P., Redlich, K.** and **Stachel, J.**, *Statistical hadronization of heavy quarks in ultra-relativistic nucleus-nucleus collisions*, Nucl. Phys. A, Vol. 789, pp. 334–356, 2007, doi: https://doi.org/10.1016/j.nuclphysa.2007.02.013.

[144] **Andronic, A., Braun-Munzinger, P., Redlich, K.** and **Stachel, J.**, *Evidence for charmonium generation at the phase boundary in ultra-relativistic nuclear collisions*, Phys. Lett. B, Vol. 652, pp. 259–261, 2007, doi: https://doi.org/10.1016/j.physletb.2007.07.036.

[145] **ALICE Collaboration, Acharya, S. et al.**, *Studies of J/ψ production at forward rapidity in Pb-Pb collisions at $\sqrt{s_{\rm NN}}$ = 5.02 TeV*, JHEP, Vol. 02, pp. 041, 2020, doi: https://doi.org/10.1007/JHEP02(2020)041.

[146] **Arleo, F.**, *Quenching of Hadron Spectra in Heavy Ion Collisions at the LHC*, Phys. Rev. Lett., Vol. 119, No. 6, pp. 062302, 2017, doi: https://doi.org/10.1103/PhysRevLett.119.062302.

[147] **Armesto, N., Capella, A.** and **Ferreiro, E. G.**, *Charmonium suppression in lead-lead collisions: Is there a break in the J/ψ cross section?*, Phys. Rev. C, Vol. 59, pp. 395–404, Jan 1999, doi: https://doi.org/10.1103/PhysRevC.59.395.

[148] **NA50 Collaboration, Abreu, M. et al.**, *Anomalous J/ψ suppression in Pb–Pb interactions at 158 GeV/c per nucleon*, Phys. Lett. B, Vol. 410, pp. 337–343, 1997, doi: https://doi.org/10.1016/S0370-2693(97)00915-5.

[149] **Ferreiro, E.**, *Charmonium dissociation and recombination at LHC: Revisiting comovers*, Phys. Lett. B, Vol. 731, pp. 57–63, 2014, doi: https://doi.org/10.1016/j.physletb.2014.02.011.

[150] **Capella, A.** and **Ferreiro, E. G.**, *J/ψ suppression and the decrease of nuclear absorption with increasing energy*, Phys. Rev. C, Vol. 76, pp. 064906, Dec 2007, doi: https://doi.org/10.1103/PhysRevC.76.064906.

[151] **Gribov, V.**, *Glauber corrections and the interaction between high-energy hadrons and nuclei*, Sov. Phys. JETP, Vol. 29, pp. 483–487, 1969.

[152] **Aubert, J. et al.**, *The ratio of the nucleon structure functions F_2^n for iron and deuterium*, Phys. Lett. B, Vol. 123, pp. 275–278, 1983, doi: https://doi.org/10.1016/0370-2693(83)90437-9.

[153] **New Muon Collaboration, Amaudruz, P. et al.**, *A Re-evaluation of the nuclear structure function ratios for D, He, Li-6, C and Ca*, Nucl. Phys. B, Vol. 441, pp. 3–11, 1995, doi: https://doi.org/10.1016/0550-3213(94)00023-9.

[154] **Armesto, N.**, *Nuclear shadowing*, J. Phys. G, Vol. 32, pp. R367–R394, 2006, doi: https://doi.org/10.1088/0954-3899/32/11/R01.

[155] **Rith, K.**, *Present Status of the EMC effect*, Subnucl. Ser., Vol. 51, pp. 431–449, 2015, arXiv:1402.5000.

[156] **ALICE collaboration, Abelev, B. B. et al.**, *J/ψ production and nuclear effects in p-Pb collisions at $\sqrt{S_{NN}}$ = 5.02 TeV*, JHEP, Vol. 02, pp. 073, 2014, doi: https://doi.org/10.1007/JHEP02(2014)073.

[157] **Eskola, K. J., Paakkinen, P., Paukkunen, H.** and **Salgado, C. A.**, *EPPS16: Nuclear parton distributions with LHC data*, Eur. Phys. J. C, Vol. 77, No. 3, pp. 163, 2017, doi: https://doi.org/10.1140/epjc/s10052-017-4725-9.

[158] **Arleo, F.** and **Tram, V.-N.**, *A Systematic study of J/ψ suppression in cold nuclear matter*, Eur. Phys. J. C, Vol. 55, pp. 449–461, 2008, doi: https://doi.org/10.1140/epjc/s10052-008-0604-8.

[159] **Lourenco, C., Vogt, R.** and **Woehri, H. K.**, *Energy dependence of J/ψ absorption in proton-nucleus collisions*, JHEP, Vol. 02, pp. 014, 2009, doi: https://doi.org/10.1088/1126-6708/2009/02/014.

[160] **Vitev, I., Goldman, T., Johnson, M. B.** and **Qiu, J. W.**, *Open charm tomography of cold nuclear matter*, Phys. Rev. D, Vol. 74, pp. 054010, Sep 2006, doi: https://doi.org/10.1103/PhysRevD.74.054010.

[161] **Lappi, T.**, *Gluon saturation at RHIC and LHC*, eCONF, Vol. C0906083, pp. 27, 2009.

[162] **Tarhini, M.**, Measurement of Z-boson and J/ψ Production in p-Pb and Pb-Pb Collisions at $\sqrt{s_{\rm NN}}$ = 5.02 TeV with ALICE at the LHC, Theses, Université Paris-Saclay, Jun. 2017, tel-01691725.

[163] **ALICE Collaboration, Acharya, S. et al.**, *Coherent J/ψ photoproduction at forward rapidity in ultra-peripheral Pb-Pb collisions at* $\sqrt{s_{\rm NN}}$ = 5.02 *TeV*, Phys. Lett. B, Vol. 798, pp. 134926, 2019, doi: https://doi.org/10.1016/j.physletb.2019.134926.

[164] **ALICE Collaboration, Adam, J. et al.**, *Measurement of an excess in the yield of J/ψ at very low* $p_{\rm T}$ *in Pb-Pb collisions at* $\sqrt{s_{\rm NN}}$ = *2.76 TeV*, Phys. Rev. Lett., Vol. 116, No. 22, pp. 222301, 2016, doi: https://doi.org/10.1103/PhysRevLett.116.222301.

[165] **Massacrier, L.**, *Coherent J/ψ photo-production in Pb–Pb collisions with nuclear overlap, studied with ALICE at the LHC*, PoS, Vol. HardProbes2018, pp. 181, 2019, doi: https://doi.org/10.22323/1.345.0181.

[166] **STAR Collaboration, Adam, J. et al.**, *Measurement of inclusive J/ψ suppression in Au+Au collisions at* $\sqrt{s_{\rm NN}}$ = *200 GeV through the dimuon channel at STAR*, Phys. Lett. B, Vol. 797, pp. 134917, 2019, doi: https://doi.org/10.1016/j.physletb.2019.134917.

[167] **STAR Collaboration, Adamczyk, L. et al.**, *J/ψ production at low* $p_{\rm T}$ *in Au + Au and Cu + Cu collisions at* $\sqrt{s_{\rm NN}}$ = *200 GeV with the STAR detector*, Phys. Rev. C, Vol. 90, No. 2, pp. 024906, 2014, doi: https://doi.org/10.1103/PhysRevC.90.024906.

[168] **STAR Collaboration, Adamczyk, L. et al.**, *J/ψ production at high transverse momenta in p + p and Au+Au collisions at* $\sqrt{s_{\rm NN}}$ = *200 GeV*, Phys. Lett. B, Vol. 722, pp. 55–62, 2013, doi: https://doi.org/10.1016/j.physletb.2013.04.010.

[169] **PHENIX Collaboration, Adare, A. et al.**, *J/ψ Production versus Centrality, Transverse Momentum, and Rapidity in Au+Au Collisions at* $\sqrt{s_{\rm NN}}$ = *200 GeV*, Phys. Rev. Lett., Vol. 98, pp. 232301, 2007, doi: https://doi.org/10.1103/PhysRevLett.98.232301.

[170] **ALICE Collaboration, Adam, J. et al.**, *Inclusive, prompt and non-prompt J/ψ production at mid-rapidity in Pb-Pb collisions at* $\sqrt{s_{\rm NN}}$ = *2.76 TeV*, JHEP, Vol. 07, pp. 051, 2015, doi: https://doi.org/10.1007/JHEP07(2015)051.

[171] **CMS Collaboration, Khachatryan, V. et al.**, *Suppression and azimuthal anisotropy of prompt and non-prompt* J/ψ *production in PbPb collisions at* $\sqrt{s_{NN}}$ = 2.76 TeV, Eur. Phys. J. C, Vol. 77, No. 4, pp. 252, 2017, doi: https://doi.org/10.1140/epjc/s10052-017-4781-1.

[172] **Zhou, K., Xu, N., Xu, Z.** and **Zhuang, P.**, *Medium effects on charmonium production at ultrarelativistic energies available at the CERN Large Hadron Collider*, Phys. Rev. C, Vol. 89, No. 5, pp. 054911, 2014, doi: https://doi.org/10.1103/PhysRevC.89.054911.

[173] **Sharma, R.** and **Vitev, I.**, *High transverse momentum quarkonium production and dissociation in heavy ion collisions*, Phys. Rev. C, Vol. 87, No. 4, pp. 044905, 2013, doi: https://doi.org/10.1103/PhysRevC.87.044905.

[174] **Du, X.** and **Rapp, R.**, *Sequential Regeneration of Charmonia in Heavy-Ion Collisions*, Nucl. Phys. A, Vol. 943, pp. 147–158, 2015, doi: https://doi.org/10.1016/j.nuclphysa.2015.09.006.

[175] **ATLAS Collaboration, Aad, G. et al.**, *Measurement of charged-particle spectra in Pb+Pb collisions at* $\sqrt{s_{\mathrm{NN}}} = 2.76$ *TeV with the ATLAS detector at the LHC*, JHEP, Vol. 09, pp. 050, 2015, doi: https://doi.org/10.1007/JHEP09(2015)050.

[176] **CMS Collaboration, Sirunyan, A. M. et al.**, *Nuclear modification factor of* D^0 *mesons in PbPb collisions at* $\sqrt{s_{\mathrm{NN}}} = 5.02$ *TeV*, Phys. Lett. B, Vol. 782, pp. 474–496, 2018, doi: https://doi.org/10.1016/j.physletb.2018.05.074.

[177] **Kopeliovich, B. Z., Potashnikova, I. K., Schmidt, I.** and **Siddikov, M.**, *Survival of charmonia in a hot environment*, Phys. Rev. C, Vol. 91, pp. 024911, Feb 2015, doi: https://doi.org/10.1103/PhysRevC.91.024911.

[178] **Aronson, S., Borras, E., Odegard, B., Sharma, R.** and **Vitev, I.**, *Collisional and thermal dissociation of* J/ψ *and* Υ *states at the LHC*, Phys. Lett. B, Vol. 778, pp. 384–391, 2018, doi: https://doi.org/10.1016/j.physletb.2018.01.038.

[179] **Spousta, M.**, *On similarity of jet quenching and charmonia suppression*, Phys. Lett. B, Vol. 767, pp. 10–15, 2017, doi: https://doi.org/10.1016/j.physletb.2017.01.041.

[180] **Faccioli, P., Lourenco, C., Seixas, J.** and **Wohri, H. K.**, *Towards the experimental clarification of quarkonium polarization*, Eur. Phys. J. C, Vol. 69, pp. 657–673, 2010, doi: https://doi.org/10.1140/epjc/s10052-010-1420-5.

[181] **ALICE Collaboration, Acharya, S. et al.**, *First measurement of quarkonium polarization in nuclear collisions at the LHC*, May 2020, arXiv:2005.11128.

[182] **ALICE Collaboration, Acharya, S. et al.**, *Measurement of the inclusive* J/ψ *polarization at forward rapidity in pp collisions at* $\sqrt{\mathrm{s}} = \mathbf{8}$ *TeV*, Eur. Phys. J. C, Vol. 78, No. 7, pp. 562, 2018, doi: https://doi.org/10.1140/epjc/s10052-018-6027-2.

[183] **LHCb Collaboration, Aaij, R. et al.**, *Measurement of* J/ψ *polarization in pp collisions at* $\sqrt{s} = 7$ *TeV*, Eur. Phys. J. C, Vol. 73, No. 11, pp. 2631, 2013, doi: https://doi.org/10.1140/epjc/s10052-013-2631-3.

[184] **Bruning, O. S. et al.**, *LHC Design Report*, Geneva: CERN, Vol. the LHC Main Ring, 2004, doi: https://doi.org/10.5170/CERN-2004-003-V-1.

[185] **Schaumann, M. et al.**, *First Xenon-Xenon Collisions in the LHC*, *9th International Particle Accelerator Conference*, p. MOPMF039, 2018, doi: https://doi.org/10.18429/JACoW-IPAC2018-MOPMF039.

[186] **Schindl, K.**, *The Injector Chain for the LHC*, pp. 47–52, Mar. 1999, CERN-PS-99-018-DI.

[187] **Boltezar, E. et al.**, *The New CERN 50-MeV LINAC.*, 10th International Linear Accelerator Conference, 1979.

[188] **Reich, K. H.**, *The CERN Proton Synchrotron Booster*, IEEE Trans.Nucl.Sci., Vol. 16, pp. 959, 1969, doi: https://doi.org/10.1109/TNS.1969.4325414.

[189] **Gilardoni, S. et al.**, *Fifty years of the CERN Proton Synchrotron : Volume 2*, CERN-2013-005, 2013, doi: https://doi.org/10.5170/CERN-2013-005.

[190] **Doble, N. et al.**, *The Super Proton Synchrotron (SPS): A Tale of Two Lives*, Technology Meets Research, p. 135, 2017, doi: https://doi.org/10.1142/9789814749145_0005.

[191] **Beuret, A. et al.**, *The LHC Lead Injector Chain*, p. 1153, Aug 2004, LHC-Project-Report-776.

[192] **Belochitskii, P. et al.**, *LEIR Commissioning*, p. 4p, Jul 2006, LHC-PROJECT-Report-923; CERN-LHC-Project-Report-923.

[193] **ATLAS Collaboration, G. A. et al.**, *The ATLAS Experiment at the CERN Large Hadron Collider*, Journal of Instrumentation, Vol. 3, pp. S08003, 2008, doi: http://dx.doi.org/10.1088/1748-0221/3/08/S08003.

[194] **CMS Collaboration, S. C. et al.**, *The CMS experiment at the CERN LHC*, Journal of Instrumentation, Vol. 3, pp. S08004, 2008, doi: https://doi.org/10.1088/1748-0221/3/08/S08004.

[195] **LHCb Collaboration**, *The LHCb Detector at the LHC*, Journal of Instrumentation, Vol. 3, pp. S08005, 2008, doi: http://dx.doi.org/10.1088/1748-0221/3/08/S08005.

[196] **ALICE Collaboration**, *The ALICE experiment at the CERN LHC*, Journal of Instrumentation, Vol. 3, pp. S08002, 2008, doi: https://doi.org/10.1088/1748-0221/3/08/S08002.

[197] **ALICE Collaboration, Abelev, B. et al.**, *Technical Design Report for the Upgrade of the ALICE Inner Tracking System*, J. Phys. G, Vol. 41, pp. 087002, 2014, doi: https://doi.org/10.1088/0954-3899/41/8/087002.

[198] **ALICE Collaboration, Lippmann, C.**, *Upgrade of the ALICE Time Projection Chamber*, 3 2014, CERN-LHCC-2013-020.

[199] **ALICE Collaboration, Acharya, S. et al.**, *The ALICE Transition Radiation Detector: construction, operation, and performance*, Nucl. Instrum. Meth. A, Vol. 881, pp. 88–127, 2018, doi: https://doi.org/10.1016/j.nima.2017.09.028.

[200] **ALICE Collaboration, Alici, A.**, *The MRPC-based ALICE Time-Of-Flight detector: status and performance*, Nucl. Instrum. Meth. A, Vol. 706, pp. 29–32, 2013, doi: https://doi.org/10.1016/j.nima.2012.05.004.

[201] **Lippmann, C.**, *Particle identification in ALICE boosts QGP studies*, Cern Courier, 2012, url: https://cerncourier.com/a/particle-identification-in-alice-boosts-qgp-studies/.

[202] **ALICE collaboration, Aamodt, K. et al.**, *Centrality Dependence of the Charged-Particle Multiplicity Density at Midrapidity in Pb-Pb Collisions at* $\sqrt{s_{\mathrm{NN}}}$ *= 2.76 TeV*, Physical review letters, Vol. 106, No. 032301, 2011, doi: https://doi.org/10.1103/PhysRevLett.106.032301.

[203] **ALICE collaboration, Cortese, P. et al.**, *ALICE technical design report on forward detectors: FMD, T0 and V0*, Sep. 2004, CERN-LHCC-2004-025.

[204] **ALICE collaboration, P. C. et al.**, *Performance of the ALICE Zero Degree Calorimeters and upgrade strategy*, Journal of Physics: Conference Series, Vol. 1162, pp. 012006, jan 2019, doi: https://doi.org/10.1088/1742-6596/1162/1/012006.

[205] **ALICE collaboration**, *ALICE technical design report of the dimuon forward spectrometer*, Aug. 1999, CERN-LHCC-99-22.

[206] **Saha institute of nuclear physics**, *Large Area Cathode Pad Chambers*, 2016, url: http://www.saha.ac.in/web/henppd-introduction-detector-working.

[207] **Zhang, X.**, Study of Heavy Flavours from Muons Measured with the ALICE Detector in Proton-Proton and Heavy-Ion Collisions at the CERN-LHC, Theses, Université Blaise Pascal - Clermont-Ferrand II, May 2012, tel-00786269.

[208] **ALICE Collaboration, Fabjan, C. W. et al.**, ALICE trigger data-acquisition high-level trigger and control system: Technical Design Report, Technical Design Report ALICE, CERN, 2004, CERN-LHCC-2003-062.

[209] **Engel, H. et al.**, *The alice high-level trigger read-out upgrade for LHC run2*, Journal of Instrumentation, Vol. 11, No. 01, 2016, doi: http://dx.doi.org/10.1088/1748-0221/11/01/C01041.

[210] **Carena, F. et al.**, *The ALICE data acquisition system*, Nuclear Instruments and Methods in Physics Research Section A: Accelerators, Spectrometers, Detectors and Associated Equipment, Vol. 741, pp. 130–162, 2014, doi: https://doi.org/10.1016/j.nima.2013.12.015.

[211] **ALICE Collaboration, J. G.-O. et al.**, *The ALICE Online-Offline Framework for the Extraction of Conditions Data* , Journal of Physics: Conference Series, Vol. 219, No. 022010, 2010, doi: https://doi.org/10.1088/1742-6596/219/2/022010.

[212] **ALICE Collaboration**, *Performance of the ALICE experiment at the CERN LHC*, Int. J. Mod. Phys. A, Vol. 29, No. 1430044, 2014, doi: https://doi.org/10.1142/S0217751X14300440.

[213] **Geant4 Collaboration**, *Geant4—a simulation toolkit*, Nucl. Instrum. Meth. A, Vol. 506, pp. 250, 2003, doi: https://doi.org/10.1016/S0168-9002(03)01368-8.

[214] **Brun, R., Bruyant, F., Maire, M., McPherson, A. C.** and **Zanarini, P.**, GEANT 3: user's guide Geant 3.10, Geant 3.11; rev. version, CERN, Geneva, 1987, url: https://cds.cern.ch/record/1119728.

[215] **F. Bossu, Z. C. d. V. et al.**, *Phenomenological interpolation of the inclusive J/ψ cross section to proton-proton collisions at 2.76 TeV and 5.5 TeV*, 2012, arXiv:1103.2394.

[216] **Lange, D. J.**, *The EvtGen particle decay simulation package*, Nucl. Instrum. Meth. A, Vol. 462, pp. 152–155, 2001, doi: https://doi.org/10.1016/S0168-9002(01)00089-4.

[217] **ALICE Collaboration**, *ALICE 2017 luminosity determination for pp collisions at $\sqrt{s}$ = 5 TeV*, Nov 2018, ALICE-PUBLIC-2018-014.

[218] **Pillot, P. et al.**, *J/ψ production in pp collisions at $\sqrt{s}$ = 5.02 TeV*, , No. 500, 2017, ALICE analysis note.

[219] **Blanco, J. M.**, *Study of J/ψ production dependence with the charged particle multiplicity in p-Pb collisions at $\sqrt{s_{\rm NN}}$ = 5.02 TeV and pp collisions at $\sqrt{s}$ = 8 TeV with the ALICE experiment at the LHC*, Vol. Ph.D. Thesis, SUBATECH, Nantes, 2016, CERN-THESIS-2016-070.

[220] **Stocco, D.**, Development of the ALICE Muon Spectrometer: Preparation for data taking and heavy flavor measurement, Theses, Turin U., 2008, CERN-THESIS-2008-144.

[221] **ALICE Collaboration, Abelev, B. B. et al.**, *Measurement of quarkonium production at forward rapidity in pp collisions at $\sqrt{s}$ = 7 TeV*, Eur. Phys. J. C, Vol. 74, No. 8, pp. 2974, 2014, doi: https://doi.org/10.1140/epjc/s10052-014-2974-4.

[222] **ALICE Collaboration, Adam, J. et al.**, *Inclusive quarkonium production at forward rapidity in pp collisions at $\sqrt{s}$ = 8 TeV*, Eur. Phys. J. C, Vol. 76, No. 4, pp. 184, 2016, doi: https://doi.org/10.1140/epjc/s10052-016-3987-y.

[223] **ALICE and LHCb Collaborations**, *Reference pp cross-sections for J/ψ studies in proton-lead collisions at $\sqrt{s_{NN}}$ = 5.02 TeV and comparisons between ALICE and LHCb results*, Dec. 2013, LHCb-CONF-2013-013; CERN-LHCb-CONF-2013-013; ALICE-PUBLIC-2013-002.

[224] **Suire, C. et al.**, *Centrality, rapidity and transverse momentum dependence of J/ψ suppression in Pb-Pb collisions at* $\sqrt{s_{\rm NN}}$ *= 2.76 TeV*, Vol. ALICE analysis note, No. 340, 2014.

[225] **ALICE Collaboration, Abelev, B. B. et al.**, *Centrality, rapidity and transverse momentum dependence of J/ψ suppression in Pb-Pb collisions at* $\sqrt{s_{\rm NN}}$*=2.76 TeV*, Phys. Lett. B, Vol. 734, pp. 314–327, 2014, doi: https://doi.org/10.1016/j.physletb.2014.05.064.

[226] **Crochet, P.** and **Braun-Munzinger, P.**, *Investigation of background subtraction techniques for high mass dilepton physics*, Nucl. Instrum. Meth. A, Vol. 484, pp. 564–572, 2002, doi: https://doi.org/10.1016/S0168-9002(01)02005-8.

[227] **ALICE Collaboration**, *Z boson production in p-Pb collisions at* $\sqrt{s_{\rm NN}}$ *= 8.16 TeV and Pb-Pb collisions at* $\sqrt{s_{\rm NN}}$ *= 5.02 TeV*, JHEP, Vol. 09, pp. 076, 2020, doi: https://doi.org/10.1007/JHEP09(2020)076.

[228] **ALICE Collaboration**, *Centrality determination in heavy ion collisions*, 2018, ALICE-PUBLIC-2018-011.

[229] **Bugnon, O.**, *Muon tracking efficiency for LHC18r and LHC18q*, url: https://indico.cern.ch/event/796503/contributions/3359823/attachments/1822060/2980665/MuonTrackingEfficiency_PbPb5TeV.pdf".

[230] **Ng, E.** and **Geller, M.**, *A table of integrals of the error functions*, Journal of Research of the National Bureau of Standards, Vol. 73B, 1969.

[231] **ALICE Collaboration, Adam, J. et al.**, *J/ψ suppression at forward rapidity in Pb-Pb collisions at* $\sqrt{s_{\rm NN}}$ **= 5.02** *TeV*, Phys. Lett. B, Vol. 766, pp. 212–224, 2017, doi: https://doi.org/10.1016/j.physletb.2016.12.064.

[232] **ALICE Collaboration**, *Quarkonium signal extraction in ALICE*, 2015, ALICE-PUBLIC-2015-006.

[233] **LHCb Collaboration, Aaij, R. et al.**, *Production of J/ψ and Upsilon mesons in pp collisions at* $\sqrt{s}$ *= 8 TeV*, JHEP, Vol. 06, pp. 064, 2013, doi: https://doi.org/10.1007/JHEP06(2013)064.

université PARIS-SACLAY | ÉCOLE DOCTORALE PHENIICS

Titre: Production inclusive de J/ψ en collisions pp et Pb-Pb à rapidité vers l'avant et à $\sqrt{s_{\rm NN}}$ = 5.02 TeV avec l'expérience ALICE au LHC

Mots clés: J/ψ, collisions hadroniques, collisions d'ions lourds, plasma de quarks et de gluons, ALICE, LHC

Résumé: Les collisions hadroniques de haute énergie sont considérés comme un outil précieux pour comprendre les mécanismes de production avec l'aide de la théorie de la chromodynamique quantique (QCD). À très haute température et/ou densité, la matière ordinaire subit une transition de phase, prédite par la QCD, et atteint une nouvelle phase de matière pour laquelle les quarks et les gluons sont confinés. Cette nouvelle phase de matière de la QCD est appelée le plasma de quarks et de gluons (PQG). En laboratoire, les collisions d'ions lourds ultra-relativistes sont utilisées pour atteindre les conditions de temperature et de densité pour recréer le PQG. Pour sonder et caractériser les propriétés du PQG, beaucoup d'observables ont été proposées. En particulier, la production de charmonia, constituée d'une paire de quark et d'antiquark charmés, est une des sondes proposés car la paire ccbar est produite au stade initial de la collision et peut traverser et interagir avec le milieu formé chaud et dense. De plus, la production de charmonia implique des échelles d'énergie dure et molle et permet d'étudier à la fois des aspects de la QCD perturbative et non perturbative. Dans ce document, les productions inclusives de J/ψ à rapidité vers l'avant en collisions pp et Pb-Pb mesurées à $\sqrt{s_{\rm NN}}$ = 5.02 TeV avec l'expérience ALICE (A Large Ion Collider Experiment) sont présentées. Les mesures sont effectuées dans le canal de désintégration du J/ψ en dimuon avec le spectromètre à muon d'ALICE. L'échantillon de données de haute statistique pp ainsi que l'ensemble des données Pb-Pb du Run 2 du LHC sont analysés et ces données permettent d'obtenir des résultats plus précis que les données précédemment publiées. La section efficace de production de J/ψ en collisions pp qui sert de référence aux mesures en collisions Pb-Pb est présentée en fonction de l'impulsion transverse ($p_{\rm T}$) et de la rapidité (y). Le facteur de modification nucléaire du J/ψ, défini comme le rapport entre le taux de J/ψ en collisions Pb-Pb et la section efficace pp, normalisée par la fonction de recoupement nucléaire, est exposé en fonction de $p_{\rm T}$. Ces mesures étendent le domaine en pt des précédentes mesures jusqu'à 20 GeV/c. La section efficace de production de J/ψ mesurée en collisions pp est comparé aux différents calculs théoriques basés sur les modèles NRQCD (non-relativistic QCD) et CEM (colour evaporation model). En collisions Pb-Pb, une comparaison entre les mesures du factor de modification nucléaire du J/ψ et les calculs théoriques basés sur des modèles de transport et statistique sont présentés.

Title: Inclusive J/ψ production in pp and Pb-Pb collisions at forward rapidity at $\sqrt{s_{\rm NN}}$ = 5.02 TeV in ALICE at the LHC

Keywords: J/ψ, hadron-hadron collisions, heavy-ion collisions, quark-gluon plasma, ALICE, LHC

Abstract: High-energy hadron-hadron collisions are considered as a useful tool which helps us to understand particle production mechanisms with the help of the Quantum Chromodynamics (QCD) theory. At extremely high temperature and/or high density, ordinary matter undergoes a phase transition, predicted by QCD, and reaches a new phase of matter in which quarks and gluons are deconfined. This new phase of QCD matter is called quark-gluon plasma (QGP). In laboratory, ultra-relativistic heavy-ion collisions are used to satisfy the temperature and density condition in order to recreate the QGP. To probe and characterize the QGP properties, many observables have been proposed. In particular, charmonium, made of a pair of charm and anticharm quarks, is one of the proposed probes because the $c\bar{c}$ are produced at the initial stage of the heavy-ion collision and can cross and interact with the hot and dense formed medium. Besides, charmonium production involves hard and soft energy scales and therefore provides an opportunity to study both perturbative and non-perturbative aspects of the QCD. In this manuscript, we report on inclusive J/ψ production at forward rapidity in pp and Pb-Pb collisions measured at $\sqrt{s_{\rm NN}}$ = 5.02 TeV in A Large Ion Collider Experiment (ALICE) at the LHC. The measurements are performed in the J/ψ dimuon decay channel with the muon spectrometer. The high-statistic pp data sample and the full Pb-Pb data sample of the LHC Run 2 period are analyzed and those datasets permit to obtain more precise results than the earlier published results. The J/ψ production cross section in pp collisions that serves as a reference for the measurements in Pb-Pb collisions is presented as a function of the transverse momentum ($p_{\rm T}$) and of the rapidity (y). The J/ψ nuclear modification factor, defined as the ratio of the yield in Pb-Pb collisions to the cross section in pp collisions scaled by the nuclear overlap function, is shown as a function of $p_{\rm T}$. The measurements are extended in $p_{\rm T}$, with respect to previous results, up to 20 GeV/c. The J/ψ production cross section measured in pp collisions is compared to different theoretical calculations based on non-relativistic QCD (NRQCD) model and on colour evaporation model (CEM). In Pb-Pb collisions, a comparison between the measured J/ψ nuclear modification factor and the theoretical calculations based on transport and on statistical model is presented.

Université Paris-Saclay
Espace Technologique / Immeuble Discovery
Route de l'Orme aux Merisiers RD 128 / 91190 Saint-Aubin, France